

## Design, fabrication and characterizations of AlGaIn/GaN heterostructure sensors

Sun, Jianwen

**DOI**

[10.4233/uuid:e8068b85-f8f6-4ebd-951f-e9216eb2cc2c](https://doi.org/10.4233/uuid:e8068b85-f8f6-4ebd-951f-e9216eb2cc2c)

**Publication date**

2020

**Document Version**

Final published version

**Citation (APA)**

Sun, J. (2020). *Design, fabrication and characterizations of AlGaIn/GaN heterostructure sensors*. [Dissertation (TU Delft), Delft University of Technology]. <https://doi.org/10.4233/uuid:e8068b85-f8f6-4ebd-951f-e9216eb2cc2c>

**Important note**

To cite this publication, please use the final published version (if applicable). Please check the document version above.

**Copyright**

Other than for strictly personal use, it is not permitted to download, forward or distribute the text or part of it, without the consent of the author(s) and/or copyright holder(s), unless the work is under an open content license such as Creative Commons.

**Takedown policy**

Please contact us and provide details if you believe this document breaches copyrights. We will remove access to the work immediately and investigate your claim.

# **DESIGN, FABRICATION AND CHARACTERIZATIONS OF ALGAN/GAN HETEROSTRUCTURE SENSORS**



# **DESIGN, FABRICATION AND CHARACTERIZATIONS OF ALGAN/GAN HETEROSTRUCTURE SENSORS**

## **Proefschrift**

ter verkrijging van de graad van doctor  
aan de Technische Universiteit Delft,  
op gezag van de Rector Magnificus Prof. dr. ir. T.H.J.J. van der Hagen,  
voorzitter van het College voor Promoties,  
in het openbaar te verdedigen op  
donderdag 25 juni 2020 om 12:30 uur

door

**Jianwen SUN**

Master of Engineering in Integrated Circuit Engineering,  
Tsinghua University, Beijing, China,  
geboren te Anhui, China.

Dit proefschrift is goedgekeurd door de

Samenstelling promotiecommissie:

Rector magnificus,	voorzitter
Prof. dr. ir. P. M. Sarro	Technische Universiteit Delft, promotor
Prof. dr. ir. G. Q. Zhang	Technische Universiteit Delft, promotor

Onafhankelijke leden

Prof. dr. ir. R. H. J. Fastenau	Technische Universiteit Delft
Prof. dr. P. J. French	Technische Universiteit Delft
Prof. dr. J. A. Ferreira	Technische Universiteit Twente
Prof. dr. X. J. Fan	Lamar University
Prof. dr. Y. F. Qiu	Xiamen University



*Keywords:* AlGaIn/GaN, HEMT, MEMS, Micro-heater, Pressure sensor, UV sensor, Gas sensor

*Printed by:* GILDEPRINT printing

*Front & Back:* Jianwen Sun

Copyright © 2020 by Jianwen Sun

ISBN 978-94-6402-350-3

All rights reserved. No part of the material protected by this copyright notice may be reproduced or utilized in any form or by any other means, electronic or mechanical, including photocopying, recording or by any other information storage and retrieval system, without the prior permission of the author.

An electronic version of this dissertation is available at

<http://repository.tudelft.nl/>.

*To all those who have helped me.*

Jianwen Sun



# CONTENTS

<b>Summary</b>	<b>ix</b>
<b>Samenvatting</b>	<b>xi</b>
<b>1 Introduction</b>	<b>1</b>
1.1 Background . . . . .	2
1.2 Wideband Semiconductor . . . . .	3
1.3 AlGaIn/GaN Heterostructure Sensors . . . . .	4
1.3.1 Gas Sensing . . . . .	4
1.3.2 Ultraviolet (UV) Detection . . . . .	5
1.3.3 Pressure Sensing . . . . .	6
1.4 Research Objective . . . . .	7
1.5 Thesis Structure . . . . .	8
References . . . . .	9
<b>2 Basic Theory of AlGaIn/GaN Heterostructure Sensors</b>	<b>13</b>
2.1 Introduction . . . . .	14
2.2 GaN Properties . . . . .	14
2.2.1 Polarization Effects in GaN Semiconductors . . . . .	15
2.2.2 2DEG Forming . . . . .	18
2.3 AlGaIn/GaN Heterostructure Sensors . . . . .	20
2.3.1 Surface Chemistry and Gas Sensing Mechanisms . . . . .	20
2.3.2 UV detection . . . . .	23
2.3.3 Pressure sensing . . . . .	25
2.4 Chapter Summary . . . . .	27
References . . . . .	27
<b>3 Design and Fabrication of AlGaIn/GaN Heterostructure Sensors</b>	<b>31</b>
3.1 Introduction . . . . .	32
3.2 Design and Fabrication of the basic HEMT MEMS Sensors . . . . .	32
3.2.1 The Sensor Geometry Design . . . . .	32
3.2.2 Mask Design and Process Flow . . . . .	33
3.2.3 Substrate material Selection . . . . .	34
3.2.4 Device Isolation . . . . .	36
3.2.5 Metalization . . . . .	37
3.2.6 Deep reaction ion etching (DRIE) . . . . .	40
3.3 Sensor Packaging . . . . .	40
3.3.1 Choice of Sensor Packaging . . . . .	43
3.3.2 Comparison of Two Packages . . . . .	43

3.4	Electrical Characterization of the HEMT Sensor Platform . . . . .	45
3.4.1	Ohmic Contact Measurement . . . . .	45
3.4.2	Micro-heater Calibration and Self-heating Influence. . . . .	46
3.4.3	I-V Characteristics of AlGaIn/GaN Sensor . . . . .	48
3.5	Chapter Summary . . . . .	52
	References . . . . .	52
<b>4</b>	<b>AlGaIn/GaN Heterostructure for Gas Sensing</b>	<b>55</b>
4.1	Introduction . . . . .	56
4.2	Nano WO <sub>3</sub> /AlGaIn/GaN Gas Sensor . . . . .	57
4.2.1	Device fabrication . . . . .	57
4.2.2	Gas Testing Setup . . . . .	59
4.2.3	Improving NO <sub>2</sub> Limit of Detection . . . . .	60
4.2.4	Response to Acetone . . . . .	65
4.3	Enhanced Sensitivity Using a Two-step Gate Recess Technique . . . . .	69
4.3.1	Two-step Gate Recess Technique. . . . .	69
4.3.2	Pt-Gate recessed HEMT Characterization . . . . .	70
4.4	Chapter Summary . . . . .	71
	References . . . . .	72
<b>5</b>	<b>AlGaIn/GaN Heterostructures Deep Ultraviolet Detectors</b>	<b>87</b>
5.1	Introduction . . . . .	88
5.2	Deep UV Illumination of AlGaIn/GaN Heterostructure Photodetectors . . . . .	90
5.2.1	Fabrication of Photodetectors . . . . .	90
5.2.2	Photodetector measurements . . . . .	91
5.2.3	Results and Discussion. . . . .	91
5.3	Suppression of Persistent Photoconductivity (PPC) Effect of AlGaIn/GaN Photodetectors . . . . .	95
5.3.1	Persistent Photoconductivity (PPC) Effect . . . . .	95
5.3.2	DC Heating Mode . . . . .	95
5.3.3	Pulsed Heating Mode . . . . .	97
5.3.4	Short-time Mono-pulse Heating Reset Mode. . . . .	100
5.4	Chapter Summary . . . . .	109
	References . . . . .	110
<b>6</b>	<b>Low Power AlGaIn/GaN MEMS Pressure Sensor</b>	<b>117</b>
6.1	Introduction . . . . .	118
6.2	GaN-based MEMS Pressure Sensor . . . . .	118
6.2.1	Device Fabrication. . . . .	118
6.2.2	Pressure Measurement Setup . . . . .	120
6.2.3	Static Measurement . . . . .	120
6.2.4	Dynamic Measurement . . . . .	123
6.2.5	Working principle of pressure sensing . . . . .	126
6.3	Chapter Summary . . . . .	128
	References . . . . .	128

---

<b>7</b>	<b>Conclusions and Research outlook</b>	<b>131</b>
7.1	Conclusions. . . . .	131
7.2	Research Outlook . . . . .	133
	<b>Acknowledgements</b>	<b>139</b>
	<b>Curriculum Vitæ</b>	<b>141</b>
	<b>List of Publications</b>	<b>143</b>



# SUMMARY

The microelectronics industry, next to the powerful, continuously scaling of integrated circuits, is currently evolving in the diversification of integrated functions, generally referred to as more than Moore (MtM). MtM concerns all technologies enabling micro-systems to be elevated to a higher integration level, and with small package size, lower power consumption and lower cost. Microelectromechanical (MEMS) are crucial within this development. While Si has proven to be the primary contestant in the MEMS sensor market, there is a growing need for sensors operating at conditions beyond the limits of Si. Si-based micro-sensors cannot operate in harsh environments such as high temperature, high radiation, high pressure, and chemically corrosive conditions. Wide bandgap semiconductors such as Gallium Nitride (GaN) are potential candidates to replace silicon due to their specific characteristics and proven performance in the power or LED applications. The research objective of this thesis is to develop a MEMS sensor platform utilizing GaN-based materials. The design, fabrication, packaging, and measurement of pressure, deep UV photodetector, and gas sensors are presented and discussed.

Due to the strong piezoelectric and spontaneous polarization effects in GaN and AlGa<sub>N</sub>, a high sheet density of two-dimensional electron gas (2DEG) is formed at the interface between AlGa<sub>N</sub> and GaN layers. These epitaxial layers were grown on <111> silicon substrates by MOCVD. The fabrication process started with mesa isolation by ICP etching. Then, a process module was specifically developed for low ohmic contact resistance. Afterward, e-beam evaporation and lift-off process were employed for deposition and patterning of metal layers for an integrated micro-heater and the device interconnect layers. Furthermore, a DRIE process was tuned to form the membrane structure, using silicon oxide as a hard mask. The completed sensors were packaged into CFQN packages due to the stable output current observed, compared to the COB package. The membrane temperature was affected by not only the micro-heater heating but also by the self-heating of the sensor. The device is not affected when exposed to high relative humidity ambient and the saturated current temperature coefficient is -0.63 mA/mm\*K.

The AlGa<sub>N</sub>/GaN heterojunctions exhibit great potential for high performance sensors development due to high carrier density two-dimensional electron gas (2DEG) at the interface introduced by the strong polarization effect, which is sensitive to the changes in surface potential. AlGa<sub>N</sub>/GaN HEMT sensors integrated with micro-heater on the suspended membrane were investigated for gas detection. The adoption of nano WO<sub>3</sub> as a functional layer result in the capability to detect low concentration of 100 ppb NO<sub>2</sub>/N<sub>2</sub> at 300 °C. When exposed to a 1 ppm NO<sub>2</sub> gas, a high sensing sensitivity of 1.1 % with a response (recovery) time of 88 seconds (132 seconds) is obtained. The WO<sub>3</sub>/AlGa<sub>N</sub>/GaN chip was packaged and further tested to determine detection limit and response time. Besides the improvement of detection limit, the WO<sub>3</sub> nanofilm also improved the sensitivity and selectivity to acetone gas. At 300 °C, a drain current change  $\Delta I_{DS}$  of 0.31 mA, as well as a high sensitivity of 25.7 % for 1000 ppm acetone were observed. For 1000 ppm

acetone concentration  $t_{Res}$  ( $t_{Rec}$ ) reduced from 147 (656) s at  $V_H = 3.5$  V (210 °C) to 48 (319) s at  $V_H = 4$  V (300 °C). Moreover, the response to 1000 ppm acetone gas was significantly larger than for ethanol, ammonia and CO gases at the same 1000 ppm concentration. The temperature of the sensor can be adjusted by the integrated micro-heater. Transient measurements of the sensor showed stable operation and good repeatability at different temperatures.

Also, based on the newly introduced, high precision two-step gate recess technique, a suspended gate recess Pt/AlGaIn/GaN heterostructure  $\text{NO}_2$  gas sensor integrated with a micro-heater was microfabricated. This gate recess technique dramatically enhances the performance of AlGaIn/GaN devices. The sensitivity and current change of AlGaIn/GaN heterostructure to 1-200 ppm  $\text{NO}_2/\text{air}$  are increased up to 20 times and 12 times compared to conventional gate devices respectively with the faster response time. The suspended membrane structure and integrated micro-hotplate also improve response time and sensitivity by adjusting the optimum working temperature with low power consumption. The sensitivity (response time) to 40 ppm  $\text{NO}_2/\text{air}$  increases from 0.75 % (1250 s) to 3.5% (75 s) when temperature increases from 60 °C to 300 °C.

The AlGaIn/GaN heterostructure UV photodetector with functionalized  $\text{WO}_3$  nanofilm deposited by PVD technology shows high response to the deep UV wavelength and exhibits high responsivity of  $1.67 \times 10^4$  A/W at 240 nm, and a sharp cut-off wavelength is 275 nm. The long decay time of photodetector introduced by the PPC effect was optimized by three kinds of heating methods. The photodetector shows a rapid response and recovery (175 s) time under 240 nm illumination at the DC heating temperature of 150 °C. To further reduce the decay time of the AlGaIn/GaN heterostructure photodetectors, a reduction of 30-45 % in decay time is measured by 50 Hz pulsed heating mode compared to DC heating. More importantly, the PPC effect can be eliminated by a novel method: mono-pulse heating reset (MHR) by applying a pulse voltage of micro-heater after the removal of UV illumination. The recovery time was reduced from hours to seconds without reducing the high responsivity and stability of photodetector. This novel method solved the long-term problem of long decay time introduced by PPC of GaN-based photoconductive photodetectors.

The piezoresistive gauge factor of AlGaIn/GaN heterostructures is approximately three times higher than the highest gauge factor reported for SiC. The chip was bonded to a second silicon wafer using silicone (BISON) to create a reference pressure inside. The suspended membrane AlGaIn/GaN heterostructure sensor showed a rapid response in drain current change when exposed to different vacuum pressures, especially in low pressure range. And the higher temperature increased the sensitivity due to the larger deflection of the membrane at the higher temperature. The dynamic percent current change of the AlGaIn/GaN heterostructure pressure sensor was 18.75 % under pressure of 10 Pa at 100 °C with a low operating power consumption of 1.8  $\mu\text{W}$ . The maximum sensitivity was obtained as 22.8 %/kPa with pressure ranging from 600 Pa to 10 Pa.

# SAMENVATTING

De industrie van micro-elektronica ontwikkelt zich vandaag de dag – behalve op het gebied van de schaal van geïntegreerde circuits – ook in de richting van de veelzijdigheid in geïntegreerde functies, meestal More than Moore (MtM) genoemd. MtM omvat alle technologieën die microsystemen naar een hoger niveau van integratie tillen, met kleinere pakketvolume (package size), lager verbruik en lagere kosten. Micro-elektromechanische systemen (MEMS) zijn bij deze ontwikkeling cruciaal. Hoewel er aangevoerd is dat Si vooraanstaand is op de markt van MEMS-sensoren, is er een toenemende vraag naar sensoren die werkzaam zijn onder toestanden die buiten de capabiliteit van Si vallen. Si-gebaseerde microsensoren kunnen niet functioneren in barre omgevingen met bijvoorbeeld hoge temperatuur, veel straling, hoge druk en chemisch corrosieve middelen. Halfgeleiders met een brede bandkloof zoals galliumnitride (GaN) zijn potentiële kandidaten om silicium te vervangen vanwege hun specifieke karakteristieken en het aantoonbare functioneren in elektriciteitsnet- of LED-toepassingen. Deze dissertatie heeft als doel om een MEMS-sensorplatform te ontwikkelen met het gebruik van GaN-gebaseerde materialen. Het ontwerp, de fabricage, verpakking (packaging), drukmeting, diep-UV fotodetector en gassensoren worden voorgelegd en bediscussieerd.

Vanwege de sterke piëzo-elektrische en spontane polarisatie-effecten in GaN en Al-GaN, wordt tweedimensionaal elektrongas (2DEG) met een hoge plaatdichtheid gevormd op het grensvlak tussen AlGaIn- en GaN-lagen. Deze epitaxiale lagen zijn door MOCVD op <111> siliciumsubstraten gekweekt. Het fabricageproces begon met mesa-isolatie door ICP-etsen. Vervolgens is een procesmodule speciaal ontwikkeld voor lage ohmse contactweerstand. Daarna werden e-beam verdampings- en liftoff-processen gebruikt voor het afzetten en vormgeven van metalen lagen voor een geïntegreerde microverwarmer en de apparaatverbindingslagen. Verder werd een DRIE-proces afgestemd om de membraanstructuur te vormen, met SiO<sub>2</sub> als een hard masker. De voltooide sensoren zijn verpakt in CFQN-pakketten vanwege de stabiele waargenomen uitgangsstroom in vergelijking met het COB-pakket. De membraantemperatuur wordt niet alleen beïnvloed door de opwarming van de microverwarming, maar ook door de zelfverwarming van de sensor. Het apparaat wordt niet beïnvloed bij blootstelling aan een hoge relatieve vochtigheidsomgeving en de verzadigde huidige temperatuurcoëfficiënt is -0,63 mA/mm\*K.

De AlGaIn/GaN-heterojuncties vertonen een groot potentieel voor de ontwikkeling van hoogwaardige sensoren als gevolg van tweedimensionaal elektrongas (2DEG) met hoge dragerdichtheid aan de interface die wordt geïntroduceerd door het sterke polarisatie-effect, dat gevoelig is voor de veranderingen in oppervlaktepotentiaal. AlGaIn/GaN HEMT-sensoren geïntegreerd met microverwarming op een hangend membraan werden onderzocht op gasdetectie. De toepassing van nano-WO<sub>3</sub> als functionele laag resulteert in het vermogen om een lage concentratie van 100 ppb NO<sub>2</sub>/N<sub>2</sub> bij 300 °C te detecteren. Bij blootstelling aan een NO<sub>2</sub>-gas van 1 ppm wordt een hoge detectiegevoeligheid

van 1,1 % bereikt met een respons (herstel) tijd van 88 seconden (132 seconden). De  $\text{WO}_3/\text{AlGaIn}/\text{GaIn}$ -chip werd verpakt en verder getest om de detectielimiet en reactietijd te bepalen. Naast de verbetering van de detectielimiet, verbeterde de  $\text{WO}_3$ -nanofilm ook de gevoeligheid en selectiviteit voor acetongas. Bij 300 °C werd een verandering in de drain-stroom  $\Delta I_{DS}$  van 0,31 mA waargenomen, evenals een hoge gevoeligheid van 25,7 % voor 1000 ppm aceton. Voor een acetonconcentratie van 1000 ppm verminderde  $t_{Res}$  ( $t_{Rec}$ ) van 147 (656) s bij  $V_H = 3.5$  V (210 °C) tot 48 (319) s bij  $V_H = 4$  V (300 °C). Bovendien was de respons op 1000 ppm acetongas significant groter dan voor ethanol, ammoniak en CO-gassen bij dezelfde 1000 ppm-concentratie. De temperatuur van de sensor kan worden aangepast door de geïntegreerde microverwarmer. Voorbijgaande metingen van de sensor lieten een stabiele werking en goede herhaalbaarheid bij verschillende temperaturen zien.

Hierbij is, gebaseerd op de nieuw geïntroduceerde en zeer nauwkeurige tweestaps gate recess techniek, een hangende gate recess Pt/AlGaIn/GaIn heterostructuur  $\text{NO}_2$ -gassensor micro-gefabriceerd met een geïntegreerde microverwarmer. Deze gate recess techniek verbetert de prestaties van AlGaIn/GaIn-devices drastisch. De gevoeligheid en de stroomsterkteverschil van de AlGaIn/GaIn-heterostructuur naar 1-200 ppm  $\text{NO}_2$ /lucht worden tot 20 keer respectievelijk 12 keer verhoogd in vergelijking met conventionele gate-apparaten, respectievelijk met de snellere responstijd. De hangende membraanstructuur en geïntegreerde microkookplaat verbeteren ook de reactietijd en gevoeligheid door de optimale werktemperatuur aan te passen met een laag stroomverbruik. De gevoeligheid (reactietijd) tot 40 ppm  $\text{NO}_2$ /lucht neemt toe van 0,75 % (1250 s) tot 3,5 % (75 s) als de temperatuur stijgt van 60 °C tot 300 °C.

De AlGaIn/GaIn-heterostructuur UV-fotodetector met gefunctionaliseerde  $\text{WO}_3$ -nanofilm afgezet met PVD-technologie vertoont een sterke reactie op de verre UV-golflengte en vertoont een hoge responsiviteit van  $1.67 \times 10^4$  A/W bij 240 nm, en een scherpe cut-off golflengte van 275 nm. De lange vervaltijd van de fotodetector geïntroduceerd door het PPC-effect werd geoptimaliseerd door drie soorten verwarmingsmethoden. De fotodetector toont een snelle respons- en hersteltijd (175 s) onder een verlichting van 240 nm bij een gelijkstroom-verwarmingstemperatuur van 150 °C. Om de vervaltijd van de AlGaIn/GaIn-heterostructuur fotodetectoren verder te verminderen, wordt een vermindering van 30-45 % in vervaltijd gemeten met een gepulseerde verwarmingsmodus van 50 Hz, vergelijkbaar met de gelijkstroomverwarming. Een belangrijker punt is dat het persistente effect van fotoconductiviteit (PPC) kan worden geëlimineerd door een nieuwe methode: monopulsverwarmingsreset (MHR) door een pulsspanning van microverwarming toe te passen na het verwijderen van UV-verlichting. De hersteltijd werd teruggebracht van uren naar seconden zonder de hoge reactiviteit en stabiliteit van de fotodetector te verminderen. Deze nieuwe methode loste het langetermijnprobleem op van lange vervaltijd, geïntroduceerd door PPC van op GaIn gebaseerde fotoconductieve fotodetectoren.

De piëzoresistieve meetfactor van AlGaIn/GaIn-heterostructuren is ongeveer driemaal hoger dan de hoogste meetfactor die is gerapporteerd voor SiC. De chip werd met silicium (BISON) aan een tweede siliciumwafer gehecht om een referentiedruk binnenin te creëren. De AlGaIn/GaIn heterostructuursensor met een hangend membraan vertoont een snelle respons bij verandering van de drain-stroom bij blootstelling aan ver-

schillende vacuümdrukken, met name in het lage drukbereik. De hogere temperatuur verhoogde de gevoeligheid door de grotere afbuiging van het membraan. De dynamische procentuele stroomverandering van de AlGa<sub>N</sub>/Ga<sub>N</sub>-heterostructuur-druksensor was 18,75 % onder druk van 10 Pa bij 100 °C met een laag stroomverbruik van 1,8 μW.



# 1

## INTRODUCTION



Table 1.1: Physical characteristics of Si and main wide bandgap semiconductors.

Property	Si	GaAs	4H-SiC	GaN	Diamond
$E_g$ (eV)	1.12	1.43	3.26	3.40	5.47
$E_c$ (kV/cm)	300	400	2200	3300	10000
$\mu_n$ ( $cm^2V^{-1}s^{-1}$ )	1500	8500	1250	2000 (2DEG)	2000
$\lambda$ (W/cm.K)	1.5	0.46	4.9	1.3	20
$v_{sat}$ ( $10^7$ cm/s)	1	1	2	2.2	2

$E_g$ : Bandgap energy;  $E_c$ : Electric breakdown field;  $\mu_n$ : Electron mobility;  $\lambda$ : Thermal conductivity;  $v_{sat}$ : Saturated electron drift velocity.

quantity, such as acceleration, pressure, displacement, flow, electromagnetic field, image, temperature, gas composition, and ionic concentration. The MEMS sensor, as a key device for information acquisition, plays a significant role in promoting the miniaturization of various sensor systems, which have been widely used in aerospace, biomedicine, and consumer electronics. At present, with the introduction of new materials such as nanomaterials, biological materials, and intelligent materials, in addition to the continuous development of nanomanufacturing technology, MEMS sensors are rapidly developing into high precision, high-reliability, and multi-functional integrated system. In addition, the emergence of the IOT has greatly increased the demands for wireless MEMS sensors, and reducing the power supply of these devices has become a key point.

## 1.2. WIDEBAND SEMICONDUCTOR

With the many years of development in silicon fabrication and processing techniques, Si-based MEMS sensors have the advantage of producing uniform, accurate micro/nano size structures, suitable for mass production. While Si has proven to be the primary material in the MEMS sensor market, there is a growing need for sensors operating at conditions beyond the limits of Si. Si-based micro-sensors can't be operated in harsh environments such as in high temperature, high radiation, high pressure, and chemically corrosive conditions. Developing sensors capable to operate in harsh environments is especially urgent. Appropriate materials for such environments are the key factor in whether the sensor will operate as designed over its required lifetime. During the design of devices for harsh environment, the properties of the materials used that are important to consider are the coefficient of thermal expansion, thermal conductivity, elastic modulus, and resistance to creep and fatigue.

A number of materials have been investigated as potential candidates to replace silicon in electronic and MEMS devices in high-temperature or harsh environment applications. A comparison among the characteristics of silicon and main wide bandgap semiconductor is summarized in table 1-1. Wide bandgap semiconductors ( $E_g > 2.3$  eV) such as Gallium Nitride (GaN), diamond, and Silicon Carbide (SiC) are potential candidates to attain superior and robust performances. The larger bandgap implies an ability to handle higher electric fields, thus enabling devices with higher operating temperatures (600 °C) at which conventional Si based sensors fail. An operation temperature limit up

to 175 °C for silicon sensors and 500 °C for silicon-on-insulator (SOI) sensors has been reported [4]. The ability of GaN-based materials to function at high temperature, high power and high radiation environment will enable large performance enhancements in a wide variety of applications, such as spacecraft [5][6], satellite [7][8], automobile[9], nuclear power and radar [10].

### 1.3. ALGaN/GaN HETEROSTRUCTURE SENSORS

In recent years, GaN has attracted great attention for both optoelectronics and electronics applications due to its superior material properties such as direct band gap, higher electric breakdown field strength, both higher electron mobility and saturation velocity, high melting point and the ability to form a heterostructure. Especially, it is already commercialized in power switch devices, such as Schottky diodes and high electron mobility transistor (HEMT)[5]. The major advantage of using GaN-based materials, such as AlGaN and InGaN, is the formation of the heterostructure which results in the creation of a two-dimensional electron gas (2DEG)[11], where energy states for electrons are quantized and electrons can only move laterally. Very high electron mobility can be achieved in AlGaN/GaN heterostructures, since carriers are screened from their respective donors, mitigating ionized impurity scattering. The ability to form a heterostructure and the fact that GaN epitaxial layers can be grown on different, affordable such as Si, and sapphire are additional advantages. The high piezoelectric gauge factor of GaN makes them ideal for pressure and stress detection[12]. The wide energy bandgap of GaN and AlGaN make these materials suitable for UV detection[15, 16]. And the 2DEG is sensitive to changes of surface states, which indicates the AlGaN/GaN heterojunctions great potential for chemical sensors[13], such as gas sensors and PH sensors as well as for biological sensors. Among all possible applications, three very promising ones are gas sensing, UV detection and pressure sensing.

#### 1.3.1. GAS SENSING

Gas sensors are increasingly used in the growing markets of automotive, aerospace, health care, environment protection, consumer products. Within these domains, gas sensors play an important role in providing comfort and safety or in enabling process control or smart maintenance functionalities. As shown in Figure 1.2, Yole Development's Gas Sensor report estimates that the gas sensor market is currently growing in most of these applications areas. Moreover, in the essential pursue of improving sensitivity and selectivity of gas detection, it should be noticed that these various applications require very different levels of sensor performance.

In spite of the progress achieved with silicon-based gas sensors in most of these applications, they are not suitable for operation in corrosive environments and high temperatures (>250 °C) due to the narrow bandgap of silicon. Operation in harsh environments is essential for industrial manufacturing, powertrain, and automotive industries. Therefore, wide bandgap semiconductor-based gas sensors are required. SiC-based gas sensors have already shown their high temperature properties. However, the cost of the SiC substrate is still very high. GaN is a highly promising material for harsh environments. Especially the AlGaN/GaN heterostructures form a highly conductive electron

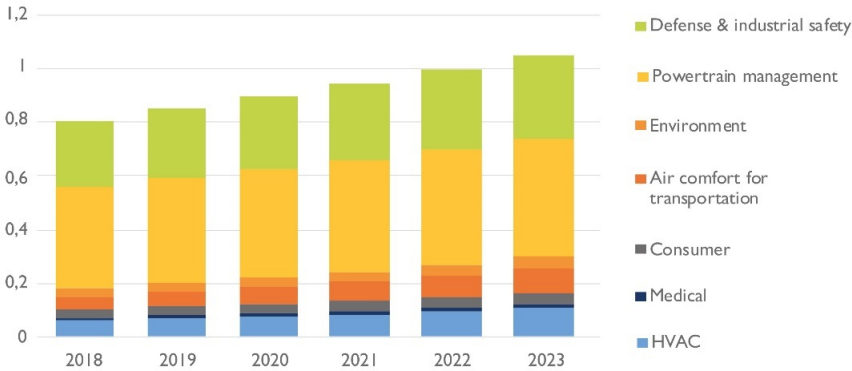


Figure 1.2: 2018-2023 gas sensor market in value (\$B). (source: Yole development November 2018)

channel, and this channel, as mentioned earlier, is very sensitive to the surface state. Consequently, the potential of these structures for a high sensitivity gas sensor with high stability for harsh environments is significant.

### 1.3.2. ULTRAVIOLET (UV) DETECTION

An ideal UV detector should work in a radiation environment and not be susceptible to long-wave electromagnetic interference. It does not detect signals to targets by actively radiating electromagnetic waves outwards but it recognizes signals by passively receiving ultraviolet radiation. UV photodetectors have a wide range of applications in military and civilian fields as shown in Figure 1.3, such as missile warning, fire warning, marine oil pollution detection, biomedical detection, and environment UV detection.

The representative UV detector in the early stage is the Photomultiplier tube (PMT). PMT UV photodetectors with unique features such as high stability, high sensitivity, high speed, the high signal-to-noise ratio are generally bulky, fragile and require high bias voltages.[14] Moreover, the growing needs and expectations are exceeding the performances of traditional UV photodetectors, and UV photodetectors with some special function and multiple functions have become more and more essential for practical applications. More compact and smart UV photodetectors are urgently needed to guarantee high performance in the future.

In order to meet the requirement of compactness, silicon-based UV photodetectors were considered due to their small size, high integration level, suitability for large area arrays, and low cost. However, the optical spectral response of the silicon photodetector is in the infrared region due to the narrow bandgap (1.12 eV). Also, the responsivity of silicon to UV range is low and its stability is not high. In real application, the silicon UV photodetector needs an expensive infrared filter to remove the interference of visible and infrared light. In addition, the low UV absorption of silicon makes the quantum efficiency of silicon photodetector very low and exhibits poor radiation resistance.

Wide bandgap semiconductors (SiC, diamond, III-nitrides, and some III-V compounds)

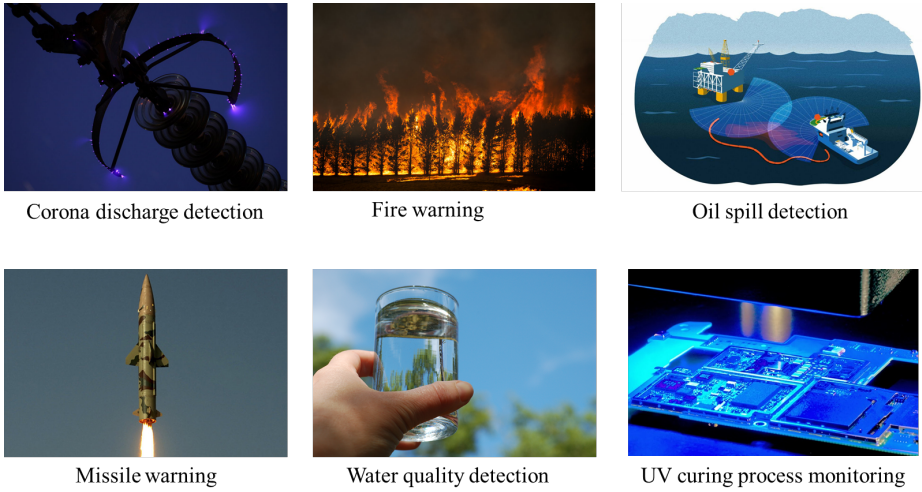


Figure 1.3: Typical applications of UV photodetector.

have high chemical bonding structures and intrinsic visible-blindness. However, the wide bandgap semiconductor-based photodetectors have not been sufficiently exploited so far due to insufficient materials and technology maturity. With the progress recently made in the development of wide bandgap semiconductor materials and technology, wide bandgap semiconductor-based UV photodetector inject new vitality to the research and development of high-performance UV photodetectors. In recent years, GaN based UV light detectors have been reported [15, 16]. GaN is particularly suitable for UV light detection due to its direct wide band gap and robust nature. GaN PIN diodes [17, 18], Schottky diodes [19] and metal semiconductor metal (MSM) [20–22] based photodetectors have been demonstrated by various researches. From the aspect of technology, the ideal photodetector would exhibit lower dark current to minimize the interference noise and higher responsivity to maximize the photo signal. Currently, the avalanche-type detector [23–25] can obtain high responsivity but at the expense of increased noise, highly rigorous requirements of structure and processing techniques. Another common approach to improve responsivity is a photoconductive type, which is easy to fabricate at lower cost and has a good commercial prospect. However, persistent photoconductivity (PPC) effect associated with a 2DEG in an AlGaIn/GaN HEMT devices has been observed. That is a big challenge that needs to be addressed to develop a UV photodetector with high responsivity and fast response at the same time.

### 1.3.3. PRESSURE SENSING

There are lots of applications in the automotive, medical, consumer, aerospace, and industrial fields for robust miniaturized pressure sensors as illustrated in Figure 1.4. Automotive is the largest market by far and with significant growth. The consumer market is much smaller due to low pricing but grows considerably. Avionics & high end is a niche market but with high growth. Today, MEMS pressure sensor technologies are quite ma-

ture for most of these applications and are basically separated into piezoresistive and capacitive types. The piezoelectric is leading in terms of market share. And most of MEMS pressure sensors are based on silicon technology. In high end applications, the pressure sensor need to operate at elevated temperature ( $>150\text{ }^{\circ}\text{C}$ ). While many papers have been published about this, there are no commercial semiconductor-based sensors for temperature ranges above  $250\text{ }^{\circ}\text{C}$ . Numerous solid-state pressure sensors are based on the mechanism of the piezoelectric effect [26–31]. Among them, silicon-on-insulator (SOI) [32] and silicon carbide (SiC) [33–35] based pressure platforms are the most promising technology. While GaN is a less mature technology than SiC, an advantage of GaN-based devices is their potential for monolithic integration. The piezoresistive gauge factor of AlGa<sub>N</sub>/Ga<sub>N</sub> heterostructures is approximately three times higher than the highest gauge factor reported for SiC. It means that the AlGa<sub>N</sub>/Ga<sub>N</sub> heterostructure could be used for pressure or stress sensors. In addition, the demonstration of sensing using Al<sub>x</sub>Ga<sub>1-x</sub>N/Ga<sub>N</sub> platform for vacuum application has been hardly reported.



Figure 1.4: MEMS pressure sensor applications. (source: Yole Development 2018)

## 1.4. RESEARCH OBJECTIVE

Although AlGa<sub>N</sub>/Ga<sub>N</sub> HEMTs have been prevailing in microwave and power electronics, their potential in sensing applications is not fully developed yet. In order to expand the sensing applications of Ga<sub>N</sub> devices and meet the requirements of next generation sensors (low cost, high volume, highly miniaturized, high reliability and low power consumption), the objective of this thesis is to develop a MEMS sensor platform utilizing Ga<sub>N</sub>-based materials. As first step, gas sensing, deep UV photodetector and vacuum pressure sensor, are targeted.

The following objectives are identified as steps towards the realization of the men-

tioned goals:

1. Select the optimal substrate and epitaxial structure for MEMS AlGaN/GaN sensor fabrication.
2. Design, fabricate and package the MEMS AlGaN/GaN sensor platform.
3. Gas detection: Test gas sensor response to NO<sub>2</sub> and acetone and optimize the dynamic performance by functional materials and chip-level heating unit. Investigate the gas response effect of gate recess on AlGaN/GaN heterostructure sensor performance.
4. UV detection: Measure the UV response and optimize the dynamic performance of the WO<sub>3</sub>/AlGaN/GaN heterostructure photodetectors by an integrated micro-heater.
5. Pressure sensor: test vacuum static and dynamic performance and investigate the temperature effects on MEMS AlGaN/GaN heterostructure sensor.

## 1.5. THESIS STRUCTURE

The rest of this thesis is structured as indicated by the block diagram shown in Figure 1.5.

**Chapter 2** focuses on the theory of AlGaN/GaN heterostructure sensors, including the polarization effect in GaN semiconductors and the 2DEG formation. Afterward, the piezoelectric, optical and chemical sensing mechanisms of AlGaN/GaN heterostructure sensors are presented.

**Chapter 3** presents the base design, simulation and fabrication process of the MEMS AlGaN/GaN heterostructure device. Then, the sensor package is discussed and the wafer-level testing including ohmic contact, temperature and humidity effect on the device are measured and discussed.

**Chapter 4** shows the application of the AlGaN/GaN heterostructure sensor to gas sensing. A WO<sub>3</sub> nanolayer deposited by physical vapor deposition (PVD) on the gate is studied as a way to improve selectivity. A two-step method to precisely etch the AlGaN layer is developed and the gate recess AlGaN/GaN sensor transient response to different gases is compared.

**Chapter 5** describes the application of the AlGaN/GaN heterostructure device as a deep ultraviolet photodetector. The mechanism of the GaN-based photoconductive detector and its persistent photoconductivity (PPC) effect are studied and discussed. Three methods, DC heating, pulse heating and mono-pulse heating reset (MHR) to suppress the PPC effect are investigated.

**Chapter 6** reports on the investigation of the application the AlGaN/GaN MEMS heterostructure sensor for pressure sensing, especially the vacuum range. The deformation of the GaN membrane is discussed. Static and dynamic sensor response characteristics are studied under different temperatures, and the temperature effect on the sensitivity of the sensor is assessed.

**Chapter 7** summarizes the result of this research and draws some conclusions on the potential of AlGaN/GaN heterostructures for sensing. The achievements of this thesis

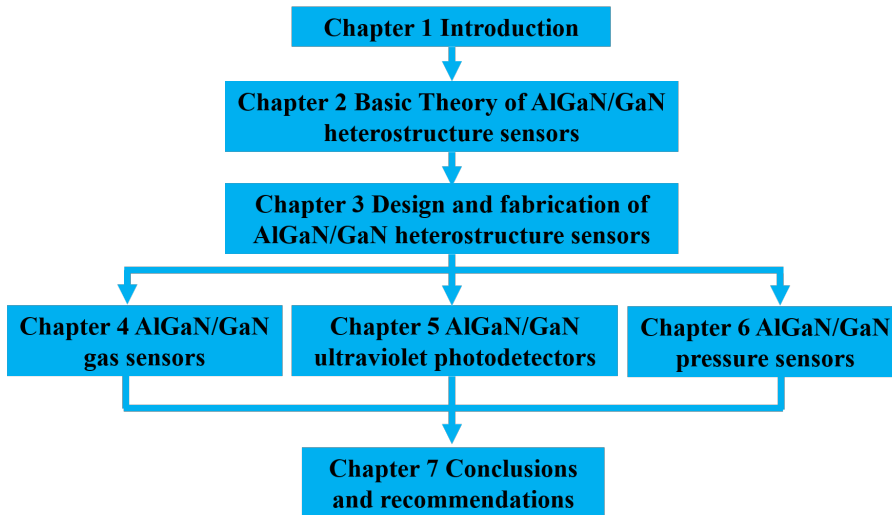


Figure 1.5: The block diagram of this thesis structure.

open up an opportunity for future potential applications as well as further technology development. A brief outlook for future research is also given.

## REFERENCES

- [1] G.Q. Zhang, Strategic Research Agenda of "More than Moore". Proceedings of the 7th international conference on thermal, mechanical and multi-physics simulation and experiments in micro-electronics and micro-systems. ISBN: 1-4244-0275-1. Como, Italy. pp. 4-10. April 23-26, 2006.
- [2] G.Q. Zhang, Alfred van Roosmalen. More than Moore - Creating High Value Micro/Nanoelectronics Systems. ISBN: 978-0-387-75592-2, Springer. 2009
- [3] W. Arden, M. Brillouët, P. Coge, M. Graef, B. Huizing, and R. Mahnkopf, "More-than-Moore white paper," Version, vol. 2, p. 14, 2010.
- [4] M. A. Fraga, R. S. Pessoa, H. S. Maciel, and M. Massi, "Recent developments on silicon carbide thin films for piezoresistive sensors applications," Silicon Carbide. Rijeka: Intech-Open Access Publisher, vol. 1, pp. 369-388, 2011.
- [5] Y. Kobayashi et al., "GaN HEMT based rectifier for spacecraft health monitoring system using microwave wireless power transfer," in 2012 Asia Pacific Microwave Conference Proceedings, 2012, pp. 391-393: IEEE.
- [6] S. Yoshida, N. Hasegawa, and S. Kawasaki, "Experimental demonstration of microwave power transmission and wireless communication within a prototype reusable spacecraft," IEEE Microwave and Wireless Components Letters, vol. 25, no. 8, pp. 556-558, 2015.

- [7] Y. S. Noh and I. B. Yom, "A linear GaN high power amplifier MMIC for Ka-band satellite communications," *IEEE Microwave and Wireless Components Letters*, vol. 26, no. 8, pp. 619-621, 2016.
- [8] K. Nakade, K. Seino, A. Tsuchiko, and J. Kanaya, "Development of 150W S-band GaN solid state power amplifier for satellite use," in *2010 Asia-Pacific Microwave Conference*, 2010, pp. 127-130: IEEE.
- [9] R. Ma, K. H. Teo, S. Shinjo, K. Yamanaka, and P. M. Asbeck, "A GaN PA for 4G LTE-Advanced and 5G: Meeting the telecommunication needs of various vertical sectors including automobiles, robotics, health care, factory automation, agriculture, education, and more," *IEEE Microwave Magazine*, vol. 18, no. 7, pp. 77-85, 2017.
- [10] P. Blount, S. Huettner, and B. Cannon, "A High Efficiency, Ka-Band Pulsed Gallium Nitride Power Amplifier for Radar Applications," in *2016 IEEE Compound Semiconductor Integrated Circuit Symposium (CSICS)*, 2016, pp. 1-4: IEEE.
- [11] O. Ambacher et al., "Two-dimensional electron gases induced by spontaneous and piezoelectric polarization charges in N- and Ga-face AlGaIn/GaN heterostructures," *Journal of Applied Physics*, vol. 85, no. 6, pp. 3222-3233, 1999.
- [12] M. S. Shur, A. D. Bykhovski, and R. Gaska, "Pyroelectric and piezoelectric properties of GaN-based materials," (in English), *Mrs Internet Journal of Nitride Semiconductor Research*, vol. 4, 1999.
- [13] B. S. Kang, K. Suku, F. Ren, B. P. Gila, C. R. Abernathy, and S. J. Pearton, "AlGaIn/GaN-based diodes and gateless HEMTs for gas and chemical sensing," *IEEE Sensors Journal*, vol. 5, no. 4, pp. 677-680, 2005.
- [14] A. Bouvier et al., "Photosensor characterization for the Cherenkov Telescope Array: silicon photomultiplier versus multi-anode photomultiplier tube," in *Hard X-Ray, Gamma-Ray, and Neutron Detector Physics XV*, 2013, vol. 8852, p. 88520K: International Society for Optics and Photonics.
- [15] E. Munoz, E. Monroy, J. L. Pau, F. Calle, F. Omnes, and P. Gibart, "III nitrides and UV detection," (in English), *Journal of Physics-Condensed Matter*, vol. 13, no. 32, pp. 7115-7137, Aug 13 2001.
- [16] P. E. Malinowski et al., "Backside-Illuminated GaN-on-Si Schottky Photodiodes for UV Radiation Detection," (in English), *Ieee Electron Device Letters*, vol. 30, no. 12, pp. 1308-1310, Dec 2009.
- [17] B. Butun, T. Tut, E. Ulker, T. Yelboga, and E. Ozbay, "High-performance visible-blind GaN-based p-i-n photodetectors," (in English), *Applied Physics Letters*, vol. 92, no. 3, p. 033507, Jan 21 2008.
- [18] T. Tut, T. Yelboga, E. Ulker, and E. Ozbay, "Solar-blind AlGaIn-based p-i-n photodetectors with high breakdown voltage and detectivity," (in English), *Applied Physics Letters*, vol. 92, no. 10, p. 103502, Mar 10 2008.

- [19] K. H. Lee, P. C. Chang, S. J. Chang, Y. C. Wang, C. L. Yu, and S. L. Wu, "AlGaIn/GaN Schottky Barrier UV Photodetectors With a GaN Sandwich Layer," (in English), *Ieee Sensors Journal*, vol. 9, no. 7, pp. 814-819, Jul 2009.
- [20] C. K. Wang et al., "GaN MSM UV photodetectors with titanium tungsten transparent electrodes," (in English), *Ieee Transactions on Electron Devices*, vol. 53, no. 1, pp. 38-42, Jan 2006.
- [21] R. W. Chuang et al., "Gallium nitride metal-semiconductor-metal photodetectors prepared on silicon substrates," (in English), *Journal of Applied Physics*, vol. 102, no. 7, p. 073110, Oct 1 2007.
- [22] C. K. Wang et al., "GaN MSM UV Photodetector With Sputtered AlN Nucleation Layer," (in English), *Ieee Sensors Journal*, vol. 15, no. 9, pp. 4743-4748, Sep 2015.
- [23] J. Zheng et al., "A PMT-like high gain avalanche photodiode based on GaN/AlN periodically stacked structure," *Applied Physics Letters*, vol. 109, no. 24, p. 241105, 2016.
- [24] C. Bayram, J. Pau, R. McClintock, and M. Razeghi, "Performance enhancement of GaN ultraviolet avalanche photodiodes with p-type -doping," *Applied Physics Letters*, vol. 92, no. 24, p. 241103, 2008.
- [25] Q. Cai et al., "AlGaIn ultraviolet Avalanche photodiodes based on a triple-mesa structure," *Applied Physics Letters*, vol. 113, no. 12, p. 123503, 2018.
- [26] Y. Watanabe, S. Uemura, and S. Hoshino, "Printed pressure sensor array sheets fabricated using poly (amino acid)-based piezoelectric elements," *Japanese Journal of Applied Physics*, vol. 53, no. 5S3, p. 05HB15, 2014.
- [27] J. Yoo et al., "Piezoelectric and dielectric properties of La<sub>2</sub>O<sub>3</sub> added Bi (Na, K) TiO<sub>3</sub>-SrTiO<sub>3</sub> ceramics for pressure sensor application," *Sensors and Actuators A: Physical*, vol. 126, no. 1, pp. 41-47, 2006.
- [28] R. Bao et al., "Flexible and controllable piezo-phototronic pressure mapping sensor matrix by ZnO NW/p-polymer LED array," *Advanced Functional Materials*, vol. 25, no. 19, pp. 2884-2891, 2015.
- [29] D. Mandal, S. Yoon, and K. J. Kim, "Origin of piezoelectricity in an electrospun poly (vinylidene fluoride-trifluoroethylene) nanofiber web-based nanogenerator and nano-pressure sensor," *Macromolecular rapid communications*, vol. 32, no. 11, pp. 831-837, 2011.
- [30] M. Peng et al., "High-resolution dynamic pressure sensor array based on piezo-phototronic effect tuned photoluminescence imaging," *ACS nano*, vol. 9, no. 3, pp. 3143-3150, 2015.
- [31] P. Khanna, B. Hornbostel, R. Grimme, W. Schäfer, and J. Dörner, "Miniature pressure sensor and micromachined actuator structure based on low-temperature-cofired ceramics and piezoelectric material," *Materials chemistry and physics*, vol. 87, no. 1, pp. 173-178, 2004.

- [32] S. Guo, H. Eriksen, K. Childress, A. Fink, and M. Hoffman, "High temperature smart-cut SOI pressure sensor," *Sensors and Actuators A: Physical*, vol. 154, no. 2, pp. 255-260, 2009.
- [33] R. S. Okojie, D. Lukco, V. Nguyen, and E. Savrun, "4H-SiC piezoresistive pressure sensors at 800 C with observed sensitivity recovery," *IEEE Electron Device Letters*, vol. 36, no. 2, pp. 174-176, 2014.
- [34] C. A. Zorman and R. J. Parro, "Micro-and nanomechanical structures for silicon carbide MEMS and NEMS," *physica status solidi (b)*, vol. 245, no. 7, pp. 1404-1424, 2008.
- [35] L. Chen and M. Mehregany, "A silicon carbide capacitive pressure sensor for in-cylinder pressure measurement," *Sensors and Actuators A: Physical*, vol. 145, pp. 2-8, 2008.

# 2

## BASIC THEORY OF ALGaN/GaN HETEROSTRUCTURE SENSORS

## 2.1. INTRODUCTION

This chapter discusses the properties of GaN materials and AlGaN/GaN heterostructures, the 2DEG formation, and the operation principles of basic AlGaN/GaN devices. Then the mechanism and structures of the developed AlGaN/GaN heterostructure based sensors, gas sensors, UV detectors, and pressure sensors, are presented.

## 2.2. GAN PROPERTIES

Gallium nitride (GaN) was first synthesized using hydride vapor phase epitaxy (HVPE) in 1969 [1], and was identified as a direct bandgap semiconductor (3.4 eV). But GaN started to attract attention only when a suitable metal organic chemical vapor deposition (MOCVD) equipment was developed in 1991 by Nakamura [2, 3]. GaN semiconductors can grow with Zinc blende and Wurtzite crystal formation on a variety of substrates such as Silicon (Si), silicon carbide (SiC) and sapphire. However, the ternary alloys of GaN (such as  $\text{Al}_x\text{Ga}_{1-x}\text{N}$  and  $\text{In}_x\text{Ga}_{1-x}\text{N}$ ) possess a wurtzite crystal structure, which is thermodynamically the most stable phase under ambient conditions. In this thesis, we focus on properties of wurtzite GaN. The wurtzite crystal structure is formed by hexagonal unit cells which consist of two intercepting hexagonal close-packed (hcp) sublattices. The base lattice constant and the height of the cell are  $a_0$  and  $c_0$  as shown in Figure 2.1.

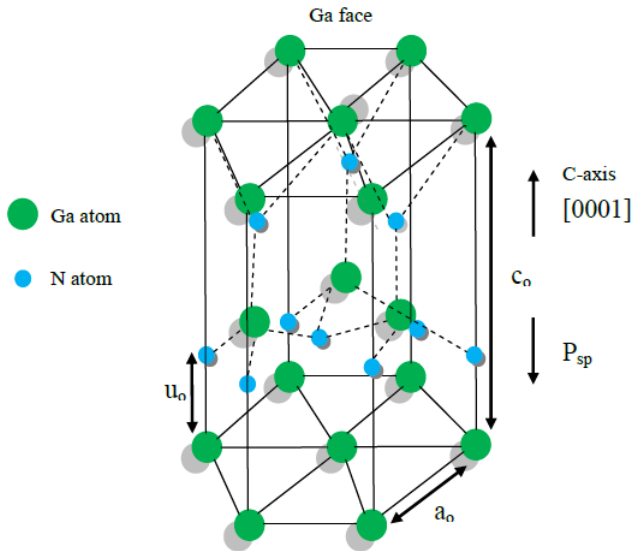


Figure 2.1: Hexagonal wurtzite Ga-face terminated GaN lattice structure[4].

The electromechanical properties of GaN and other semiconductors are summarized in Table 2-1. The piezoelectric coefficient of GaN is about three times larger than SiC and GaAs, which means that GaN is suitable for piezoelectric devices. From the mechanical parameters of GaN, such as Young's modulus, it can be seen that GaN is one of

Table 2.1: Electromechanical properties of semiconductor materials.[5]

Materials	Elastic Modulus $c_{33}$ (GPa)	Acoustic Velocity (m/s)	Piezoelectric Coefficient $e_{33}$ ( $Cm^{-2}$ )	Young's Modulus (Gpa)
Si	165	8415	N/A	130-187
SiC	605	13100	0.2	450
GaAs	118	2470	-0.16	85.5
AlN	390	11000	1.55	344.83
LiNbO <sub>3</sub>	60	3900	3.65	170
GaN	398	8044	0.65	210-405

Table 2.2: Spontaneous polarization coefficients and lattice constants of GaN and AlN. [6]

Parameters	GaN	AlN
$P_{sp}$ ( $C/m^2$ )	-0.029	-0.081
$a$ (Å)	3.189	3.112
$c$ (Å)	5.158	4.982

the most promising materials for electromechanical system.

### 2.2.1. POLARIZATION EFFECTS IN GAN SEMICONDUCTORS

Due to the electronegativity difference of bonded atoms, the chemical bonds of compound semiconductors are both covalent and ionic together. The unique characteristic of group III-Nitride semiconductors are related to the presence of the large electronegativity of nitrogen. The GaN wurtzite structure is non-centrosymmetric along the c-axis or [0001] direction, which results in polarization along this axis, namely spontaneous polarization. The spontaneous polarization ( $P_{sp}$ ) is present without any external mechanical and electrical perturbation. The magnitude of spontaneous polarization depends on the  $c_0/a_0$  ratio. The spontaneous polarization coefficients of GaN, AlN along with lattice parameters are shown in Table 2-2.

The lattice constants  $a_0$  and  $c_0$  of the ternary nitride alloy ( $Al_xGa_{1-x}N$ ) are altered by the Al incorporation, resulting in the change of the spontaneous polarization of AlGaN. The lattice constants and the spontaneous polarization of AlGaN as a function of  $Al(x)$

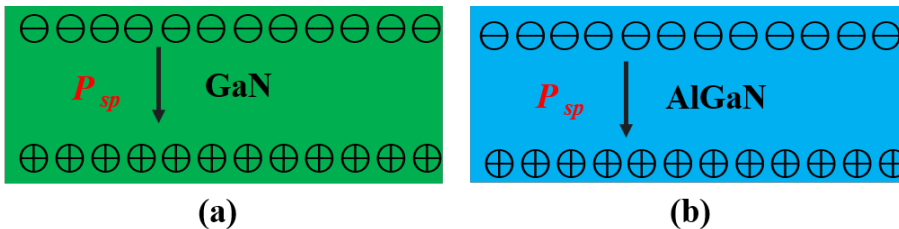


Figure 2.2: Spontaneous polarization in Ga-face (a) GaN and (b) AlGaN.

can be expressed as following, [7]

$$a_{Al_xGa_{1-x}N} = -0.077x + 3.189[\text{\AA}] \quad (2.1)$$

$$c_{Al_xGa_{1-x}N} = 0.203x + 5.185[\text{\AA}] \quad (2.2)$$

$$P_{sp}(Al_xGa_{1-x}N) = -0.09x - 0.034(1-x) + 0.021x(1-x) \quad (2.3)$$

When a junction is formed between two different semiconductor materials with distinct band gap energies it is called a heterojunction or heterostructure.[8] The AlGaN/GaN heterostructure is formed by a Ga-face 1-5  $\mu\text{m}$  GaN buffer layer on a foreign substrate, followed by a 10-30 nm AlGaN barrier layer. The lattice constants of AlGaN is smaller than that of GaN. When an AlGaN layer is grown on top of a GaN buffer, the lattice mismatch is accommodated by some tensile strain in the barrier layer as shown in Figure 2.3. Then, the tensile strain results in the piezoelectric polarization ( $P_{pz}$ ) in the AlGaN layer. In contrast to spontaneous polarization, the piezoelectric polarization is due to externally exerted strain by growth in the crystal structure. This strain causes distortion in the crystal and results in a high strain induced piezoelectric field.[9]

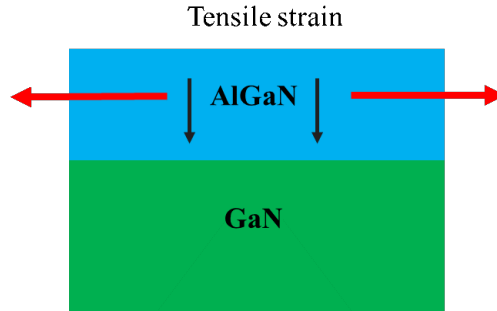


Figure 2.3: Piezoelectric polarization in Ga-face Wurtzite AlGaN due to tensile strain.

The magnitude for piezoelectric polarization in AlGaN along the c-axis can be expressed as,[10]

$$P_{pz}(AlGaN) = 2 \times \frac{a_{GaN} - a_{AlGaN}}{a_{AlGaN}} + (e_{31} - e_{33} \frac{c_{13}}{c_{33}}) \quad (2.4)$$

$$C_{13} = (5x + 103) \times 10^9 [Pa]$$

$$C_{33} = (-32x + 405) \times 10^9 [Pa]$$

$$e_{33} = 0.7x + 0.73 [C/m^2]$$

$$e_{31} = 0.11x - 0.49 [C/m^2]$$

where  $e_{13}$  and  $e_{33}$  are the piezoelectric coefficients of the  $Al_xGa_{1-x}N$  barrier layer,  $c_{13}$  and  $c_{33}$  are the elastic constants of the  $Al_xGa_{1-x}N$  barrier layer,  $a_{GaN}$  and  $a_{AlGaN}$  are the

lattice constant of the GaN layer and relaxed AlGaIn layer, respectively. The piezoelectric polarization in the AlGaIn barrier layer depends on the  $Al(x)$ . As the lattice constant of the AlGaIn decreases with an increase in  $Al(x)$  the piezoelectric polarization increases. For any given,  $Al(x)$  as the AlGaIn barrier layer exceeds a maximum critical thickness, strain relaxation tends to occur in the crystal structure resulting in reduction of piezoelectric polarization. Therefore, piezoelectric polarization in equation (2.4) can be modified as, [10]

$$P_{pz}(AlGaIn) = 2[1 - r(x)] \frac{a_{GaN} - a_{AlGaIn}}{a_{AlGaIn}} + (e_{31} - e_{33} \frac{c_{13}}{c_{33}}) \quad (2.5)$$

where,

$$r(x) = \frac{a_{AlGaIn,strained} - a_{GaN}}{a_{AlGaIn,relaxed} - a_{GaN}}$$

$a_{AlGaIn,strained}$  and  $a_{AlGaIn,relaxed}$  are the lattice constant of AlGaIn barrier under stress and relaxed conditions respectively. The value of  $(e_{31} - e_{33} \frac{c_{13}}{c_{33}}) < 0$  is always negative for the full range of  $Al(x)$ , therefore under tensile strain ( $a_{GaN} > a_{AlGaIn}$ ) the magnitude of piezoelectric polarization is always negative and for compressive strain ( $a_{GaN} < a_{AlGaIn}$ ) it is positive. Since the spontaneous polarization is always negative and points towards the substrate (in Ga-face) for GaN and AlGaIn as shown previously, the alignment of spontaneous and piezoelectric polarization is parallel for tensile strain and anti-parallel for compressive strain. Another important feature in III-nitrides is that if the polarity of growth is flipped from Ga-face to N-face or vice versa then both spontaneous and piezoelectric polarizations change directions.[9] The combined effect and constructive combination of spontaneous and piezoelectric polarization in AlGaIn/GaN heterostructure with Ga-face growth is illustrated in Figure 2.4. The difference in spontaneous and piezoelectric polarizations of two materials causes a high polarization sheet charge density to accumulate near the bottom of AlGaIn/GaN interface which is illustrated as,

$$\rho_{Pol} = P_{AlGaIn} - P_{GaN} = P_{AlGaIn,Spontaneous} + P_{AlGaIn,Piezoelectric} - P_{GaN,Spontaneous} \quad (2.6)$$

It is noteworthy that GaN buffer layer is fully relaxed and there is no piezoelectric polarization.

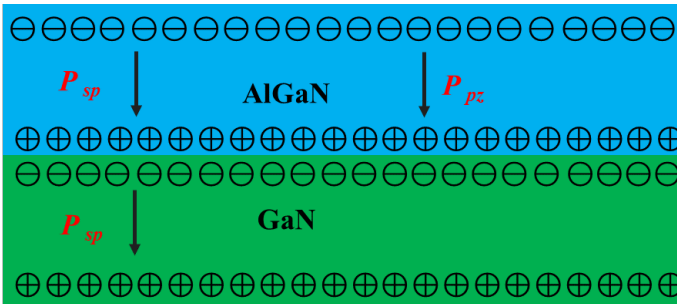


Figure 2.4: Combined spontaneous and piezoelectric polarization in AlGaIn/GaN heterostructure.

### 2.2.2. 2DEG FORMING

If a heterostructure is formed between these two semiconductors then, because of the difference in band gap energies, the conduction ( $E_C$ ) and valance band ( $E_V$ ) cannot be continuous across the interface as shown in Figure 2.5. When the semiconductors are brought together the Fermi level ( $E_f$ ) aligns and band bending occurs to accommodate the discontinuity. [8]

A triangular well containing the 2DEG emerges where electrons come from the donor like surface state or bulk GaN material. The maximum sheet carrier concentration formed at the interface of AlGa<sub>x</sub>N/GaN is expressed as, [9]

$$n_x(x) = \frac{\sigma_x}{e} - \left( \frac{\epsilon_0 \epsilon(x)}{d_d e^2} \right) (e\phi_B(x) + E_F(x) - \Delta E_c(x)) \quad (2.7)$$

where  $\epsilon_0$  is the electric permittivity,  $\epsilon(x) = 9.5 - 0.5x$  is the relative permittivity,  $x$  is the Al mole fraction of  $Al_xGa_{1-x}N$ ,  $d_d$  is the AlGa<sub>x</sub>N layer thickness,  $e\phi_B$  is the barrier height of the gate contact on AlGa<sub>x</sub>N ( $e\phi_B(x) = 0.84 + 1.3x$  [eV]),  $E_F$  is the Fermi level,  $E_C$  is the conduction band ( $E_C(x) = 6.2x + 3.4(1-x) - x(1-x)$  [eV]) and  $\Delta E_c$  is the conduction band discontinuity between AlGa<sub>x</sub>N and GaN ( $\Delta E_c(x) = 0.7[E_g(x) - E_g(0)]$ ), as shown in Table 2-3.

Table 2-3 band gap and band offsets of Al<sub>0.26</sub>Ga<sub>0.74</sub>N and GaN

	Al <sub>0.26</sub> Ga <sub>0.74</sub> N	GaN
Band Gap (eV)	3.93	3.40
$\Delta E_c$ (eV)		0.41
$\Delta E_v$ (eV)		-0.24

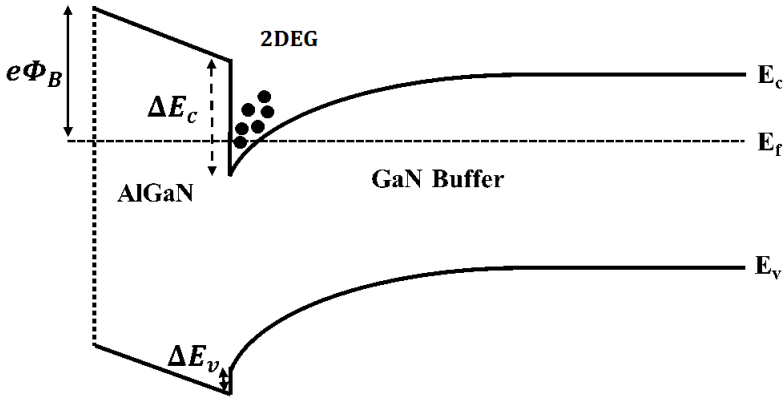


Figure 2.5: Energy Band diagram of AlGa<sub>x</sub>N on Ga-face GaN after heterostructure formation.

The 2DEG sheet charge concentration as mentioned in equation (2.7) increases with the Al content in the barrier layer, because the  $Al(x)$  concentration increases both piezoelectric polarization and AlGa<sub>x</sub>N band gap energy resulting in greater conduction band offset  $\Delta E_c(x)$ . However, some of the difficulties in making a wider band gap barrier layer are formation of good quality ohmic contacts and growth strain issues. The 2DEG sheet charge concentration also increases with the AlGa<sub>x</sub>N barrier thickness but only up to a

maximum critical thickness, typically 40 nm, and then flattens out with further increase in the thickness due to strain relaxation.

Recently, more modified barrier designs have been reported to further improve the AlGa<sub>N</sub>/Ga<sub>N</sub> HFETs performance such as AlGa<sub>N</sub>/AlN/GaN structures. The major restrictions in achieving very high electron mobility in the 2DEG are interface scattering, dislocation scattering and alloy disorder scattering. With the insertion of a very thin (1 nm) and wide band gap (6.2 eV) AlN material layer sandwiched between the AlGa<sub>N</sub> and Ga<sub>N</sub> layers as shown in Figure 2.6, the conduction band offset,  $\Delta E_C$ , is further increased and electron alloy disorder scatterings is reduced. The binary AlN spacer layer reduces the penetration of electrons from the Ga<sub>N</sub> channel into the ternary AlGa<sub>N</sub> barrier layer, thereby significantly improving the electron mobility.

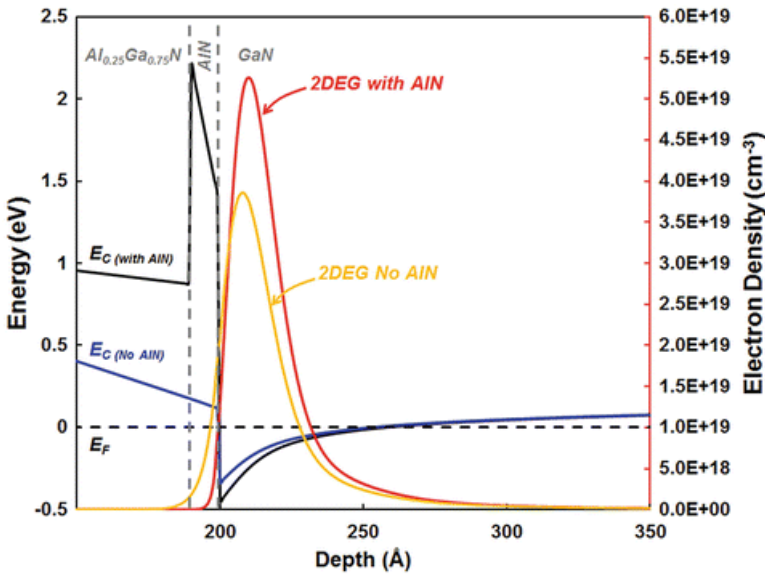


Figure 2.6: Energy Band diagram of AlGa<sub>N</sub>/AlN/GaN heterostructure and a 2DEG distribution with and without a 1 nm AlN interlay.[11]

In summary, the inherent advantage of a heterostructure in HEMTs is the formation of 2DEG, which is formed by the confinement of electrons in a defined triangular quantum well. The electrons have quantized energy levels in a one spatial direction and are only free to move laterally, along the heterostructure interface. This 2DEG has a unique characteristic of extremely high electron mobility ( $2000 \text{ cm}^2\text{V}^{-1}\text{s}^{-1}$ ) leading to much reduced on-state resistance ( $R_{on}$ ) and improved high frequency performance. The presence of very high polarization effects in Ga<sub>N</sub> makes it possible to fabricate devices without the intentional doping of the upper wide band gap material. This significantly reduces ionized impurity scattering and Coulomb scattering as the 2D electrons are separated from the supply atoms. Due to these polarization effects the 2DEG sheet charge density in AlGa<sub>N</sub>/Ga<sub>N</sub> heterostructures is about five times higher than that in doped AlGaAs/GaAs HEMTs. Therefore, AlGa<sub>N</sub>/Ga<sub>N</sub> heterostructures are widely used

in microwave and power device. However, the application of AlGaN/GaN heterostructure based sensor are not fully developed. Next section introduces the basic mechanism and structures of the AlGaN/GaN heterostructure based sensors reported in this thesis, namely gas sensors, UV detectors, and pressure sensors.

## 2.3. ALGaN/GaN HETEROSTRUCTURE SENSORS

### 2.3.1. SURFACE CHEMISTRY AND GAS SENSING MECHANISMS

The most commonly used structures of AlGaN/GaN heterostructure gas sensors are the HEMT and the Schottky barrier diode (SBD) as depicted in Figure 2.7. Compared with the traditional power and microwave HEMT/SBD devices, the main differences are that the gate/anode active area are without passivation and replaced by gas reactive materials, such as catalytic metal, metal oxide, polymers, or nano materials. Upon exposure to the gas, the interaction with the functional gate changes the surface state, which leads the change of the sheet carrier concentration of 2DEG channel at the interface of the AlGaN/GaN heterostructure. This effect is used in gas sensors which are able to detect the surface polarity change by gases or liquids.

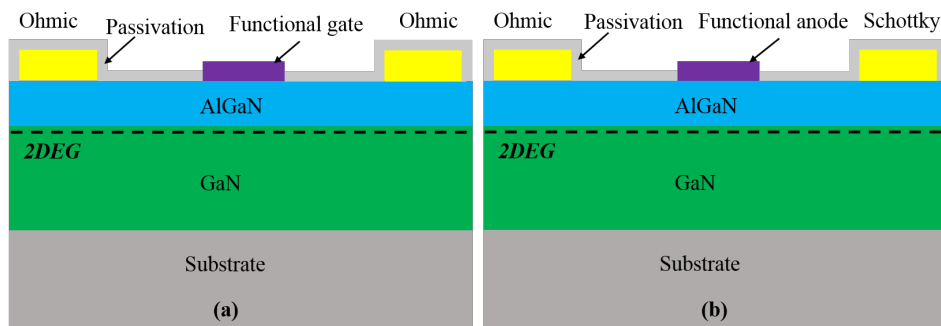


Figure 2.7: Schematic image of AlGaN/GaN heterostructure sensors (a)HEMT; (b) Schottky barrier diode.

According to the strength of interaction between the gas molecule and the functional material surface, there are two adsorption phenomena: physisorption and chemisorption. The energy curve along with reaction distance for a gas molecule approaching a material surface is shown in Figure 2.8 to illustrate the adsorption process. Physisorption is a weak interaction and the bonding is due to van der Waals forces. The physisorption usually happens at relative low temperature and the typical binding energies are 10-100 meV. If the molecules can overcome an activation energy barrier  $E_{conv}$ , it will become chemisorption, which involves covalent or ionic bonds. The binding energies are 1-10 eV at a distance of 1-3 Å from the surface. Chemisorption is usually a dissociative process in which the activation barrier height is related to that energy to dissociate the gas molecules. The activation energy is highly dependent on the material, its surface structure, and molecular orientation. And the adsorption sites of the material surface and the temperature also play a vital role in the chemisorption process. The desorption is the reverse process of adsorption. Therefore, a heating unit for gas sensor is usually needed to speed up the rate of chemisorption and desorption.

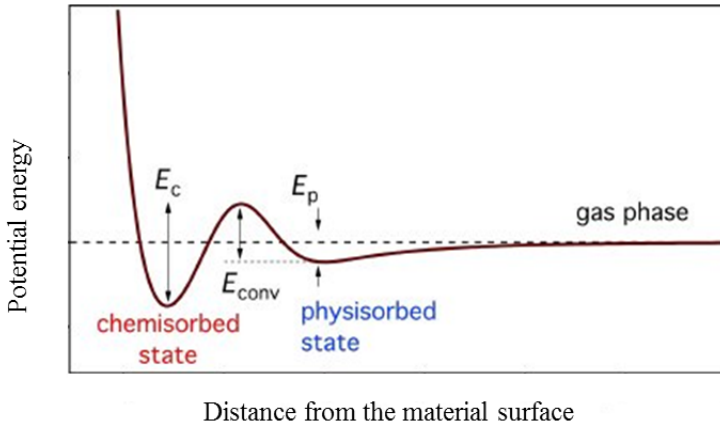


Figure 2.8: The potential energy vs. distance from the material surface.  $E_{conv}$ : activation energy barrier height.  $E_p$ : physisorption potential well;  $E_c$ : chemisorption potential well. [12]

For a bare gate or porous gate, direct adsorption of the gaseous molecules occurs on the top surface of the GaN layer. As these open areas are exposed to an oxygen-containing atmosphere during processing and measurement, the GaN probably is oxidized so that the adsorption in the pores takes place on some form of non-stoichiometric Ga-oxynitride. The adsorption leads to a change in the GaN depletion layer. In general, oxidizing gases lead to an increased depletion layer and a decreased source-drain current, whereas sensor signals appear opposite upon exposure to reducing gases like CO, H<sub>2</sub>. [13] The modulation of the depletion layer caused by chemisorption of gaseous species on bare GaN areas results in changes in the electron density of 2DEG and therefore, in the source-drain current. For different functional materials and different molecular species, the basic principle is almost the same, namely the surface state is changed by the gas absorption and then results in the changes of the depletion layer. Therefore, the functional materials play an important role to selectively sensitive behaviour to target gases.

A representative example is the Pt surface on AlGaN/GaN heterostructure for gas detection as shown in Figure 2.9. Molecular hydrogen adsorbs on the Pt surfaces and the hydrogen species diffuse rapidly through the metal to build up a H-induced dipole layer at the Pt-GaN interface. The dipole moment is oriented out of the GaN leading to a negative voltage drop. The potential drop at the interface is balanced by a modulation of the depletion layer, which leads to a decrease in the barrier height and an increase in the drain current. The change of barrier height based on different gases is illustrated in Figure 2.10. The sensing mechanism could be explained at the saturation region of an AlGaN/GaN HEMT as following equations,

$$I_{DS} = \frac{\mu C_g W_g}{2L_g} (V_{GS} - V_T)^2 \quad (2.8)$$

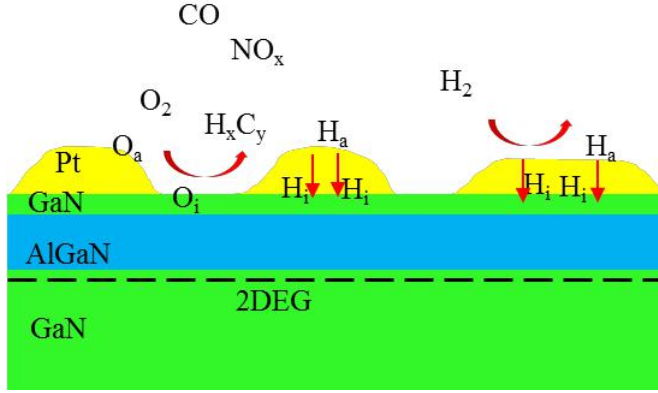


Figure 2.9: A representative example: Pt/AlGaIn/GaN gas sensor ( $H_a$ : absorbed Hydrogen,  $H_i$ : interfacial Hydrogen,  $O_a$ : absorbed Oxygen,  $O_i$ : interfacial Oxygen). [12]

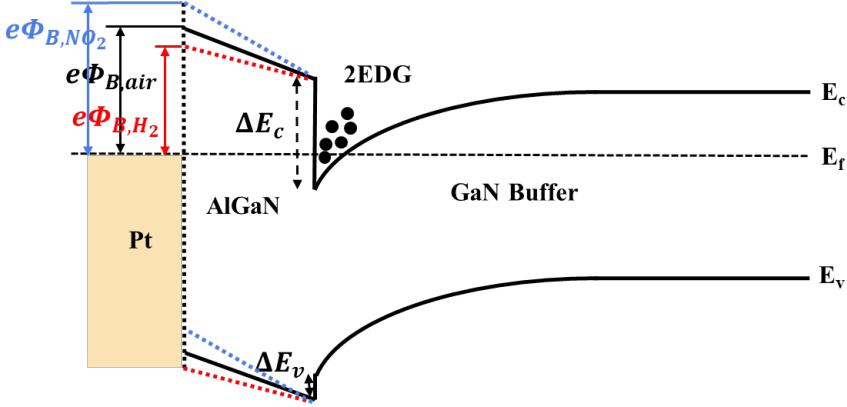


Figure 2.10: Energy band diagram of a Pt/AlGaIn/GaN heterostructure sensor in air (black line) and under hydrogen (red dotted line) or  $\text{NO}_2$  (blue dotted line) gas.

$$V_T = \Phi_B - \frac{\Delta E_C}{e} - \frac{en_s}{C_g} \quad (2.9)$$

$$n_s = \frac{\sigma}{e} - \left( \frac{\epsilon_0 \epsilon}{d_d e^2} \right) [e(\Phi_B - V_{GS}) + E_F - \Delta E_C] \quad (2.10)$$

where  $\mu$  is the 2DEG mobility,  $W_g$  and  $L_g$  are the gate width and length,  $C_g$  is the gate to channel capacitance,  $\Phi_B$  is the barrier height,  $\Delta E_C$  is the conduction band discontinuity,  $e$  is the elementary charge,  $n_s$  is the sheet carrier density,  $\sigma$  is the channel density,  $\epsilon_0$  and  $\epsilon$  are the electric permittivity and the relative permittivity of AlGaIn layer,  $d_d$  is the AlGaIn layer thickness,  $E_F$  is the Fermi level. For metal gate, the barrier height is related to the work function of the metal ( $\phi_m$ ) and the semiconductor electron affinity ( $\chi_s$ ),  $\Phi_B = \phi_m - \chi_s$ . For semiconductor gate materials, the barrier height depends on the

difference of the two semiconductors electron affinity,  $\Phi_B = \chi_{s1} - \chi_{s2}$ . Also, the sheet carrier density changes with the barrier height. The increase of barrier height results in a decrease of the sheet carrier density, which leads to an increase of  $V_T$  and a decrease of drain current.

### 2.3.2. UV DETECTION

The basic principle of semiconductor photo sensor or detector is the internal photoelectric effect. The internal photoelectric effect does not produce photoelectrons which can be observed outside the material, but only excites electrons from the valence band to the conduction band in the semiconductor material as shown in Figure 2.11. An excited electron and the vacancy the promoted electron leaves behind, are referred to as electron-hole pair. In general, the electron-hole pair will recombine if they are left in the material long enough. This time is called the recombination lifetime,  $\tau_r$ . The electrons and holes in impurity energy level also could absorb the photon. Common devices based on the internal photoelectric effect are solar cells and photodetectors (PDs).

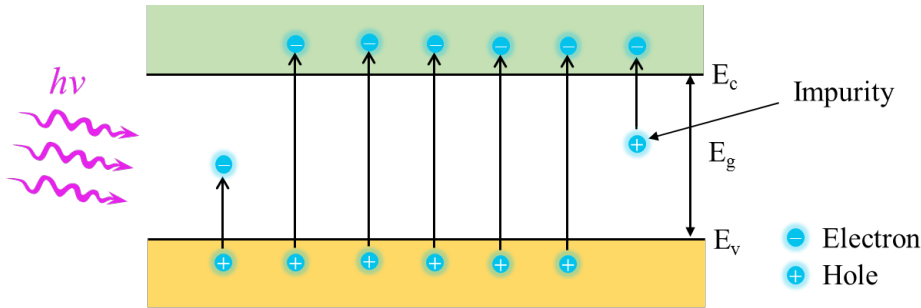


Figure 2.11: Schematic drawing of the internal photoelectric effect.

For the intrinsic semiconductor, the absorption condition is according to the following equation:

$$h\nu \geq E_g \quad (2.11)$$

$$\lambda \leq \frac{hc}{E_g} = \frac{1.24}{E_g} [\mu m] \quad (2.12)$$

where  $h$  is the Planck constant,  $\nu$  and  $\lambda$  are the frequency and wavelength of the incoming light, respectively;  $E_g$  is the bandgap of semiconductor materials. The bandgap of semiconductor materials should be above 3.1 eV (400 nm) if the photodetectors need to be blind for visible light. For UV detection, the wide-bandgap materials, such as GaN [14–16], AlN [17–19], ZnO [20–22], Ga<sub>2</sub>O<sub>3</sub> [23–25], WO<sub>3</sub> [26–28] and their combinations, are of great interest. GaN is one of the most promising semiconductors for the UV detection because of its large direct bandgap (3.4 eV at room temperature in wurtzitic structure), high thermal and chemical stability, and resistance in harsh environment conditions.

Numerous UV photodetectors based on GaN-based materials have been reported in various configurations, such as photoconductor[29–31], phototransistor, metal-semiconductor-metal (MSM) detector [14–16], Schottky diodes[32] and p-n or p-i-n photodiode[33, 34]. The most common structures of GaN-based UV photodetector are shown in Figure 2.12. An ideal photodetector would exhibit low dark current to minimize the interference noise and high responsivity to maximize the signal. Compared to other photodetector architectures, AlGaIn/GaN heterostructure photodetectors are able to provide an extremely large photoconductive gain due to the high electron density and velocity ( $10^7$  cm/s) of 2DEG. In other words, the AlGaIn/GaN heterostructure have higher responsivity.

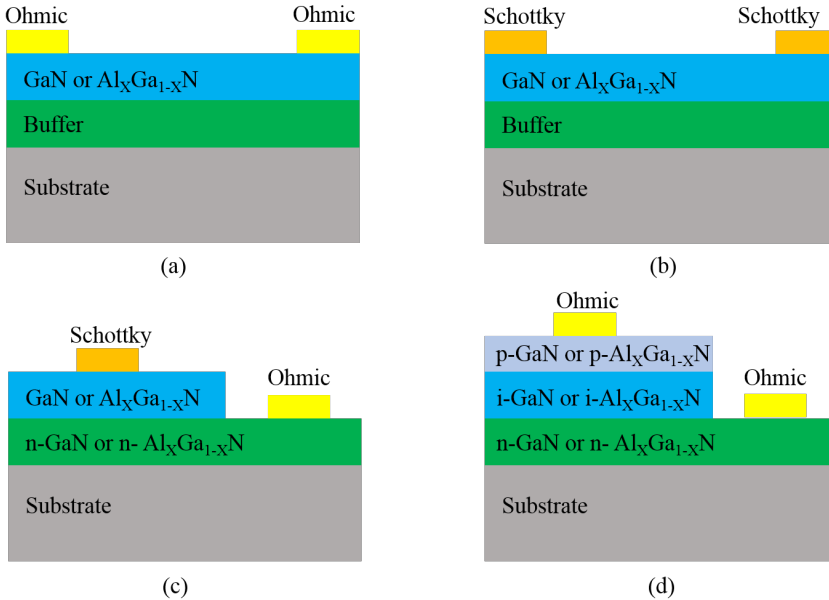


Figure 2.12: Typical GaN-based UV photodetector structures: (a) photoconductor; (b) MSM photodetector; (c) Schottky photodiode; (d) PIN photodiode.

The basic mechanism of AlGaIn/GaN heterostructure photodetector is illustrated in Figure 2.13. Upon exposure to the ultraviolet light ( $h\nu > E_g$ ), the electron-hole pairs are generated in both the AlGaIn layer and GaN layer. For the AlGaIn layer, the optical generated electrons move into the 2DEG channel due to the built-in polarization field and the holes are swept to the surface. There are several mechanisms to explain the movement of the electron-hole pair generated in the GaN buffer layer [35–37]. Vetry et al[35] proposed that the photogenerated holes moved to the surface due to the electric field in the AlGaIn layer. Yun et al[38] considered that the movement to the surface occurs because of the thermal energy from the light illumination and neutralization of the surface state. Zaffar et al[37] proposed that the generated holes moved to the GaN/substrate interface due to the barrier height of the valence band (0.26 eV) and the direction of the built-in electric field of the GaN layer is towards the substrate. In this thesis, we suggest that the generated holes in the GaN layer are pulled by the built-in electric field to the substrate

as a virtual back-gate; the electrons move to the 2DEG channel; the photo generated electrons in the AlGa<sub>N</sub> layer move to the 2DEG channel and the holes are swept to the surface as a virtual top-gate.

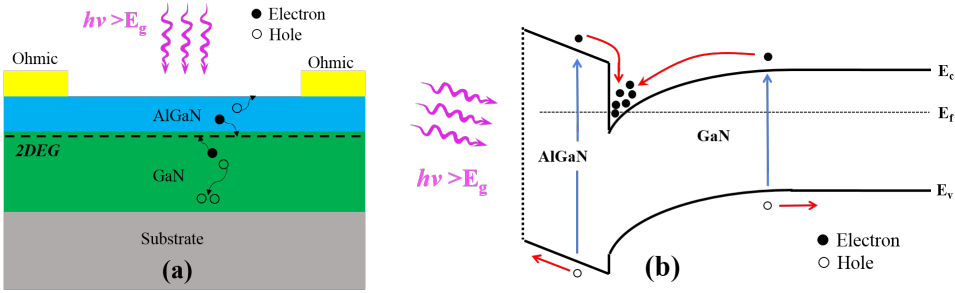


Figure 2.13: (a) Schematic diagram of a AlGa<sub>N</sub>/Ga<sub>N</sub> heterostructure photodetector under illumination showing the electron-hole pair generation and movement. (b) Equivalent mechanisms of band gap structure.

The spectral current responsivity of the photodetector is expressed:

$$R_{\lambda} = \frac{I_p}{P} [A/W] \quad (2.13)$$

where  $I_p$  is the output current of AlGa<sub>N</sub>/Ga<sub>N</sub> heterostructure photodetector,  $P$  is the incident power. For the AlGa<sub>N</sub>/Ga<sub>N</sub> heterostructure photodetector, the drain current is affected by the photocurrent both in the AlGa<sub>N</sub> layer and the Ga<sub>N</sub> layer. According to the theory of internal photoelectric effect and HEMT device, the change in drain current ( $\Delta I = \Delta I_1 + \Delta I_2$ ) is expressed by the following equations[37, 39]:

$$\Delta I_1 = I_{ph,AlGaN} \times \frac{\tau_h}{\tau_e} \quad (2.14)$$

$$\Delta I_2 = \frac{g_m n k T}{q} \ln \left[ 1 + \frac{I_{ph,GaN}}{I_s} \right] \quad (2.15)$$

where  $I_{ph,AlGaN}$  and  $I_{ph,GaN}$  are the photocurrent in AlGa<sub>N</sub> and Ga<sub>N</sub> layer, respectively,  $\tau_h$  and  $\tau_e$  are effective holes lifetime on the surface and channel electron lifetime,  $n$ ,  $k$ ,  $T$ ,  $q$  and  $I_s$  are the ideality factor for the heterostructure, Boltzmann constant, temperature in  $K$ , electronic charge, reverse saturation current, respectively, and  $g_m$  is the appropriate transconductance for the back-gate bias.

### 2.3.3. PRESSURE SENSING

The piezoelectric and spontaneous polarization properties of AlGa<sub>N</sub>/Ga<sub>N</sub>-based materials suggests that the AlGa<sub>N</sub>/Ga<sub>N</sub> heterostructure would be an excellent candidate for a pressure or stress sensors. They can be realized by etching away the substrate to form a moveable MEMS structure and building the AlGa<sub>N</sub>/Ga<sub>N</sub> sensing unit on it. The schematic diagram of a AlGa<sub>N</sub>/Ga<sub>N</sub> membrane structure pressure is shown in Figure 2.14. The direction of pressure to membrane depends on the difference pressure between the outside pressure ( $P_{Out}$ ) and the inside pressure ( $P_{In}$ ). A deflection of the

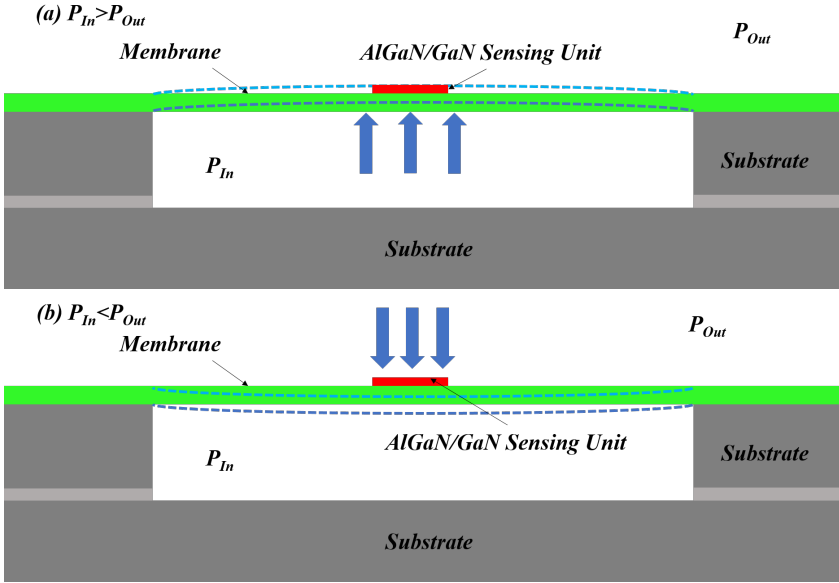


Figure 2.14: Schematic drawing of an AlGaN/GaN circular membrane, suspended on substrate (a)  $P_{In} > P_{Out}$ ; (b)  $P_{In} < P_{Out}$ .

membrane due to the differential pressure on the two sides of the membrane, produces a tensile strain ( $P_{In} > P_{Out}$ ) or compressive strain ( $P_{In} < P_{Out}$ ). The basic principle of AlGaN/GaN pressure sensor is reflected in the following equations.

$$P_{pz}(AlGaN) = 2[1 - r(x)] \frac{a_{GaN} - a_{AlGaN}}{a_{AlGaN}} + (e_{31} - e_{33} \frac{c_{13}}{c_{33}}) \quad (2.16)$$

where  $a_{AlGaN,strained}$  and  $a_{AlGaN,relaxed}$  are the lattice constant of the AlGaN barrier under stress and relaxed conditions, respectively. The value of  $(e_{31} - e_{33} \frac{c_{13}}{c_{33}}) < 0$  is always negative for the full range of Al (x) content. Therefore, the magnitude of piezoelectric polarization would change according to the magnitude of the tensile strain ( $a_{GaN} > a_{AlGaN}$ ) or compressive strain ( $a_{GaN} < a_{AlGaN}$ ). Then the sheet charge density ( $\sigma_{Pol}$ ) and the electron sheet carrier density ( $n_s$ ) change with the strain or external pressure, thus leading to the change of current output of the AlGaN/GaN devices [40]. The energy band diagrams of an AlGaN/GaN heterostructure under tension and compression condition are shown in Figure 2.15. Since the spontaneous polarization is always negative and points towards the substrate (in Ga-face) for GaN and AlGaN, the alignment of spontaneous and piezoelectric polarization is parallel for tensile strain and anti-parallel for compressive strain. Therefore, under tension condition as illuminated in Figure 2.15(a), the negative piezoelectric polarization charges are introduced along the AlGaN/GaN interface and the energy band of the AlGaN close to AlGaN/AlN interface tilts up and the energy band of the GaN near AlN/GaN interface is bent down. Meantime, the increased sheet charge density ( $\sigma_{Pol}$ ) results in more free electrons and the 2DEG increases. In contrast, under compression condition as shown in 2.15(b), the energy band of the AlGaN close to AlGaN/GaN

interface is bend down and the energy band of the GaN side is elevated. Thus, the 2DEG quantum well becomes shallower, resulting in a decrease of the 2DEG density.

$$\sigma_{Pol} = P_{Sp}(AlGaN) + P_{Pz}(AlGaN) - P_{Sp}(GaN) - P_{Pz}(GaN) \quad (2.17)$$

$$n_s = \frac{\sigma_{Pol}}{e} - \left(\frac{\epsilon_0 \epsilon}{d_d e^2}\right)(e\phi_B + E_F - \Delta E_c) \quad (2.18)$$

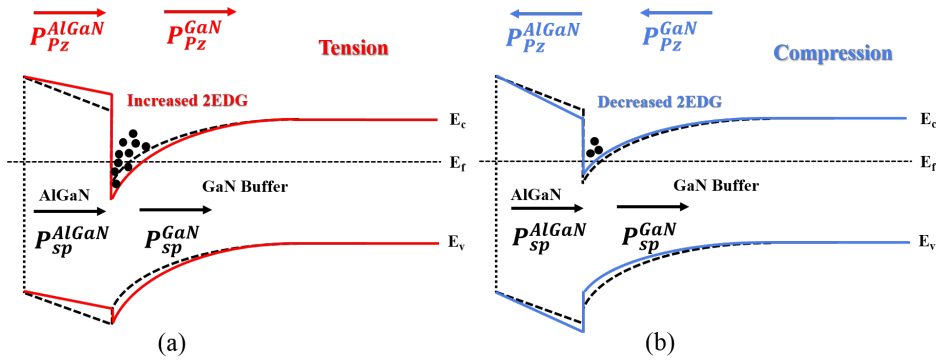


Figure 2.15: Energy band diagram of AlGaN/GaN heterostructure under (a) tension and (b) compression condition[40].

## 2.4. CHAPTER SUMMARY

In this chapter, the properties of GaN materials and AlGaN/GaN heterostructures, the 2DEG forming, and operating principles of AlGaN/GaN devices are discussed. Then the mechanism and structures of AlGaN/GaN heterostructure based sensors, namely gas sensors, UV detectors, and pressure sensors are introduced. In the next chapter a concept of sensor platform based on AlGaN/GaN heterostructures is presented and the main microfabrication steps to realize the sensors are discussed.

## REFERENCES

- [1] H. P. Maruska and J. Tietjen, "The preparation and properties of vapor-deposited single-crystal-line GaN," Applied Physics Letters, vol. 15, no. 10, pp. 327-329, 1969.
- [2] S. Nakamura, "GaN growth using GaN buffer layer," Japanese Journal of Applied Physics, vol. 30, no. 10A, p. L1705, 1991.
- [3] S. Nakamura, Y. Harada, and M. Seno, "Novel metalorganic chemical vapor deposition system for GaN growth," Applied physics letters, vol. 58, no. 18, pp. 2021-2023, 1991.
- [4] S. Z. H. Zaidi, "Applications of GaN HFETs in UV detection and Power electronics," University of Sheffield, 2014.

- [5] M. Rais-Zadeh et al., "Gallium nitride as an electromechanical material," *Journal of Microelectromechanical Systems*, vol. 23, no. 6, pp. 1252-1271, 2014.
- [6] O. Ambacher et al., "Two-dimensional electron gases induced by spontaneous and piezoelectric polarization charges in N- and Ga-face AlGa<sub>N</sub>/Ga<sub>N</sub> heterostructures," *Journal of applied physics*, vol. 85, no. 6, pp. 3222-3233, 1999.
- [7] O. Ambacher et al., "Pyroelectric properties of Al (In) Ga<sub>N</sub>/Ga<sub>N</sub> hetero- and quantum well structures," *Journal of physics: condensed matter*, vol. 14, no. 13, p. 3399, 2002.
- [8] D. Masse, "Modern microwave transistors-theory, design and performance.(The Book End)," *Microwave Journal*, vol. 46, no. 6, pp. 152-153, 2003.
- [9] O. Ambacher et al., "Two-dimensional electron gases induced by spontaneous and piezoelectric polarization charges in N- and Ga-face AlGa<sub>N</sub>/Ga<sub>N</sub> heterostructures," *Journal of Applied Physics*, vol. 85, no. 6, pp. 3222-3233, 1999.
- [10] I. R. Gatabi et al., "PECVD silicon nitride passivation of AlGa<sub>N</sub>/Ga<sub>N</sub> heterostructures," *IEEE Transactions on Electron Devices*, vol. 60, no. 3, pp. 1082-1087, 2013.
- [11] C. S. Suh, "Lateral Ga<sub>N</sub> HEMT Structures," in *Gallium Nitride-enabled High Frequency and High Efficiency Power Conversion*: Springer, 2018, pp. 29-49.
- [12] M. Toth, C. Lobo, V. Friedli, A. Szkudlarek, and I. Utke, "Continuum models of focused electron beam induced processing," *Beilstein journal of nanotechnology*, vol. 6, no. 1, pp. 1518-1540, 2015.
- [13] J. Schalwig, G. Müller, M. Eickhoff, O. Ambacher, and M. Stutzmann, "Gas sensitive Ga<sub>N</sub>/AlGa<sub>N</sub>-heterostructures," *Sensors and Actuators B: Chemical*, vol. 87, no. 3, pp. 425-430, 2002.
- [14] R. W. Chuang et al., "Gallium nitride metal-semiconductor-metal photodetectors prepared on silicon substrates," (in English), *Journal of Applied Physics*, vol. 102, no. 7, p. 073110, Oct 1 2007.
- [15] C. K. Wang et al., "Ga<sub>N</sub> MSM UV photodetectors with titanium tungsten transparent electrodes," (in English), *Ieee Transactions on Electron Devices*, vol. 53, no. 1, pp. 38-42, Jan 2006.
- [16] C. K. Wang et al., "Ga<sub>N</sub> MSM UV Photodetector With Sputtered Al<sub>N</sub> Nucleation Layer," (in English), *Ieee Sensors Journal*, vol. 15, no. 9, pp. 4743-4748, Sep 2015.
- [17] J. Li, Z. Fan, R. Dahal, M. Nakarmi, J. Lin, and H. Jiang, "200 nm deep ultraviolet photodetectors based on Al<sub>N</sub>," *Applied physics letters*, vol. 89, no. 21, p. 213510, 2006.
- [18] W. Zheng, F. Huang, R. Zheng, and H. Wu, "Low-Dimensional Structure Vacuum-Ultraviolet-Sensitive ( $\lambda < 200$  nm) Photodetector with Fast-Response Speed Based on High-Quality Al<sub>N</sub> Micro/Nanowire," *Advanced Materials*, vol. 27, no. 26, pp. 3921-3927, 2015.

- [19] R. Dahal, T. Al Tahtamouni, J. Lin, and H. Jiang, "AlN avalanche photodetectors," *Applied Physics Letters*, vol. 91, no. 24, p. 243503, 2007.
- [20] Y. Wang, Z. Liao, G. She, L. Mu, D. Chen, and W. Shi, "Optical modulation of persistent photoconductivity in ZnO nanowires," *Applied Physics Letters*, vol. 98, no. 20, p. 203108, 2011.
- [21] S. Dogar, W. Khan, and S.-D. Kim, "Ultraviolet photoresponse of ZnO nanostructured AlGaN/GaN HEMTs," *Materials Science in Semiconductor Processing*, vol. 44, pp. 71-77, 2016.
- [22] M. Chen, L. Hu, J. Xu, M. Liao, L. Wu, and X. Fang, "ZnO hollow-sphere nanofilm-based high-performance and low-cost photodetector," *Small*, vol. 7, no. 17, pp. 2449-2453, 2011.
- [23] Y. Li et al., "Efficient assembly of bridged  $\beta$ -Ga<sub>2</sub>O<sub>3</sub> nanowires for solar-blind photodetection," *Advanced Functional Materials*, vol. 20, no. 22, pp. 3972-3978, 2010.
- [24] W. Y. Kong et al., "Graphene- $\beta$ -Ga<sub>2</sub>O<sub>3</sub> heterojunction for highly sensitive deep UV photodetector application," *Advanced Materials*, vol. 28, no. 48, pp. 10725-10731, 2016.
- [25] R. Zou et al., "High detectivity solar-blind high-temperature deep-ultraviolet photodetector based on multi-layered (100) facet-oriented  $\beta$ -Ga<sub>2</sub>O<sub>3</sub> nanobelts," *Small*, vol. 10, no. 9, pp. 1848-1856, 2014.
- [26] D. L. Shao, M. P. Yu, J. Lian, and S. Sawyer, "Optoelectronic properties of three dimensional WO<sub>3</sub> nanoshale and its application for UV sensing," (in English), *Optical Materials*, vol. 36, no. 5, pp. 1002-1005, Mar 2014.
- [27] Z. Hai, M. K. Akbari, C. Y. Xue, H. Y. Xu, L. Hyde, and S. Zhuiykov, "Wafer-scaled monolayer WO<sub>3</sub> windows ultra-sensitive, extremely-fast and stable UV-A photodetection," (in English), *Applied Surface Science*, vol. 405, pp. 169-177, May 31 2017.
- [28] J. Sun et al., "Suspended tungsten trioxide (WO<sub>3</sub>) gate AlGaN/GaN heterostructure deep ultraviolet detectors with integrated micro-heater," *Optics Express*, vol. 27, no. 25, pp. 36405-36413, 2019/12/09 2019.
- [29] E. Munoz et al., "Photoconductor gain mechanisms in GaN ultraviolet detectors," *Applied physics letters*, vol. 71, no. 7, pp. 870-872, 1997.
- [30] F. González-Posada, R. Songmuang, M. Den Hertog, and E. Monroy, "Room-temperature photodetection dynamics of single GaN nanowires," *Nano letters*, vol. 12, no. 1, pp. 172-176, 2012.
- [31] K. Xiong et al., "Single crystal gallium nitride nanomembrane photoconductor and field effect transistor," *Advanced Functional Materials*, vol. 24, no. 41, pp. 6503-6508, 2014.

- [32] K. H. Lee, P. C. Chang, S. J. Chang, Y. C. Wang, C. L. Yu, and S. L. Wu, "AlGa<sub>N</sub>/Ga<sub>N</sub> Schottky Barrier UV Photodetectors With a Ga<sub>N</sub> Sandwich Layer," (in English), *Ieee Sensors Journal*, vol. 9, no. 7, pp. 814-819, Jul 2009.
- [33] B. Butun, T. Tut, E. Ulker, T. Yelboga, and E. Ozbay, "High-performance visible-blind Ga<sub>N</sub>-based p-i-n photodetectors," (in English), *Applied Physics Letters*, vol. 92, no. 3, p. 033507, Jan 21 2008.
- [34] T. Tut, T. Yelboga, E. Ulker, and E. Ozbay, "Solar-blind AlGa<sub>N</sub>-based p-i-n photodetectors with high breakdown voltage and detectivity," (in English), *Applied Physics Letters*, vol. 92, no. 10, p. 103502, Mar 10 2008.
- [35] R. Vetry, N. Q. Zhang, S. Keller, and U. K. Mishra, "The impact of surface states on the DC and RF characteristics of AlGa<sub>N</sub>/Ga<sub>N</sub> HFETs," *IEEE Transactions on Electron Devices*, vol. 48, no. 3, pp. 560-566, 2001.
- [36] Y. C. Chang, "Effects of illumination on the excess carrier dynamics and variations of the surface states in an AlGa<sub>N</sub>/Ga<sub>N</sub> heterostructure," (in English), *Journal of Applied Physics*, vol. 107, no. 3, p. 033706, Feb 2010.
- [37] Z. H. Zaidi and P. A. Houston, "Highly sensitive UV detection mechanism in AlGa<sub>N</sub>/Ga<sub>N</sub> HEMTs," *IEEE Transactions on electron devices*, vol. 60, no. 9, pp. 2776-2781, 2013.
- [38] Y.-C. Chang, "Effects of illumination on the excess carrier dynamics and variations of the surface states in an AlGa<sub>N</sub>/Ga<sub>N</sub> heterostructure," *Journal of Applied Physics*, vol. 107, no. 3, p. 033706, 2010.
- [39] T. Narita, A. Wakejima, and T. Egawa, "Ultraviolet photodetectors using transparent gate AlGa<sub>N</sub>/Ga<sub>N</sub> high electron mobility transistor on silicon substrate," *Japanese Journal of Applied Physics*, vol. 52, no. 1S, p. 01AG06, 2013.
- [40] X. Wang et al., "Piezotronic effect modulated heterojunction electron gas in AlGa<sub>N</sub>/Al<sub>N</sub>/Ga<sub>N</sub> heterostructure microwire," *Advanced materials*, vol. 28, no. 33, pp. 7234-7242, 2016.

# 3

## DESIGN AND FABRICATION OF ALGAN/GAN HETEROSTRUCTURE SENSORS

### 3.1. INTRODUCTION

In this chapter, the design, fabrication and characterization techniques used for the realization and evaluation of the proposed AlGaN/GaN devices are described. First, the basic design of the MEMS AlGaN/GaN heterostructure sensor is introduced. The device fabrication has been mainly performed at the microelectronics laboratory (clean room class 1000) of the institute of Semiconductors, Chinese Academy of Sciences. Process investigation includes the selection of the epitaxial structure and device isolation as well as selection and implementation through deposition, patterning and etching of the metal stack for low ohmic contacts definition and for the microheater realization. Then two package solutions, chip on board (COB) and ceramic quad flat no-lead (CQFN) package, are compared with respect to heat dissipation and signal stability. The resistance of the ohmic contacts is measured based on the transmission line model (TLM). The microheater calibration and self-heating influence study are carried out, followed by the I-V characterization of the devices before and after the membrane release step. The temperature and humidity effect on the AlGaN/GaN device performance is studied.

## 3.2. DESIGN AND FABRICATION OF THE BASIC HEMT MEMS SENSORS

### 3.2.1. THE SENSOR GEOMETRY DESIGN

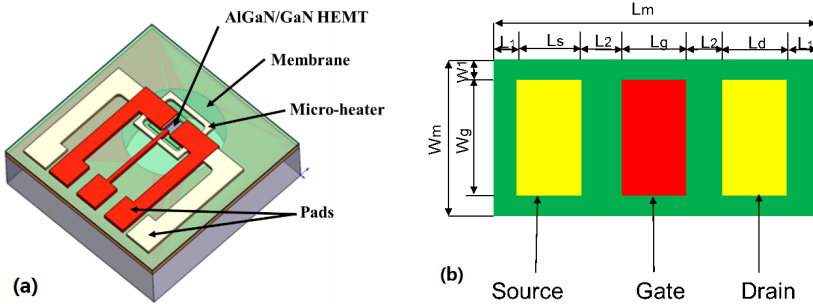


Figure 3.1: The HEMT MEMS Sensor: (a) Schematic drawing of the basic structure; (b) top view configuration and main geometrical parameters.

The basic schematic of the AlGaN/GaN structure with an integrated micro-heater is illustrated in Figure 3.1(a). A voltage or current controlled MEMS micro-heater, with a suspended and thus thermally isolated structure, enables low power heating. The micro-heater and HEMT sensor area were defined as active area. From previous work [1], it is known that a  $\text{SiO}_2$  layer with low thermal conductivity provides effective thermal isolation between the active sensor area and the silicon frame. This layer configuration allows for substantial reduction of power consumption, down to 5-100 mW, when the active area of the sensor is heated to the desired operating temperature. The layout and main geometrical parameters of the HEMT are indicated in Figure 3.1(b). The main design parameters are the gate length  $L_g$  and width  $W_g$ , and the gate to source/drain  $L_2$ . Gate area

Table 3.1: Gate dimensions of HEMT devices ( $\mu\text{m}$ ).

Structure	$L_1$	$L_{s-d}$	$L_2$	$L_g$	$W_g$	$W_1$	$W_g/L_g$
<b>A1</b>	15	60	30	40	160	5	4
<b>A2</b>	15	60	30	40	80	5	2
<b>A3</b>	15	60	30	40	40	5	1
<b>A4</b>	15	60	30	40	20	5	0.5
<b>B1</b>	15	60	10	40	320	5	8
<b>B2</b>	15	60	10	40	160	5	4
<b>B3</b>	15	60	10	40	80	5	2
<b>B4</b>	15	60	10	40	40	5	1

dimensions directly impact the drain-source current magnitude. Higher  $W_g/L_g$  ratios give higher current output. Consequently, varying these parameters would result in different sensing response, signal variation magnitude and transient response. The chosen dimension of the HEMT device are reported in Table 3-1.

### 3.2.2. MASK DESIGN AND PROCESS FLOW

The layout (single die) of the suspended of the AlGaIn/GaN based sensor is shown in Figure 3.2. The die size is 10 mm x 10 mm, and it contains 24 chips with dimensions of 2 mm x 2 mm. The chips contain different geometries of  $W_g$  and  $L_g$  and micro-heater configurations with different membrane size in the center of the chip. The active area of each chip is at the center and the bonding pads are around the chip. At the bottom-right of the die, test structures containing transmission line model (TLM) and circular transmission line model (CTLM) for contact resistance and sheet resistance measurements, Hall measurement structures, and mesa leakage test structures are included. The top-right of the die are 2 x 2 arrays and the size of each element in each sensor array is 1 mm x 1 mm.

The main steps for the fabrication of the suspended AlGaIn/GaN HEMT sensor with integrated micro-heater are shown in Figure 3.3. After cleaning the wafers, the fabrication process flow started with a mesa etching using a chlorine/boron chloride ( $\text{Cl}_2/\text{BCl}_3$ ) plasma to define the sensor geometry. Then, Ti/Al/Ti/Au (20/110/40/50 nm) metal contacts were e-beam evaporated and patterned by lift-off technology. Rapid thermal annealing (RTP) at 870°C for 45 seconds under  $\text{N}_2$  ambient in a RTP-500 system was conducted to make the contacts ohmic and improve reliability at high temperature. A 200-nm silicon oxide was then deposited by plasma-enhanced chemical vapor deposition (PECVD), followed by the e-beam evaporation of a Ti/Pt (30/200nm) metal stack, patterned by lift-off to form the microheater, then followed by a 200-nm PECVD silicon oxide layer for isolation from the interconnect layer. The silicon oxide was patterned in buffer oxide etch (BOE) solution and the thick metal interconnect formed using evaporated Ti/Au (20/300 nm) layer stack. The topside of the wafer was covered by PECVD silicon oxide layer and the backside was polished down to 400  $\mu\text{m}$ . Next, a 5  $\mu\text{m}$ -thick silicon oxide layer was deposited as hard mask during the deep reactive ion etching (DRIE) process to etch the silicon substrate. Then backside silicon oxide was patterned by inductively coupled plasma (ICP) etching using AZ4620 photoresist as a mask and the top-side silicon oxide layer was etched in BOE solution to form an opening for the contact

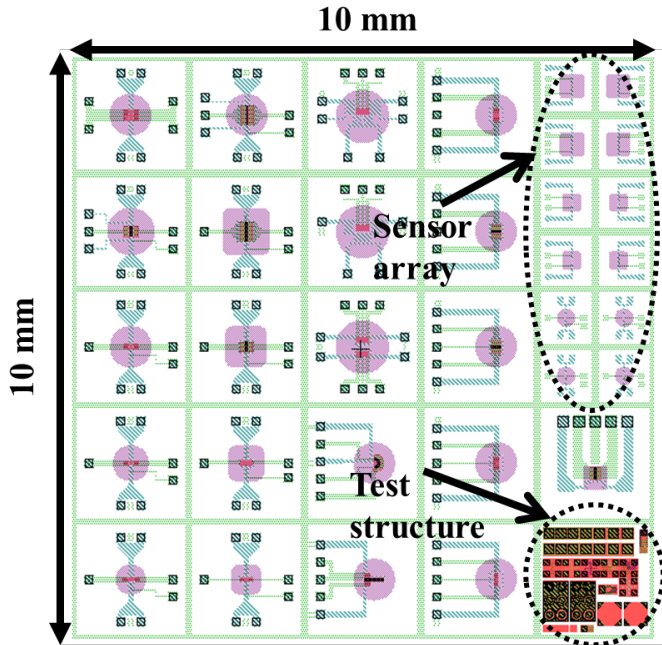


Figure 3.2: Layout of the (single die) AlGaN/GaN sensors. The block (bottom right) for test purposes and sensor arrays (top right) are also included.

pads and gate windows. The functional material layer was deposited on the gate area. The final step is the removal of the silicon substrate below the active area by dry etching from the backside. Some steps are optional according to the requirement of different sensors.

### 3.2.3. SUBSTRATE MATERIAL SELECTION

Ideal GaN structures are grown on a substrate that has matching crystal structure and lattice constant, similar thermal expansion coefficient (TEC), no mechanical stress, large size, and low cost. The growth of crystalline GaN needs high temperature and high pressure conditions, such as high nitrogen pressure solution (HNPS) [2] and halide vapor phase epitaxy (HVPE) [3], which make it an expensive material and mass production not available. Currently, the most commercially available epitaxial GaN substrate materials are sapphire, silicon carbide (SiC) and Si. The properties of the substrates are summarized in Table 3-2. The SiC carbide substrate has the lowest thermal expansion coefficient and lattice mismatch for GaN structures. However, it is very difficult to etch silicon carbide and the wafer price is still high. GaN-on-Sapphire is the most mature growth technology that has been widely used in the LED industry. Sapphire is also difficult to etch, making it not suitable for micromachining, required for the suspended MEMS structure. Silicon substrates have gained much attention for GaN epitaxial structures due to the wide availability of high quality, large size, and low-cost substrates. In addition, silicon-based

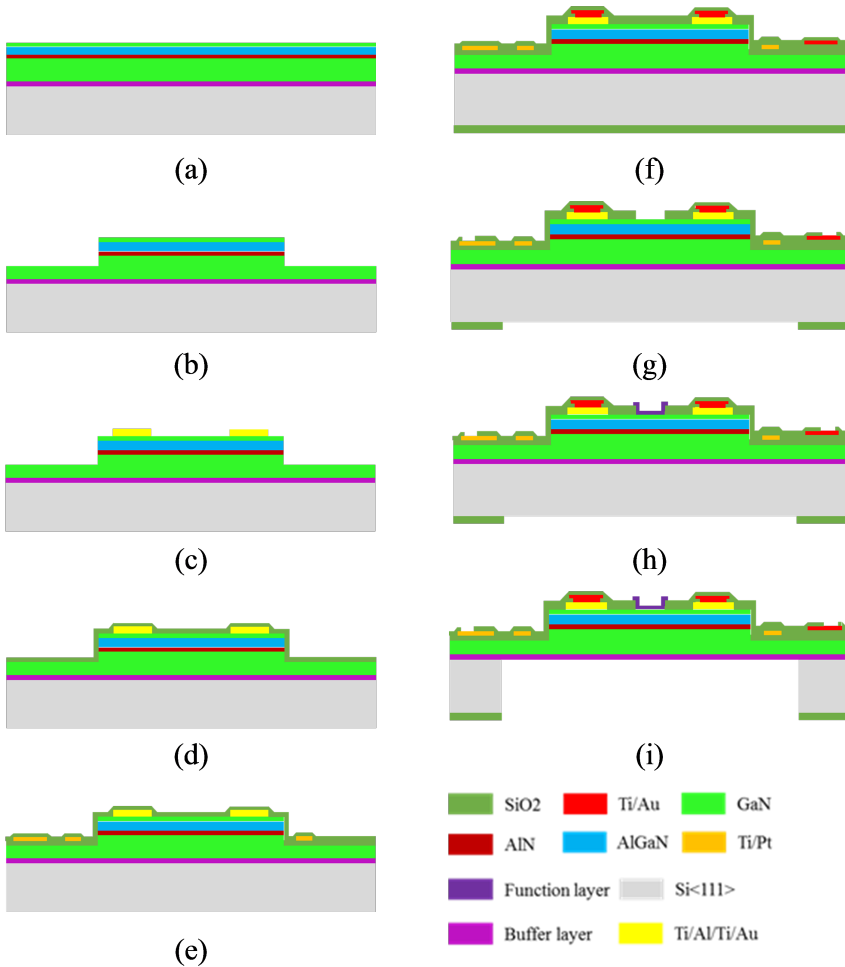


Figure 3.3: Main steps for the fabrication of the suspended AlGaIn/GaN HEMT sensor integrated with micro-heater. (a) starting wafer with epitaxial layers; (b) mesa etching to define sensor area; (c) Ohmic contact deposition and annealing; (d) PECVD SiO<sub>2</sub>; (e) micro-heater deposition and passivation; (f) metal deposition and top/bottom passivation; (g) opening contact pads at the frontside and etching window at the backside; (h) gate recess or functional material deposition; (i) substrate etching from the backside to form the suspended structure.

Table 3.2: Properties of substrates for GaN epitaxial growth.

Substrate	4H-SiC	Thick GaN	Crystalline GaN	Sapphire	Si
<b>Lattice mismatch (%)</b>	3.1	0	0	16	-17
<b>TEC mismatch (%)</b>	21.4	0	0	-34	53.6
<b>Dislocation density (<math>cm^{-2}</math>)</b>	$10^8-10^{10}$	$10^5-10^7$	$10^2-10^5$	$10^8-10^{10}$	$10^8-10^{10}$
<b>Substrate size (mm)</b>	150	100	50	150	300
<b>Substrate price</b>	High	High	Very High	Medium	Low

MEMS technology is quite mature. Therefore, for GaN epitaxial growth silicon substrates are used in this work.

For this research, all the AlGaN/GaN epitaxial wafers were grown by Suzhou Nanowin Co. on a 2-inch silicon <111> 1 mm-thick wafers using Metal-organic Chemical Vapor Deposition (MOCVD). Starting from the substrate, the structure consisted of, a 2  $\mu$ m-thick undoped GaN buffer layer, followed by a 1 nm-thick AlN interlayer, an undoped 25 nm-thick Al<sub>0.26</sub>Ga<sub>0.74</sub>N barrier layer, and a 3 nm-thick GaN epitaxial cap layer. The electron mobility was  $1500\text{ cm}^2\text{V}^{-1}\text{s}^{-1}$ , with a sheet electron density of  $1\times 10^{13}\text{ cm}^{-2}$ . The epilayer stack structure is shown in Figure 3.4. The specification of AlGaN/GaN epilayers on silicon substrate can be found in appendix A.

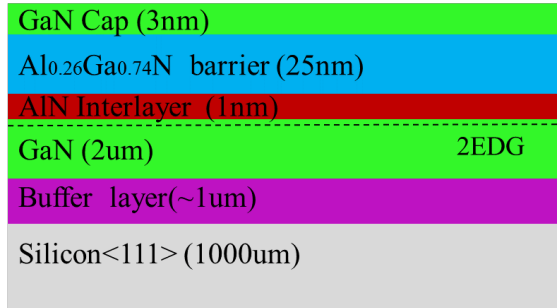


Figure 3.4: Epilayer stack structure on silicon substrate.

Due to the lattice mismatch between the silicon and GaN, a buffer layer is necessary to reduce the dislocation density. Also, this buffer layer provides isolation between the substrate and the epitaxial layers. A 1-nm AlN interlayer inserted between the GaN and AlGaN layers increases the effective conduction band offset, resulting in the reduction of alloy scattering and increase of electron mobility [4]. This layer also helps to relieve the stress introduced by thermal mismatch between AlGaN and GaN layers [5].

### 3.2.4. DEVICE ISOLATION

The devices must be isolated from one another to prevent the outside 2DEG interference in the active area. Generally, for mesa isolation there are two methods: dry etching and ion implantation. Ion implantation isolation can keep device planarity, which may be

advantageous in certain processing sequences where etching or step coverage of metal layer off mesa sidewalls is undesirable. High-density, inductively-coupled plasma (ICP) is the most common method to etch GaN due to high plasma uniformity over large area and low ion energy relative to reactive-ion etching (RIE). In this research, inductively-coupled plasma (ICP) is used for mesa isolation. The schematic diagram of a HEMT mesa structure is shown in Figure 3.5(a). The ICP etching was carried out in a AST Cirie-200 etcher using an RF/ICP power of 15 W/300 W, and gas  $Ar_2/Cl_2/BCl_3$  gas flowrate of 5/40/5 sccm. An optical image (top view) after mesa etching is shown in Figure 3.5(b). The thickness of the etched step is measured by profilometer and is about 105 nm as shown in Figure 3.5(c).

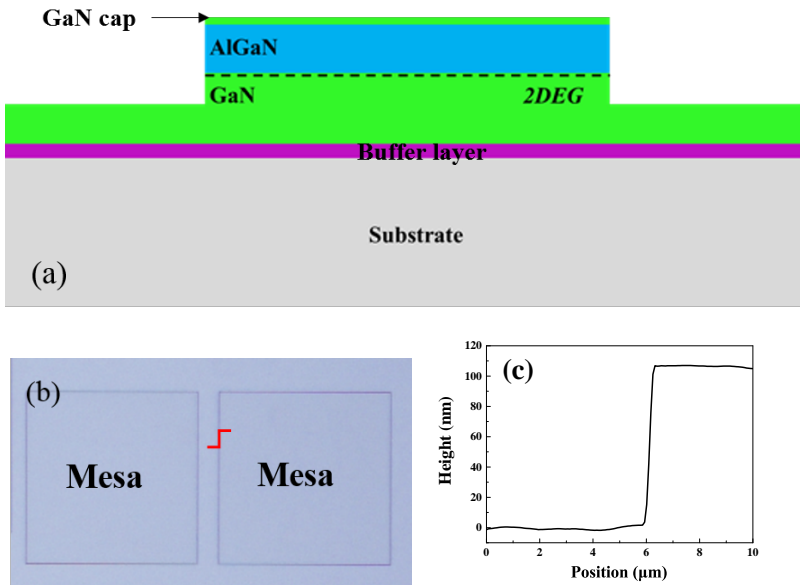


Figure 3.5: (a) Schematic diagram of the HEMT isolation via plasma etching; (b) optical image (top view) after mesa isolation; (c) AFM step profile.

### 3.2.5. METALIZATION

#### Ohmic contact metal layers

Currently, ohmic contact for GaN are formed using a Ti/Al/x/Au stack, which yields lower contact resistance compared to Ti-only and Al-only stack, where x is a diffusion barrier materials (Ti, Ni, Pt, W, Mo, Pd etc.) needed to prevent the formation of Al/Au intermetallic. The metal stack are generally e-beam evaporated and patterned by lift-off process.

In order to minimize contact resistance, extremely high temperatures are required to form the GaN HEMT contact. Typical annealing conditions are 850 °C, 30 s, in a  $N_2$  ambient. The time and temperature of the anneal are highly dependent upon the composi-

tion and thickness of the AlGaN barrier layer. Higher and lower aluminum concentration require higher and lower temperature, respectively.

The high annealing temperature over the melting point of Al (661°C) will lead to rough ohmic contact morphology. It may be an issue for very small device features. For Ti/Al-based scheme, a trade-off between contact resistance and surface morphology, with smoother morphologies available at lower annealing temperature while sacrificing contact resistance, has to be found.

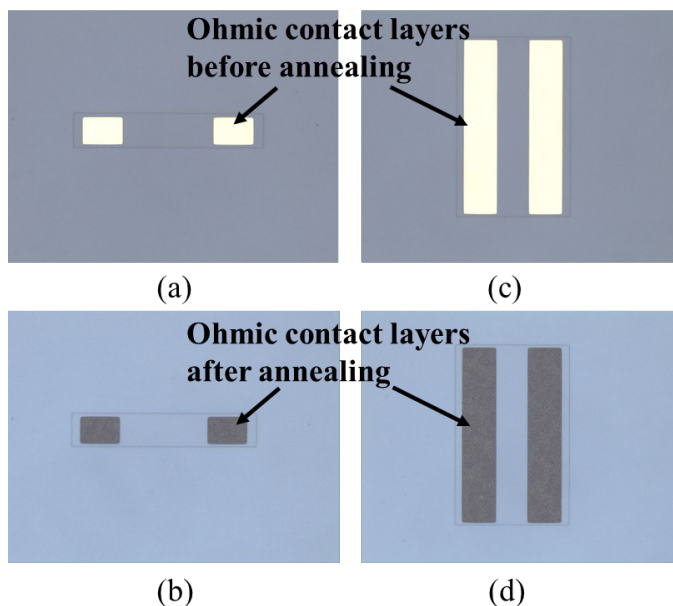


Figure 3.6: Optical image of ohmic contact stack layer: before annealing (a)  $W/L=0.5$  and (c)  $W/L=8$ ; after annealing (b)  $W/L=0.5$  and (d)  $W/L=8$ . (The background color of images change resulting from the different optical intensity of the microscope during taking pictures)

In this research, we use Ti/Al/Ti/Au ohmic contact stack. The thickness of each layer is 20/110/40/50 nm and they are deposited by e-beam evaporation. Then, rapid thermal annealing at the optimum temperature of 870 °C for 47 s under  $N_2$  ambient in a RTP-500 system is performed. Optical images of the ohmic contact stack layer before and after annealing are shown in Figure 3.6. Although the surface roughness increases after annealing, no surface defects such as blistering or cracking occur. The SEM image of a cross-section of the Ti/Al/Ti/Au layers stacks after annealing is shown in Figure 3.7. From the image, it can be seen that the boundaries of the metal layers have been faded, which means that the layers merged with each other after the high temperature annealing.

### Micro-heater metal layers

Micro-heaters and micro-hotplates are integrated with chemical and gas sensors [6, 7], humidity sensor [8, 9], infrared emitter, and MEMS microfluid pumps [13]. Ideally, a

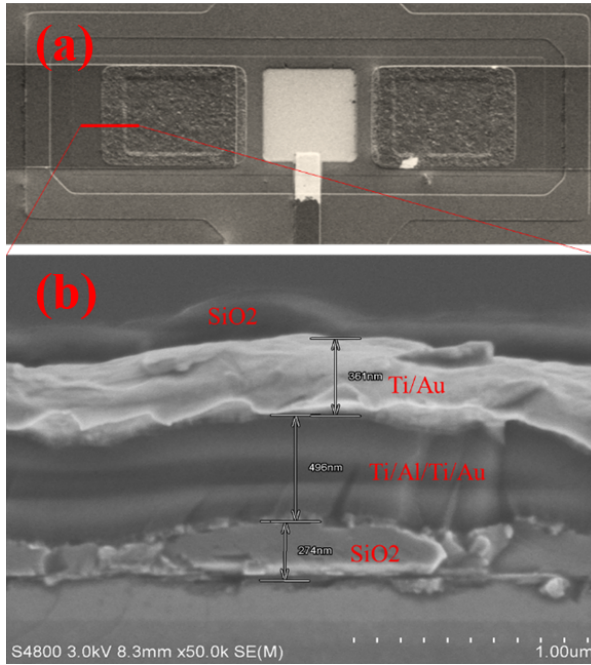


Figure 3.7: SEM images of (a) top view and (b) cross-section of the ohmic contact metal layers after annealing.

heater generates the required high temperature in a small confined area, at very low power consumption. The main properties of commonly used materials for micro heaters, such as gold (Au) [12, 14], Titanium Nitride (TiN) [15], Platinum (Pt) [16, 17] and Poly Silicon [18], are reported in table 3-3. Compared to TiN and Poly Si, Au and Pt have low resistance. Pt has a highly linear positive correlation between resistivity and temperature and long-term chemical stability at high temperature compared to gold. Therefore, in this research Pt is selected as the micro-heater material and Ti as the adhesion layer. A Ti/Pt (30/200 nm) metal layer was deposited by e-beam evaporation and patterned by lift-off to form the microheater, followed by a 200-nm PECVD silicon oxide layer for isolation from the interconnect layer. There are two types of micro-heater design considered: surrounding structure and cross-gate structure as shown in Figure 3.8. These two struc-

Table 3.3: Comparison of material properties used for micro-heaters.

Substrate	Au	TiN	Pt	Poly Si
$\rho$ ( $Kg.m^{-3}$ )	19300	5430	21500	23000
MP ( $^{\circ}C$ )	1000	3233	1768.4	1410
R ( $\mu\Omega.cm$ )	2.4	250	22.2	~k
$\lambda$ ( $W/m^{-1}.K^{-1}$ )	320	30	72	34
C ( $J/kg^{-1}.K^{-1}$ )	129	220	133	768

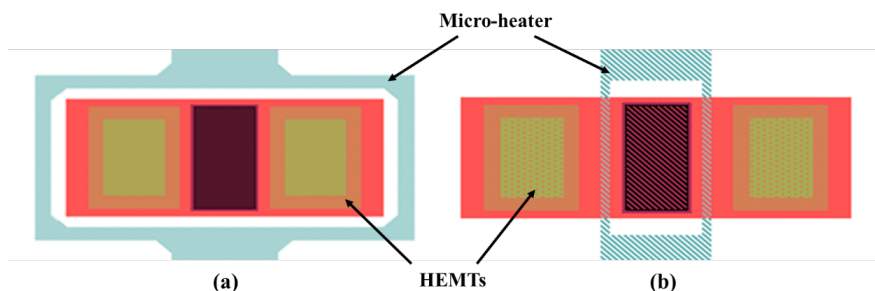


Figure 3.8: Layout of AlGaN/GaN HEMTs with (a) surrounding micro-heater and (b) cross-gate micro-heater.

tures were considered as they are expected to distribute the heat more uniformly over the device area [6, 10–12]. The optical image of the micro-heater metal layer is shown in Figure 3.9.

### Interconnect metal layers

To interconnect the source and drain, a Ti/Au metal stack with the thickness of 20/300 nm was deposited by e-beam evaporation and patterned by lift-off process. The optical image of the interconnect metal layer is shown in Figure 3.10, while a SEM image of the cross-section of metal and passivation layers in Figure 3.11. From the image, it appears that step coverage of both the metal and the passivation layer is good.

### 3.2.6. DEEP REACTION ION ETCHING (DRIE)

In order to form the membrane structure, the silicon substrate under the heater needs to be removed. Deep reaction ion etching (DRIE) is chosen as the silicon substrate is  $\langle 111 \rangle$  orientation and is difficult to remove by wet anisotropic etching. There are two main technologies for high aspect ratio etching of silicon by dry etching: cryogenic and Bosch, although the Bosch process is significantly more developed in terms of tools and industrial applications. The Bosch process consists of the cyclic isotropic etching and fluorocarbon-based protection film deposition by quick gas switching. The  $\text{SF}_6$  plasma cycle etches silicon, and the  $\text{C}_4\text{F}_8$  plasma cycle creates a protection layer [19].

A  $5\ \mu\text{m}$  silicon oxide layer was deposited by PECVD as a hard mask and patterned by ICP-RIE etching. The GaN buffer layer is used as the stopping layer. In the first batch, the silicon substrate is incompletely etched after 600 cycles of etching and passivation as shown in Figure 3.12(a) and Figure 3.13. The residue part is visible around the membrane structure. After another 50 loops, the residue is etched completely as shown in Figure 3.12(b).

## 3.3. SENSOR PACKAGING

The optical image of the completed wafer and a close up of a die are shown in Figure 3.14. The completed wafers are diced into single chips for packaging and testing. Due to the fragile membrane structure on the sensor chip, the traditional blade dicing is not suitable for the MEMS wafer due to the contamination and stress loads during the dicing

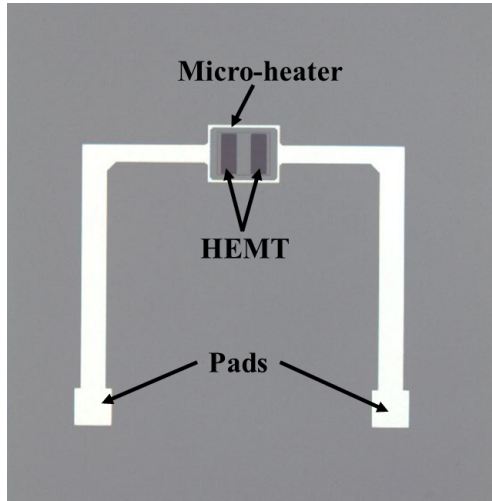


Figure 3.9: Optical image of the device with Ti/Pt micro-heater.

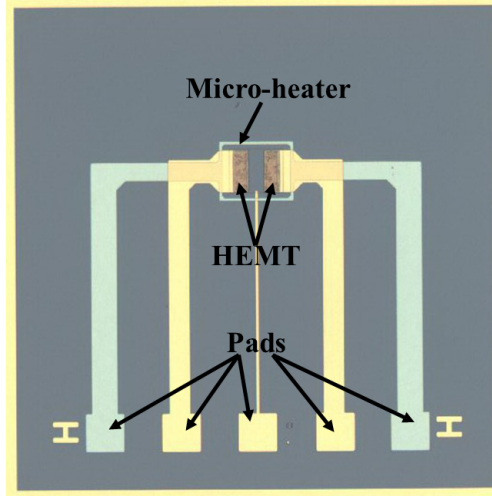


Figure 3.10: Optical images of the device after interconnect metal layer deposition and patterning.

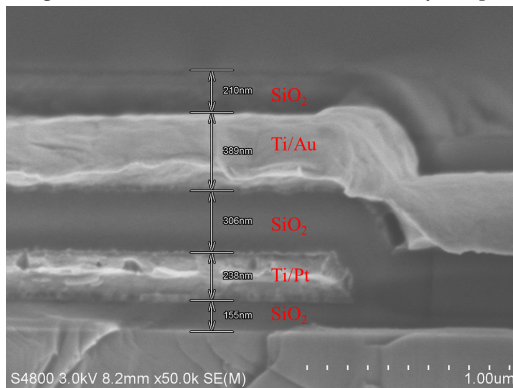


Figure 3.11: SEM image of cross section of metal and passivation layers.

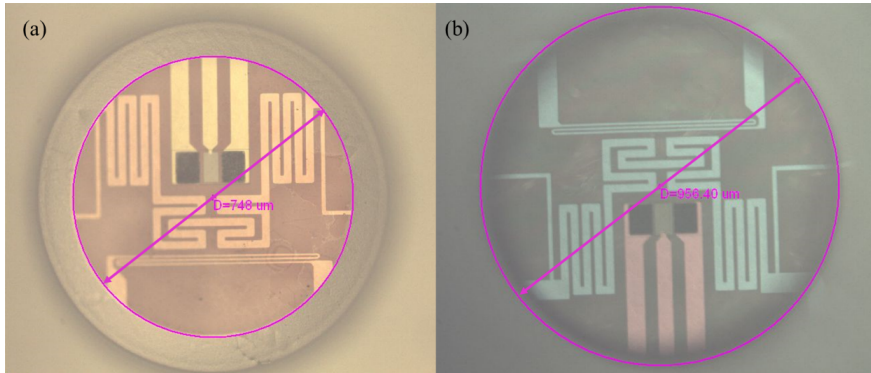


Figure 3.12: Optical images from backside view of (a) The incompletely etched chip and (b) completely etched chip.

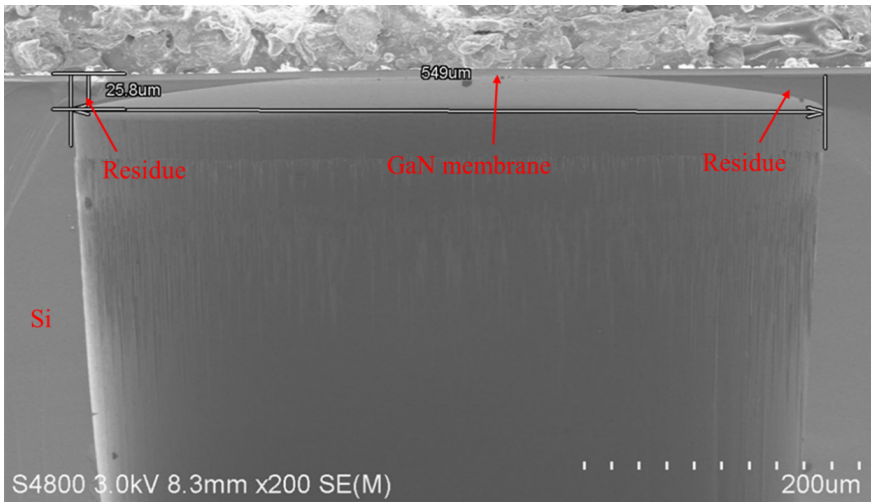


Figure 3.13: SEM image of a cross-section of the device with residue.

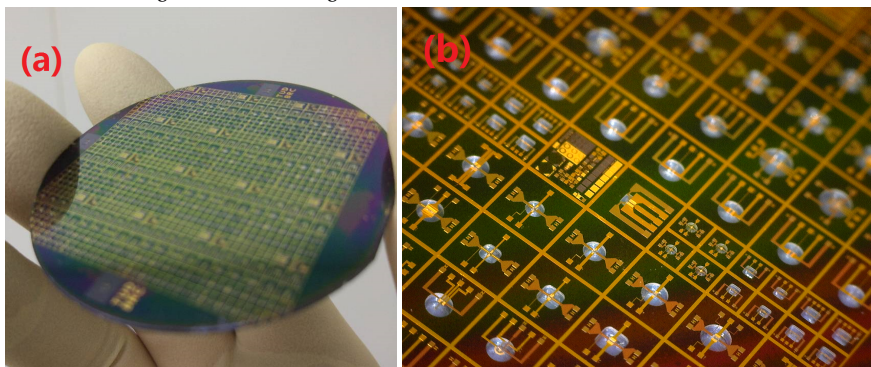


Figure 3.14: Optical image of completed wafer and a close up of a die.

process. In this work, laser scribing is done from the backside and chips are separated by breaking and expanding film. One sensor chip after dicing is shown in Figure 3.15.

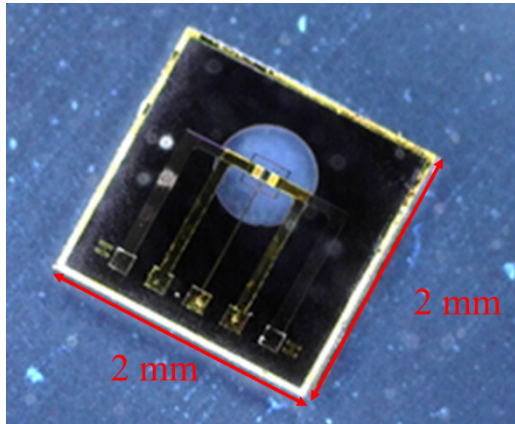


Figure 3.15: Optical image of signal chip after dicing.

### 3.3.1. CHOICE OF SENSOR PACKAGING

There are several packages solutions for gas sensors, such as transistor outline (TO) package [20], dual inline package (DIP) [21], surface mounted device (SMD) package [22], printed circuit board (PCB) package [23], and ceramic quad flat no-lead (CQFN) packaging. For the perspective of minimization and easy commercialization, Chip on board (COB) and CQFN package are selected and compared in this research. The schematic diagrams of CQFN and COB packaging are shown in Figure 3.16.

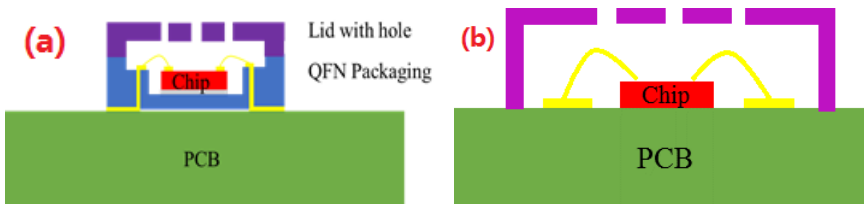


Figure 3.16: Schematic diagram of (a) CQFN and (b) COB packaging.

### 3.3.2. COMPARISON OF TWO PACKAGES

As we known, the package influences the heat dissipation. The gate surface temperature of the device with COB and CQFN packaging at different micro-heater voltages is shown in Figure 3.17. The temperatures of COB packaging and CQFN packaging at  $V_{DS}=2$  V are 55.9 °C and 65.6 °C, respectively. That is due to the thermal coefficient of ceramic (1.5 W/m.K) being larger than that of PCB (0.2-0.3 W/m.K). As the aspect of low power is here of relevance, COB packaging is more suitable.

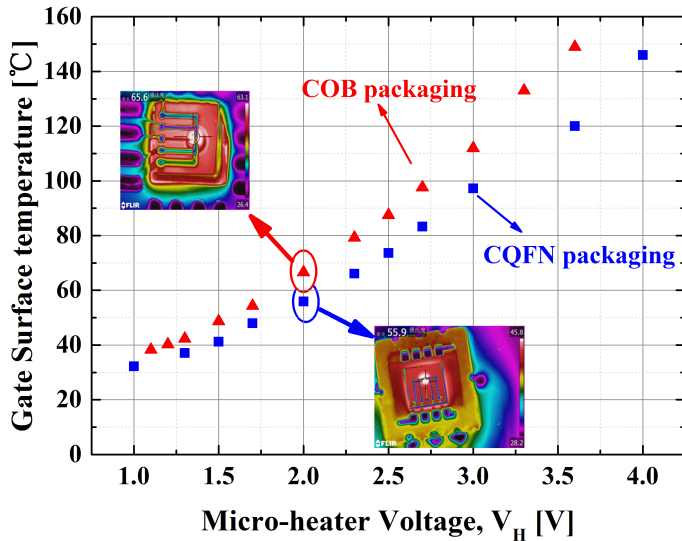


Figure 3.17: The gate surface temperature of chip for COB packaging and CQFN packaging.

The signal stability of sensor chips with COB and CQFN packaging are shown in Figure 3.18. The noise current output of the sensor with COB packaging is about  $30 \mu\text{A}$ . The diameter of gold wire bonding is 8 mil, which is influenced by gas flow. By contrast, the current signal of the chip with CQFN packaging is more stable, and the noise of output is about  $1\text{--}2 \mu\text{A}$ , resulting in CQFN packaging that could enhance the sensitivity and limit of detection of sensors.

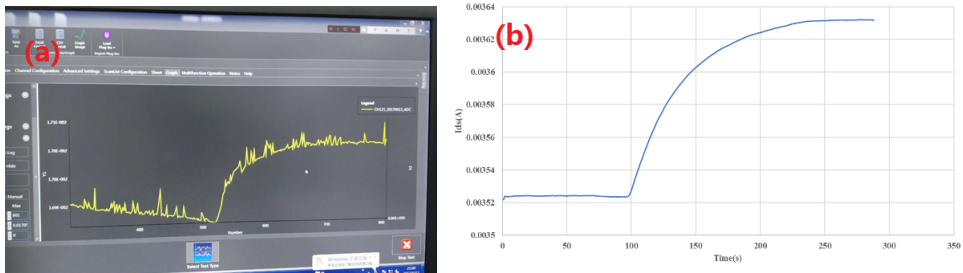


Figure 3.18: Current signal of sensor with (a) COB packaging and (b) CQFN packaging during gas measurement.

Considering the heat dissipation and signal stability of the sensor with COB and CQFN packages, the most suitable type is selected. In spite that the sensor with COB package has lower power consumption, the chip with the CQFN package exhibits more stable signal output. For the perspective of sensor measurement, the CQFN package so-

lution is suitable for obtaining higher accuracy. Of course, the COB package solution also is a good option if the signal output would be optimized.

### 3.4. ELECTRICAL CHARACTERIZATION OF THE HEMT SENSOR PLATFORM

#### 3.4.1. OHMIC CONTACT MEASUREMENT

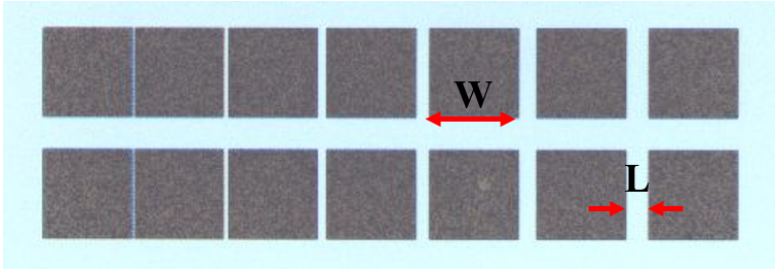


Figure 3.19: Optical image of TLM test structure of ohmic contacts measurement after annealing at 870 °C for 45 s.

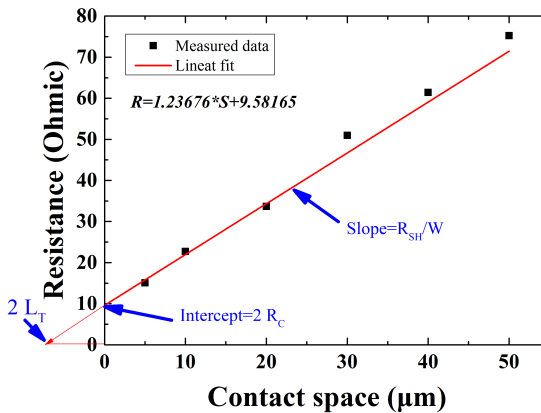


Figure 3.20: Measured resistance versus TLM gap spacing of ohmic contacts after annealing at 870 °C for 45 s.

The transmission line model (TLM) test structures are included in our mask design as shown in Figure 3.2. Optical image after annealing is shown in Figure 3.19. According to the theory of TLM, the total resistance between the two adjacent pads can be expressed as:

$$R_T = 2R_C + L \times \frac{R_{SH}}{W} \quad (3.1)$$

where  $R_{SH}$  is the sheet resistance of materials,  $R_C$  is the contact resistance,  $L$  is the space between the pads and  $W$  is the width of the pad. And the specific contact resistance ( $\rho_c$ ) can be expressed by

$$\rho_c = R_{SH} \times L_T^2 \quad (3.2)$$

where  $L_T$  is the transfer length. The measured data points of  $R_T$  versus the pad space and its linear fitting are shown in Figure 3.20. The  $R_{SH}$  is determined from the slope, the  $R_C$  is the  $1/2 R_T$  extracted from the intercept of y-axis and the intercept of x-axis is  $2L_T$ . The wafer map specific contact resistance ( $\rho_c$ ) indicates the uniformity of the process as shown in Figure 3.21. The average value of the specific contact resistance is about  $3.71 \times 10^{-5} \Omega \cdot \text{cm}^2$ , which can satisfy the requirement of the sensors.

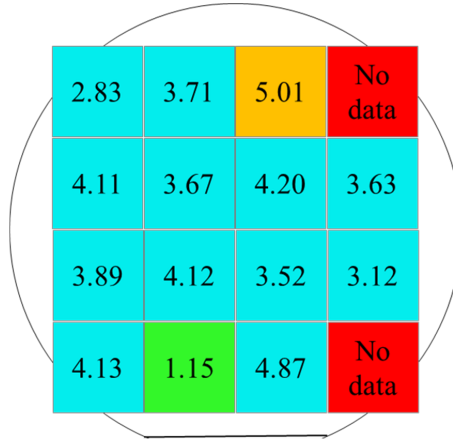


Figure 3.21: Special resistivity map ( $10^{-5} \Omega \cdot \text{cm}^2$ ): showing good process uniformity.

### 3.4.2. MICRO-HEATER CALIBRATION AND SELF-HEATING INFLUENCE

Before the heater is used as a heating element, it is necessary to perform a calibration for extracting the temperature of the active area, which is between source and gate. The sample is placed in an oven and the temperature varied from 303.15 K up to 353.15 K. The resistance versus temperature curve was recorded as shown in Figure 3.22. Low current values were supplied to the Pt heater element to prevent the self-heating of the heater itself. The temperature dependence of the resistivity is well described by the following linear equation:

$$\rho_H(T) = \rho_0[1 + \alpha(T - T_0)] \quad (3.3)$$

where  $\rho_H$  and  $\rho_0$  are, respectively, the heater resistivity at temperature  $T$  and at ambient temperature  $T_0$ ;  $\alpha$  is the thermal coefficient of resistance (TCR). The measured TCR of the heater is equal to 3861 ppm/K with a deviation of 10 ppm/K according to the RTD standard [20].

The surface temperature can also be measured by infrared radiation (IR) thermal camera extracted by the resistance change of the micro-heater at ambient temperature with the 4-wire testing method [24]. The measured gate surface temperature of chips by

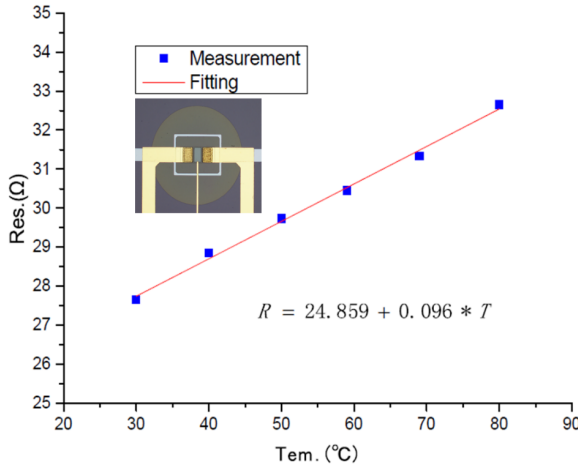


Figure 3.22: Resistance of micro-heater versus temperature (the insert is the optical image of the test chip).

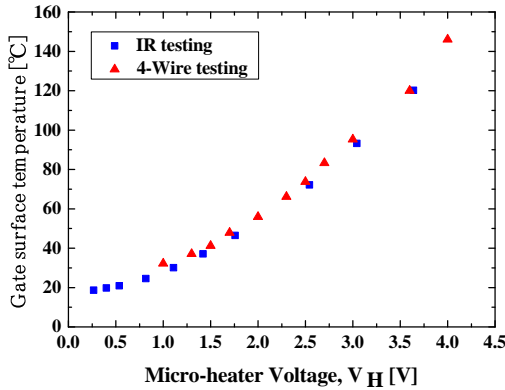


Figure 3.23: Measured surface temperature of chips by 4-wire testing and IR camera method in air.

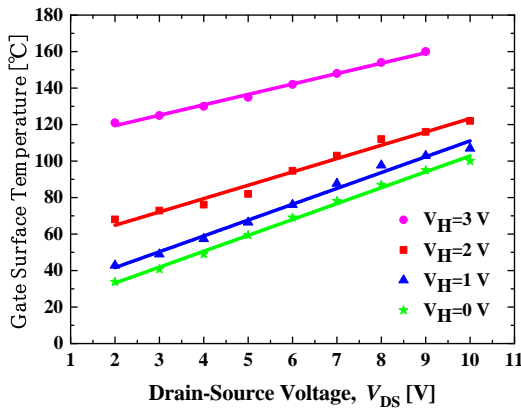


Figure 3.24: Combined heating characteristic of the Pt micro-heater and HEMT self-heating at ambient temperature of 298.15 K for voltage of micro-heater, V<sub>H</sub> = 0 V to 3 V and V<sub>DS</sub> = 2 V to 10 V with 1 V increments.

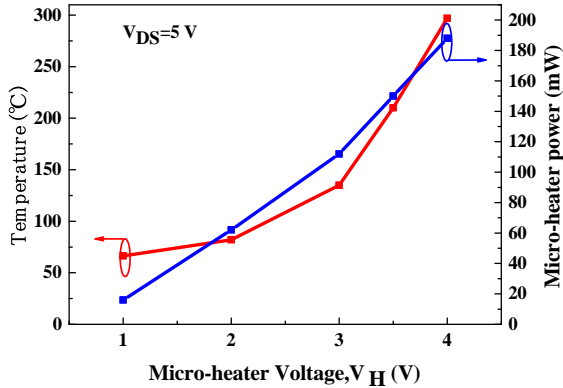


Figure 3.25: Measured micro-heater power consumption and temperature versus microheater voltage at  $V_{DS}=5$  V.

4-wire testing and IR camera method is shown in Figure 3.23. These two methods give consisting results with the electrical calibration.

However, the self-heating effect of the AlGaN/GaN HEMT device also causes a local increase in crystal temperature due to the dissipated Joule electric power. The combined thermal characteristic of the Pt micro-heater and the HEMT self-heating at ambient temperature is shown in Figure 3.24. The surface temperature can be measured by infrared radiation (IR) thermal camera or extracted by the resistance change of the micro-heater at ambient temperature, showing a linear growth with increasing the drain-source voltage,  $V_{DS}$ . Figure 3.24 shows the max temperature distribution on the gate surface when changing the drain-source voltage,  $V_{DS}$ , and micro-heater voltage,  $V_H$ . Figure 3.25 shows the measured heating power consumption of micro-heater and temperature versus microheater voltage at  $V_{DS}=5$  V. The max temperature of the gate surface will nonlinear increase with the voltage of micro-heater,  $V_H$ . When the voltage of the micro-heater is  $V_H=4$  V and  $V_H=3$  V, the max gate surface temperature is calculated to be about  $297.87^{\circ}\text{C}$  and  $135^{\circ}\text{C}$ , respectively. In fact, the generated power of the sensor is about 200 mW when the operating temperature is about  $300^{\circ}\text{C}$ . The power consumption could be optimized by process and package: the residual Si around the membrane during the DRIE process and the ceramic package with a high thermal conductivity coefficient resulting in increased power consumption. In addition, the power of the sensor can be further optimized by a larger size membrane and cycle heating [25].

### 3.4.3. I-V CHARACTERISTICS OF ALGaN/GaN SENSOR

The I-V characteristics of AlGaN/GaN devices with  $W/L=1, 2, 4$  before and after removing the substrate is shown in Figure 3.26. The current of the device with the membrane structure is much lower than that of bulk structure devices. There are three possible reasons to explain the current drop. First, the membrane structure has higher 2DEG channel temperature generated by self-heating due to the thermal coefficient of the Si

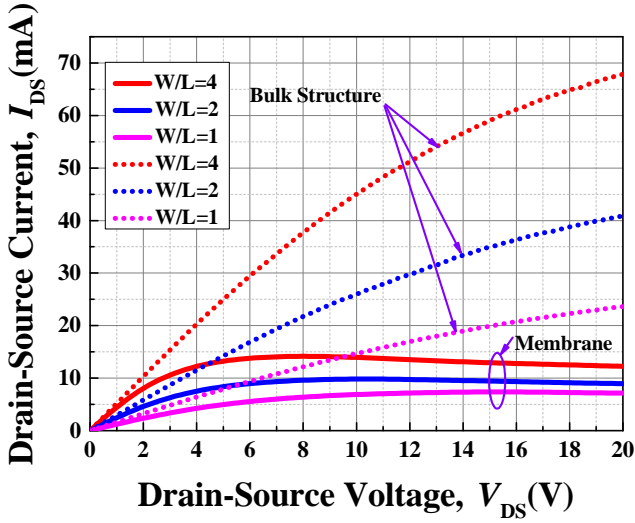


Figure 3.26: I-V characteristics of AlGaIn/GaN devices with W/L=1, 2, 4 before and after removal of the substrate.

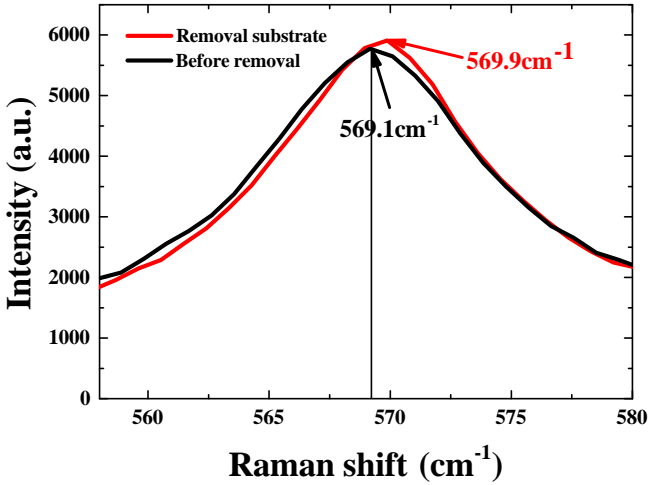


Figure 3.27: Raman spectra at E<sub>2</sub> Peak of GaN on membrane (red line) and silicon substrate (black line).

substrate (150 W/m.K) being much higher than air (0.023 W/m.K), which led to a decrease of the drain current. The second possible reason is the increase of strain during the DRIE fabrication. To confirm the strain change, we have performed Raman spectroscopy measurements on the  $E_2$  GaN line before and after the substrate removal. As shown in Figure 3.27, the  $E_2$  peak of GaN has shifted towards more compressive strain, resulting in a decrease of 2DEG density ( $N_S$ ) [26, 27]. The last possible reason is that the source of 2DEG is from not only the surface state [28], but also the interface between the GaN layer and the substrate. This reason is a hypothesis for now, which needs further research to confirm. However, from the power consumption perspective, the decrease of the source-drain current of HEMT devices can have a positive effect to reduced the power consumption of the sensors.

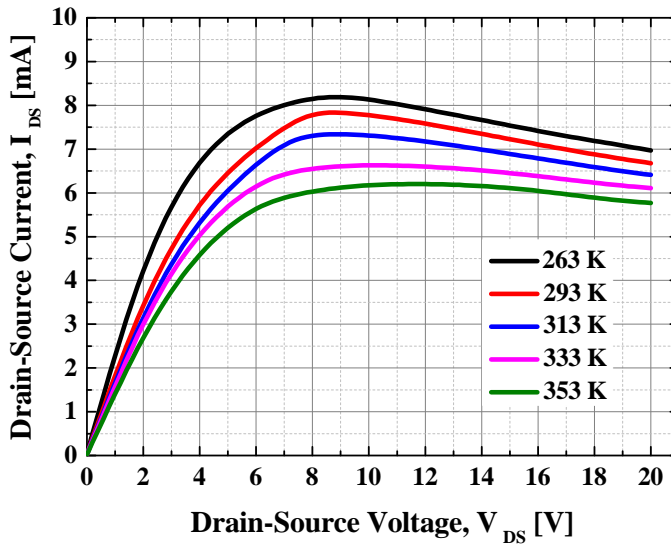


Figure 3.28: I-V characteristics of AlGaIn/GaN sensor under variable ambient temperature at 20 % relative humidity.

The AlGaIn/GaN HEMT devices were tested versus ambient temperature and humidity. Temperature was varied from 263 K to 353 K, with 10 K steps, and the humidity was in the 5% RH to 90 % RH range. The gate voltage of the HEMT device was left floating and  $V_{DS}$  varied from 0 V to 20 V. As shown in Figure 3.28, the saturated current has a little drop with raising  $V_{DS}$  due to the thermal and lattice scattering of the 2DEG. The  $I_{DS}$  decreases remarkably for increasing temperature at 20 % RH. The saturated current temperature coefficient is  $-0.63 \text{ mA/mm}^2\text{K}$ , which is in agreement with results from the literature [29]. Figure 3.29 indicates that the relative humidity has no significant effect on the I-V characteristics of HEMT at 353.15 K. The humidity effect at different temperatures is shown in Figure 3.30. The  $I_{DS}$  decrease upon increasing the relative humidity from 5 % to 90 % at low temperatures. However, the effect of relative humidity on  $I_{DS}$

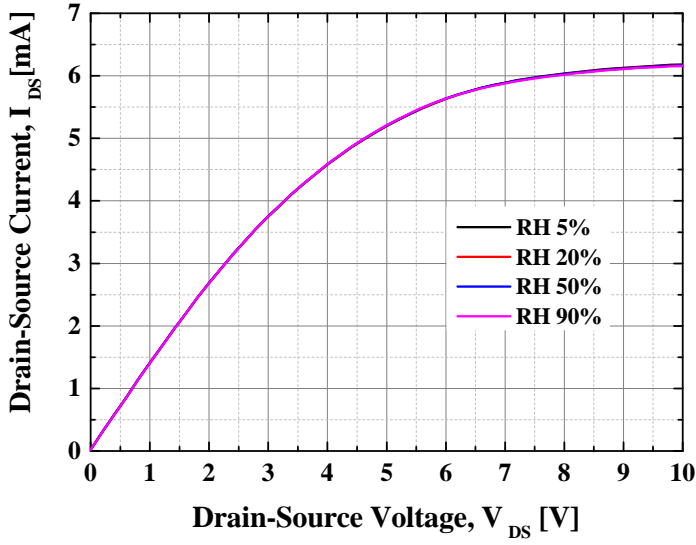


Figure 3.29: I-V characteristics of AlGaIn/GaN sensor under different relative humidity at 353.15 K.

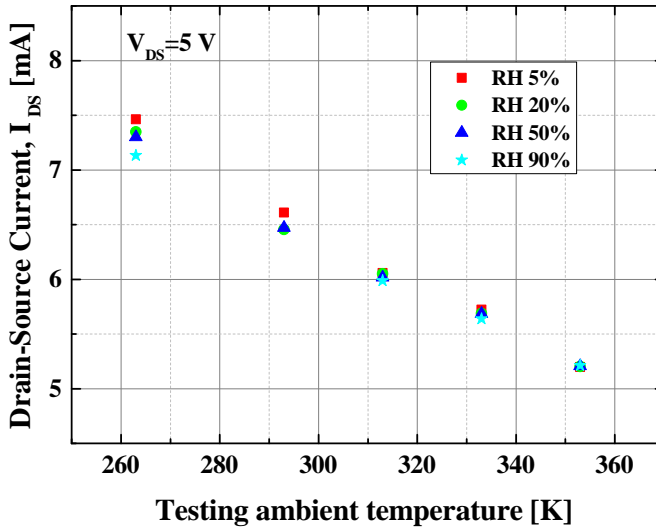


Figure 3.30: Temperature and relative humidity effect on the  $I_{DS}$  of AlGaIn/GaN sensor at  $V_{DS} = 5$  V.

becomes insignificant with increasing ambient temperature. In order to eliminate the temperature interference, a differential method (including a second structure with the same geometry but not exposed to gas/humidity in one chip) can be a suitable solution.

### 3.5. CHAPTER SUMMARY

In this chapter, the MEMS AlGaIn/GaN devices with integrated micro-heater are presented. The fabrication process is described highlighting the main critical modules. An important issue, successfully addressed was to achieve the low ohmic contacts. Proper material stack selection and tailored annealing process as well as a suitable micro-heater design and implementation are discussed in detail. An analysis of possible packaging concepts is also presented. The sensor with the COB package has lower power efficiency, the chip with the CQFN package exhibits more stable signal output.

The average value of specific contact resistance is about  $3.71 \times 10^{-5} \Omega \cdot \text{cm}^2$ . The drop in drain current after the removal of the substrate could be explained as following three possible reasons: higher temperature introduced by self-heating, the more compressive strain by the DRIE process and the source of 2DEG from the interlayer between GaN layer and substrate. The combined effect of micro-heater heating and self-heating on the membrane has been studied the first time. From the temperature and humidity results, it can be concluded that the device is not significantly affected by high relative humidity ambient while the temperature influence is substantial and needs to be avoided/compensated for obtaining high performance. In conclusion, the electrical characterization of these devices indicates their suitability for the envisioned sensing applications which will be discussed in the following chapters.

### REFERENCES

- [1] J. Lee et al., "Low power consumption solid electrochemical-type micro CO<sub>2</sub> gas sensor," *Sensors and Actuators B: Chemical*, vol. 248, pp. 957-960, 2017.
- [2] S. Porowski, "Bulk and homoepitaxial GaN-growth and characterisation," *Journal of crystal growth*, vol. 189, pp. 153-158, 1998.
- [3] E. Aujol, J. Napierala, A. Trassoudaine, E. Gil-Lafon, and R. Cadoret, "Thermodynamical and kinetic study of the GaN growth by HVPE under nitrogen," *Journal of crystal growth*, vol. 222, no. 3, pp. 538-548, 2001.
- [4] S. Kamiyama et al., "Low-temperature-deposited AlGaIn interlayer for improvement of AlGaIn/GaN heterostructure," *Journal of crystal growth*, vol. 223, no. 1-2, pp. 83-91, 2001.
- [5] R. Jin, J. Liu, J. Zhang, and H. Yang, "Growth of crack-free AlGaIn film on thin AlN interlayer by MOCVD," *Journal of crystal growth*, vol. 268, no. 1-2, pp. 35-40, 2004.
- [6] W.-J. Hwang, K.-S. Shin, J.-H. Roh, D.-S. Lee, and S.-H. Choa, "Development of micro-heaters with optimized temperature compensation design for gas sensors," *Sensors*, vol. 11, no. 3, pp. 2580-2591, 2011.

- [7] M. Baroncini, P. Placidi, G. Cardinali, and A. Scorzoni, "Thermal characterization of a microheater for micromachined gas sensors," *Sensors and Actuators A: Physical*, vol. 115, no. 1, pp. 8-14, 2004.
- [8] C.-L. Dai, "A capacitive humidity sensor integrated with micro heater and ring oscillator circuit fabricated by CMOS-MEMS technique," *Sensors and Actuators B: Chemical*, vol. 122, no. 2, pp. 375-380, 2007.
- [9] Y. Kim, B. Jung, H. Lee, H. Kim, K. Lee, and H. Park, "Capacitive humidity sensor design based on anodic aluminum oxide," *Sensors and Actuators B: Chemical*, vol. 141, no. 2, pp. 441-446, 2009.
- [10] S. Lee, D. Dyer, and J. Gardner, "Design and optimisation of a high-temperature silicon micro-hotplate for nanoporous palladium pellistors," *Microelectronics Journal*, vol. 34, no. 2, pp. 115-126, 2003.
- [11] S. E. Moon et al., "Low power consumption micro C<sub>2</sub>H<sub>5</sub>OH gas sensor based on micro-heater and ink jetting technique," *Sensors and Actuators B: Chemical*, vol. 217, pp. 146-150, 2015.
- [12] J. M. Son, J. H. Lee, J. Kim, and Y. H. Cho, "Temperature distribution measurement of Au micro-heater in microfluidic channel using IR microscope," *International Journal of Precision Engineering and Manufacturing*, vol. 16, no. 2, pp. 367-372, 2015.
- [13] A. Górecka-Drzazga, "Miniature and MEMS-type vacuum sensors and pumps," *Vacuum*, vol. 83, no. 12, pp. 1419-1426, 2009.
- [14] K. Zhang, S. Chou, and S. Ang, "Fabrication, modeling and testing of a thin film Au/Ti microheater," *International Journal of Thermal Sciences*, vol. 46, no. 6, pp. 580-588, 2007.
- [15] J. Creemer et al., "Microhotplates with TiN heaters," *Sensors and Actuators A: Physical*, vol. 148, no. 2, pp. 416-421, 2008.
- [16] Y. Mo, Y. Okawa, M. Tajima, T. Nakai, N. Yoshiike, and K. Natukawa, "Micro-machined gas sensor array based on metal film micro-heater," *Sensors and Actuators B: Chemical*, vol. 79, no. 2-3, pp. 175-181, 2001.
- [17] J.-g. Kang, J.-S. Park, and H.-J. Lee, "Pt-doped SnO<sub>2</sub> thin film based micro gas sensors with high selectivity to toluene and HCHO," *Sensors and Actuators B: Chemical*, vol. 248, pp. 1011-1016, 2017.
- [18] N. Das, M. Jhabvala, D. Robinson, and P. Shu, "Low power polysilicon sources for IR applications," in *1998 5th International Conference on Solid-State and Integrated Circuit Technology. Proceedings (Cat. No. 98EX105)*, 1998, pp. 884-886: IEEE.
- [19] F. Laermer and A. Urban, "MEMS at Bosch—Si plasma etch success story, history, applications, and products," *Plasma Processes and Polymers*, vol. 16, no. 9, p. 1800207, 2019.

- [20] S. J. Pearton et al., "GaN-based diodes and transistors for chemical, gas, biological and pressure sensing," *Journal of Physics: Condensed Matter*, vol. 16, no. 29, pp. R961-R994, 2004.
- [21] P. Offermans, R. Vitushinsky, M. Crego-Calama, and S. H. Brongersma, "Ultra-Sensitive NO<sub>2</sub> Detection with AlGa<sub>N</sub>/Ga<sub>N</sub> 2DEG Channels for Air Quality Monitoring," (in English), 2012 *Ieee Sensors Proceedings*, pp. 905-907, 2012.
- [22] K. Galatsis and W. Wlodarski, "Car cabin air quality sensors and systems," *Encycl. Sens*, vol. 8, no. 111, p. 15, 2006.
- [23] M. S. Abidin, A. M. Hashim, M. E. Sharifabad, S. F. Rahman, and T. Sadoh, "Open-gated pH
- [24] C. Silvestri, P. Picciafoco, B. Morana, F. Santagata, G. Q. Zhang, and P. M. Sarro, "Electro-thermal simulation and characterization of vertically aligned CNTs directly grown on a suspended microhoptate for thermal management applications," (in English), 2014 *Ieee Sensors*, 2014.
- [25] P. Offermans et al., "Suspended AlGa<sub>N</sub>/Ga<sub>N</sub> membrane devices with recessed open gate areas for ultra-low-power air quality monitoring," in 2015 *IEEE International Electron Devices Meeting (IEDM)*, 2015, pp.
- [26] A. Wang, L. Zeng, W. Wang, and Z. Luo, "Static and dynamic simulation studies on the AlGa<sub>N</sub>/Ga<sub>N</sub> pressure sensor," *Semiconductor Science and Technology*, 2019.
- [27] J. Zhu, X. Zhou, L. Jing, Q. Hua, W. Hu, and Z. L. Wang, "Piezotronic Effect Modulated Flexible AlGa<sub>N</sub>/Ga<sub>N</sub> High-Electron-Mobility Transistors," *ACS nano*, 2019.
- [28] J. P. Ibbetson, P. Fini, K. Ness, S. DenBaars, J. Speck, and U. Mishra, "Polarization effects, surface states, and the source of electrons in AlGa<sub>N</sub>/Ga<sub>N</sub> heterostructure field effect transistors," *Applied Physics Letters*, vol. 77, no. 2, pp. 250-252, 2000.
- [29] Y. Halfaya et al., "Investigation of the Performance of HEMT-Based NO, NO(2) and NH(3) Exhaust Gas Sensors for Automotive Antipollution Systems," *Sensors (Basel)*, vol. 16, no. 3, p. 273, Feb 23 2016.

# 4

## ALGAN/GAN HETEROSTRUCTURE FOR GAS SENSING

*This chapter is based on:*

*Sun, J., Sokolovskij, R., Iervolino, E., Liu, Z., Sarro, P. M., and Zhang, G. (2019). Suspended AlGa<sub>N</sub>/Ga<sub>N</sub> HEMT NO<sub>2</sub> Gas Sensor Integrated With Micro-heater. Journal of Microelectromechanical Systems, 28(6), 997-1004.*

*Sun, J., Sokolovskij, R., Iervolino, E., Santagata, F., Liu, Z., Sarro, P. M., and Zhang, G. (2019). Characterization of an Acetone Detector Based on a Suspended WO<sub>3</sub>-Gate Al-GaN/GaN HEMT Integrated With Microheater. IEEE Transactions on Electron Devices, 66(10), 4373-4379.*

*Sun, J., Zhan T., Sokolovskij, R., Liu, Z., Sarro, P. M., and Zhang, G. "Enhanced Sensitivity Gate-recessed Pt/AlGa<sub>N</sub>/Ga<sub>N</sub> Heterostructure NO<sub>2</sub> Sensor Fabricated by Oxygen-based Etching Method" To be submitted to Sensors and Actuators B.*

## 4.1. INTRODUCTION

As mentioned in chapter 1, gas sensors play a more important role in providing comfort and safety in industrial and consumer applications, especially for environmental pollution monitoring. Various applications require very different levels of sensor performance and impose price, size and power consumption on an acceptable solution. The increasing demand for low power, compact, gas sensors for industrial and consumer applications drives the research of novel technologies towards miniaturization of the sensor without sacrificing sensitivity. Over the past decades, the metal oxide sensors based on metal oxide materials such as stannic oxide ( $\text{SnO}_2$ ) [1], indium oxide ( $\text{In}_2\text{O}_3$ ) [2], tungsten trioxide ( $\text{WO}_3$ ) [3] and many others have found widespread commercial applications.

The AlGaN/GaN heterojunctions exhibit great potential for high performance sensors development due to the high carrier density two-dimensional electron gas (2DEG) at the interface introduced by the strong polarization effect, which is sensitive to the changes in surface potential [7]. Many types of GaN based devices have been studied for gas and chemical detection. Among them Schottky diodes, metal oxide semiconductor (MOS) diodes, and AlGaN/GaN HEMTs. Compared to AlGaN/GaN Schottky diode sensors for nitric oxide (NO) [8], ammonia ( $\text{NH}_3$ ) [9, 10], nitrogen dioxide ( $\text{NO}_2$ ) [11], hydrogen ( $\text{H}_2$ ) [12], and acetone [13], AlGaN/GaN HEMT sensors provide several advantages: firstly, the current to be measured is larger than that in Schottky diodes, resulting in higher current changes and lower theoretical detection limits. This is introduced by the higher carrier density two-dimensional electron gas (2DEG) introduced by piezoelectric and spontaneous polarization at the interface between AlGaN and GaN layers. AlGaN layers with 30 % Al concentration contain 5-10 times higher channel sheet densities compared to gallium arsenide (GaAs) or indium phosphide (InP) HEMTs. Secondly, the sensitivity can be modulated and optimized by changing the gate bias. Finally, the 2DEG does not interact with the analytes but is sensitive to surface states. By functionalizing the gate area of a HEMT sensor for different analytes, such as enzymes, polyimides, or metals, sensitivity to  $\text{H}_2$  [12], CO [14–16], NO [17, 18],  $\text{NO}_2$  [18–20],  $\text{NH}_3$  [10, 17, 21], methane ( $\text{CH}_4$ ) [22],  $\text{H}_2\text{S}$  [23, 24],  $\text{C}_2\text{H}_2$  [25], pH [26], urea [27], glucose [28], chloride ion [29], heavy metal [30], and DNA [31] have been reported.

As shown in various reports [32–34] on chemical sensors, the important parameters, such as selectivity, sensitivity, and response time of gas sensors can be improved by increasing the surface temperature. To sustain elevated operating temperature from a minimum amount of input energy, a heating element is often integrated into the sensor system.

A thin (5-20 nm) AlGaN barrier recess has also been applied for enhancement mode HEMTs [35], Au-free [36], complementary metal oxide semiconductor (CMOS) compatible ohmic resistance reduction [37] and to improve the sensitivity of HEMT-based sensors [19, 20, 26, 38]. AlGaN/GaN recess would be commonly done by reactive ion etching (RIE) using  $\text{Cl}_2/\text{BCl}_3$  plasma with low power or thermal oxidation at 650 °C coupled with potassium hydroxide (KOH) oxide etching at 70 °C [39]. However, dry RIE etching processes, often exhibits difficulties of depth control, non-uniformities, etching residues and lattice damage due to ion bombardment. Furthermore, cyclic oxidation using oxygen plasma, followed wet etching to fabricate gate recess in GaN device, was reported

[40]. However, the etching rate (0.38 nm/cycle) was too slow for practical application. Our early work investigated the oxygen plasma oxidation and hydrogen chloride (HCl) wet etching for AlGa<sub>n</sub>/Ga<sub>n</sub>, and obtained a controllable etching rate of 0.6-11 nm/cycle [41].

A gate recess of AlGa<sub>n</sub>/Ga<sub>n</sub> heterostructure sensor using ICP-RIE dry etching with low-ppb level sensitivity was demonstrated by Peter Offermans et al. [20, 38, 42]. However, the current change is nA level and response time is about 30 mins for 100 ppb NO<sub>2</sub>, which is not suitable for practical application but offer nevertheless indisputably high potential [20, 35]. The sensitivity of a urea biosensor based on gate-recess AlGa<sub>n</sub>/Ga<sub>n</sub> adapted by photoelectrochemical etching method was improved to about 40% [27].

In this chapter, we first introduce a suspended nanolayer WO<sub>3</sub> gate AlGa<sub>n</sub>/Ga<sub>n</sub> heterostructure sensor with an integrated micro-heater. The WO<sub>3</sub> nanolayer was deposited by physical vapor deposition (PVD) for gas sensing and the suspended micro-heater was fabricated by MEMS process for low power consumption. The response of WO<sub>3</sub> gate AlGa<sub>n</sub>/Ga<sub>n</sub> to NO<sub>2</sub> and acetone at different temperatures were demonstrated. Afterwards, based on our proposed precision two-step gate recess technique, a suspended gate-recessed Pt/AlGa<sub>n</sub>/Ga<sub>n</sub> heterostructure gas sensor with an integrated micro-heater was also fabricated and characterized. The controllable two-step gate recess etching method, which includes O<sub>2</sub> plasma oxidation of nitride and wet etching, improves gas sensing performance. Then NO<sub>2</sub> gas response characteristics of gate recess Pt/AlGa<sub>n</sub>/Ga<sub>n</sub> heterostructure are studied and discussed. The repeatability and cross-sensitivity of the sensor are also demonstrated.

## 4.2. NANO WO<sub>3</sub>/ALGAN/GAN GAS SENSOR

### 4.2.1. DEVICE FABRICATION

As shown in Figure 4.1, a voltage or current controlled MEMS micro-heater, with a suspended and thus thermally isolated structure, enables low power heating. The micro-heater and HEMT sensor area were defined as active area. From previous work [43], it is known that a SiO<sub>2</sub> layer with low thermal conductivity provides an effective thermal isolation between the active sensor area and the silicon frame for substantial reduction of power consumption, down to 5-100 mW, when the active area of sensor is heated to the desired operating temperature. The HEMT sensor is placed together with the micro-heater surrounding the source/gate/drain area on a suspended membrane. The contact pads are on the thick silicon frame. The silicon substrate (400 μm) is backside etched away by deep reactive ion etching (DRIE) to form a circular membrane (650 μm in diameter).

The AlGa<sub>n</sub>/Ga<sub>n</sub> heterostructure was grown by Suzhou Nanowin Co. on a 2-inch silicon <111> 1 mm-thick wafers using Metal-organic Chemical Vapor Deposition (MOCVD). Starting from the substrate, the structure consisted of, a 2 μm-thick undoped GaN buffer layer, followed by a 1 nm-thick AlN interlayer, an undoped 25 nm-thick Al<sub>0.26</sub>Ga<sub>0.74</sub>N barrier layer, and a 3 nm-thick GaN epitaxial cap layer. The electron mobility was 1500 cm<sup>2</sup>/V-s, with a sheet electron density of 1×10<sup>13</sup> cm<sup>-2</sup>.

The fabrication process flow (Figure 4.2) started with a mesa etching using a chlorine/boron chloride (Cl<sub>2</sub>/BCl<sub>3</sub>) plasma to define the sensor geometry. Then, Ti/Al/Ti/Au

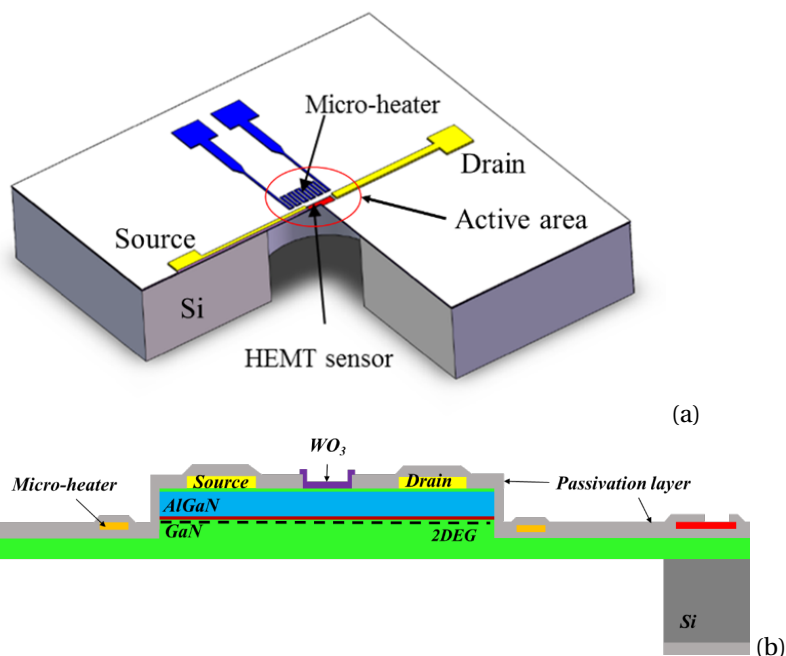


Figure 4.1: (a) Schematic and (b) cross-section of  $\text{WO}_3$  gate AlGaN/GaN HEMT with integrated micro-heater.

(20/110/40/50 nm) metal contacts were e-beam evaporated and patterned by lift-off technology. Rapid thermal annealing at  $870^\circ\text{C}$  for 45 seconds under  $\text{N}_2$  ambient in a RTP-500 system was conducted to make the contacts Ohmic and improve reliability at high temperature. A 200-nm thick silicon oxide was then deposited by plasma-enhanced chemical vapor deposition (PECVD). A Ti/Pt (30/200 nm) metal layer was deposited by e-beam evaporation and patterned by lift-off to form the microheater, followed by a 200-nm PECVD silicon oxide layer for isolation from the interconnect layer. The silicon oxide was patterned in buffer oxide etch (BOE) solution and the thick metal interconnect formed using evaporated a Ti/Au (20/300 nm) layer stack. The topside of the wafer was covered by PECVD silicon oxide layer and the backside was polished down to  $400\ \mu\text{m}$  and 5  $\mu\text{m}$ -thick silicon oxide layer was deposited as hard mask during the DRIE process to etch the silicon substrate. Then backside silicon oxide was patterned by inductively coupled plasma (ICP) etching using AZ4620 photoresist as mask and the topside silicon oxide layer was etched in BOE solution to form opening for the contact pads and gate windows. The  $\text{WO}_3$  (10 nm) functional material layer was deposited on the gate area of  $80\ \mu\text{m} \times 40\ \mu\text{m}$  by physical vapor deposition (PVD). For comparison, the reference chip is without  $\text{WO}_3$  layer deposition on the gate area. The Silicon substrate is etched away below the active area in the final step.

The microheater has a rectangle geometry around a central area of  $230\ \mu\text{m} \times 290\ \mu\text{m}$ , as showed in Figure 4.3 (a). Figure 4.3(b) and (d) show SEM images of the gate area from  $45^\circ$  angle and cross-sectional view of the fabricated sensor, respectively. Figure 4.3(c)

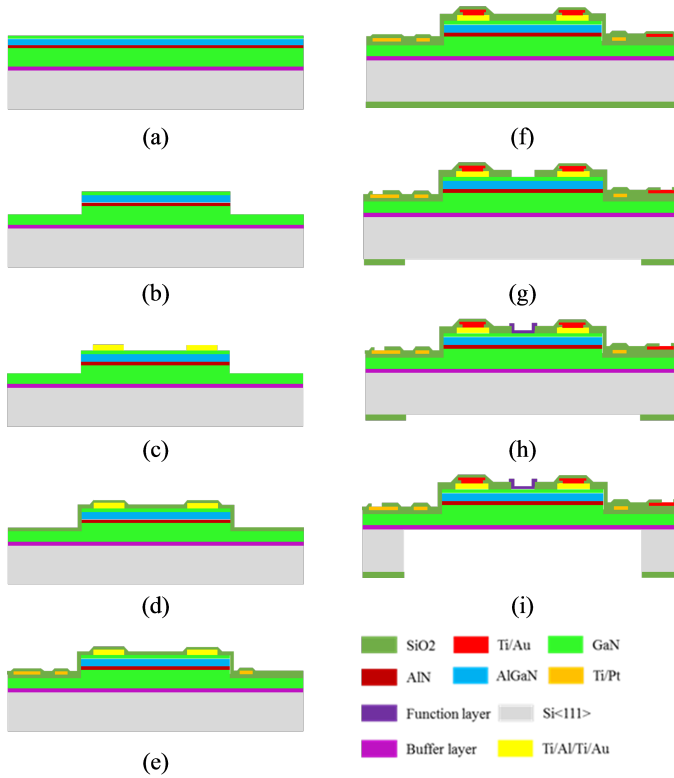


Figure 4.2: Main steps for the fabrication of the suspended AlGaIn/GaN HEMT sensor integrated with micro-heater. (a) starting wafer with epitaxial layers; (b) mesa etching to define sensor area; (c) Ohmic contact deposition and annealing; (d) PECVD SiO<sub>2</sub>; (e) micro-heater deposition and passivation; (f) metal deposition and top/bottom passivation; (g) opening contact pads at the frontside and etching window at the backside; (h) WO<sub>3</sub> deposition; (i) substrate etching from the backside to form the suspended structure.

shows the AFM image and step height measurement of the 10 nm WO<sub>3</sub> layer. The energy dispersive spectrum (EDS) of the device gate area surface is reported in Figure 4.4. The corresponding peaks of Ga, W, N, Al, O elements are observed. Clearly, the deposition of WO<sub>3</sub> on the gate surface by magnetron sputtering is confirmed.

#### 4.2.2. GAS TESTING SETUP

For gas testing experiments, the HEMT sensors were placed in a stainless-steel chamber (20 mL) and connected to a Keithley 2700 and a power source. Gas sources of pure N<sub>2</sub> and varying concentration of NO<sub>2</sub> were inserted in the testing chamber based on dynamic gas distribution instrument at atmospheric pressure. The gas flow rate was controlled at 100 sccm and the concentration of NO<sub>2</sub> in N<sub>2</sub> was varied from 100 ppb to 50 ppm at ambient temperature. The gas measurements were conducted in a gas exposure system, which is shown in the Figure 4.5. The gas system allows the introduction of analyte gases

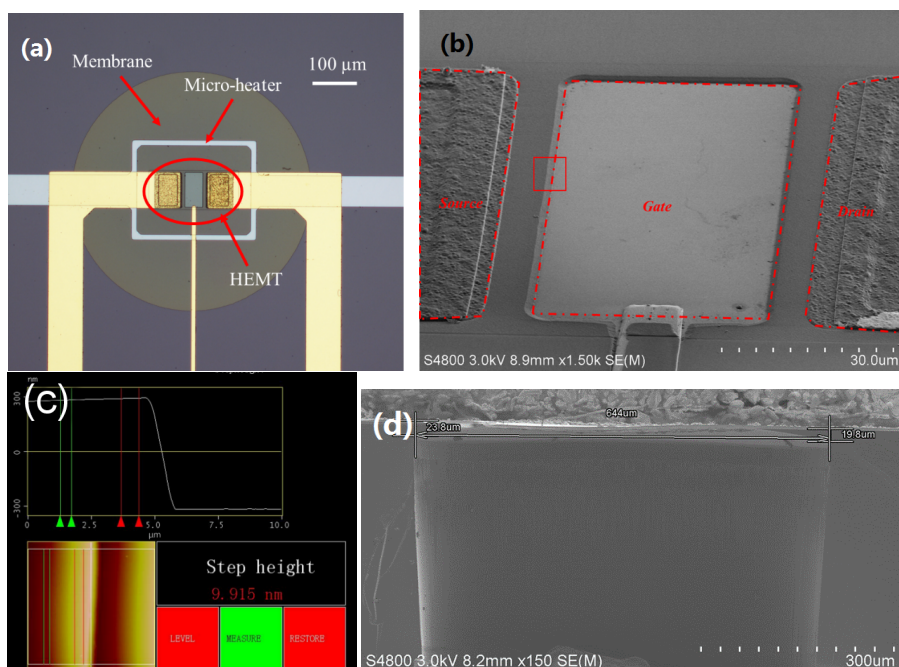


Figure 4.3: The fabricated device: (a) optical image; (b) SEM image of HEMT sensor from 45° angle; (c) AFM image and step height measurement taken in the area labeled with the red square in figure 4.3(b); (d) SEM image of the device cross section.

( $H_2$ ,  $C_xH_y$ , etc) and diluent gases ( $N_2$ , Ar, air, etc.) into the gas chamber. The flow of gases is controlled using mass flow controllers (MFC) and MFC power supply.

The static gas measurement system is schematically depicted in Figure 4.6. It is very important to measure the sensitivity and selectivity of sensors to specific gases. The static measurement system consists of three components, a gas chamber (150/500 mL), a source meter and post treatment of gases. The target gas was injected into the test chamber by a micro-injector. The target liquid, e.g. acetone, ethanol was injected into the chamber where it evaporated. After completing one measurement, the chamber was purged using a micropump connected to the chamber. The current signal of each sensor was monitored using Keithley 2400 by software (Ke2400S Measurement Software, Zeal Yong Technology) installed on computer. The signal data was displayed in real-time on the monitor.

### 4.2.3. IMPROVING $NO_2$ LIMIT OF DETECTION

Among polluting gases, nitrogen dioxide ( $NO_2$ ) is one of the most harmful gases originating mainly from combustion of automobile exhaust (0.1-50 ppm) [44], furnaces, plants, etc. [8]. Various concentration ranges need to be detected, depending on a specific application and environmental conditions, which creates the need for wearable, low power, continuous environmental monitoring systems. Current sensors are not suited for con-

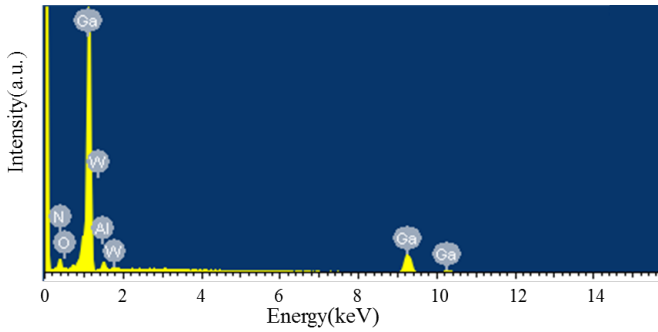


Figure 4.4: EDS spectrum of the gate surface of the HEMT sensor showing the corresponding peaks of Ga, W, N, Al, O elements.

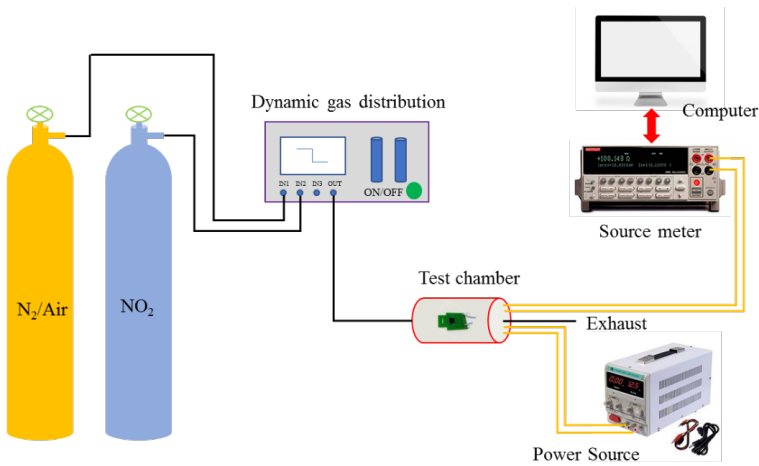


Figure 4.5: Schematic diagram of the dynamic measurement system.

tinuous air quality monitoring due to high power consumption, slow response, and low sensitivity (ppb level).

Here, for the first time, we reported on the fabrication of a suspended AlGaN/GaN HEMT sensors with WO<sub>3</sub> nano-film modified gate and integrated MEMS microheater as a sensor platform. The sensor comprises an AlGaN/GaN membrane suspended within a silicon frame micromachined out of the silicon wafer, and the following elements are over the membrane: a micro-heater which controls the temperature of the sensing layer, two silicon oxide insulating layers, a HEMT sensing structure and a WO<sub>3</sub> nano-layer on top. The micro-heater performance and the AlGaN/GaN self-heating on the membrane structure are studied first. In addition, the temperature on AlGaN/GaN sensor device are investigated and discussed. Finally, the response properties of HEMT sensor to NO<sub>2</sub> gas with concentration of 0.1-40 ppm are presented.

After dicing, the chips were wire-bonded to a prototype with ceramic quad flat no-

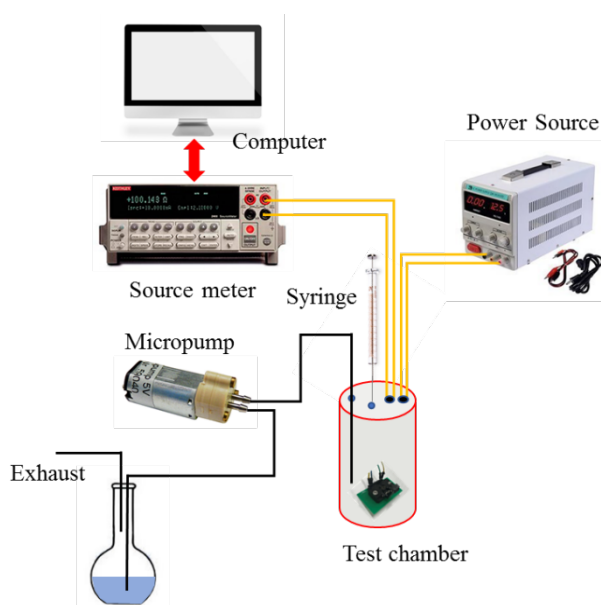


Figure 4.6: Schematic diagram of the static measurement system.

lead (CQFN) package with size of 4 mm x 4 mm (Figure 4.7). This sensor package is designed to eliminate the effect of gas flow as for a perforated lid.

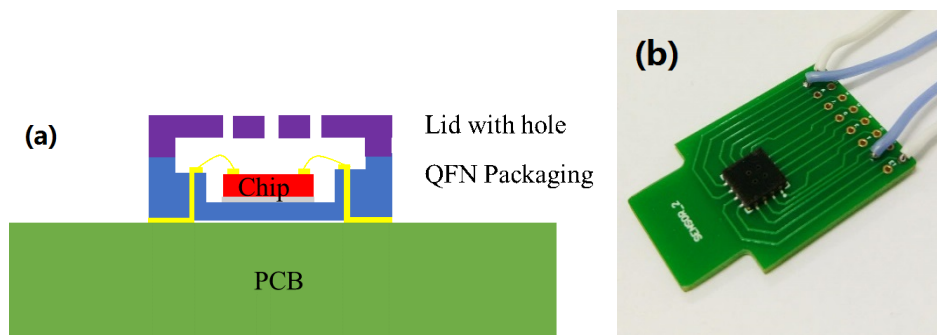


Figure 4.7: (a) the schematic diagram of a gas sensor package; (b) the photograph of a packaged sensor on test PCB.

For gas testing experiments, the HEMT sensors were placed in a stainless-steel chamber (20 mL) and connected to a Keithley 2700 and a power source. Gas sources of pure  $N_2$  and varying concentration of  $NO_2$  were inserted in the testing chamber. The gas flow rate was kept at 100 sccm and the concentration of  $NO_2$  in  $N_2$  was varied from 100 ppb to 50 ppm at ambient temperature. Two important parameters to be determined are the response time and the recovery time. Response time ( $t_{Response}$ ) and recovery time ( $t_{Recovery}$ ) were defined as the time required for the drain current to change/return from

10% to 90 % of its saturated response value to NO<sub>2</sub> gas.

The gas sensors were placed in the testing chamber and heated to 571 K while exposed to 0.1-40 ppm NO<sub>2</sub> gas in pure N<sub>2</sub>. Figure 4.8 (a) presents the transient response of AlGa<sub>0.1</sub>N/GaN sensor for 0.1-1 ppm at the operating bias of  $V_{DS}=5$  V and  $V_H=4$  V. A clear change of drain current is observed under a low concentration of 100 ppb NO<sub>2</sub>/N<sub>2</sub> at 300 °C. Figure 4.8 (b) shows the enlarged parts of data in Figure 4.8 (a) measured at a NO<sub>2</sub> concentration of 1 ppm. As shown in Figure 4.9, the current change values ( $\Delta I$ ) and sensitivity ( $S = \Delta I/I$ ) toward NO<sub>2</sub> gas increase after WO<sub>3</sub> layer deposition. At the concentration of 10 ppm,  $\Delta I$  and  $S$  were found to increase from 9  $\mu$ A and 0.25 % to 29  $\mu$ A and 1.21 %, respectively. The limit of sensor detection also be improved from 2 ppm to 100 ppb. Figure 4.10 reports the response time and recovery time as function of NO<sub>2</sub> concentration with WO<sub>3</sub> layer and without WO<sub>3</sub> layer. The response time of the sensor with WO<sub>3</sub> layer is improved from 423 second to 91 second at 10 ppm. However, the recovery time of the device without WO<sub>3</sub> layer are faster. A plausible reason is that the AlGa<sub>0.1</sub>N surface facilitates NO<sub>2</sub> molecule desorption. At the concentration of 1 ppm,  $\Delta I$  and  $S$  were found to be 26  $\mu$ A and 1.1 % with a response and recovery time of 88 second and 132 second, respectively. The response times could be further reduced with a shorter distance between the gas cylinder and the sensor. The effect of the working temperature, known to have great influence on the sensitivity of gas sensor, was studied as well. The current change and sensitivity as a function of micro-heater voltage are plotted in Figure 4.11. The sensitivity of sensor exposed to 10 ppm NO<sub>2</sub> at  $V_H=3$  V (135 °C),  $V_H=3.5$  V (210 °C) and  $V_H=4$  V (300 °C) are 0.29 %, 0.9 % and 1.4 %, respectively. The sensing properties are significantly enhanced with increasing micro-heater voltage (temperature). Nano WO<sub>3</sub> gate AlGa<sub>0.1</sub>N/GaN HEMT sensors have shown a great potential to detect low NO<sub>2</sub> concentration with a fast response time.

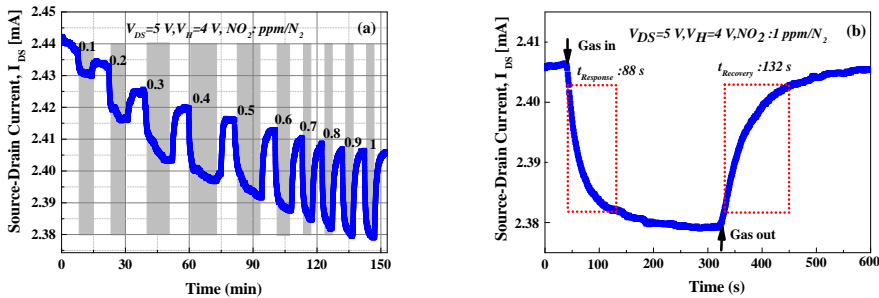


Figure 4.8: Transient response of AlGa<sub>0.1</sub>N/GaN HEMT sensor to NO<sub>2</sub> gas concentrations at 300 °C (a) 0.1-1 ppm; (b) Enlarged part of the response curve of 1 ppm.

Several potential sensing mechanisms have been reported based on adsorption on surface of catalytic metal dissociate and release electrons.[18, 21, 42] When the sensor are exposed to NO<sub>2</sub> gas, chemisorption reaction on the WO<sub>3</sub> surface results in gas ions (negatively charged for NO<sub>2</sub>) that rapidly diffuse at the surface. NO<sub>2</sub> gas adsorb directly on the surface of WO<sub>3</sub> layer as well as reacts with adsorbed O<sup>-</sup> ions according to the following reaction.[43]

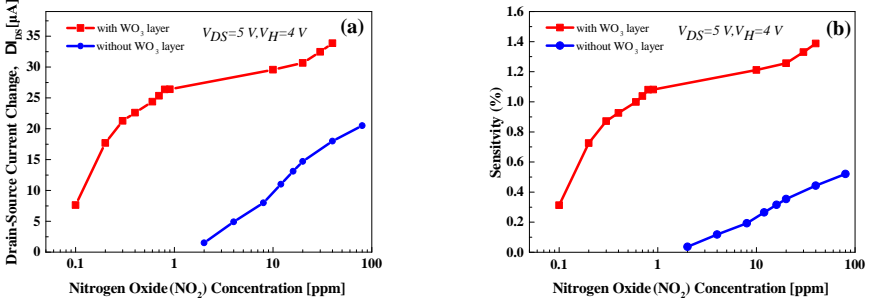


Figure 4.9: Gas concentration dependent sensing properties of HEMT sensor for 0.1-50 ppm  $\text{NO}_2$  gas at 300 °C.

4

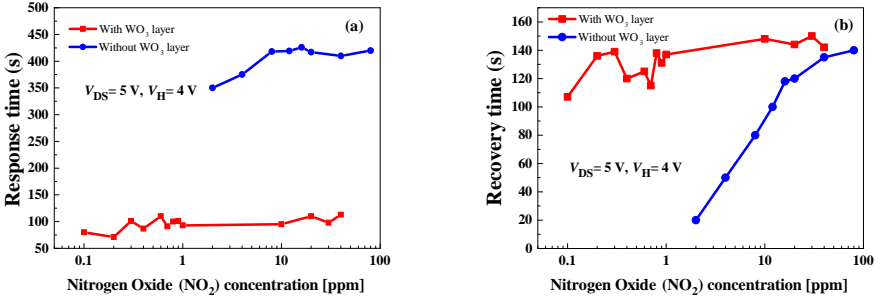
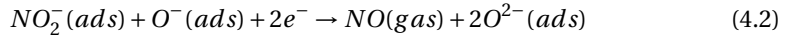


Figure 4.10: Response time (a) and recovery time (b) versus  $\text{NO}_2$  concentration.



On the other hand, the surface states would be altered by the polar  $\text{NO}_2$  molecules, which would manipulate the 2DEG concentration. Therefore, the surface potential of the  $\text{WO}_3$  and AlGaN are changed, resulting in the variation of drain current of the HEMT device. The changed surface potential can mathematically be represented by the Helmholtz model

$$\Delta V = N_s p (\cos\theta) / \epsilon \epsilon_0 \quad (4.3)$$

Where  $p$  is the dipole moment,  $N_s$  is the dipole density per unit area,  $\theta$  is the angle between the dipole and the normal surface,  $\epsilon$  is the relative permittivity of the material, and  $\epsilon_0$  is the permittivity of free space. The surface potential is mainly affected by the value of  $p/\epsilon$  of the polar molecules.

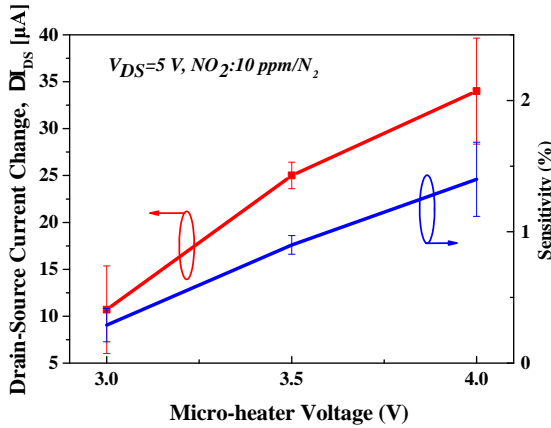


Figure 4.11: Current change and sensitivity of sensor with WO<sub>3</sub> layer to 10 ppm NO<sub>2</sub> at different micro-heater voltages (temperature).

#### 4.2.4. RESPONSE TO ACETONE

Acetone as volatile, flammable and irritant odor organic solvent is extensively used in industrial applications, particularly in the pharmaceutical industry and for pesticide preparation. In addition, long-term exposure to high concentrations of acetone (over 1000 ppm) may endanger human health, causing headache, fatigue, coma and even death [47]. Therefore, the detection of acetone concentration is an urgent and crucial matter, especially in view of public safety and human health.

A variety of analytical techniques, such as gas/liquid chromatography [48], electrochemistry [49], infrared spectroscopy [50], and semiconductor [51], have been proposed for acetone detection. Among these techniques, the sensor based on semiconductors have the attractive features of a fast response, low power consumption and compact size. Most of the research into semiconductor sensors have focused on metal oxide semiconductors such as ZnO [51–53], SnO<sub>2</sub> [54–56], WO<sub>3</sub> [57–59], NiO [60, 61], In<sub>2</sub>O<sub>3</sub> and Fe<sub>2</sub>O<sub>3</sub> [62–65]. Tungsten trioxide (WO<sub>3</sub>) is an n-type bandgap semiconductor material and has excellent properties for gas detection, because it shows a high catalytic behavior both in oxidation and reduction reactions on its surface [66]. So far very few results of acetone detection with AlGaN/GaN devices have been reported [67].

In this section, we demonstrate the successful sensing of acetone vapor using a suspended WO<sub>3</sub>-gate AlGaN/GaN HEMT sensor with an integrated microheater. The transient characteristics of the sensor at various surface temperatures and acetone concentrations in dry air ambient are investigated. The sensor shows a current increase and rapid response to different acetone concentrations. Moreover, the selectivity and reproducibility of the sensor are demonstrated.

The fabrication process of WO<sub>3</sub>/AlGaN/GaN is the same as what reported in section 6.2.3. After dicing, the chips were wire-bonded to a ceramic quad flat no-lead (CQFN) package with a size of 4 mm x 4 mm (Figure 4.12(a)). This sensor package is designed to eliminate the effect of gas flow see previous section. The 8-pins QFN testing socket

Figure 4.12(b) is placed in a gas chamber and electrically connected to a Keithley 2400 source meter. The target gas was injected into the test chamber by a micro-injector. The target liquid, e.g. acetone, ethanol, were injected into the chamber. After the drain current reached a new saturation, the test chamber was opened and the gas removed by micro air pump. The gas sensitivity  $S(\%) = \Delta I_{DS} / I_{DS,air} \times 100\%$ , Where  $\Delta I_{DS} = I_{DS,acetone} - I_{DS,acetone}$  is the drain current change between response to acetone and to air ambient.

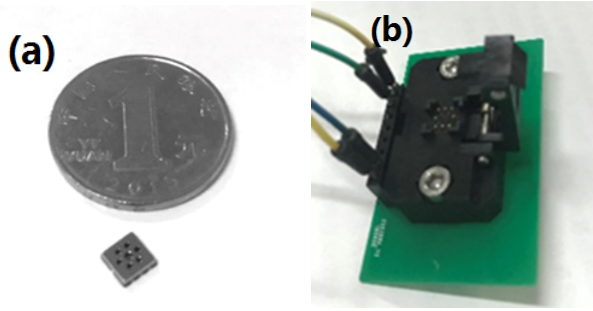


Figure 4.12: (a) Optical photograph of CQFN packaged sensor next to a 1 RMB coin to show its size; (b) QFN testing socket.

Figure 4.13 and Figure 4.14 show the transient performance of  $\text{WO}_3$  HEMT sensors at the applied micro-heater voltage ( $V_H = 3.5 \text{ V}$  and  $4 \text{ V}$ ) in the gas concentration range from 100 ppm to 1000 ppm. Upon exposure to acetone the source-drain current increases from the baseline value in dry air. The sensor shows stable operation and good repeatability, both for increasing (Figure 4.13(a)) and decreasing (Figure 4.13(b)) gas concentration.

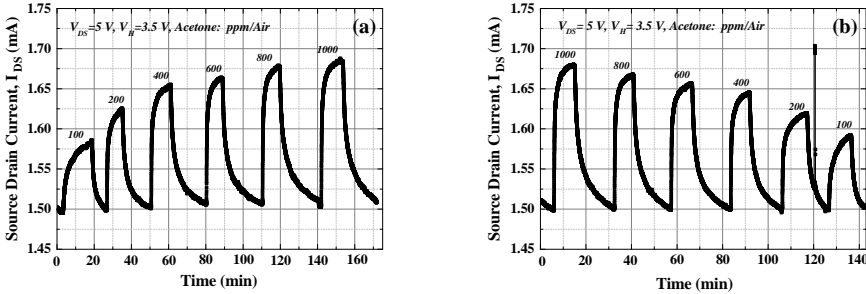


Figure 4.13: Transient response characteristics upon injection and purge of acetone in dry air ambient. During all measurements  $V_{DS} = 5 \text{ V}$ ,  $V_H = 3.5 \text{ V}$ . (a) with concentration increasing (b) with concentration decreasing.

An important sensor parameter is the magnitude of sensing signal variation,  $\Delta I_{DS}$ . Previously reported gas sensors based on AlGaN/GaN Schottky diodes shows very high sensitivities, in order of 1000 % at ppm level gas concentrations. However, current change was in nA- $\mu\text{A}$  range, due to low baseline signal values. Low  $\Delta I_{DS}$  will result in higher

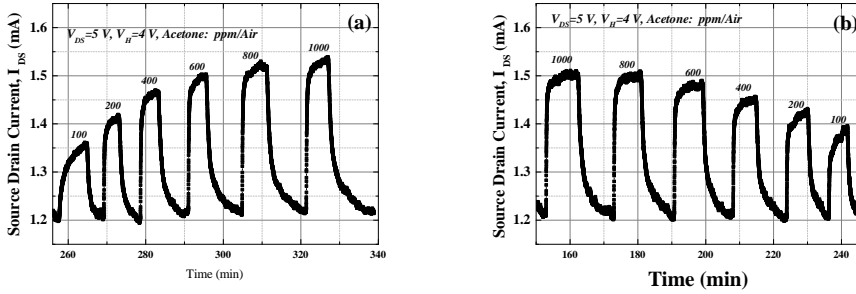


Figure 4.14: Transient response characteristics upon injection and purge of acetone in dry air ambient. During all measurements  $V_{DS}=5$  V,  $V_H=3.5$  V. (a) with concentration increasing (b) with concentration decreasing.

noise susceptibility of the sensor and higher limit of detection. Figure 4.15 shows the drain-source current change and sensitivity as a function of acetone concentration for  $V_{DS}=5$  V at  $V_H=3.5$  V (210 °C) and  $V_H=4$  V (300 °C). It is obvious that the response increased at higher temperature. In this work, for 1000 ppm acetone concentration the measured  $\Delta I_{DS}$  and sensitivity shown an almost twofold increase, from 0.18 mA (12 %) at  $V_H=3.5$  V to 0.31 mA (25.7 %) at  $V_H=4$  V, while at 100 ppm  $\Delta I_{DS} = 0.16$  mA, which is larger than the reported value of  $\Delta I \sim 12 \mu$  A at 100 ppm acetone for a Schottky type sensor [64, 65]. Figure 4.13, Figure 4.14 and Figure 4.15 show the lower concentration of acetone could be detected due to the large drain current change.

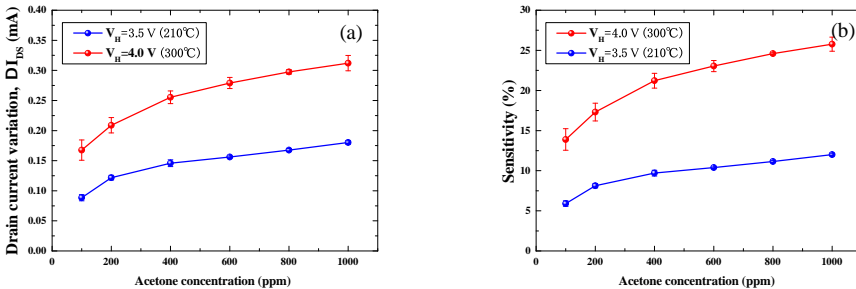


Figure 4.15: Drain current variation (a) and sensitivity (b) as a function of acetone concentration for  $V_{DS}=5$  V,  $V_H=3.5$  V (210 °) and  $V_H=4$  V (300 °).

The drain current change and sensitivity to 1000 ppm acetone at different drain-source voltage is shown in Figure 4.16. The current variation and sensitivity increase when  $V_{DS}$  increases from 0 to 5 V. However, the current variation and sensitivity decrease with  $V_{DS}$  increasing, due to the sensor working in saturation range. The optimized  $V_{DS}$  of this sensor is around 5 V. The repeatability of the sensor measured at  $V_H=3$  V (135 °C),  $V_H=3.5$  V (210 °C) and  $V_H=4$  V (300 °C) is shown in Figure 4.17. The drain current response to acetone gas when the acetone concentration is swept back and forth from 0 to

1000 ppm is reported.

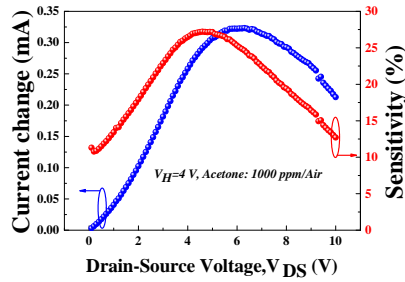


Figure 4.16: Current change and sensitivity to 1000 ppm acetone at different drain-source voltage ( $V_{DS}$ ).

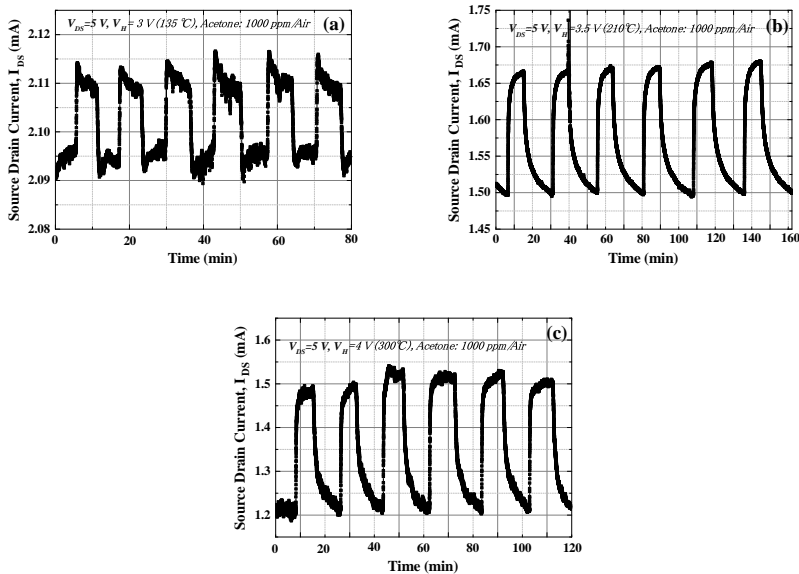


Figure 4.17: Six repetitive cycles of sensor exposure to 1000 ppm acetone at  $V_H = 3$  V (135 °C),  $V_H = 3.5$  V (210 °C) and  $V_H = 4$  V (300 °C).

The effect of the working temperature, known to have great influence on the sensitivity of a gas sensor, was studied as well. Six repetitive cycles of sensor exposure to 1000 ppm acetone at various working temperatures regulated by the integrated micro-heater voltage are shown in Figure 4.17. The sensitivity as a function of micro-heater voltage is plotted in Figure 4.18. The sensitivity of sensor exposed to 1000 ppm acetone at  $V_H = 3$  V (135 °C),  $V_H = 3.5$  V (210 °C) and  $V_H = 4$  V (300 °C) are 0.8 %, 12 % and 25.7 %, respectively.

Figure 4.19 characterizes the  $t_{Res}$  and  $t_{Rec}$  as function of acetone concentration at the applied micro-heater voltages. The transient response times decreased with increasing gas concentration for  $V_H = 3.5$  V (210 °C) and  $V_H = 4$  V (300 °C), while the recovery times

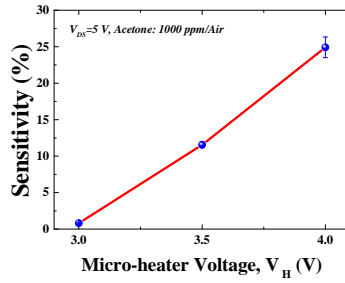


Figure 4.18: Sensitivity to 1000 ppm acetone at different micro-heater voltage (Temperature).

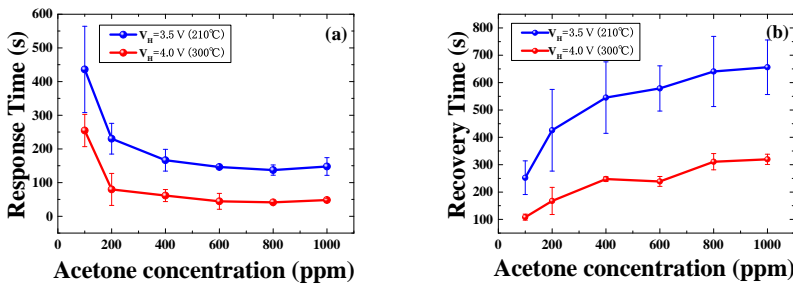


Figure 4.19: Response time (a) and recovery time (b) versus acetone concentration at  $V_H=3.5$  V (210 °C) and  $V_H=4$  V (300 °C).

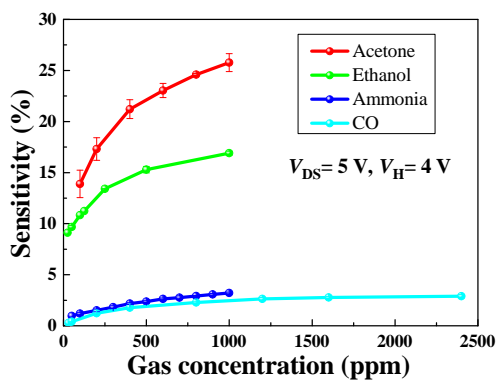
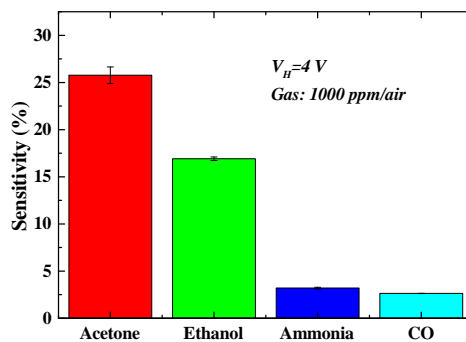
increased with increasing gas concentration. From a concentration of 400 ppm  $t_{Res}$  is stable. The response time and recovery time at different temperature are shown in Table 4-1. At 1000 ppm acetone concentration  $t_{Res}$  ( $t_{Rec}$ ) reduced from 148 (656) s at  $V_H=3.5$  V (210 °C) to 48 (320) s at  $V_H=4$  V (300 °C). At the concentration of 100 ppm,  $t_{Res}$  and ( $t_{Rec}$ ) also decreased from 436 (255) s to 252 (108) s with increasing temperature. The shorter response (recovery) time are attributed to faster gas adsorption and desorption rate at gate surface at higher temperature.

Another important characteristic of the sensor is selectivity. Figure 4.20 and Figure 4.21 present the acetone selective performance of HEMT sensor to other typical interfering gases such as ethanol, ammonia and CO at  $V_H=4$  V. Figure 4.21 shows the gas sensing response to the 1000 ppm of Acetone, ethanol, ammonia and CO at  $V_H=4$  V. The sensor sensitivity to 1000 ppm acetone is 25.7 % and the sensitivity to ethanol, ammonia and CO are as low as 16.9 %, 3.2 % and 2.6 %, respectively. It is evident that the HEMT gas sensor exhibit good selectivity toward acetone.

Previously it was found that gas molecules containing oxygen, upon adsorption on the surface of catalytic metals (e.g. Pt, Pd, or Ag) dissociate and release electrons [21, 45, 69]. When the sensor is in contact with air as shown in Figure 4.22, because of the presence of oxygen in the air, oxygen adsorption on the WO<sub>3</sub> surface traps electron from the conduction band of the semiconductor to form oxygen species ( $O_2^-$ ,  $O^-$  or  $O^{2-}$ ) [45, 67]. In

TABLE 4-1 RESPONSE TIME AND RECOVERY TIME VERSUS ACETONE CONCENTRATION AND TEMPERATURES

Acetone conc. (ppm)	$t_{Res}$ (s)		$t_{Rec}$ (s)	
	210 °C	300 °C	210 °C	300 °C
100	436	255	252	108
200	230	80	426	167
400	166	61	545	247
600	146	44	579	239
800	137	41	641	311
1000	148	48	656	320

Figure 4.20: Gas (or vapor) sensitivity of  $\text{WO}_3/\text{AlGaIn}/\text{GaIn}$  heterostructure sensorFigure 4.21: The gas sensing response to 1000 ppm of Acetone, ethanol, ammonia and CO at  $V_H=4$  V.

this ionosorbption process, this doubly charged adsorbed oxygen  $O^{2-}$  is not stable when doubly charge oxygen ions do not react immediately or are trapped by oxygen vacancies.

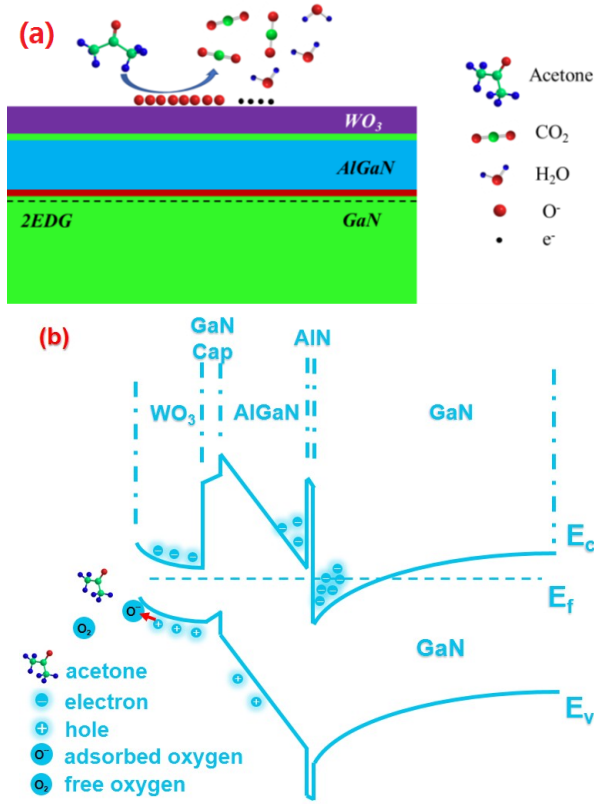
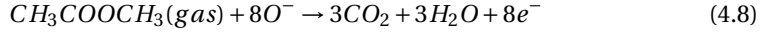


Figure 4.22: (a) Schematic of oxidation of acetone in the gate region of the WO<sub>3</sub>/AlGaN/GaN sensor; (b) Energy band diagram of WO<sub>3</sub>/AlGaN/GaN heterostructure. E<sub>c</sub>: conduction band edge, E<sub>v</sub>: valance band edge, E<sub>f</sub>: fermi level.



Such oxygen ions will act as electron trap on the sensing surface. When the temperature of the sensing area is above the 150 °C,  $O^-$  dominates during the ionosorbption process. The reaction rate of  $O^-$  is greater than  $O^{2-}$ . Accordingly, once the sensor is

exposed to acetone gas, the acetone molecules react with the adsorbed oxygen ions  $O^-$ , then produce  $CO_2$ ,  $H_2O$  and release electrons following the equation 4.5 [56, 70, 71]. Releasing electrons in the conduction band leads to the bending of band toward lower energy and move to 2DEG channel, which increases the drain current after exposure to acetone gas.



In addition, the surface states would be altered by the polar acetone molecules, which would manipulate the 2DEG concentration. Therefore, the surface potential of the  $WO_3$  and AlGaN are changed, resulting in the variation of drain current of the HEMT device. The changed surface potential can mathematically be represented by the Helmholtz model as the equation 4.3. Compared to other gases such as ethanol and ammonia, acetone is one of the most polar molecules. Consequently, the sensitivity of the device to acetone is larger than for other gases.

### 4.3. ENHANCED SENSITIVITY USING A TWO-STEP GATE RECESS TECHNIQUE

#### 4.3.1. TWO-STEP GATE RECESS TECHNIQUE

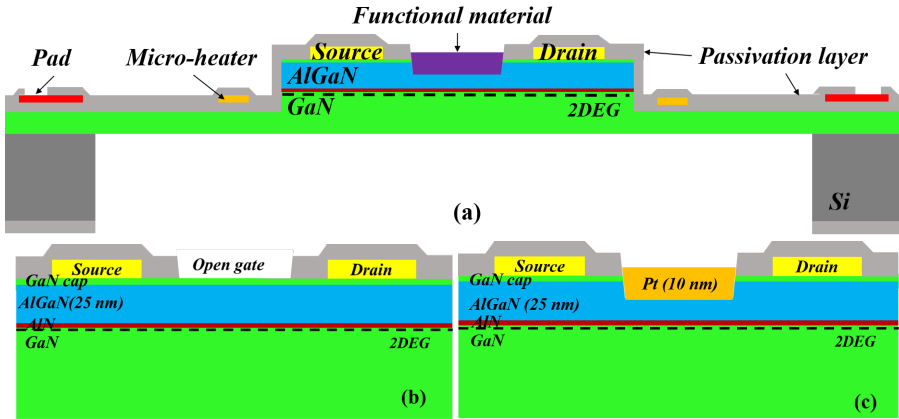


Figure 4.23: Cross-section schematic representation of GaN-based HEMT sensor with integrated micro-heater. (a) Cross-section schematic representation of GaN-based HEMT sensor. Cross-section schematic of (b) open gate and (c) 10 nm Pt thin film on recess gate.

In this section, we have implemented a suspended gate recessed Pt/AlGaN/GaN heterostructure gas device with an integrated micro-heater. The gate recess is etched by a specifically developed precise two-step etching method, consisting of  $O_2$  plasma oxidation and wet etching. We find that the sensitivity and current change to  $NO_2$  gas exposure of these devices are boosted with the additional benefit of faster response time. The temperature of the membrane is modulated by the micro-heater unit based on Joule

heating. The sensing performance of the sensor at different temperatures are studied. The repeatability and selectivity of the sensor are also demonstrated.

Figure 4.23 depicts a schematic representation of the cross-section of GaN based membrane sensor with integrated micro-heater. Figure 4.23(b) and (c) show the enlarged active area of the open gate and recess gate structures. The same epitaxial Al-GaN/GaN structure was used to fabricate the gate recess  $\text{WO}_3/\text{AlGaN}/\text{GaN}$  gas sensors. The fabrication process, schematically depicted in Figure 4.24, started with a mesa etching to define the active area. Then, Ti/Al/Ti/Au (20/110/40/50 nm) metal contacts were evaporated, followed by a rapid thermal anneal at 870°C for 45 s under  $\text{N}_2$  ambient. Next, an evaporated Ti/Pt (30/200 nm) layer was patterned by lift-off to form the microheater, followed by a 200-nm PECVD  $\text{SiO}_2$  layer for isolation from the interconnect layer. The evaporated Ti/Au (20/300 nm) layer stack is then used to form metal interconnect. The topside of the wafer was passivated with a 300 nm PECVD  $\text{SiO}_2$  layer and the backside was polished to 400  $\mu\text{m}$ . The topside  $\text{SiO}_2$  layer was etched in the BOE solution to open the contact pads and gate windows. To fabricate the gate-recessed structure, nitride oxidation was done in an ICP-RIE etcher using  $\text{O}_2$  plasma for 3 min, followed by 1 min oxide etching in a 1:4 HCl:H $_2\text{O}$  solution at room temperature. Then a 10 nm-thick Pt layer was evaporated and patterned on the 80  $\mu\text{m}$  x 40  $\mu\text{m}$  gate area. The silicon substrate was etched from the backside by deep reactive ion etching (DRIE) using 5  $\mu\text{m}$ -thick  $\text{SiO}_2$  layer as hard mask to form a circular membrane (650  $\mu\text{m}$  in diameter).

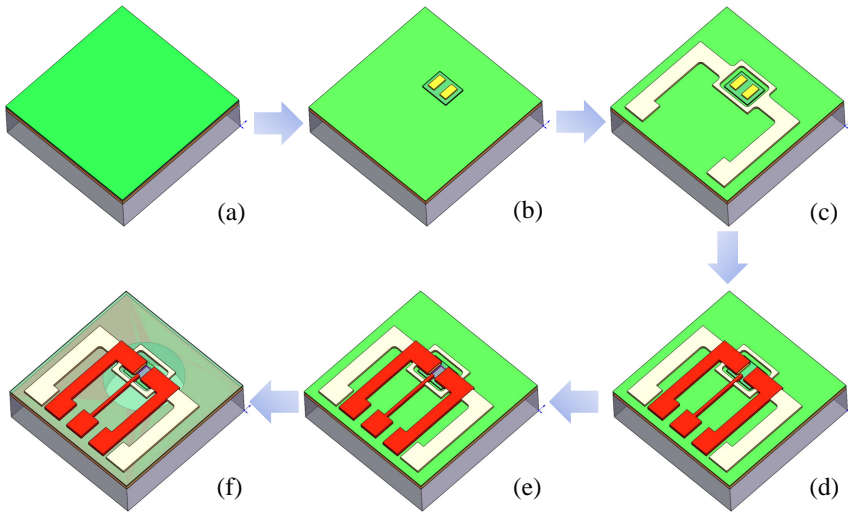


Figure 4.24: Main steps of fabrication process: (a) silicon substrate with epitaxial layers; (b) mesa and ohmic contact forming; (c) micro-heater deposition and passivation; (d) interconnect metal deposition and passivation; (e) Gate recess and functional materials deposition; (f) backside etching to form suspended membrane.

Figure 4.25(a) shows (top view) an optical image of a gate recess Pt/AlGaN/GaN device. Figure 4.25(b) shows the optical image of the complete sensor with the size of 2

mm\*2 mm. Then, the chip was attached to ceramic quad flat no lead (CQFN) package, and Au-wire bonding was utilized to interconnect the bond pads of the Pt/AlGaN/GaN device to the electrical contact points of CQFN, as shown in Figure 4.25(c).

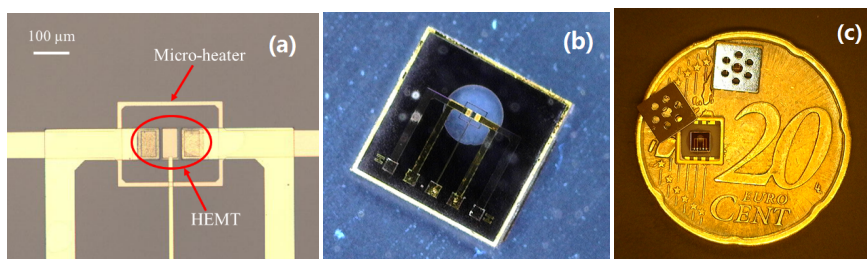


Figure 4.25: (a) Optical image of recess gate Pt/AlGaN/GaN device; (b) optical image of complete sensor; (c) Sensors with CQFN package on 20 Euro cent coin.

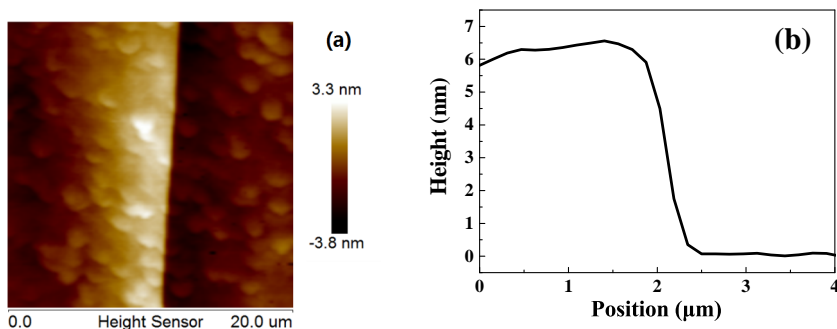


Figure 4.26: (a) AFM image of GaN step on a testing wafer (b) Step profile of the two-step gate recess .

The packaged sensor was placed in a chamber and electrically connected to a Keithley 2400 source meter. Before testing, the sensors were preheated at different temperatures for about 30 mins to get a stable output. The AFM image of the surface morphology and the step profile of the gate recess on a test wafer are shown in Figure 4.26(a) and (b). The depth of the gate-recessed region after etching was about 6 nm.

### 4.3.2. PT-GATE RECESSED HEMT CHARACTERIZATION

Figure 4.27 shows the transient response characteristic of the gate recessed Pt/AlGaN/GaN heterostructure sensor to 1-40 ppm NO<sub>2</sub>/air at the temperature of 300 °C ( $V_H = 4$  V). The source-drain current of the device decreases upon exposure to NO<sub>2</sub>, which is attributed to a decreased 2DEG density by interaction with surface donor state. Surface donor states are considered to be the source of electrons in the formation of 2DEG [72]. NO<sub>2</sub> molecule capture electrons from the non-ionized donor states, reducing the positive surface charge and thereby decreasing the 2DEG density. Also, the 2DEG mobility may be affected by surface trapping of electrons by NO<sub>2</sub> [73]. The sensor shows stable operation both for increasing [Figure 4.27(a)] and decreasing [Figure 4.27(b)] gas concentration.

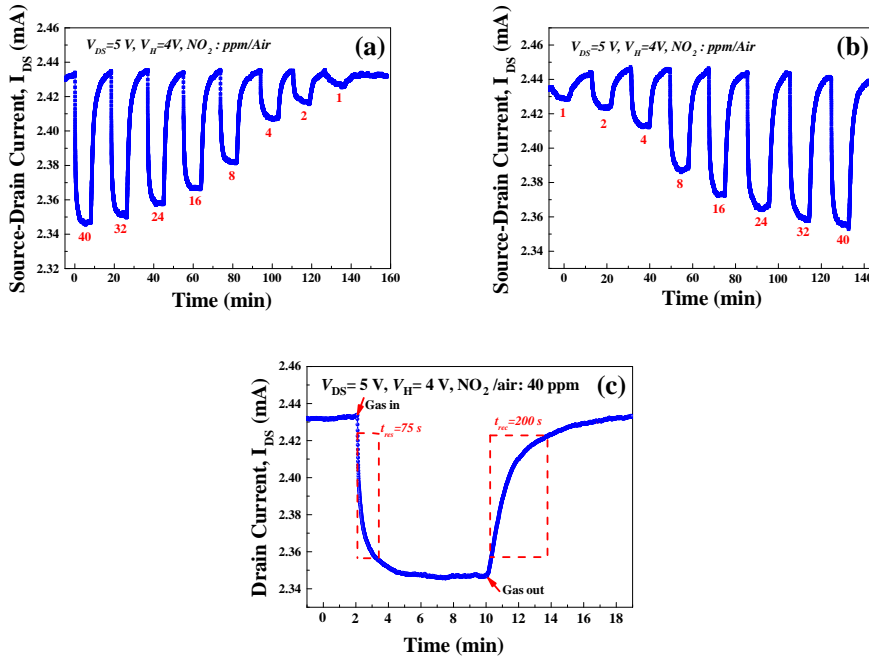


Figure 4.27: (a) Transient response characteristics upon injection and purge of  $\text{NO}_2$  in dry air ambient. During all measurements  $V_{DS} = 5$  V,  $V_H = 4$  V (a) with  $\text{NO}_2$  gas concentration decreasing (b) with  $\text{NO}_2$  gas concentration increasing (c) Enlarge part of the response curve of 40 ppm

The use of a gate recess is well known for improving the device characteristics of AlGaN/GaN HEMT.[38] As shown in Figure 4.28(a) and (b), the current change values ( $\Delta I_{DS}$ ) and sensitivity  $S$  (%) of recessed gate AlGaN/GaN heterostructure to 1-200 ppm  $\text{NO}_2$ /air gas, are about 7.5 to 20 times and 4.5 to 12 times compared to open gate device, respectively. In a thinner AlGaN layer, the reduced surface barrier potential causes fewer surface states to be ionized [72, 74]. The boost in sensing response may be explained by the increase in the number of non-ionized surface states that become available to interact with  $\text{NO}_2$ . Figure 4.29 shows the band energy diagram of AlGaN/GaN heterostructure before and after gate recess. The removal cap layer and thinner AlGaN layer on gate area result in higher barrier height [75]. Also, the gate recessed structure with shorter distance between the sensing surface and 2DEG layer make it much easier to modulate by  $\text{NO}_2$  molecule. Consequently, the sensitivity and current change of gate recessed AlGaN/GaN can be effectively improved. This could also explain the observed decrease in response time as shown in Figure 4.28(c) and (d). The response time to 40 ppm  $\text{NO}_2$ /air decreased from 400 s to 75 s.

As known, the working temperature has a considerable influence on the sensitivity and response rate of the gas sensor. The response time, recovery time and sensitivity to 40 ppm/air  $\text{NO}_2$  as a function of the microheater voltage are shown in Figure 4.30(a) and (b). The response time decreases with increasing micro-heater voltage, which is

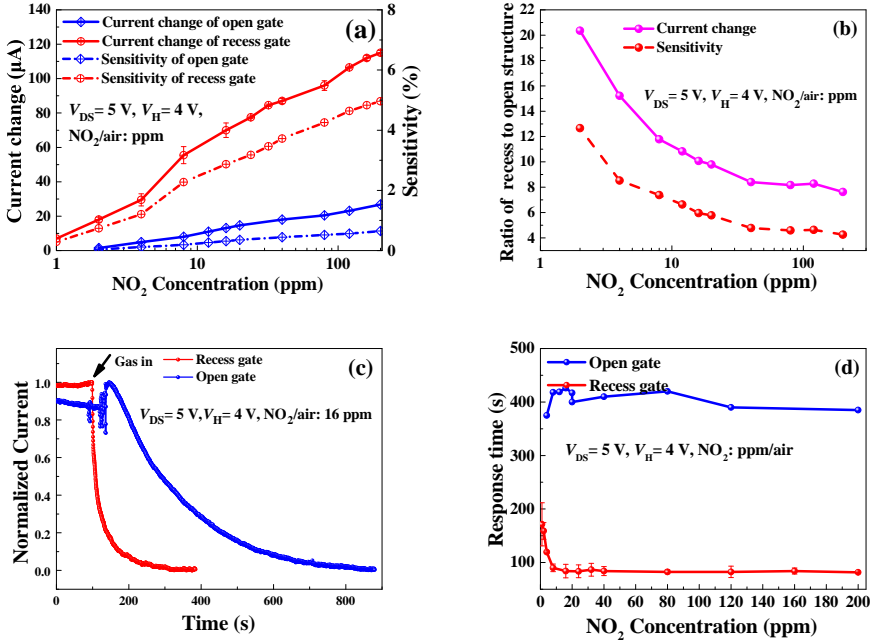


Figure 4.28: (a) Current change/sensitivity and (b) corresponding ratio of the sensor with recess gate and open gate structure toward 1-200 ppm NO<sub>2</sub>/air gas. (c) Normalized drain current response of the sensor with open gate and recess gate toward 16 ppm NO<sub>2</sub>/air gas. (d) Response time of the sensor with open gate and recess gate. During the measurement the  $V_{DS} = 5 \text{ V}$  and  $V_H = 4 \text{ V}$ .

attributed to faster gas molecule adsorption rate at the surface at higher temperature [18, 73]. The recovery time is almost constant when the micro-heater voltage increases from 1 V to 3 V. However, it is greatly reduced down to 200 s when the temperature is up to 300 °C ( $V_H = 4 \text{ V}$ ). The sensitivity (response time) increases from 0.75 % (1250 s) to 3.5 % (75 s) to 40 ppm NO<sub>2</sub>/air when temperature increases from 60 °C to 300 °C.

The repeatability and selectivity of the sensor measured at  $V_H = 4 \text{ V}$  are shown in Figure 4.31. The drain current response when the NO<sub>2</sub> gas concentration is swept repeatedly from 0 to 20 ppm is demonstrated in Figure 4.31(a). Figure 4.31(b) presents the cross-sensitivity performance of the AlGaIn/GaN sensor to other gases such as ammonia, ethanol, acetone, CH<sub>4</sub> and CO in air at  $V_H = 4 \text{ V}$ .

#### 4.4. CHAPTER SUMMARY

In this chapter, nano-film WO<sub>3</sub> gate AlGaIn/GaN HEMT sensors with an integrated micro-heater on suspended membrane have been microfabricated and characterized. The combined effect of micro-heater heating and self-heating on membrane has been studied for the first time. Significant detection is observed under a low concentration of 100 ppb NO<sub>2</sub>/N<sub>2</sub> at 300 °C. As exposed to a 1 ppm NO<sub>2</sub> gas, a high sensing sensitivity of 1.1 % with a response (recovery) time of 88 second (132 second) is obtained. The perfor-

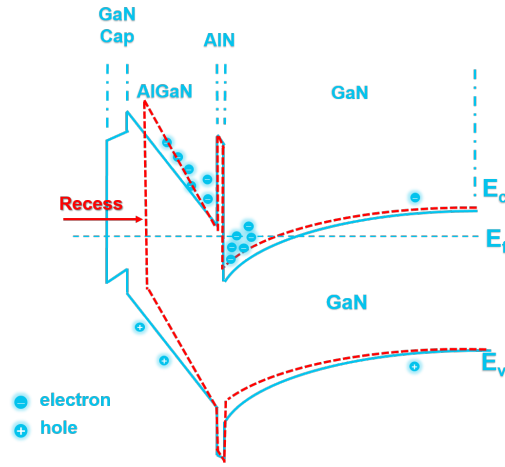


Figure 4.29: Band energy diagram of AlGaN/GaN heterostructure before and after gate recess.

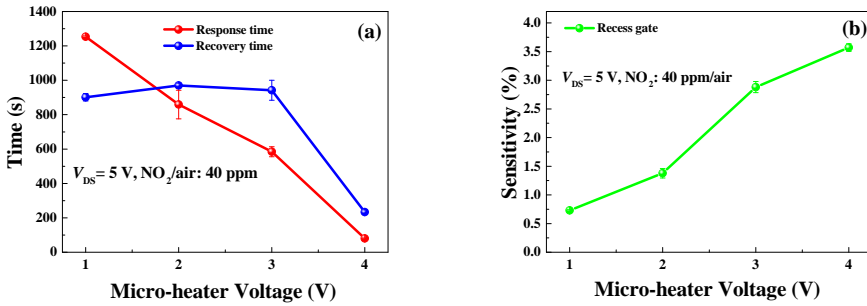


Figure 4.30: Response time, recovery time and sensitivity of the AlGaN/GaN heterostructure gas sensor with gate-recess as a function of micro-heater voltage toward 40 ppm  $\text{NO}_2$  gas.

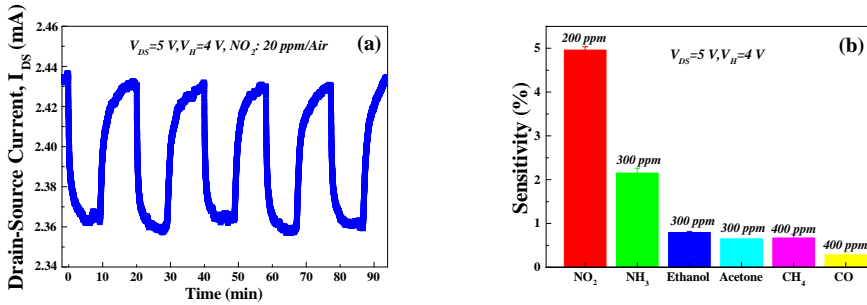


Figure 4.31: (a) Repeatability of sensor to 20 ppm/Air  $\text{NO}_2$  at 300 °C and (b) Gas response to ammonia, ethanol, acetone, methane and CO at 300 °C.

mance including limitation of detection (LOD), sensitivity and response time of sensor were improved compared to that of devices without the  $\text{WO}_3$  nanolayer. Afterwards, the  $\text{WO}_3/\text{AlGaIn}/\text{GaIn}$  chip was packaged into CQFN package. Then, ppm level acetone gas response of packaged sensor was also presented and studied, which is opposite direction to that of  $\text{NO}_2$  gas. The temperature of the sensor can be adjusted by the integrated micro-heater and the membrane structure was designed for operation at high temperature and low power. At  $300^\circ\text{C}$ , a drain current change  $\Delta I_{DS}$  of 0.31 mA as well as a high sensitivity of 25.7 % for 1000 ppm acetone were observed. Transient measurements indicated stable operation and good repeatability at different temperatures. For 1000 ppm acetone concentration  $t_{Res}(t_{Rec})$  reduced from 147 (656) s at  $V_H = 3.5\text{ V}$  ( $210^\circ\text{C}$ ) to 48 (319) s at  $V_H = 4\text{ V}$  ( $300^\circ\text{C}$ ). Moreover, the response to 1000 ppm acetone gas was significantly larger than for ethanol, ammonia and CO gases at the same 1000 ppm concentration. sensor response is not altered in high relative humidity conditions, while the temperature influence needs to be considered and avoided. Based on the excellent sensing performance and inherent advantages of low power consumption, the HEMT sensor combined nano-film  $\text{WO}_3$  functional gate and micro-heater provides an attractive alternative for high performance in industrial and medical applications.

Finally, based on the proposed accurate two-step gate recess technique, a suspended gate recess Pt/AlGaIn/GaIn heterostructure  $\text{NO}_2$  gas sensor integrated with a micro-heater was fabricated and characterized. This gate recess technique dramatically enhances the performance of AlGaIn/GaIn devices. The sensitivity and current change of AlGaIn/GaIn heterostructure to 1-200 ppm  $\text{NO}_2/\text{air}$  are increased up 20 times and 12 times compared to conventional gate device respectively with faster response time. The suspended membrane structure and integrated micro-hotplate also improve response time and sensitivity by adjusting the optimum working temperature with low power consumption. The sensitivity (response time) increases from 0.75 % (1250 s) to 3.5 % (75 s) toward 40 ppm  $\text{NO}_2/\text{air}$  when temperature increases from  $60^\circ\text{C}$  to  $300^\circ\text{C}$ . The repeatability and selectivity of sensor are also demonstrated. The characteristics of the here presented suspended gate-recess AlGaIn/GaIn devices integrated with a micro-heater, form an encouraging first step towards the development of a high accuracy and fast response gas sensor.

## REFERENCES

- [1] S. Das and V. Jayaraman, "SnO<sub>2</sub>: A comprehensive review on structures and gas sensors," *Progress in Materials Science*, vol. 66, pp. 112-255, 2014.
- [2] T. Waitz, T. Wagner, T. Sauerwald, C. D. Kohl, and M. Tiemann, "Ordered mesoporous In<sub>2</sub>O<sub>3</sub>: synthesis by structure replication and application as a methane gas sensor," *Advanced Functional Materials*, vol. 19, no. 4, pp. 653-661, 2009.
- [3] X.-L. Li, T.-J. Lou, X.-M. Sun, and Y.-D. Li, "Highly sensitive WO<sub>3</sub> hollow-sphere gas sensors," *Inorganic chemistry*, vol. 43, no. 17, pp. 5442-5449, 2004.
- [4] D. Briand, B. van der Schoot, N. F. de Rooij, H. Sundgren, and I. Lundstrom, "A low-power micromachined MOSFET gas sensor," *Journal of microelectromechanical systems*, vol. 9, no. 3, pp. 303-308, 2000.

- [5] C.-H. Kim, I.-T. Cho, J.-M. Shin, K.-B. Choi, J.-K. Lee, and J.-H. Lee, "A new gas sensor based on MOSFET having a horizontal floating-gate," *IEEE Electron Device Letters*, vol. 35, no. 2, pp. 265-267, 2013.
- [6] Y. Hong et al., "Highly selective ZnO gas sensor based on MOSFET having a horizontal floating-gate," *Sensors and Actuators B: Chemical*, vol. 232, pp. 653-659, 2016.
- [7] O. Ambacher et al., "Two-dimensional electron gases induced by spontaneous and piezoelectric polarization charges in N- and Ga-face AlGaIn/GaN heterostructures," *Journal of Applied Physics*, vol. 85, no. 6, pp. 3222-3233, 1999.
- [8] V. Tilak, K. Matocha, and P. Sandvik, "Pt/GaN Schottky diodes for harsh environment NO sensing applications," *physica status solidi (c)*, vol. 2, no. 7, pp. 2555-2558, 2005.
- [9] T. Y. Chen et al., "Ammonia Sensing Properties of a Pt/AlGaIn/GaN Schottky Diode," *IEEE Transactions on Electron Devices*, vol. 58, no. 5, pp. 1541-1547, 2011.
- [10] P.-C. Chou et al., "Study of an electroless plating (EP)-based Pt/AlGaIn/GaN Schottky diode-type ammonia sensor," *Sensors and Actuators B: Chemical*, vol. 203, pp. 258-262, 2014.
- [11] J. Schalwig, G. Muller, M. Eickhoff, O. Ambacher, and M. Stutzmann, "Group III-nitride-based gas sensors for combustion monitoring," (in English), *Materials Science and Engineering B-Solid State Materials for Advanced Technology*, vol. 93, no. 1-3, pp. 207-214, May 30 2002.
- [12] S. Jang, P. Son, J. Kim, S.-N. Lee, and K. H. Baik, "Hydrogen sensitive Schottky diode using semipolar (112̄ 2) AlGaIn/GaN heterostructures," *Sensors and Actuators B: Chemical*, vol. 222, pp. 43-47, 2016.
- [13] S. Das, S. Majumdar, R. Kumar, S. Ghosh, and D. Biswas, "Thermodynamic analysis of acetone sensing in Pd/AlGaIn/GaN heterostructure Schottky diodes at low temperatures," *Scripta Materialia*, vol. 113, pp. 39-42, 2016.
- [14] S. C. Hung, C. W. Chen, C. Y. Shieh, G. C. Chi, R. Fan, and S. J. Pearton, "High sensitivity carbon monoxide sensors made by zinc oxide modified gated GaN/AlGaIn high electron mobility transistors under room temperature," *Applied Physics Letters*, vol. 98, no. 22, 2011.
- [15] C.-F. Lo et al., "Carbon monoxide detection sensitivity of ZnO nanorod-gated AlGaIn/GaN high electron mobility transistors in different temperature environments," *Journal of Vacuum Science & Technology B, Nanotechnology and Microelectronics: Materials, Processing, Measurement, and Phenomena*, vol. 30, no. 1, 2012.
- [16] S. C. Hung, W. Y. Woon, S. M. Lan, F. Ren, and S. J. Pearton, "Characteristics of carbon monoxide sensors made by polar and nonpolar zinc oxide nanowires gated AlGaIn/GaN high electron mobility transistor," *Applied Physics Letters*, vol. 103, no. 8, 2013.

- [17] Y. Halfaya et al., "Investigation of the Performance of HEMT-Based NO, NO(2) and NH(3) Exhaust Gas Sensors for Automotive Antipollution Systems," *Sensors (Basel)*, vol. 16, no. 3, p. 273, Feb 23 2016.
- [18] C. Bishop et al., "Experimental Study and Device Design of NO, NO<sub>2</sub>, and NH<sub>3</sub> Gas Detection for a Wide Dynamic and Large Temperature Range Using Pt/AlGa<sub>N</sub>/Ga<sub>N</sub> HEMT," *IEEE Sensors Journal*, vol. 16, no. 18, pp. 6828-6838, 2016.
- [19] P. Offermans and R. Vitushinsky, "NO<sub>2</sub> Detection With AlGa<sub>N</sub>/Ga<sub>N</sub> 2DEG Channels for Air Quality Monitoring," *IEEE Sensors Journal*, vol. 13, no. 8, pp. 2823-2827, 2013.
- [20] P. Offermans, R. Vitushinsky, M. Crego-Calama, and S. H. Brongersma, "Ultra-Sensitive NO<sub>2</sub> Detection with AlGa<sub>N</sub>/Ga<sub>N</sub> 2DEG Channels for Air Quality Monitoring," (in English), 2012 *Ieee Sensors Proceedings*, pp. 905-907, 2012.
- [21] T.-Y. Chen et al., "On an Ammonia Gas Sensor Based on a Pt/AlGa<sub>N</sub> Heterostructure Field-Effect Transistor," *IEEE Electron Device Letters*, vol. 33, no. 4, pp. 612-614, 2012.
- [22] Y. Y. Xi et al., "Methane detection using Pt-gated AlGa<sub>N</sub>/Ga<sub>N</sub> high electron mobility transistor based Schottky diodes," (in English), *Journal of Vacuum Science & Technology B*, vol. 31, no. 3, p. 032203, May 2013.
- [23] R. Sokolovskij et al., "Hydrogen sulfide detection properties of Pt-gated AlGa<sub>N</sub>/Ga<sub>N</sub> HEMT-sensor," *Sensors and Actuators B: Chemical*, vol. 274, pp. 636-644, 2018.
- [24] R. Sokolovskij et al., "Pt-AlGa<sub>N</sub>/Ga<sub>N</sub> HEMT-Sensor for Hydrogen Sulfide (H<sub>2</sub>S) Detection," in *Multidisciplinary Digital Publishing Institute Proceedings*, 2017, vol. 1, no. 4, p. 463.
- [25] N. Kornilios, N. Chaniotakis, and G. Konstandinidis, "Gallium Nitride-Based Chemical Sensors."
- [26] M. S. Abidin, A. M. Hashim, M. E. Sharifabad, S. F. Rahman, and T. Sadoh, "Open-gated pH sensor fabricated on an undoped-AlGa<sub>N</sub>/Ga<sub>N</sub> HEMT structure," *Sensors (Basel)*, vol. 11, no. 3, pp. 3067-77, 2011.
- [27] C.-T. Lee and Y.-S. Chiu, "Gate-recessed AlGa<sub>N</sub>/Ga<sub>N</sub> ISFET urea biosensor fabricated by photoelectrochemical method," *IEEE Sensors Journal*, vol. 16, no. 6, pp. 1518-1523, 2016.
- [28] B. H. Chu et al., "Aluminum gallium nitride (Ga<sub>N</sub>)/Ga<sub>N</sub> high electron mobility transistor-based sensors for glucose detection in exhaled breath condensate," *J Diabetes Sci Technol*, vol. 4, no. 1, pp. 171-9, Jan 01 2010.
- [29] B.-H. Chu et al., "Chloride ion detection by In<sub>N</sub> gated AlGa<sub>N</sub>/Ga<sub>N</sub> high electron mobility transistors," *Journal of Vacuum Science & Technology B, Nanotechnology and Microelectronics: Materials, Processing, Measurement, and Phenomena*, vol. 28, no. 1, pp. L5-L8, 2010.

- [30] J. Cheng et al., "Ultrasensitive detection of Hg<sup>2+</sup> using oligonucleotide-functionalized AlGa<sub>N</sub>/Ga<sub>N</sub> high electron mobility transistor," *Applied Physics Letters*, vol. 105, no. 8, 2014.
- [31] N. Espinosa, S. U. Schwarz, V. Cimalla, and O. Ambacher, "Detection of different target-DNA concentrations with highly sensitive AlGa<sub>N</sub>/Ga<sub>N</sub> high electron mobility transistors," *Sensors and Actuators B: Chemical*, vol. 210, pp. 633-639, 2015.
- [32] Zhu L, Zeng W. Room-temperature gas sensing of ZnO-based gas sensor: A review[J]. *Sensors and Actuators A: Physical*, 2017, 267: 242-261.
- [33] Yang S, Liu Y, Chen W, et al. High sensitivity and good selectivity of ultralong MoO<sub>3</sub> nanobelts for trimethylamine gas[J]. *Sensors and Actuators B: Chemical*, 2016, 226: 478-485.
- [34] Walker J M, Akbar S A, Morris P A. Synergistic effects in gas sensing semiconducting oxide nano-heterostructures: A review[J]. *Sensors and Actuators B: Chemical*, 2019, 286: 624-640.
- [35] W. Saito, Y. Takada, M. Kuraguchi, K. Tsuda, and I. Omura, "Recessed-gate structure approach toward normally off high-voltage AlGa<sub>N</sub>/Ga<sub>N</sub> HEMT for power electronics applications," *IEEE Transactions on electron devices*, vol. 53, no. 2, pp. 356-362, 2006.
- [36] H.-S. Lee, D. S. Lee, and T. Palacios, "AlGa<sub>N</sub>/Ga<sub>N</sub> high-electron-mobility transistors fabricated through a Au-free technology," *IEEE Electron Device Letters*, vol. 32, no. 5, pp. 623-625, 2011.
- [37] J. Zhang et al., "Mechanism of Ti/Al/Ti/W Au-free ohmic contacts to AlGa<sub>N</sub>/Ga<sub>N</sub> heterostructures via pre-ohmic recess etching and low temperature annealing," *Applied Physics Letters*, vol. 107, no. 26, p. 262109, 2015.
- [38] R. Vitushinsky, M. Crego-Calama, S. H. Brongersma, and P. Offermans, "Enhanced detection of NO<sub>2</sub> with recessed AlGa<sub>N</sub>/Ga<sub>N</sub> open gate structures," *Applied Physics Letters*, vol. 102, no. 17, 2013.
- [39] Z. Xu et al., "Demonstration of normally-off recess-gated AlGa<sub>N</sub>/Ga<sub>N</sub> MOSFET using Ga<sub>N</sub> cap layer as recess mask," *IEEE Electron Device Letters*, vol. 35, no. 12, pp. 1197-1199, 2014.
- [40] Y. Wang et al., "High-Performance Normally-Off Al<sub>2</sub>O<sub>3</sub>/Ga<sub>N</sub> MOSFET Using a Wet Etching-Based Gate Recess Technique," *IEEE Electron Device Letters*, vol. 34, no. 11, pp. 1370-1372, 2013.
- [41] R. Sokolovskij et al., "Precision Recess of AlGa<sub>N</sub>/Ga<sub>N</sub> with Controllable Etching Rate Using ICP-RIE Oxidation and Wet Etching," *Procedia Engineering*, vol. 168, pp. 1094-1097, 2016.

- [42] P. Offermans, R. Vitushinsky, M. Crego-Calama, and S. H. Brongersma, "Gas Sensing with AlGa<sub>N</sub>/Ga<sub>N</sub> 2DEG Channels," *Procedia Engineering*, vol. 25, pp. 1417-1420, 2011.
- [43] J. Lee et al., "Low power consumption solid electrochemical-type micro CO<sub>2</sub> gas sensor," *Sensors and Actuators B: Chemical*, vol. 248, pp. 957-960, 2017.
- [44] M. A. Chougule, S. Sen, and V. B. Patil, "Fabrication of nanostructured ZnO thin film sensor for NO<sub>2</sub> monitoring," *Ceramics International*, vol. 38, no. 4, pp. 2685-2692, 2012.
- [45] B. Urasinska-Wojcik, T. A. Vincent, M. F. Chowdhury, and J. W. Gardner, "Ultrasensitive WO<sub>3</sub> gas sensors for NO<sub>2</sub> detection in air and low oxygen environment," *Sensors and Actuators B: Chemical*, vol. 239, pp. 1051-1059, 2017.
- [46] S. Park, H. Ko, S. Kim, and C. Lee, "Gas sensing properties of multiple networked Ga<sub>N</sub>/WO<sub>3</sub> core-shell nanowire sensors," *Ceramics International*, vol. 40, no. 6, pp. 8305-8310, 2014.
- [47] X. Liu, J. Hu, B. Cheng, H. Qin, and M. Jiang, "Acetone gas sensing properties of SmFe<sub>1-x</sub>Mg<sub>x</sub>O<sub>3</sub> perovskite oxides," *Sensors and Actuators B: Chemical*, vol. 134, no. 2, pp. 483-487, 2008/09/25/ 2008.
- [48] T. E. Kiehn, E. M. Bernard, J. Gold, and D. Armstrong, "Candidiasis: detection by gas-liquid chromatography of D-arabinitol, a fungal metabolite, in human serum," *Science*, vol. 206, no. 4418, pp. 577-580, 1979.
- [49] S. M. Hicks and A. J. Killard, "Electrochemical impedance characterisation of tungsten trioxide-polyaniline nanocomposites for room temperature acetone sensing," *Sensors and Actuators B: Chemical*, vol. 194, pp. 283-289, 2014.
- [50] L. Ciaffoni et al., "Demonstration of a mid-infrared cavity enhanced absorption spectrometer for breath acetone detection," *Analytical chemistry*, vol. 85, no. 2, pp. 846-850, 2012.
- [51] S. B. Khan, M. Faisal, M. M. Rahman, and A. Jamal, "Low-temperature growth of ZnO nanoparticles: photocatalyst and acetone sensor," *Talanta*, vol. 85, no. 2, pp. 943-949, 2011.
- [52] P. Sahay, "Zinc oxide thin film gas sensor for detection of acetone," *Journal of Materials Science*, vol. 40, no. 16, pp. 4383-4385, 2005.
- [53] Y. Zeng et al., "Growth and selective acetone detection based on ZnO nanorod arrays," *Sensors and Actuators B: Chemical*, vol. 143, no. 1, pp. 93-98, 2009.
- [54] L. Qin et al., "The template-free synthesis of square-shaped SnO<sub>2</sub> nanowires: the temperature effect and acetone gas sensors," *Nanotechnology*, vol. 19, no. 18, p. 185705, 2008.

- [55] S. F. Bamsaoud, S. Rane, R. Karekar, and R. Aiyer, "Nano particulate SnO<sub>2</sub> based resistive films as a hydrogen and acetone vapour sensor," *Sensors and Actuators B: Chemical*, vol. 153, no. 2, pp. 382-391, 2011.
- [56] S.-J. Choi, B.-H. Jang, S.-J. Lee, B. K. Min, A. Rothschild, and I.-D. Kim, "Selective detection of acetone and hydrogen sulfide for the diagnosis of diabetes and halitosis using SnO<sub>2</sub> nanofibers functionalized with reduced graphene oxide nanosheets," *ACS applied materials & interfaces*, vol. 6, no. 4, pp. 2588-2597, 2014.
- [57] M. Righettoni, A. Tricoli, and S. E. Pratsinis, "Si: WO<sub>3</sub> sensors for highly selective detection of acetone for easy diagnosis of diabetes by breath analysis," *Analytical chemistry*, vol. 82, no. 9, pp. 3581-3587, 2010.
- [58] L. Wang, A. Teleki, S. E. Pratsinis, and P. Gouma, "Ferroelectric WO<sub>3</sub> nanoparticles for acetone selective detection," *Chemistry of Materials*, vol. 20, no. 15, pp. 4794-4796, 2008.
- [59] S.-J. Choi et al., "Selective diagnosis of diabetes using Pt-functionalized WO<sub>3</sub> hemi-tube networks as a sensing layer of acetone in exhaled breath," *Analytical chemistry*, vol. 85, no. 3, pp. 1792-1796, 2013.
- [60] C. Wang et al., "Ultrasensitive and low detection limit of acetone gas sensor based on W-doped NiO hierarchical nanostructure," *Sensors and Actuators B: Chemical*, vol. 220, pp. 59-67, 2015.
- [61] Y. Lu et al., "Synthesis of cactus-like NiO nanostructure and their gas-sensing properties," *Materials Letters*, vol. 164, pp. 48-51, 2016.
- [62] L. Wang, T. Fei, Z. Lou, and T. Zhang, "Three-dimensional hierarchical flowerlike  $\alpha$ -Fe<sub>2</sub>O<sub>3</sub> nanostructures: synthesis and ethanol-sensing properties," *ACS applied materials & interfaces*, vol. 3, no. 12, pp. 4689-4694, 2011.
- [63] C. Zhu, Y. Chen, R. Wang, L. Wang, M. Cao, and X. Shi, "Synthesis and enhanced ethanol sensing properties of  $\alpha$ -Fe<sub>2</sub>O<sub>3</sub>/ZnO heteronanostructures," *Sensors and Actuators B: Chemical*, vol. 140, no. 1, pp. 185-189, 2009.
- [64] L. Wang, Z. Lou, J. Deng, R. Zhang, and T. Zhang, "Ethanol gas detection using a yolk-shell (core-shell)  $\alpha$ -Fe<sub>2</sub>O<sub>3</sub> nanospheres as sensing material," *ACS applied materials & interfaces*, vol. 7, no. 23, pp. 13098-13104, 2015.
- [65] A. Mirzaei, K. Janghorban, B. Hashemi, M. Bonyani, S. Leonardi, and G. Neri, "Highly stable and selective ethanol sensor based on  $\alpha$ -Fe<sub>2</sub>O<sub>3</sub> nanoparticles prepared by Pechini sol-gel method," *Ceramics International*, vol. 42, no. 5, pp. 6136-6144, 2016.
- [66] G. Eranna, *Metal oxide nanostructures as gas sensing devices*. CRC Press, 2016.
- [67] S. Das, S. Ghosh, R. Kumar, A. Bag, and D. Biswas, "Highly sensitive acetone sensor based on Pd/AlGaN/GaN resistive device grown by plasma-assisted molecular beam epitaxy," *IEEE Transactions on Electron Devices*, vol. 64, no. 11, pp. 4650-4656, 2017.

- [68] S. Das, A. Bag, R. Kumar, and D. Biswas, "Fast response (7.6 s) acetone sensing by InGaN/GaN on Si (111) at 373 K," *IEEE Electron Device Letters*, vol. 38, no. 3, pp. 383-386, 2017.
- [69] J. Schalwig, G. Müller, M. Eickhoff, O. Ambacher, and M. Stutzmann, "Gas sensitive GaN/AlGaN-heterostructures," *Sensors and Actuators B: Chemical*, vol. 87, no. 3, pp. 425-430, 2002.
- [70] Z. Zhang, L. Zhu, Z. Wen, and Z. Ye, "Controllable synthesis of Co<sub>3</sub>O<sub>4</sub> crossed nanosheet arrays toward an acetone gas sensor," *Sensors and Actuators B: Chemical*, vol. 238, pp. 1052-1059, 2017.
- [71] B. Bhowmik, H.-J. Fecht, and P. Bhattacharyya, "Vertical mode gas sensing performance of TiO<sub>2</sub> nanotube array by tuning of surface area and carrier transport length," *IEEE Sensors Journal*, vol. 15, no. 10, pp. 5919-5926, 2015.
- [72] M. Higashiwaki, S. Chowdhury, M.-S. Miao, B. L. Swenson, C. G. Van de Walle, and U. K. Mishra, "Distribution of donor states on etched surface of AlGaIn/GaN heterostructures," *Journal of Applied Physics*, vol. 108, no. 6, p. 063719, 2010.
- [73] Y. Cai, Y. Zhou, K. M. Lau, and K. J. Chen, "Control of Threshold Voltage of AlGaIn/GaN HEMTs by Fluoride-Based Plasma Treatment: From Depletion Mode to Enhancement Mode," *IEEE Transactions on Electron Devices*, vol. 53, no. 9, pp. 2207-2215, 2006.
- [74] N. Goyal, B. Iñiguez, and T. A. Fjeldly, "Analytical modeling of bare surface barrier height and charge density in AlGaIn/GaN heterostructures," *Applied Physics Letters*, vol. 101, no. 10, p. 103505, 2012.
- [75] S. Heikman, S. Keller, Y. Wu, J. S. Speck, S. P. DenBaars, and U. K. Mishra, "Polarization effects in AlGaIn/GaN and GaN/AlGaIn/GaN heterostructures," *Journal of applied physics*, vol. 93, no. 12, pp. 10114-10118, 2003.
- [76] J. Sun et al., "Characterization of an Acetone Detector Based on a Suspended WO<sub>3</sub>-Gate AlGaIn/GaN HEMT Integrated With Microheater," *IEEE Transactions on Electron Devices*, vol. 66, no. 10, pp. 4373-4379, 2019.

# 5

## ALGAN/GAN HETEROSTRUCTURES DEEP ULTRAVIOLET DETECTORS

*This chapter is based on:*

Sun, J., Zhan, T., Liu, Z., Wang, J., Yi, X., Sarro, P. M. and Zhang, G. (2019). *Suspended tungsten trioxide (WO<sub>3</sub>) gate AlGaIn/GaN heterostructure deep ultraviolet detectors with integrated micro-heater. Optics Express, 27(25), 36405-36413.*

Sun, J., Zhan, T., Liu, Z., Wang, J., Yi, X., Sarro, P. M. and Zhang, G. (2019). *Suppression of persistent photoconductivity AlGaIn/GaN heterostructure photodetectors using pulsed heating. Applied Physics Express, 12(12), 122007.*

Sun, J., Zhang, S., Zhan, T., Liu, Z., Wang, J., Yi, X., Li, J., Sarro, P. M. and Zhang, G. (2020). *A high responsivity and controllable recovery ultraviolet detector based on a WO<sub>3</sub> gate AlGaIn/GaN heterostructure with an integrated micro-heater[J]. Journal of Materials Chemistry C, 2020, 8(16): 5409-5416.*

## 5.1. INTRODUCTION

THE ultraviolet (UV) spectral region is commonly classified by electromagnetic radiation with a wavelength ( $\lambda$ ) range from 100 nm to 400 nm. and it can be divided into three spectral bands: UVA (320-400 nm), UVB (280-320 nm) and UVC (200-280 nm). Levels of ozone around the earth block different bands of ultraviolet radiation. UVA is hardly affected by ozone and most of it reaches the surface of the earth. However, UVC is strongly absorbed by the ozone layer and atmosphere, and UVB is also mostly absorbed by the ozone layer. Solar-blind region irradiation is almost non-existent in the atmosphere near the ground. Thus, UV photodetectors that respond in this region are called solar-blind photodetectors. Hence, solar-blind photodetectors have special applications including fire sensing [1], missile and rocket warning [2], non-line-of sight optical communication [3], ozone monitoring, and so on [4–7].

After a century technology development, UV photodetectors with unique features such as high stability, high sensitivity, high speed, high signal-to-noise ratio are mostly bulky, fragile and require high bias voltages. [8] As the demand for these detectors and expectation on their performance are continuously rising, conventional UV photodetectors are not sufficient anymore. Device with multiple functions and more compact and smart are in high demand for several applications. More compact and smart UV photodetectors are urgently needed in future.

Solid state detectors based on wide band gap semiconductors have attracted lots of attentions for UV detection, as semiconductor materials with band gaps larger than that of silicon need higher photon energy to create an electron-hole pair if there is no impurity or defect. The minimum photon energy is equal to the energy of the band gap between the valence and the conduction bands of semiconductors. The band gap of materials should be about 3.1 eV (400 nm) if the photodetectors need visible blind detection. The wideband materials of interest are GaN (3.4 eV), AlN[5], ZnO [9, 10], WO<sub>3</sub> [11–15], Ga<sub>2</sub>O<sub>3</sub> [16–18], Ta<sub>2</sub>O<sub>5</sub> [19], and combined layers as, for example, Al<sub>x</sub>Ga<sub>1-x</sub>N [20, 21].

In recent years, valuable process has been made in GaN based UV light detectors [22, 23]. GaN is particularly suitable for UV light detection due to its direct wide band gap and robust nature. GaN PIN diodes [24, 25], Schottky diodes[26] and metal semiconductor metal (MSM) [27–29]based photo detectors have been demonstrated by various researches. In contrast to silicon-based UV photo detectors, GaN offers improved performance at higher temperatures and it can be used in space applications because of higher radiation resistance. In comparison with other UV detectors based on photo conductors, AlGaN/GaN heterostructure based detectors can offer high gain thanks to the very high conductive 2DEG channel at the heterostructure interface. By changing the mole fraction of AlGaN layer, the cut-off wavelength can be tuned from 200-365 nm to suit special requirements. The inherent advantage of using AlGaN/GaN HEMT as a UV detector is a high response, high sensitivity, integration with the now mature HEMT technology.

An AlGaN/GaN HEMT based UV detector was first reported by Khan [30] with a maximum responsivity of 3000 A/W. In recent years, responsivity values of  $\sim 10^7$  A/W have been demonstrated [31, 32]. It is found that a drain current change can be observed and the channel conductivity of AlGaN/GaN HEMTs increases under UV illumination. The mechanism of AlGaN/GaN HEMT UV detection has been reported by various research

groups. Several reports have considered light illumination changes the charge status of surface states and varies the conductivity of the 2DEG channel [33]. Some research consider that electrons trapped in the surface states are released which enhances the 2DEG concentration under UV illumination [34].

An ideal photodetector would exhibit a lower dark current to minimize the interference noise and a higher responsivity to maximize the photo signal. Currently, avalanche-type detector [35–37] can obtain high responsivity but at the expense of increased noise and highly rigorous requirements of structure and processing techniques. Another common approach to improve responsivity is to use the photoconductive type, which is easy to fabricate at lower cost and has a good commercial prospect. However, persistent photoconductivity (PPC) effect associated with a 2DEG in an AlGaIn/GaN HEMT devices has been observed [38–40]. As a result, the device was observed to be sensitive to light and the sensitivity was associated with a permanent photoinduced increase in the 2DEG carrier mobility and density. In addition, the recovery time of GaN-based optical devices is extremely long (hours to days) after the optical stimulus has been removed [40, 41], which makes it difficult to detect the change of light intensity at high frequency and to be suitable for applications which require reliable and consistent operation [21]. The possible reasons of PPC effect in AlGaIn/GaN heterostructures, which including metastable defects, gallium vacancy, and deep-level defects in epitaxial layers, have been discussed in some reports [41–43].

Many methods have been employed to reduce the PPC effect, such as infrared irradiation, electric field, pulsed voltage [44–48]. Besides these methods, a heating process has been reported to suppress the PPC effect of a GaN-based or Ga<sub>2</sub>O<sub>3</sub>-based detector recently. Hou et al. presented a special method for suppressing PPC effect in AlGaIn/GaN photodetector by applying in-situ heating [43]. Sun et al. proposed that pulsed heating can reduce 30–45 % in decay time of suspended AlGaIn/GaN heterostructure photodetector compared to DC heating mode [49]. However, both in-situ heating and pulsed heating can't suppress the PPC effect completely, the decay time is just reduced from days or several hours to hundred seconds. Zhou et al. demonstrated that “thermal relaxation” process can effectively reduce the recovery time of a-Ga<sub>2</sub>O<sub>3</sub> detector from hours to seconds [50]. But the thermal relaxation process required the detector to be placed on a hot plate for heating and then removed to a heat sink for cooling. These operations may make the detector unsuitable or unfeasible for practical application. Therefore, a simple, effective and universal method is urgently needed for a simple and easy fabrication photodetector with high responsivity and fast recovery.

The PPC effect can be reduced by elevated temperatures which accelerate the carrier capture rate [41–43]. The tolerable working temperature of GaN materials device is about 600 °C, which supports such working conditions. External power units can be used to achieve the suitable temperature. However, it is may not be feasible for some applications. Therefore, integrated heating unit is an alternative to mitigate the PPC effect.

In this chapter, we report on the suspended WO<sub>3</sub>-gate AlGaIn/GaN HEMT UV photodetectors integrated with micro-fabricated heater. The UV photodetector, including an AlGaIn/GaN HEMT membrane and micro-heater unit, was suspended for thermal isolation from the silicon substrate. The temperature of the membrane is modulated by the micro-heater unit based on Joule heating. The transient characteristics of photode-

detector at different temperatures and different source drain voltages are investigated. The photodetector shows a rapid response and recovery under deep UV illumination. The measurement spectral response of AlGaN/GaN HEMT shows the high response to solar-blind range. In order to suppress the PPC effect, three kinds of heating mode are studied, namely DC heating, pulse heating and mono-pulse heating reset (MHR).

## 5.2. DEEP UV ILLUMINATION OF ALGaN/GaN HETEROSTRUCTURE PHOTODETECTORS

### 5.2.1. FABRICATION OF PHOTODETECTORS

Figure 5.1 presents a cross-section schematic drawing of the AlGaN/GaN heterostructure photodetector. The AlGaN/GaN heterostructure photodetector is placed together with the microheater surrounding the active area on a suspended membrane. The contact pads are on the thick silicon frame. The AlGaN/GaN heterostructure was grown on a 2-inch silicon <111> 1 mm-thick wafers using Metal-organic Chemical Vapor Deposition (MOCVD). It consisted of a 2  $\mu\text{m}$ -thick undoped GaN buffer layer, followed by a 1 nm-thick AlN interlayer, an undoped 25 nm-thick  $\text{Al}_{0.26}\text{Ga}_{0.74}\text{N}$  barrier layer, and a 3 nm-thick GaN epitaxial cap layer. The electron mobility of 2DEG was  $1500 \text{ cm}^2 \text{ V}^{-1} \text{ s}^{-1}$ , with a sheet electron density of  $1 \times 10^{13} \text{ cm}^{-2}$ . The silicon substrate (400  $\mu\text{m}$ ) is back-side etched by deep reactive ion etching (DRIE) to form a circular membrane (650  $\mu\text{m}$  in diameter).

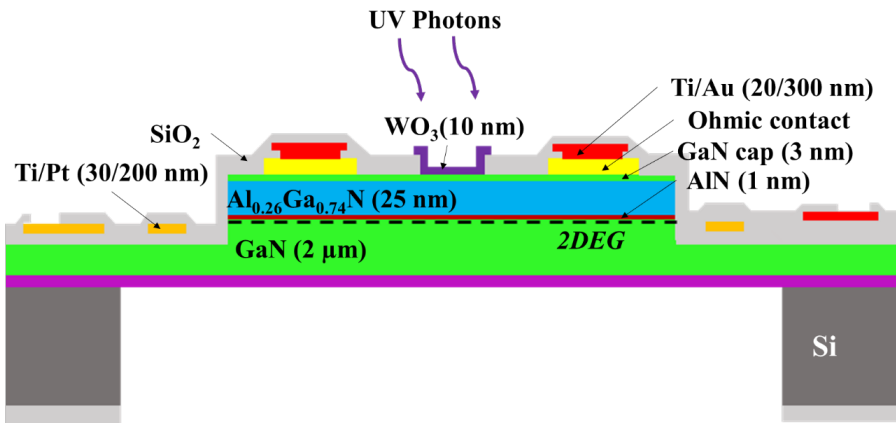


Figure 5.1: Schematic drawing of the cross-section of the AlGaN/GaN UV photodetector.

The fabrication process flow is the almost same as for the gas sensor refer to section 4.2.1 and mention here only what is difference. The ( $\text{WO}_3$ ) (10 nm) layer was deposited on the gate area of  $40 \mu\text{m} \times 40 \mu\text{m}$  by physical vapor deposition (PVD). The microheater has a rectangular geometry around a central area of  $230 \mu\text{m} \times 290 \mu\text{m}$ , as showed in Figure 5.2(a). Figure 5.2(b) shows the SEM images of the AlGaN/GaN device. The energy dispersive spectrum (EDS) of the device gate area surface is reported in Figure 5.2(c). The corresponding peaks of Ga, W, N, Al, O elements are observed. Clearly, the deposition of

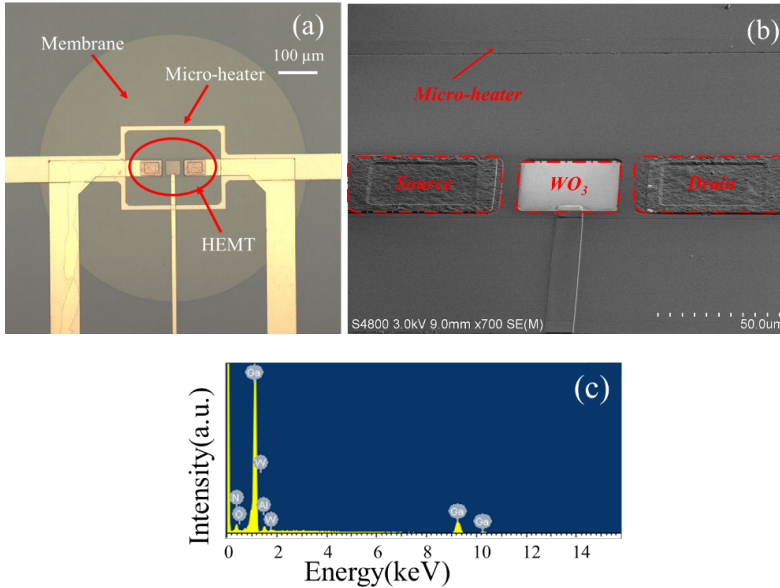


Figure 5.2: The fabricated AlGaN/GaN UV photodetector (a) Top optical micrograph; (b) SEM image of device structure; (c) EDS spectrum of gate surface of device.

WO<sub>3</sub> on the gate surface by magnetron sputtering is confirmed.

### 5.2.2. PHOTODETECTOR MEASUREMENTS

The micro-heater filament increases the temperature by Joule heating when the current passes the filament. To extract the membrane temperature a calibration of the membrane temperatures at various heating voltages is necessary. The surface temperature can be measured by infrared radiation (IR) thermal camera or extracted by the resistance change of the micro-heater at ambient temperature with the 4-wire testing method [51]. Figure 5.3 shows the measured maximum temperatures of the AlGaN/GaN heterostructure photodetector at different applied micro-heater voltages. An infrared camera (Bruker) was used to record the temperature profile of the chip heated at  $V_H=4$  V as shown in the inset of Figure 5.3. A uniform profile across the membrane was observed.

The spectral response of the AlGaN/GaN photodetectors was measured in a testing system (DSR200, Zolix Instrument CO., LTD, China) under the monochromatic light with wavelength from 200 to 400 nm at a drain-source voltage controlled by Keithley 2400 in air ambient at room temperature. The illuminating source is adopted by a 150 W Xenon lamp. The light source power measurements were calibrated using a Si detector. The schematic of spectral response measurement setup is shown in Figure 5.4.

### 5.2.3. RESULTS AND DISCUSSION

Figure 5.5 shows the equivalent mechanisms on an energy band diagram. When there is no bias applied between the electrodes of the device in the dark, the oxygen molecules

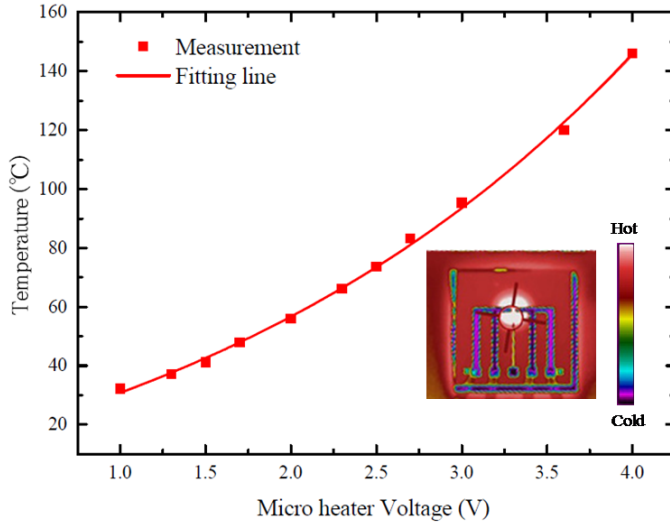


Figure 5.3: Measurement heating temperature at different applied voltages. The inset shows the temperature profile (infrared camera image) of the heated (4 V) AlGaIn/GaN photodetector.

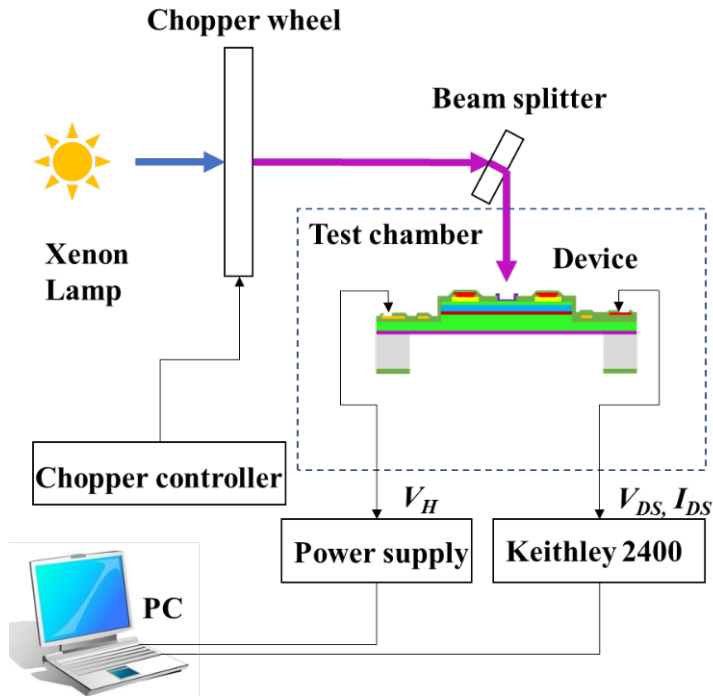


Figure 5.4: A schematic drawing of the spectral response measurement setup.

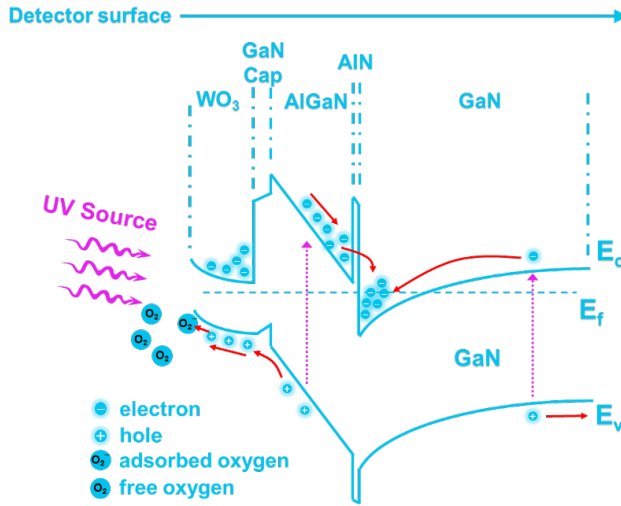


Figure 5.5:  $\text{WO}_3/\text{AlGaIn}/\text{GaN}$  heterostructure under UV illumination showing the electron-hole pairs generation and diffusion.

from the surrounding air absorb on the nanolayer ( $\text{WO}_3$ ), combining with electrons and creating a depletion sub-layer near the surface [ $\text{O}_2(\text{gas}) + e \rightarrow \text{O}_2^-(\text{adsorb})$ ], where  $\text{O}_2^-$  is the adsorbed oxygen ion on the  $\text{WO}_3$  surface. Under the UV illumination condition shown in the Figure 5.6, more electron-hole pairs are photogenerated inside the  $\text{WO}_3$ , and the generated holes travel towards the  $\text{WO}_3$  surface to recombine with the electrons trapped in  $\text{O}_2^-$  ions [ $h^+ + \text{O}_2^-(\text{adsorb}) \rightarrow \text{O}_2(\text{gas})$ ]. Then, the 2DEG population in the GaN channel layer of HEMT is enhanced and the drain current is enhanced under UV illumination, as shown in Figure 5.6.

The spectral response of  $\text{WO}_3/\text{AlGaIn}/\text{GaN}$  device shows the high response in the solar-blind range with wavelength of 210-280 nm, corresponding to the absorption area of the  $\text{WO}_3$  nanolayer [12]. The peak responsivity of a device with  $W/L=1$  was 4600 A/W at 0.5 V bias under 240 nm UVC illumination, which exceeds 100 % quantum efficiency due to the high gain of HEMT 2EDG structure. As shown in Figure 5.7, a transition is observed near the GaN cut-off wavelength at 360 nm. The spectral response at different temperatures are almost unchanged. A larger  $W/L$  ratio would lead to higher responsivity. The peak responsivity of the photodetector with  $W/L=2$  was 16700 A/W at 0.5 V bias under 240 nm illumination as shown in Figure 5.8. The excellent performance of our devices is a clear indication of the potential applicability this configuration has for deep ultraviolet photodetectors.

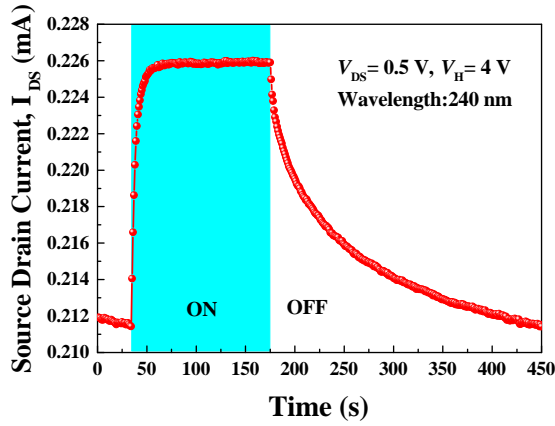


Figure 5.6: Transient photocurrent response of suspended AlGaN/GaN photodetector under 240 nm illumination at  $V_{DS} = 0.5V$  and  $V_H = 4V$ .

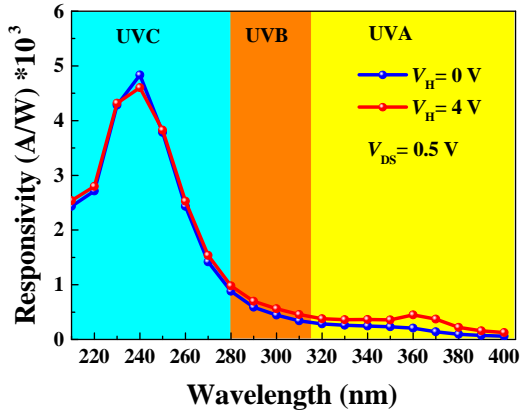


Figure 5.7: The measured spectral response of AlGaN/GaN HEMT photodetector at  $V_{DS} = 0.5 V$ ,  $V_H = 4 V$  ( $W/L=1$ ).

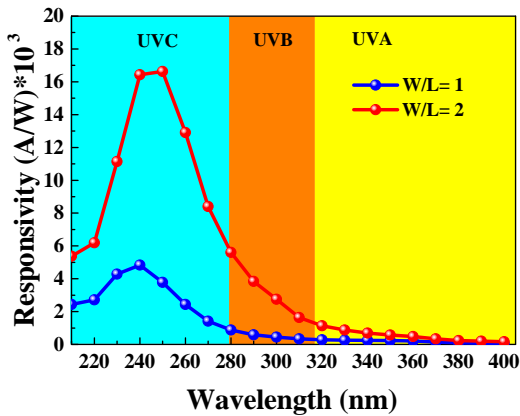


Figure 5.8: The measured spectral response of AlGaN/GaN HEMT photodetector at different  $W/L$  ratio.

### 5.3. SUPPRESSION OF PERSISTENT PHOTOCONDUCTIVITY (PPC) EFFECT OF ALGAN/GAN PHOTODETECTORS

#### 5.3.1. PERSISTENT PHOTOCONDUCTIVITY (PPC) EFFECT

Persistent photoconductivity (PPC) is a light induced change in the free carrier density that persists after the removal of illumination. PPC effect is observed in most n-type GaN and most of photoconductive metal oxide materials. This is the main drawback of such materials in terms of photoconductivity, which limits their use in many applications.

As shown in Figure 5.9, a PPC effect was also observed in our devices. After removal of illumination, the dark current can not come back to the initial dark current value. The long decay time make the photodetector unsuitable for detecting the change of light intensity at high frequency. In order to suppress or eliminate the PPC effect, three methods are investigated and the outcome is reported in the following sections.

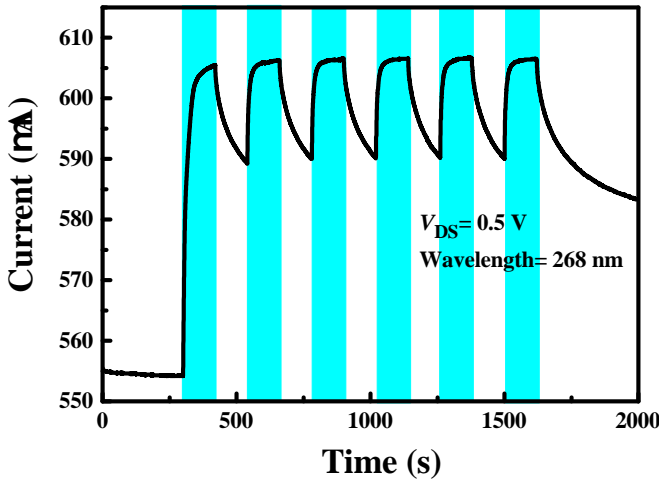


Figure 5.9: Transient photocurrent response of a suspended AlGaN/GaN photodetector under 268 nm illumination at  $V_{DS} = 0.5$  V and  $V_H = 0$  V. The blue area indicate the time of illumination.

#### 5.3.2. DC HEATING MODE

The transient photocurrent response and normalized transient drain current responses of the suspended AlGaN/GaN heterostructure detectors under 240 nm UVC light illumination, at various applied micro-heater voltages, are shown in Figure 5.10(a) and (b).

For the transient responses, the photo-to-dark-current ratio (PDCR) is defined as follows:

$$PDCR = (I_p - I_d) / I_d \tag{5.1}$$

where  $I_p$  is the photo current under illumination and  $I_d$  is the dark current. The PDCR calculated values were approximately 0.034, 0.04 and 0.07 when a micro-heater

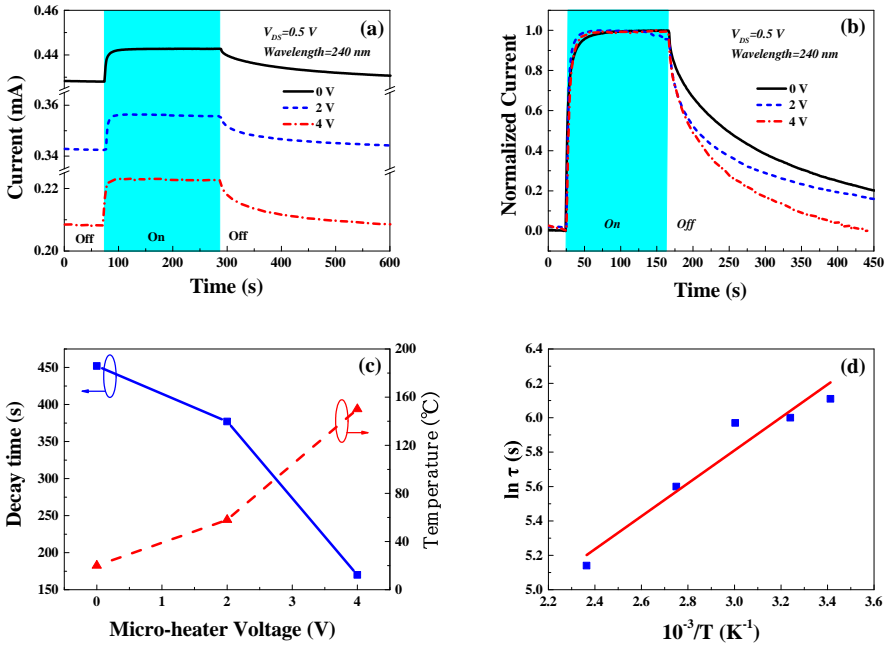


Figure 5.10: Transient photocurrent response (a) and Normalized transient photocurrent response (b) of suspended AlGaN/GaN photodetector at various applied micro-heater voltages ( $V_{micro-heater}=0$  V, 2 V, 4 V). Normalized photocurrent values: 0% is dark and 100% is maximum photocurrent under 240 nm illumination. The measured decay time and temperature of membrane at various micro-heater voltages are shown in (c). (d) Arrhenius plot of the PPC decay time constant at different temperatures.

voltage of 0 V, 2 V and 4 V was applied, respectively. The relatively low PDCR values measured in this study resulted from the low intensity of the Xenon lamp at wavelength of 240 nm ( $\sim 1.26$  mW/cm<sup>2</sup>) [43]. Another reason is the larger dark current due to the high source-drain current of AlGaN/GaN 2DEG HEMT structure compared to p-i-n and Schottky structure. The photodetector shows a rapid response (8.4 s) under illumination, but the photocurrent decay depends on the applied micro-heater voltages. The decay time of photodetector is defined as the time required for the photo current to change from 90 % to 10 % of its saturated response value. The Figure 5.10(c) shows the decay time decreases with increasing applied micro-heater voltages. The decay time is about 450 s at  $V_H=0$  V (temperature was about 20 °C), and is reduced to about 170 s when the photodetector is heated to approximately 150 °C at  $V_H=4$  V (280 mW). The decay time could be further reduced by increasing the micro-heater voltage (temperature) or a short time heating process (thermal relaxation)[50]. With the increasing temperature, electrons get more thermal energy, and the electron capture rate increases, reducing the decay times of the device [43]. The power and voltage of the heating unit can be further optimized by modifying the membrane size and layout.

Earlier research has proposed the following model to describe the temperature de-

pendency of the decay time constant ( $\tau$ ),

$$\tau = \tau_0 e^{(\Delta E/\kappa T)} \tag{5.2}$$

Where  $\tau_0$  is the high temperature limit of the time constant,  $\kappa$  is the Boltzmann constant,  $\Delta E$  is the capture barrier and  $T$  is the temperature. An electron capture energy  $\Delta E$  shown in Figure 5.10(d) of approximately 160 meV is calculated. The carrier capture barrier prevents the decay of photoexcited electrons. The carrier capture barrier has been proposed to originate from the non-overlapping vibronic states of unfilled and filled defects. Electrons in conduction band require additional energy to get into the vibronic states of filled defects in order to be captured. As electrons gain more thermal energy with rising temperature, the electron capture rate increases, and thus the decay times of the photodetectors are reduced.

### 5.3.3. PULSED HEATING MODE

In this section, we report the pulsed heating mode to reduce the PPC effect of suspended AlGaN/GaN heterostructure photodetectors. The transient characteristics of the photodetector versus voltage and frequency are studied. The transient response of the WO<sub>3</sub> gate AlGaN/GaN photodetectors was measured by Keithley 2400 during exposure of the detector to a radiation source emitting at 380 nm at a drain bias of 0.5 V, in air ambient, at room temperature. We have observed that the course of PPC was effectively accelerated by applying pulsed heating. The decay time is significantly reduced from 175 s by DC heating to 116 s by 50 Hz pulsed heating at the same power (280 mW). With the same pulse duty cycle and 50 Hz pulsed heating frequency, a reduction of 30-45 % in decay time is measured compared to DC heating.

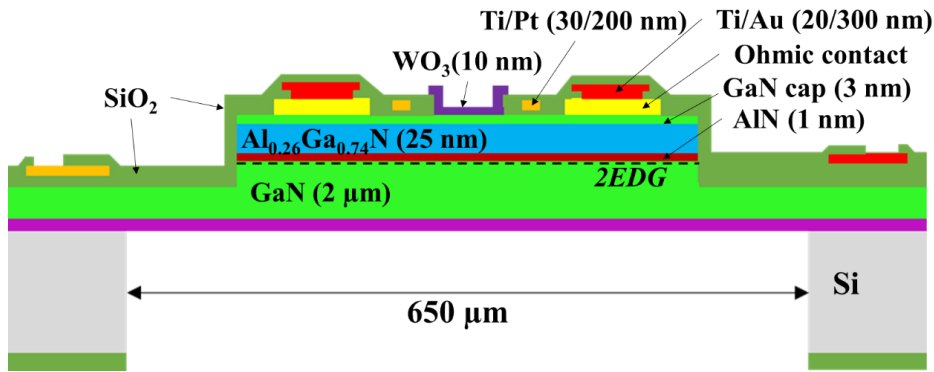


Figure 5.11: Schematic drawing of the cross-section of the AlGaN/GaN heterostructure UV photodetector and 2DEG structure.

Figure 5.11 schematically depicts the device cross-section and 2DEG structure. The photodetector is placed on a suspended membrane and a microheater across the gate area is integrated. The same epitaxial AlGaN/GaN structure for the gas sensor was used to fabricate the photodetector. The fabrication processes are same with that in this chap-

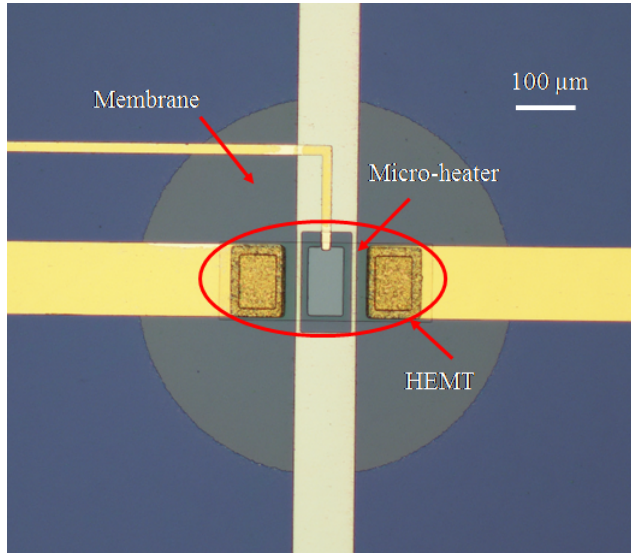


Figure 5.12: Optical micrograph of a fabricated AlGaIn/GaN heterostructure UV photodetector.

ter. The microheater is around the active area across the gate area, as showed in Figure 5.12.

In order to quantify the temperature of the membrane at various pulsed heating voltages and frequencies, it is necessary to perform a calibration for extracting the membrane temperature. The surface temperature can be measured by infrared radiation (IR) thermal camera[52, 53] or 4 wire TRD (temperature resistive device) testing of the micro-heater [51]. Figure 5.13(a) shows the measured maximum temperature of the suspended AlGaIn/GaN heterostructure photodetector at different applied micro-heater voltages and heating frequency, with duty cycle of 50%. An infrared camera (FLIR T620) was used to record the temperature profile of the chip heated at  $V_H = 4$  V as shown in the inset of Figure 5.13(a). A uniform profile across the membrane was observed. Figure 13(b) shows the power at different applied voltages and frequencies with a duty cycle of 50%. From Figure 5.13 we can observe that the maximum temperature of the membrane and the power slightly decrease from 50 Hz to 100 Hz. However, above 100 Hz, they are basically unchanged. The temperature of the membrane is directly correlated with the device power consumption.

The decay time was about 450 s when DC heating  $V_H = 0$  V was applied (temperature was about 20 °C, ambient temperature), and was reduced to about 164 s when the photodetector is DC heated to approximately 150 °C at  $V_H = 4$  V (280 mW), as shown in Figure 5.14(b). Under DC heating mode, the decrease of decay time was mainly determined by the increasing temperature of micro-heater. The decay time would be further reduced by increasing the micro-heater voltages. The temperature dependence of  $\tau$  can be described by Eq. (5-2). As shown in Figure 5.14, the decay times of the device become shorter with increasing temperature and power. Figure 5.13 shows the heating temperature at different applied voltage and frequency with duty cycle of 50%. It is ex-

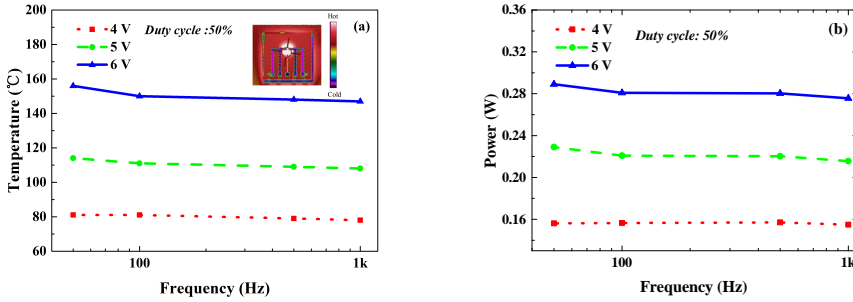


Figure 5.13: (a) Measured heating temperature at different applied voltages and heating frequency with duty cycle of 50%. The inset shows the temperature profile (infrared camera image) of the heated (4 V) AlGaN/GaN photodetector. (b) Measured power consumption at different applied voltages and heating frequency with duty cycle of 50%.

pected from Eq. (5-2) that the temperature dependence of PPC decay behavior should fit to a well-known stretched-exponential function. [54–56] Thus the decay times of the AlGaN/GaN photodetectors would be suppressed with increasing the temperature. Similar results by DC heating have been reported [43]. The heating power and voltage can be further optimized by  $\text{WO}_3$  AlGaN/GaN membrane size and layout [57, 58].

5

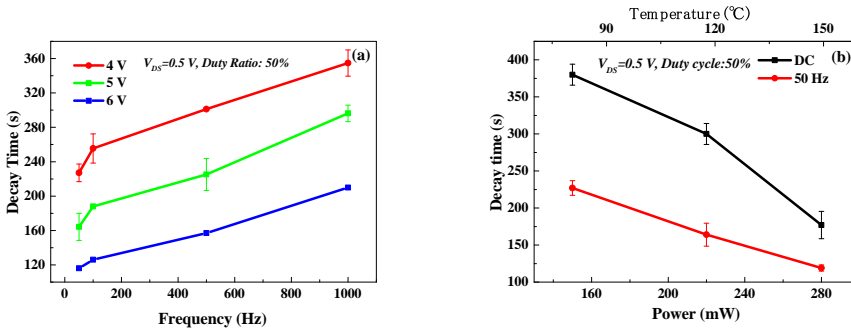


Figure 5.14: Measured decay time comparison of AlGaN/GaN heterostructure photodetector for changing power/temperature at DC heating and 50 Hz pulsed heating mode ( $V_{DS}=0.5$  V, Duty cycle=50%).

The PPC effect in the 2DEG channel implies there is an insufficient amount of energy for carriers to overcome a capture barrier  $\Delta E$  created by localized defects. This prevents recapture of electrons by the non-radiative recombination centers caused by the cluster and demonstrates metastability of the defect in  $(\text{Al}_{0.26}\text{Ga}_{0.74}\text{N})$ . The normalized transient photocurrent responses of AlGaN/GaN heterostructure detectors under 380 nm UV light illumination at various frequencies are shown in Figure 5.15. The decay time of the photodetector is defined as the time required for the photo current changes from 90% to 10% of its saturated response value. The photodetector shows a rapid response under illumination, but the photocurrent decay depends on the frequency. During a pulse cycle

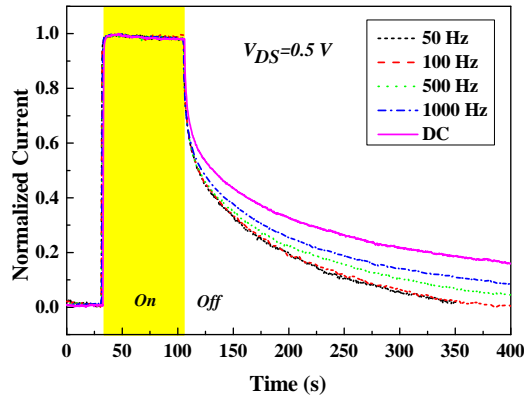


Figure 5.15: Normalized transient photocurrent response (0 % is dark and 100 % maximum photocurrent under 380 nm illumination) of suspended AlGaIn/GaN photodetector at various pulse frequency ( $V_{DS}=0.5$  V,  $P_H=220$  mW).

in the micro-heater, the decay time is reduced. Due to deep level defects concentration increase compared to DC heating, more electrons fill the extra defects with pulsed stress in the gate area of AlGaIn/GaN heterostructure. The basic theory of pulsed stress has been reported in early publications. [59, 60] The decay time comparison of these two kinds of heating modes at same heating power (temperature) are shown in Figure 5.14 (b). The decay time of the AlGaIn/GaN heterostructure photodetectors can be reduced obviously from 380 s, 300 s, 175 s by DC heating to 227 s, 164 s, 116 s by 50 Hz pulsed heating at same power (150 mW, 220 mW, 280 mW), respectively. A reduction of 30-45 % in decay time is measured compared to DC heating. This indicates that pulsed heating method can be utilized to cut down decay time and power consumption, which is an important step to solve the relative long recovery time due to PPC effect found in the literature [41, 43].

The relative long decay time introduced by the PPC effect is an important disadvantage limiting the wide application of GaN-based photodetectors. In order to continue to reduce the decay time of suspended  $WO_3$  AlGaIn/GaN heterostructure UV photodetector, a pulsed heating method based the integrated micro-heater was demonstrated and discussed. The pulsed heating method effectively reduces the decay time of the AlGaIn/GaN heterostructure photodetectors. The decay time is significantly reduced from 175 s by DC heating to 116 s by 50 Hz pulsed heating at the same power (280 mW). With the same pulse duty cycle and 50 Hz pulsed heating, a reduction of 30-45 % in decay time is measured compared to DC heating.

#### 5.3.4. SHORT-TIME MONO-PULSE HEATING RESET MODE

Although the pulsed heating mode has a reduction of 30-45 % in decay time compared to DC heating mode, the decay time is about hundred seconds, which is still undesirable for practical applications. In this section, we report the impact of mono-pulsed heating

on the PPC effect in suspended  $\text{WO}_3/\text{AlGaN}/\text{GaN}$  heterostructure photodetectors. Our novel device exhibits high responsivity under deep UV illumination and fast response/recovery characteristics using mono-pulse heating reset (MHR) after the removal of UV light. The mechanisms of PPC and its elimination will be discussed here.

The surface membrane temperature of photodetector is modulated by Joule heating of the micro-heater when the current passes through the Ti/Pt layer. To calculate the membrane temperature, a calibration is required at various heating voltages. According to the measurement results in our previous publications[61], the surface temperature of the device under the work mode ( $V_{DS}=0.5\text{ V}$ ) are  $60\text{ }^\circ\text{C}$ ,  $80\text{ }^\circ\text{C}$ ,  $100\text{ }^\circ\text{C}$  and  $120\text{ }^\circ\text{C}$  when voltages of  $2.1\text{ V}$ ,  $2.7\text{ V}$ ,  $3.2\text{ V}$  and  $3.7\text{ V}$ , respectively, are applied to the microheater. The mono-pulse heating reset process was performed by controlling the voltage of micro-heater. The peak wavelength ( $\lambda_p$ ) of UVC and UVA LED light source are  $268.2\text{ nm}$  and  $395.1\text{ nm}$ , and the half width high are  $9.1\text{ nm}$  and  $11\text{ nm}$ , respectively. More information about UVC and UVA LED chip can be found in appendix B.

Figure 5.16 shows the transient response characteristics of  $\text{WO}_3/\text{AlGaN}/\text{GaN}$  heterostructure photodetector under the  $268\text{ nm}$  light illumination at bias of  $0.5\text{ V}$ . Upon exposure to UV illumination, the photocurrent increases immediately. The dark current and UV illumination current of the photodetector were  $554\text{ }\mu\text{A}$  and  $614\text{ }\mu\text{A}$ , respectively. Once removing the UV illumination, the drain current decay slowly and the decay time is several hours (dash line). A similar decay phenomenon was observed under different UV illumination intensities and different wavelengths as shown in Figure 5.17, Figure 5.18 and Figure 5.19. This long recovery process after illumination was caused by the energy barrier delay the recombination of photogenerated carriers (PPC effect). Thus, the PPC effect has to be suppressed in order to realize fast recovery of photodetector for practical application. As shown in Figure 5.16 (red solid line inset), after removing the UV illumination, the photodetector was heated to  $120\text{ }^\circ\text{C}$  for 5 seconds by applying the integrated micro-heater voltage of  $3.7\text{ V}$ , then cooled down to RT for 2 seconds. Interestingly, the dark current dropped rapidly to  $205\text{ }\mu\text{A}$  due to increasing the temperature of  $\text{WO}_3/\text{AlGaN}/\text{GaN}$  heterostructure photodetector, then came back to after resetting the heater and remained constant. A similar behaviour was observed for different intensities as shown in Figure 5.17, Figure 5.18 and Figure 5.19. These findings indicate that the PPC effect is eliminated by this MHR process, and the decay time is reduced from hours to less than 7 seconds.

In order to further optimize the mono-pulse heating reset, the transient photocurrent response of  $\text{WO}_3/\text{AlGaN}/\text{GaN}$  heterostructure photodetector under the heating reset with different temperatures was studied (see Figure 5.17). A stable current after MHR process, which decreased with temperature is shown in figure 5.17(b). This means that process of PPC effect can be effectively accelerated by increasing the operating temperature of photodetector. The trapped photogenerated carriers get more thermal energy with the increasing temperature, and the carriers capture increases, resulting in the decrease of dark current. The current basically keeps constant when the temperature of MHR is above  $80\text{ }^\circ\text{C}$ , which means that PPC effect almost is eliminated. In spite that the PPC effect would have a little decrease with increasing the heating reset temperature, the decay time is the same but the power consumption of micro-heater would be much higher. Therefore, for our samples,  $80\text{ }^\circ\text{C}$  is enough to remove the PPC effect.

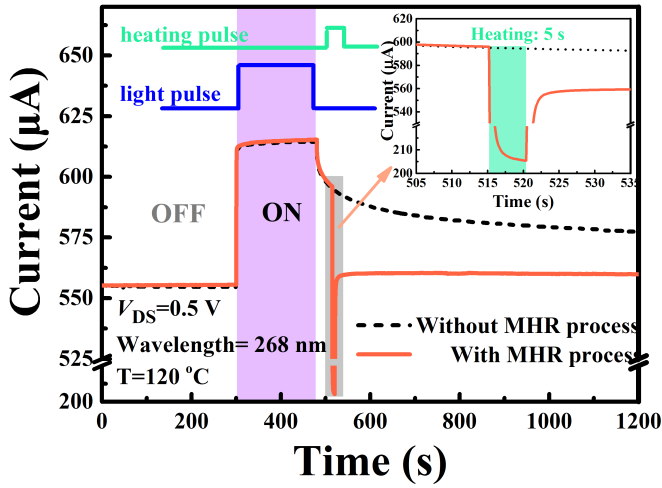


Figure 5.16: The transient response of a  $\text{WO}_3$  gate AlGaIn/GaN heterostructure photodetector to 268 nm UV illumination and the PPC effect can be removed by a novel HR process: heating reset (inset).

Figure 5.18 and Figure 5.19 show the time dependent drain current of the  $\text{WO}_3/\text{AlGaIn}/\text{GaN}$  photodetector under UVA and UVC illumination respectively. The PPC effect are eliminated effectively by this novel method: mono-pulse heating reset (MHR) under different light wavelength and light intensity. In Figure 5.18 the stable dark current after TR process were lower than that before UVA UV illumination possible because of the trapped carriers in defects. A small increase under higher light intensity is observed as shown in Figure 5.18(b) due to the more photogenerated carriers at higher intensity. The change of photocurrent to dark current versus light power or intensity as shown in Figure 5.18 (c) could also support this phenomenon.

As shown in Figure 5.19, the photocurrent change increases with the UVC light intensity and then reaches a saturation value. The response time decrease with the light intensity as shown in Figure 5.19(f). When the light intensity is  $20 \mu\text{W}/\text{cm}^2$ , the measure response time is measured 0.7 s. These measurement results mean that higher UV intensity result in more photogenerated carriers with faster speed.

$\text{WO}_3$  is an n-type semiconductor [12, 62] and Figure 5.20 shows the corresponding UV sensing and PPC mechanisms on the energy band diagram. When there is no bias applied between the source and drain of the detector in the dark, the oxygen molecules from the ambient air absorbed on the nanolayer  $\text{WO}_3$ , combine with electrons and create a depletion sub-layer near the surface [ $\text{O}_2(\text{gas}) + e \rightarrow \text{O}_2^-(\text{adsorb})$ ], where  $\text{O}_2^-$  is the adsorbed oxygen ion on the  $\text{WO}_3$  surface. So there is a depletion layer in the nanolayer  $\text{WO}_3$  surface, as shown in Figure 5.20. Under deep UV illumination conditions, more electron-hole pairs are photogenerated inside the  $\text{WO}_3$  as illustrated in Figure 5.20(b). Then the generated holes move towards the  $\text{WO}_3$  surface to recombine with the electrons trapped in  $\text{O}_2^-$  ions [ $h^+ + \text{O}_2^-(\text{adsorb}) \rightarrow \text{O}_2(\text{gas})$ ],[12] which help the adsorbed oxygen

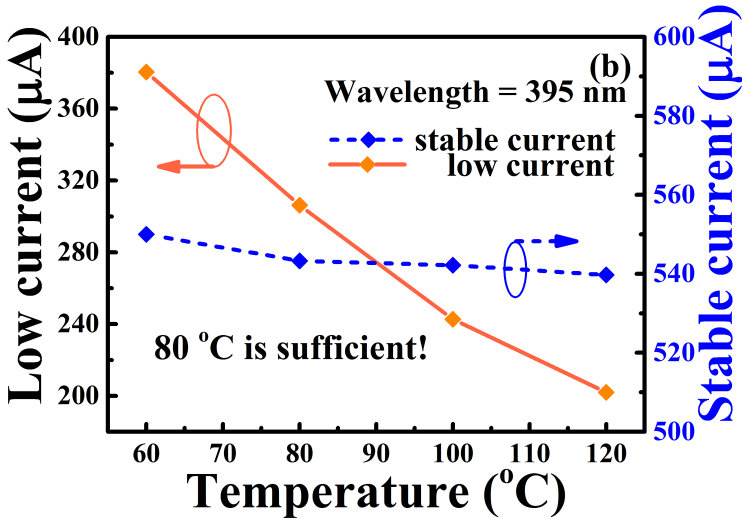
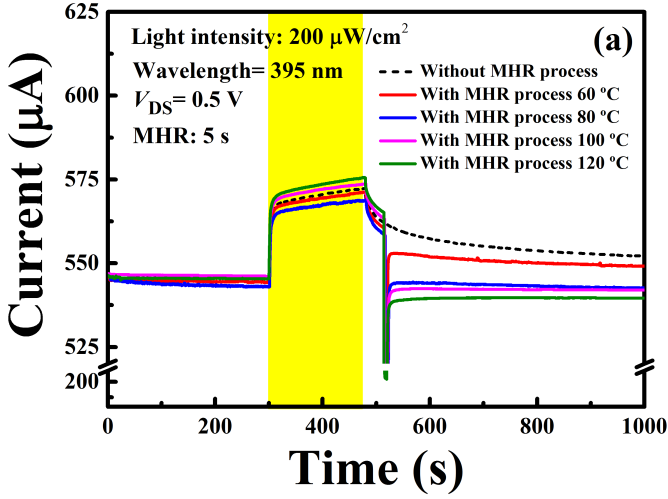


Figure 5.17: (a) The transient photocurrent response of the  $\text{WO}_3/\text{AlGaN}/\text{GaN}$  heterostructure detector measured with different temperature MHR process at  $V_{DS} = 0.5 \text{ V}$ ; (b) The low drain current and stable current at different temperature MHR process.

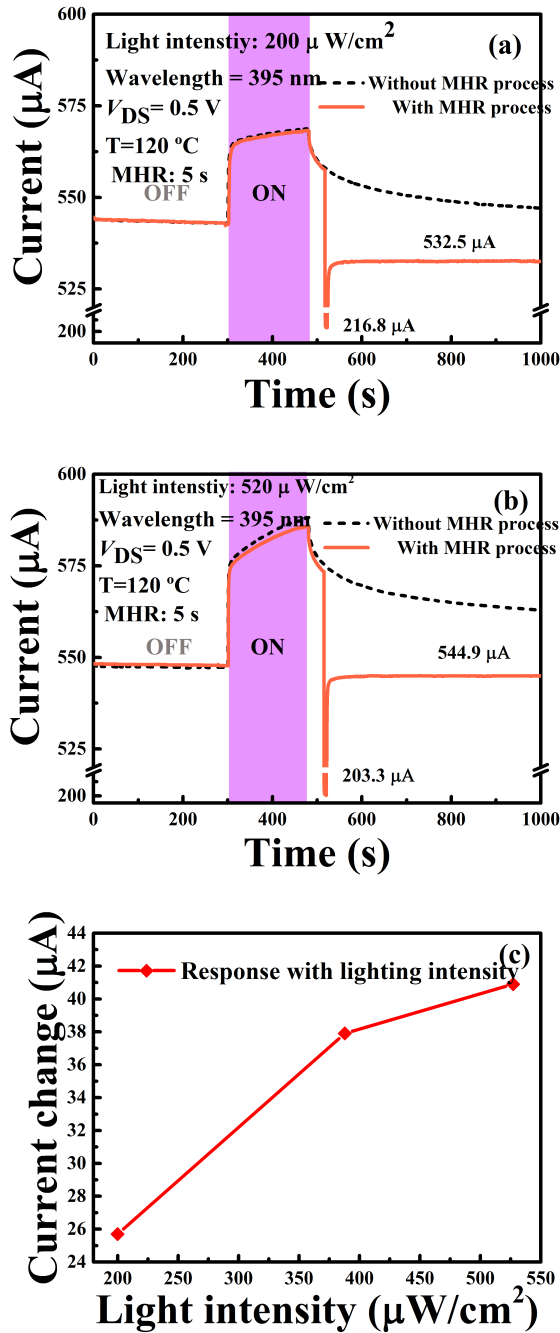


Figure 5.18: The transient response of a  $\text{WO}_3$  gate AlGaN/GaN heterostructure photodetector to 395 nm UV illumination and the PPC effect can be removed by a novel MHR process: short heating reset at different illumination intensity (a) 200  $\mu\text{W}/\text{cm}^2$ ; (b) 520  $\mu\text{W}/\text{cm}^2$ ; (c) drain current change versus light intensity.

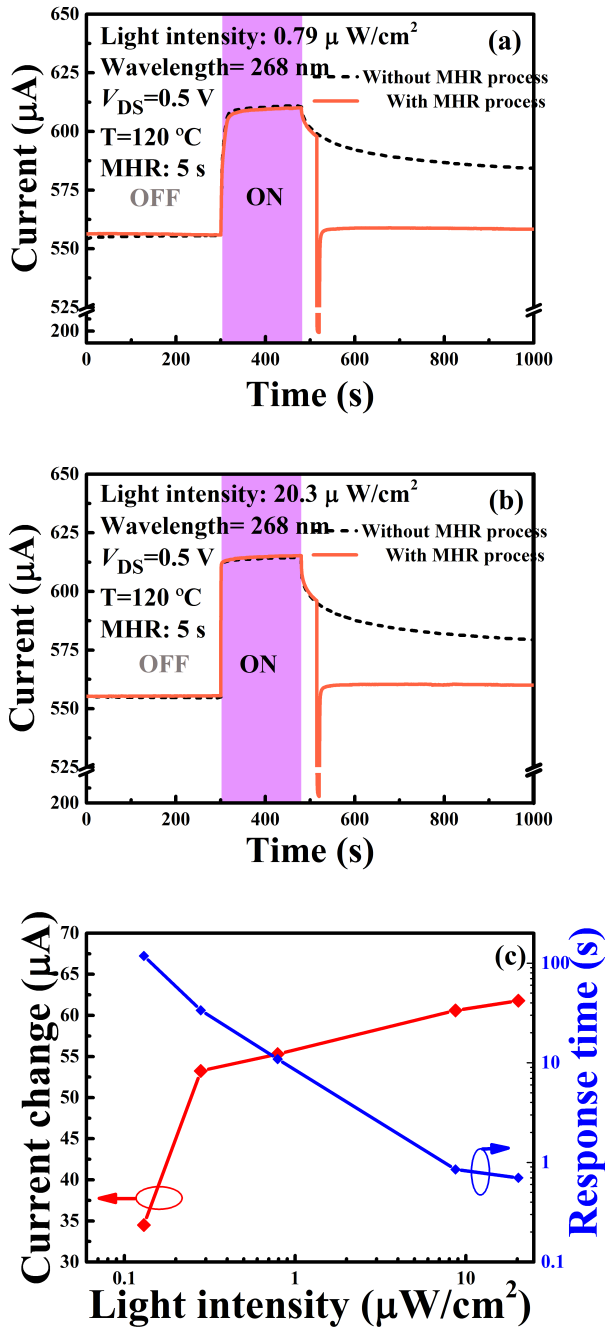


Figure 5.19: The transient response of a  $\text{WO}_3$  gate AlGaN/GaN heterostructure photodetector to 268 nm UV illumination and the PPC effect can be removed by a novel MHR process: short heating reset at different illumination intensity (a)  $0.79 \mu\text{W}/\text{cm}^2$ ; (b)  $20.3 \mu\text{W}/\text{cm}^2$ ; (c) drain current change and response time versus light intensity.

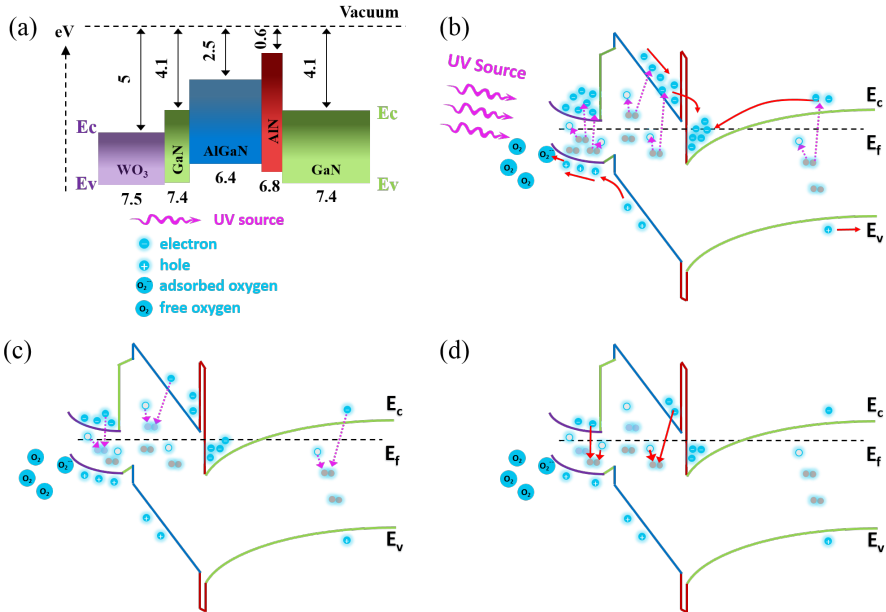


Figure 5.20: (a) Schematic illustration of the band diagram to describe the  $\text{WO}_3/\text{AlGaIn}/\text{GaN}$  heterostructure photodetector. (b) Under UV illumination; (c) Removal UV illumination; (d) Heating reset process.  $E_f$  and dashed line denote the Fermi level.

ions desorb from the  $\text{WO}_3$  surface and decrease the width of the depletion layer. Therefore, the negative potential on the  $\text{WO}_3$  nanolayer is reduced and 2DEG concentration in the channel layer of heterostructure is enhanced. Meanwhile, the generated carriers in AlGaIn and GaN layers also move to the 2DEG quantum well, as shown in Figure 5.20(b). On the other hand, the electrons in the band tail states also excited to the conduction band under light illumination. Hence, the drain-source current is increased under deep UV illumination, as shown in Figure 5.18 and Figure 5.19. After the UV illumination, the energy barrier delays the recombination of the photogenerated carriers, which results in a long recovery time (PPC effect). Only some of photogenerated electrons could recombine with the holes as shown in Figure 5.20(c). In order to suppress the PPC effect, the heating reset was conducted as shown in Figure 5.20(d). The electrons in the band tail states under the conduction band are easily excited and provide more free electrons, and the increased electrons concentration accelerates the recombination of carriers. Meantime, the electrons get more thermal energy to overcome the energy barrier and increase the capture rate at high temperature. After the MHR process, the reduced free electron concentration resulted in a significant decrease in drain current compared to the current of the photodetector without the MHR process. As a result, the dark current has a slight decrease and the PPC effect is suppressed.

Figure 5.21 and Figure 5.22 show the transient photocurrent response of  $\text{WO}_3/\text{AlGaIn}/\text{GaN}$  heterostructure photodetector with and without heating reset under UVA and UVC illumination. The heating reset is 5 seconds heating pulse. As shown in the Figure 5.21,

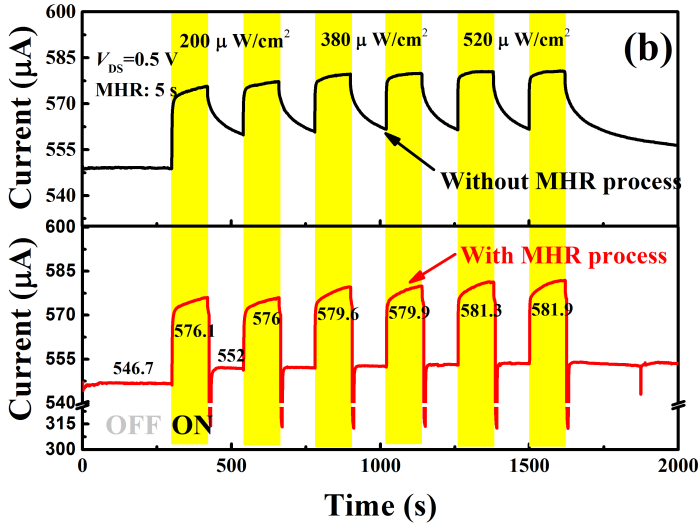
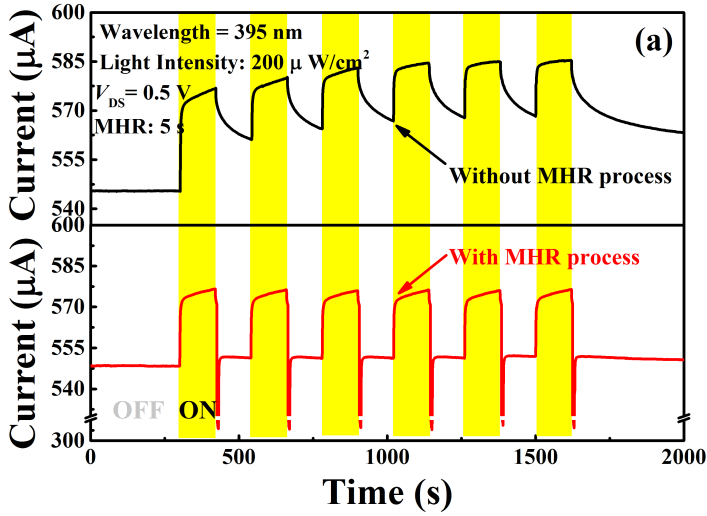


Figure 5.21: The transient photocurrent response of  $\text{WO}_3/\text{AlGaN}/\text{GaN}$  heterostructure photodetector measured under 380 nm illumination at  $V_{DS}=0.5 \text{ V}$ . (a) Six cycles at the light intensity of  $200 \mu\text{W}/\text{cm}^2$ ; (b) Every two cycles at different light intensity ( $200 \mu\text{W}/\text{cm}^2$ ;  $380 \mu\text{W}/\text{cm}^2$  and  $520 \mu\text{W}/\text{cm}^2$ ).

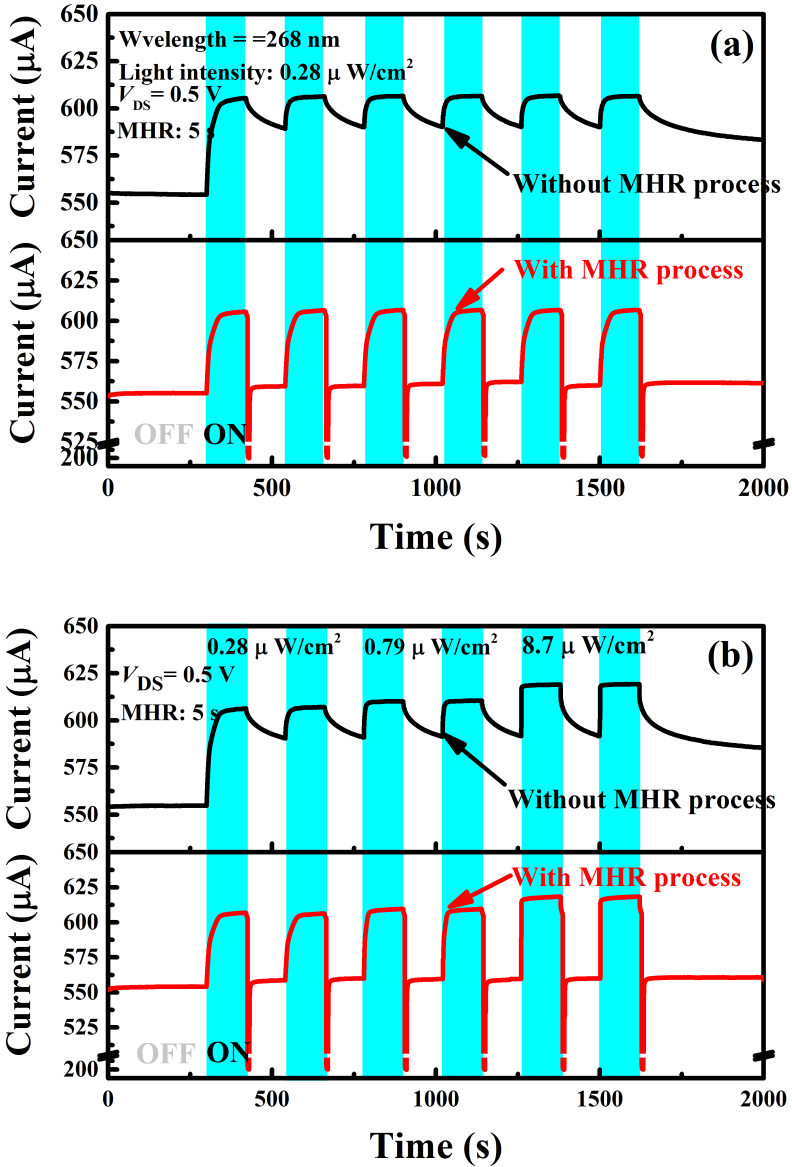


Figure 5.22: The transient photocurrent response of  $\text{WO}_3/\text{AlGaIn}/\text{GaN}$  heterostructure photodetector measured under 268 nm illumination at  $V_{DS} = 0.5 \text{ V}$ . (a) six cycles at the light intensity of  $0.28 \mu\text{W}/\text{cm}^2$ ; (b) Every two cycles at different light intensity ( $0.28 \mu\text{W}/\text{cm}^2$ ;  $0.79 \mu\text{W}/\text{cm}^2$ ;  $8.7 \mu\text{W}/\text{cm}^2$ ).

Table 5.1: Comparison of the parameters of GaN-based photodetectors.

Photodetectors	Wavelength (nm)	Responsivity (A/W)	Recovery time	Ref.
WO <sub>3</sub> /AlGaIn/GaN	240	1.67 × 10 <sup>-4</sup> (0.5 V)	<7 s	This work
V-Grooved/AlGaIn/GaN	365	4 × 10 <sup>-4</sup> (1 V)	34 s	[63]
AlGaIn/GaN	365	-	24 s	[43]
Ga <sub>2</sub> O <sub>3</sub> /AlGaIn/GaN	250-450	30 (-5 V)	~100 s	[64]
Graphene/AlGaIn/GaN	300	0.56 (-2 V)	13.8 s	[65]
p-NiO/GaN	280-380	~0.2 (-1 V)	35 ms	[66]
InAlN/GaN	367	32.9 (5 V)	3-4 ms	[67]
GaN nanoflowers	325	10.5 (1 V)	27 ms	[68]
Pt-GaN nanowire	380	6.39 × 10 <sup>-4</sup>	0.65 s	[69]
GaN/Ga <sub>2</sub> O <sub>3</sub>	365	54.43 × 10 <sup>-3</sup>	0.08 s	[70]
GaN porous film	300-380	0.315	0.03 s	[71]
Single InGaIn/GaN wire	244,360,488	8 × 10 <sup>3</sup>	3000 s	[72]

after first cycle of the UV light on/off, the photocurrent decays slowly and does not recover to the initial value. Then the light current increases slightly after further cycles. By contrast, the PPC effect was suppressed by the MHR process. After five cycles the photocurrent of photodetector still keep consistency and repeatability. The decay time is about 7 seconds including 5 seconds of MHR process and 2 seconds of dark current recovery. These results indicate that MHR process could make the WO<sub>3</sub>/AlGaIn/GaN 2DEG structure photodetectors with high gain and fast response/recovery at the same time.

Table 5.1 shows a comparison of the parameters of GaN-based photodetectors. Our WO<sub>3</sub>/AlGaIn/GaN heterostructure photodetector has a relative high responsivity than most reported. And our detector performs high responsivity and fast recovery by MHR process under deep UV illumination at the same time.

The novel device exhibits high responsivity under deep UVC illumination and fast response and recovery characteristics using mono-pulse heating reset (MHR) after the removal of UV light. The persistent photoconductivity (PPC) effect can be eliminated by a novel method: mono-pulse heating reset (MHR) by applying a pulse voltage of micro-heater after the removal of UV illumination. The recovery time was reduced from hours to seconds without reducing high responsivity and stability of photodetector. The mechanisms of PPC and its elimination have been discussed in this section. These findings make suspended AlGaIn/GaN heterostructure photodetectors possible for commercial photodetector market.

## 5.4. CHAPTER SUMMARY

In this chapter, suspended WO<sub>3</sub> gate AlGaIn/GaN heterostructure deep ultraviolet photodetector with an integrated micro-heater were fabricated and characterized. We employed the physical vapor deposition (PVD) method to grow a WO<sub>3</sub> nanolayer on AlGaIn/GaN epitaxial heterostructure for UV absorption. An integrated micro-heater around

the 2DEG area of AlGaIn/GaN device enabled the chip scale heating process without external heating. The transient optical characteristics of the photodetector at different temperatures are studied. Our devices show the high response to the deep UV wavelength and exhibits high responsivity of  $1.67 \times 10^4$  A/W at 240 nm, and the sharp cut-off wavelength is 275 nm.

The photodetector shows a rapid response and recovery (175 s) time under 240 nm illumination at the DC heating temperature of 150 °C. The relative long decay time introduced by the PPC effect is an important disadvantage limiting the wide application of GaN-based photodetectors. Then, we demonstrate that the pulsed heating method effectively reduces the decay time of the AlGaIn/GaN heterostructure photodetectors. The decay time is significantly reduced from 175 s by DC heating to 116 s by 50 Hz pulsed heating at the same power (280 mW). With the same pulse duty cycle and 50 Hz pulsed heating, a reduction of 30-45 % in decay time is measured compared to DC heating.

More interesting, the persistent photoconductivity (PPC) effect can be eliminated by a novel method: mono-pulse heating reset (MHR) by applying a pulse voltage of micro-heater after the removal of UV illumination. Under the illumination of both UVA and UVC, the recovery time was reduced from hours to seconds without reducing high responsivity and stability of photodetector. This novel method solved the long-term problem of long decay time introduced by PPC of GaN-based photoconductive photodetectors. And mono-pulse heating reset method could be applied to suppress the PPC effect in other materials as well.

These findings form an encouraging first step towards the development of a high accuracy and fast response 2DEG-based deep ultraviolet detector. The deep-UV detection, high responsivity, fast recovery process and low production cost make AlGaIn/GaN heterostructure photodetectors suitable for commercial photodetector market.

## REFERENCES

- [1] R. A. Miller, H. So, T. A. Heuser, and D. G. Senesky, "High-temperature Ultraviolet Photodetectors: A Review," arXiv preprint arXiv:1809.07396, 2018.
- [2] A. Blanc, L. Deimling, and N. Eisenreich, "UV- and IR-Signatures of Rocket Plumes," *Propellants, Explosives, Pyrotechnics*, vol. 27, no. 3, pp. 185-189, 2002.
- [3] Z. Y. Xu and B. M. Sadler, "Ultraviolet communications: Potential and state-of-the-art," (in English), *Ieee Communications Magazine*, vol. 46, no. 5, pp. 67-73, May 2008.
- [4] J. Xu, W. Zheng, and F. Huang, "Gallium Oxide Solar-Blind Ultraviolet Photodetector: A Review," *Journal of Materials Chemistry C*, 2019.
- [5] W. Zheng, F. Huang, R. Zheng, and H. Wu, "Low-Dimensional Structure Vacuum-Ultraviolet-Sensitive (< 200 nm) Photodetector with Fast-Response Speed Based on High-Quality AlN Micro/Nanowire," *Advanced Materials*, vol. 27, no. 26, pp. 3921-3927, 2015.
- [6] M. Razeghi and A. Rogalski, "Semiconductor ultraviolet detectors," *Journal of Applied Physics*, vol. 79, no. 10, pp. 7433-7473, 1996.

- [7] Y. Zou, Y. Zhang, Y. Hu, and H. Gu, "Ultraviolet detectors based on wide bandgap semiconductor nanowire: A review," *Sensors*, vol. 18, no. 7, p. 2072, 2018.
- [8] A. Bouvier et al., "Photosensor characterization for the Cherenkov Telescope Array: silicon photomultiplier versus multi-anode photomultiplier tube," in *Hard X-Ray, Gamma-Ray, and Neutron Detector Physics XV*, 2013, vol. 8852, p. 88520K: International Society for Optics and Photonics.
- [9] S. M. Hatch, J. Briscoe, and S. Dunn, "A self-powered ZnO-nanorod/CuSCN UV photodetector exhibiting rapid response," *Advanced Materials*, vol. 25, no. 6, pp. 867-871, 2013.
- [10] M. Chen, L. Hu, J. Xu, M. Liao, L. Wu, and X. Fang, "ZnO hollow-sphere nanofilm-based high-performance and low-cost photodetector," *Small*, vol. 7, no. 17, pp. 2449-2453, 2011.
- [11] D. L. Shao, M. P. Yu, J. Lian, and S. Sawyer, "Optoelectronic properties of three dimensional WO<sub>3</sub> nanoshale and its application for UV sensing," (in English), *Optical Materials*, vol. 36, no. 5, pp. 1002-1005, Mar 2014.
- [12] Z. Hai, M. K. Akbari, C. Y. Xue, H. Y. Xu, L. Hyde, and S. Zhuiykov, "Wafer-scaled monolayer WO<sub>3</sub> windows ultra-sensitive, extremely-fast and stable UV-A photodetection," (in English), *Applied Surface Science*, vol. 405, pp. 169-177, May 31 2017.
- [13] Z. He, Q. Liu, H. Hou, F. Gao, B. Tang, and W. Yang, "Tailored electrospinning of WO<sub>3</sub> nanobelts as efficient ultraviolet photodetectors with photo-dark current ratios up to 1000," *ACS applied materials interfaces*, vol. 7, no. 20, pp. 10878-10885, 2015.
- [14] D. Shao, M. Yu, J. Lian, and S. Sawyer, "Optoelectronic properties of three dimensional WO<sub>3</sub> nanoshale and its application for UV sensing," *Optical Materials*, vol. 36, no. 5, pp. 1002-1005, 2014/03/01/ 2014.
- [15] J. Sun et al., "Characterization of an Acetone Detector Based on a Suspended WO<sub>3</sub>-Gate AlGa<sub>0.5</sub>N/GaN HEMT Integrated With Microheater," *IEEE Transactions on Electron Devices*, vol. 66, no. 10, pp. 4373-4379, 2019.
- [16] W. Y. Kong et al., "Graphene--Ga<sub>2</sub>O<sub>3</sub> heterojunction for highly sensitive deep UV photodetector application," *Advanced Materials*, vol. 28, no. 48, pp. 10725-10731, 2016.
- [17] Y. Li et al., "Efficient assembly of bridged -Ga<sub>2</sub>O<sub>3</sub> nanowires for solar-blind photodetection," *Advanced Functional Materials*, vol. 20, no. 22, pp. 3972-3978, 2010.
- [18] R. Zou et al., "High detectivity solar-blind high-temperature deep-ultraviolet photodetector based on multi-layered (100) facet-oriented -Ga<sub>2</sub>O<sub>3</sub> nanobelts," *Small*, vol. 10, no. 9, pp. 1848-1856, 2014.
- [19] C. Chiu, W. Weng, T. Hsueh, S.-J. Chang, G. Huang, and H. Hsueh, "Ta<sub>2</sub>O<sub>5</sub> Solar-Blind Photodetectors," *IEEE Sensors Journal*, vol. 11, no. 10, pp. 2372-2373, 2011.

- [20] E. Cicek, R. McClintock, C. Cho, B. Rahnema, and M. Razeghi, "Al<sub>x</sub>Ga<sub>1-x</sub>N-based back-illuminated solar-blind photodetectors with external quantum efficiency of 89%," *Applied Physics Letters*, vol. 103, no. 19, p. 191108, 2013.
- [21] E. Monroy et al., "AlGa<sub>N</sub>-based UV photodetectors," (in English), *Journal of Crystal Growth*, vol. 230, no. 3-4, pp. 537-543, Sep 2001.
- [22] E. Munoz, E. Monroy, J. L. Pau, F. Calle, F. Omnes, and P. Gibart, "III nitrides and UV detection," (in English), *Journal of Physics-Condensed Matter*, vol. 13, no. 32, pp. 7115-7137, Aug 13 2001.
- [23] P. E. Malinowski et al., "Backside-Illuminated GaN-on-Si Schottky Photodiodes for UV Radiation Detection," (in English), *Ieee Electron Device Letters*, vol. 30, no. 12, pp. 1308-1310, Dec 2009.
- [24] B. Butun, T. Tut, E. Ulker, T. Yelboga, and E. Ozbay, "High-performance visible-blind GaN-based p-i-n photodetectors," (in English), *Applied Physics Letters*, vol. 92, no. 3, p. 033507, Jan 21 2008.
- [25] T. Tut, T. Yelboga, E. Ulker, and E. Ozbay, "Solar-blind AlGa<sub>N</sub>-based p-i-n photodetectors with high breakdown voltage and detectivity," (in English), *Applied Physics Letters*, vol. 92, no. 10, p. 103502, Mar 10 2008.
- [26] K. H. Lee, P. C. Chang, S. J. Chang, Y. C. Wang, C. L. Yu, and S. L. Wu, "AlGa<sub>N</sub>/Ga<sub>N</sub> Schottky Barrier UV Photodetectors With a Ga<sub>N</sub> Sandwich Layer," (in English), *Ieee Sensors Journal*, vol. 9, no. 7, pp. 814-819, Jul 2009.
- [27] C. K. Wang et al., "GaN MSM UV photodetectors with titanium tungsten transparent electrodes," (in English), *Ieee Transactions on Electron Devices*, vol. 53, no. 1, pp. 38-42, Jan 2006.
- [28] R. W. Chuang et al., "Gallium nitride metal-semiconductor-metal photodetectors prepared on silicon substrates," (in English), *Journal of Applied Physics*, vol. 102, no. 7, p. 073110, Oct 1 2007.
- [29] C. K. Wang et al., "GaN MSM UV Photodetector With Sputtered Al<sub>N</sub> Nucleation Layer," (in English), *Ieee Sensors Journal*, vol. 15, no. 9, pp. 4743-4748, Sep 2015.
- [30] M. A. Khan, M. S. Shur, Q. Chen, J. N. Kuznia, and C. J. Sun, "Gated Photodetector Based on Ga<sub>N</sub>/Alga<sub>N</sub> Heterostructure Field-Effect Transistor," (in English), *Electronics Letters*, vol. 31, no. 5, pp. 398-400, Mar 2 1995.
- [31] S. J. Chang et al., "Nitride-based 2DEG photodetectors with a large AC responsivity," (in English), *Solid-State Electronics*, vol. 47, no. 11, pp. 2023-2026, Nov 2003.
- [32] B. Poti et al., "High responsivity Ga<sub>N</sub>-based UV detectors," (in English), *Electronics Letters*, vol. 39, no. 24, pp. 1747-1749, Nov 27 2003.
- [33] Y. C. Chang, "Effects of illumination on the excess carrier dynamics and variations of the surface states in an AlGa<sub>N</sub>/Ga<sub>N</sub> heterostructure," (in English), *Journal of Applied Physics*, vol. 107, no. 3, p. 033706, Feb 2010.

- [34] R. Vetry, N. Q. Zhang, S. Keller, and U. K. Mishra, "The impact of surface states on the DC and RF characteristics of AlGa<sub>N</sub>/Ga<sub>N</sub> HFETs," *IEEE Transactions on Electron Devices*, vol. 48, no. 3, pp. 560-566, 2001.
- [35] J. Zheng et al., "A PMT-like high gain avalanche photodiode based on Ga<sub>N</sub>/Al<sub>N</sub> periodically stacked structure," *Applied Physics Letters*, vol. 109, no. 24, p. 241105, 2016.
- [36] C. Bayram, J. Pau, R. McClintock, and M. Razeghi, "Performance enhancement of Ga<sub>N</sub> ultraviolet avalanche photodiodes with p-type -doping," *Applied Physics Letters*, vol. 92, no. 24, p. 241103, 2008.
- [37] Q. Cai et al., "AlGa<sub>N</sub> ultraviolet Avalanche photodiodes based on a triple-mesa structure," *Applied Physics Letters*, vol. 113, no. 12, p. 123503, 2018.
- [38] P. J. Snyder, R. Kirste, R. Collazo, and A. Ivanisevic, "Persistent photoconductivity, nanoscale topography, and chemical functionalization can collectively influence the behavior of PC12 cells on wide bandgap semiconductor surfaces," *Small*, vol. 13, no. 24, p. 1700481, 2017.
- [39] R. Calarco et al., "Size-dependent photoconductivity in MBE-grown Ga<sub>N</sub> nanowires," *Nano letters*, vol. 5, no. 5, pp. 981-984, 2005.
- [40] Y.-H. Lee, J.-H. Kang, and S.-W. Ryu, "Enhanced photocurrent and persistent photoconductivity in nanoporous Ga<sub>N</sub> formed by electrochemical etching," *Thin Solid Films*, vol. 540, pp. 150-154, 2013.
- [41] J. Z. Li, J. Y. Lin, H. X. Jiang, M. A. Khan, and Q. Chen, "Persistent photoconductivity in a two-dimensional electron gas system formed by an AlGa<sub>N</sub>/Ga<sub>N</sub> heterostructure," (in English), *Journal of Applied Physics*, vol. 82, no. 3, pp. 1227-1230, Aug 1 1997.
- [42] C. H. Qiu and J. I. Pankove, "Deep levels and persistent photoconductivity in Ga<sub>N</sub> thin films," (in English), *Applied Physics Letters*, vol. 70, no. 15, pp. 1983-1985, Apr 14 1997.
- [43] M. M. Hou, H. Y. So, A. J. Suria, A. S. Yalamarthy, and D. G. Senesky, "Suppression of Persistent Photoconductivity in AlGa<sub>N</sub>/Ga<sub>N</sub> Ultraviolet Photodetectors Using In Situ Heating," (in English), *Ieee Electron Device Letters*, vol. 38, no. 1, pp. 56-59, Jan 2017.
- [44] Y. Wang, Z. Liao, G. She, L. Mu, D. Chen, and W. Shi, "Optical modulation of persistent photoconductivity in ZnO nanowires," *Applied Physics Letters*, vol. 98, no. 20, p. 203108, 2011.
- [45] J. Xu et al., "Electric-field effects on persistent photoconductivity in undoped n-type epitaxial Ga<sub>N</sub>," *Applied physics letters*, vol. 88, no. 7, p. 072106, 2006.
- [46] Q. Hou et al., "Influence of electric field on persistent photoconductivity in unintentionally doped n-type Ga<sub>N</sub>," *Applied Physics Letters*, vol. 98, no. 10, p. 102104, 2011.

- [47] K. Liu, M. Sakurai, M. Aono, and D. Shen, "Ultrahigh-Gain Single SnO<sub>2</sub> Microrod Photoconductor on Flexible Substrate with Fast Recovery Speed," *Advanced Functional Materials*, vol. 25, no. 21, pp. 3157-3163, 2015.
- [48] S. Jeon et al., "Gated three-terminal device architecture to eliminate persistent photoconductivity in oxide semiconductor photosensor arrays," *Nature materials*, vol. 11, no. 4, p. 301, 2012.
- [49] J. Sun et al., "Suppression of persistent photoconductivity AlGa<sub>N</sub>/Ga<sub>N</sub> heterostructure photodetectors using pulsed heating," *Applied Physics Express*, vol. 12, no. 12, p. 122007, 2019.
- [50] H. Zhou et al., "High gain broadband photoconductor based on amorphous Ga<sub>2</sub>O<sub>3</sub> and suppression of persistent photoconductivity," *Journal of Materials Chemistry C*, vol. 7, no. 42, pp. 13149-13155, 2019.
- [51] C. Silvestri, P. Picciafoco, B. Morana, F. Santagata, G. Q. Zhang, and P. M. Sarro, "Electro-thermal simulation and characterization of vertically aligned CNTs directly grown on a suspended microhotplate for thermal management applications," (in English), 2014 *Ieee Sensors*, 2014.
- [52] C. Silvestri et al., "Thermal characterization of carbon nanotube foam using MEMS microhotplates and thermographic analysis," *Nanoscale*, vol. 8, no. 15, pp. 8266-75, Apr 21 2016.
- [53] C. Lin et al., "A Wirelessly Controllable Optoelectronic Device for Optogenetics," *IEEE Photonics Technology Letters*, vol. 31, no. 12, pp. 915-918, 2019.
- [54] J. Li, J. Lin, H. Jiang, A. Salvador, A. Botchkarev, and H. Morkoc, "Nature of Mg impurities in GaN," *Applied physics letters*, vol. 69, no. 10, pp. 1474-1476, 1996.
- [55] H. Hung, C. Chen, S.-J. Chang, H. Kuan, R. Lin, and C. Liu, "Kinetics of persistent photoconductivity in InGa<sub>N</sub> epitaxial films grown by MOCVD," *Journal of crystal growth*, vol. 298, pp. 246-250, 2007.
- [56] E. Arslan, S. Bütün, S. B. Lisesivdin, M. Kasap, S. Ozelik, and E. Ozbay, "The persistent photoconductivity effect in AlGa<sub>N</sub>/Ga<sub>N</sub> heterostructures grown on sapphire and SiC substrates," *Journal of Applied Physics*, vol. 103, no. 10, p. 103701, 2008.
- [57] R. Prajesh, N. Jain, and A. Agarwal, "Low power highly sensitive platform for gas sensing application," *Microsystem Technologies*, vol. 22, no. 9, pp. 2185-2192, 2016.
- [58] J. Courbat, M. Canonica, D. Teyssieux, D. Briand, and N. De Rooij, "Design and fabrication of micro-hotplates made on a polyimide foil: Electrothermal simulation and characterization to achieve power consumption in the low mW range," *Journal of Micromechanics and Microengineering*, vol. 21, no. 1, p. 015014, 2010.
- [59] B. Dong et al., "Trap behaviours characterization of AlGa<sub>N</sub>/Ga<sub>N</sub> high electron mobility transistors by room-temperature transient capacitance measurement," *AIP Advances*, vol. 6, no. 9, p. 095021, 2016.

- [60] N. Wang et al., "Investigation of AlGaIn/GaN HEMTs degradation with gate pulse stressing at cryogenic temperature," *AIP Advances*, vol. 7, no. 9, p. 095317, 2017.
- [61] J. Sun et al., "Suspended tungsten trioxide (WO<sub>3</sub>) gate AlGaIn/GaN heterostructure deep ultraviolet detectors with integrated micro-heater," *Optics Express*, vol. 27, no. 25, pp. 36405-36413, 2019/12/09 2019.
- [62] K. Huang, Q. Zhang, F. Yang, and D. He, "Ultraviolet photoconductance of a single hexagonal WO<sub>3</sub> nanowire," *Nano Research*, vol. 3, no. 4, pp. 281-287, 2010.
- [63] H. So, J. Lim, and D. G. Senesky, "Continuous V-grooved AlGaIn/GaN surfaces for high-temperature ultraviolet photodetectors," *IEEE Sensors Journal*, vol. 16, no. 10, pp. 3633-3639, 2016.
- [64] Z.-D. Huang, W. Y. Weng, S. J. Chang, C.-J. Chiu, T.-J. Hsueh, and S.-L. Wu, "Ga<sub>2</sub>O<sub>3</sub>/AlGaIn/GaN Heterostructure Ultraviolet Three-Band Photodetector," *IEEE Sensors Journal*, vol. 13, no. 9, pp. 3462-3467, 2013.
- [65] M. Kumar, H. Jeong, K. Polat, A. Okyay, and D. Lee, "Fabrication and characterization of graphene/AlGaIn/GaN ultraviolet Schottky photodetector," *Journal of Physics D: Applied Physics*, vol. 49, no. 27, p. 275105, 2016.
- [66] L. Li, Z. Liu, L. Wang, Y. Liu, and J.-P. Ao, "Self-powered GaN ultraviolet photodetectors with p-NiO electrode grown by thermal oxidation," *Materials Science in Semiconductor Processing*, vol. 76, pp. 61-64, 2018.
- [67] S. Kumar, A. S. Pratiyush, S. B. Dolmanan, S. Tripathy, R. Muralidharan, and D. N. Nath, "UV detector based on InAlN/GaN-on-Si HEMT stack with photo-to-dark current ratio > 107," *Applied Physics Letters*, vol. 111, no. 25, p. 251103, 2017.
- [68] N. Aggarwal et al., "A highly responsive self-driven UV photodetector using GaN nanoflowers," *Advanced Electronic Materials*, vol. 3, no. 5, p. 1700036, 2017.
- [69] X. Zhang et al., "Giant UV photoresponse of a GaN nanowire photodetector through effective Pt nanoparticle coupling," *Journal of Materials Chemistry C*, vol. 5, no. 17, pp. 4319-4326, 2017.
- [70] P. Li et al., "Construction of GaN/Ga<sub>2</sub>O<sub>3</sub> p-n junction for an extremely high responsivity self-powered UV photodetector," *Journal of Materials Chemistry C*, vol. 5, no. 40, pp. 10562-10570, 2017.
- [71] M. Zhang et al., "A photoelectrochemical type self-powered ultraviolet photodetector based on GaN porous films," *Materials Letters*, vol. 162, pp. 117-120, 2016.
- [72] A. D. L. Bugallo et al., "Single-wire photodetectors based on InGaIn/GaN radial quantum wells in GaN wires grown by catalyst-free metal-organic vapor phase epitaxy," *Applied Physics Letters*, vol. 98, no. 23, p. 233107, 2011.



# 6

## LOW POWER ALGaN/GaN MEMS PRESSURE SENSOR

*This chapter is based on:*

*Sun, J., Hu, D., Liu, Z., Middelburg, L., Vollebregt S., Sarro, P.M. and Zhang, G. et al.(2020)  
"Low power AlGaN/GaN MEMS pressure sensor for low vacuum application." Sensors and  
Actuators A: Physical.(Under review)*

## 6.1. INTRODUCTION

Compact MEMS pressure sensors are in great demand for several applications such as oscillators, RF switches [1], energy harvesters[2][3] and MEMS resonators[4]. These systems containing moving parts need a vacuum environment ( $1 \times 10^{-5} \sim 10^{-3}$  Torr) for proper operation. Besides MEMS devices, advanced scientific instruments such as electron microscopes, ion mass spectrometers need a high vacuum. Therefore, it is desirable to monitor the vacuum pressure and minimize the size of the pressure gauge. Most vacuum sensors or gauges are classified into three types: mechanical, thermal conductivity and ionization vacuum. Although the ionization vacuum gauges are commercially used to detect high vacuum, the efficient electron and a sufficient electron path make it difficult to miniaturize. Thermal conductivity gauges, such as Pirani gauges have a simple structure and suitable for miniaturization, while the thermal conductivity is dependent on gas species. Another type of vacuum sensor is the mechanical gauge, such as cantilevers and membranes, which deform with the change of pressure. The membrane deforms due to the applied pressure, thus inducing a resistivity or capacitive change in the structure. [5][6]. However, the membrane is likely to suffer failure from material fatigue by long term loading and high-temperature environment.

As mentioned in chapter 1 and 2, AlGa<sub>N</sub>/Ga<sub>N</sub> heterostructures are quite attractive for sensing several chemical and physical quantities, including pressure. Compared to silicon carbide (SiC), the piezoresistive gauge factor of AlGa<sub>N</sub>/Ga<sub>N</sub> heterostructures is approximately three times higher than the highest gauge factor reported for SiC, which means that AlGa<sub>N</sub>/Ga<sub>N</sub> heterostructures have great potential in high-temperature pressure sensing applications. This can be realized by etching away the substrate to form a MEMS structure and building the AlGa<sub>N</sub>/Ga<sub>N</sub> sensing element on it. The output current or voltage of the device changes with applied pressure. The sensitivity could be enhanced by lowering the gate bias of the transistor or increasing the Al content of the AlGa<sub>N</sub> layer.

A microfabricated AlGa<sub>N</sub>/Ga<sub>N</sub> MEMS pressure sensor is reported in this chapter. We investigated the effect of vacuum pressure and temperature on the drain current of AlGa<sub>N</sub>/Ga<sub>N</sub> heterostructure sensors and quantified the dynamic sensitivity at various bias voltages and temperatures. The dynamic vacuum pressure response and repeatability at different temperatures were studied as well. The layout optimization and temperature effect on the sensitivity of AlGa<sub>N</sub>/Ga<sub>N</sub> MEMS sensor were experimentally analyzed.

## 6.2. GAN-BASED MEMS PRESSURE SENSOR

### 6.2.1. DEVICE FABRICATION

The AlGa<sub>N</sub>/Ga<sub>N</sub> structure consists of an undoped Ga<sub>N</sub> buffer layer (2 μm), followed by an AlN interlayer (1 nm), an undoped Al<sub>0.26</sub>Ga<sub>0.74</sub>N barrier layer (25 nm), and a 3 nm Ga<sub>N</sub> cap layer. The epilayers were grown on a 1 mm thick <111> silicon wafer using metal-organic chemical vapor deposition (MOCVD). The main steps for the fabrication of the MEMS AlGa<sub>N</sub>/Ga<sub>N</sub> heterostructure sensors are described below. The fabrication process started with a mesa etching to define the active area. Then, Ti/Al/Ti/Au ohmic metallization was deposited by e-beam evaporation and patterned by lift-off and annealed at 870°C for 45 s under N<sub>2</sub> ambient. Next, an evaporated Ti/Pt layer was patterned by

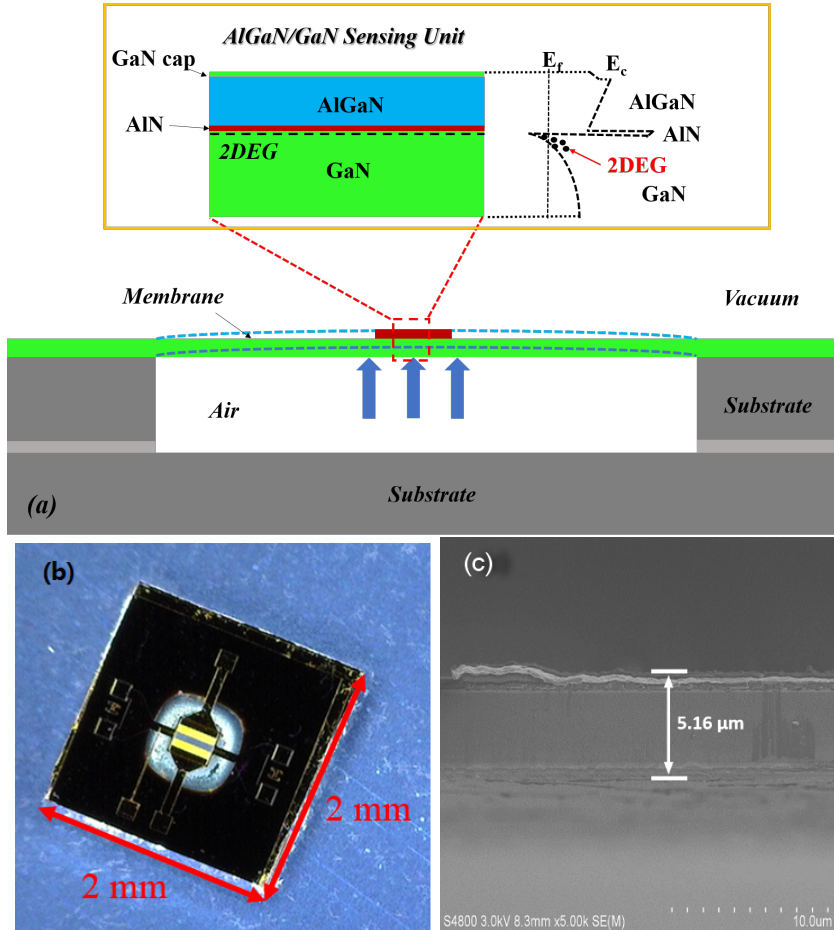


Figure 6.1: (a) Schematic image of MEMS AlGaIn/GaN pressure sensor; (b) Optical image of a micro-fabricated AlGaIn/GaN heterostructure sensor; (c) SEM image of the GaN membrane cross section.

lift-off to form the microheater, followed by a 200-nm plasma-enhanced chemical vapor deposition (PECVD) SiO<sub>2</sub> layer for isolation from the interconnect layer. The evaporated Ti/Au layer stack is then used to form the metal interconnect. The topside of the wafer was passivated with a 300 nm PECVD SiO<sub>2</sub> layer and the backside was thinned down to 400 μm by chemical mechanical polishing (CMP). The topside SiO<sub>2</sub> layer was etched in a buffered oxide etch (BOE) solution to open the contact pads and gate windows. The silicon substrate was etched from the backside by deep reactive ion etching (DRIE) using a 5 μm-thick SiO<sub>2</sub> layer as the hard mask to form a circular membrane (700 μm in diameter). After dicing, the sensor was bonded to a second silicon wafer using silicone (BISON) to create a reference pressure as shown in Figure 6.1(a) and (b). The thickness of the GaN membrane was about 5 μm as illustrated in Figure 6.1(c). Then the sensor was put in a pressure chamber integrated with a temperature-controllable microprobe station

(NEXTRON) and electrically connected to a Keithley 2612B source meter. The integrated micro-heater on the membrane was not used as temperature sensor (the temperature was controlled by the microprobe station used), but to modulate the membrane temperature to improve sensitivity. More details about the process of GaN-based sensors can be found in our earlier publications [8, 9, 12].

### 6.2.2. PRESSURE MEASUREMENT SETUP

The micro-fabricated vacuum gauge is aimed to work at an elevated temperature, so apart from room temperature, the gauge also needs to be calibrated at a high temperature. In order to meet the measurement requirements, the measurement setup must be able to provide a pressure range from a certain vacuum level to an atmospheric pressure. In addition, the test substrate needs to be heated up by the setup to a desired temperature to verify its high temperature capacity. The measurement setup, schematically shown in figure 6.2, is comprised by a micro probe station (MPS), a pressure controller, a pump and a source meter for the electrical measurement as shown in Figure 6.2.

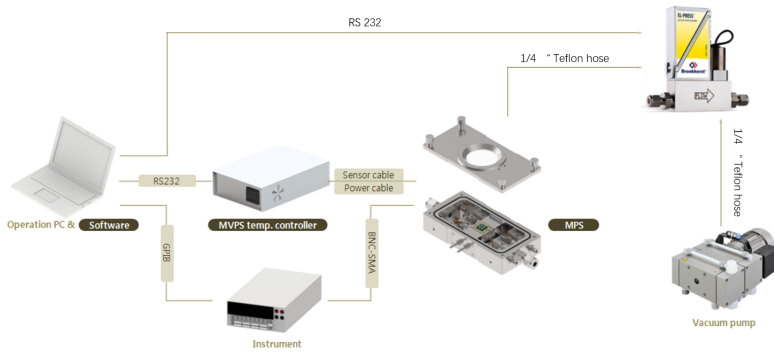


Figure 6.2: A block diagram of the measurement setup.

### 6.2.3. STATIC MEASUREMENT

The  $I_{DS} - V_{DS}$  static response of AlGaIn/GaN heterostructure pressure sensor at various temperature and vacuum pressure values is shown in Figure 6.3. From Figure 6.3(a), we see that the drain current decreases with the increasing temperature at 10 Pa, which is attributed to a large decrease in channel mobility of the HEMT device [13]. The drain current of the device increases with increasing applied vacuum pressure, as reported in Figure 6.3(b-e), which is attributed to an increase of 2DEG density ( $N_S$ ) [7]. However, the sensor current change versus vacuum pressure in the range from 101 kPa to 1 kPa was much smaller than that from 1 kPa to 10 Pa due to the smaller deflection at the vacuum pressure range from 101 kPa to 1 kPa, which means this sensor performs better in the lower pressure range. The static current change of AlGaIn/GaN heterostructure sensor is shown in Figure 6.4 as a function of source-drain voltage ( $V_{DS}$ ) at various temperatures and vacuum pressures. From Figure 6.4(a), the change in current increased with the temperature due to the larger deflection of the membrane at higher tempera-

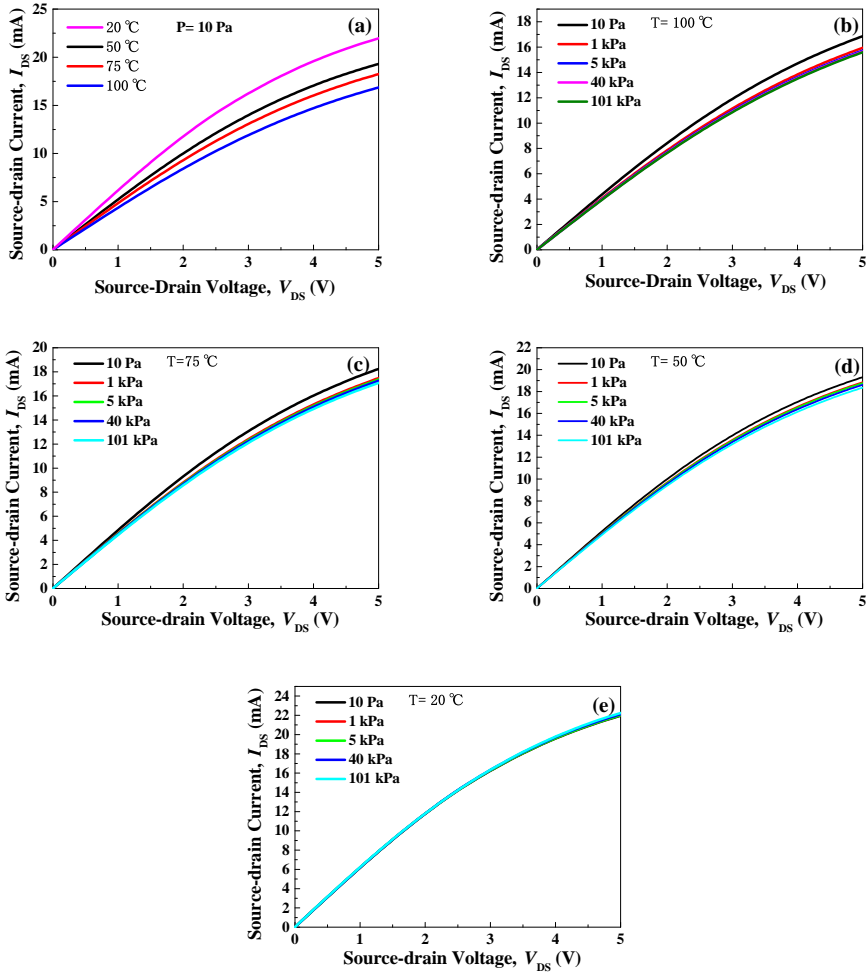


Figure 6.3: Static I-V response of AlGaN/GaN heterostructure pressure sensor at various temperature (a) pressure. (b)  $100^\circ\text{C}$ ; (c)  $75^\circ\text{C}$ ; (d)  $50^\circ\text{C}$ ; (e)  $20^\circ\text{C}$ .

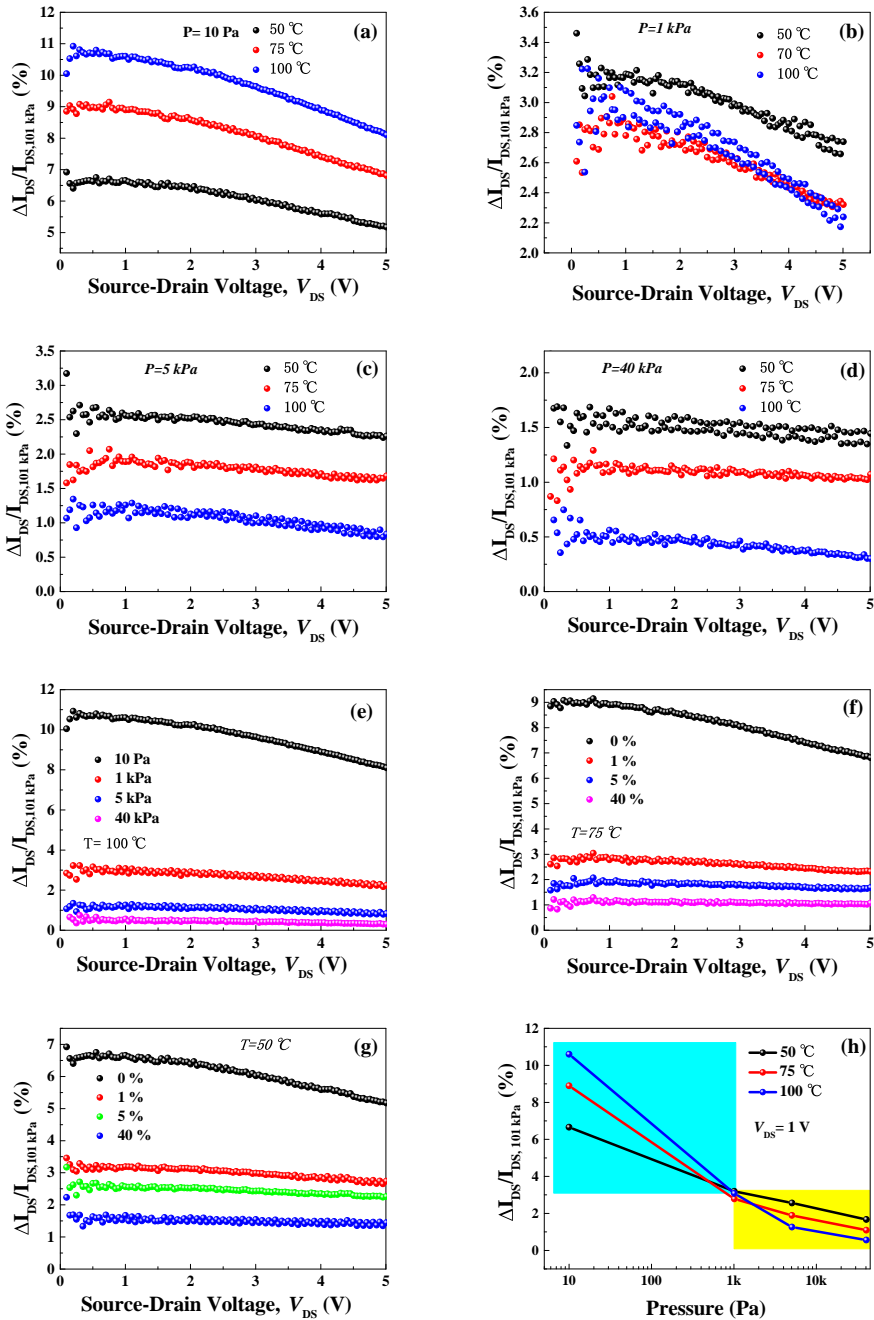


Figure 6.4: Static percent change of the AlGaN/GaN sensor as a function of source-drain voltage versus vacuum pressure (a-d) and temperature (e-g). (h) static percent current change of the device versus vacuum pressure at various temperature ( $V_{DS}=1$  V).

ture [14]. Consequently, the larger deflection introduced more tensile strain in the device, which led to an increase of  $I_{DS}$ . However, when the outside pressure varied from 1 kPa to 40 kPa as shown in Figure 6.4(b-d), the drain current change decreased with the temperature due to the lower piezotronics effect at higher temperature. This could also explain the observed increase in  $I_{DS}$  with decreasing vacuum pressure as shown in Figure 6.4(e-g). Therefore, the static response versus vacuum pressure at different temperature could be separated into 2 phases as shown in Figure 6.4(h). When the vacuum pressure changes from 100 kPa to 1 kPa, the differential pressure between the top and bottom of membrane is too small to deform. In these conditions, the current change decreases with the temperature due to negative characteristics of the AlGaIn/GaN devices. Once the pressure is lower than 1 kPa, the membrane has mechanical deformation introduced by the larger differential pressure between the top and bottom of the membrane. This deformation results in more tensile strain of the device, which increases the drain current. This could also explain the observed increase in  $I_{DS}$  with decreasing vacuum pressure as shown in Figure 6.4(e-g). Moreover, the percent current change of the AlGaIn/GaN sensor had a slight decrease with increasing  $V_{DS}$ . This phenomenon might be caused by the self-heating effect induced at elevated channel temperature [11].

#### 6.2.4. DYNAMIC MEASUREMENT

In order to examine the dynamic characterization of the device, the pressure are increased from 10 Pa to 96 kPa at first and then swept back to around 10 Pa. The pressure was maintained for 300 s at each pressure set point. The setting pressure profile is indicated by the blue curve and the drain current of the sensor versus pressure at  $V_{DS}=20$  mV and  $T=100$  °C by the red curve in Figure 6.5. The drain current decreases when applied vacuum pressure decreases, and the maximum current change is 18.75 %. At 100 °C, the sensitivity varied from 0.005 %/kPa (70 kPa – 40 kPa) to 22.8 %/kPa (600 Pa – 10 Pa). The symmetrical output curve showed a repeatable response to the pressure change. The working power consumption of the device was about 1.8  $\mu$ W. The dynamic percent drain current change of the sensor at various temperatures is shown in Figure 6.6. From these results we see that the dynamic response is larger than that of the static measurement. The current change increases with the increase of temperature at the pressure range of 10 Pa to 5 kPa, as for the static response. The AlGaIn/GaN sensor has a higher change in current at higher vacuum pressure, which indicates the feasibility for the applications in high vacuum and high-temperature. Furthermore, the repeatability of the device response was confirmed according to the drain current response when the pressure was swept back and forth from 600 Pa to 5 kPa for 5 cycles at various temperatures, as shown in Figure 6.7(a). The device shows a high stability at different temperature. The current response rapidly follows the change of pressure as shown in Figure 6.7(b). In addition, the current change increases with the temperatures when the vacuum pressure changes from 5 kPa to 600 Pa, which also explains the AlGaIn/GaN sensor have a large response at higher temperature.

Compared with prior similar works on AlGaIn/GaN pressure sensors, as shown in Table 6-1, the ability of vacuum sensing was tested instead of using the sensor at over-pressure beyond atmospheric. Another difference is that the sensing voltage used in this work is much lower than other AlGaIn/GaN HEMT pressure sensor reported in literature,

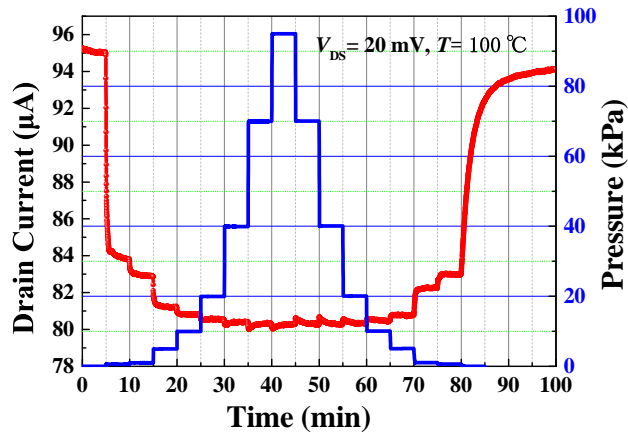


Figure 6.5: The output drain current (red curve) of AlGaN/GaN sensor as a function of pressure at  $V_{DS} = 20$  mV and  $T = 100$  °C (the blue curve shows the set pressure profile).

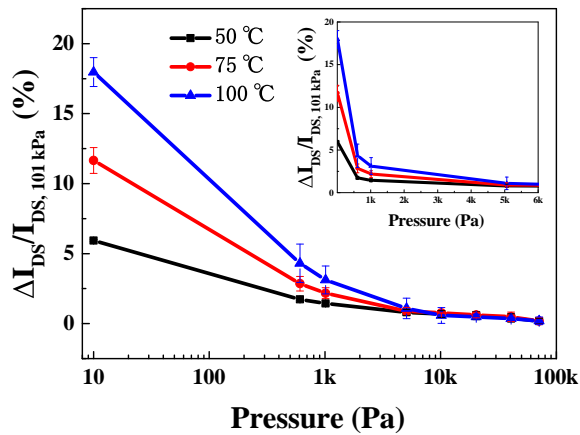


Figure 6.6: Dynamic percent current change of the device versus pressure at various temperature. The inset is the current change versus pressure in linear scale of 0-6 kPa

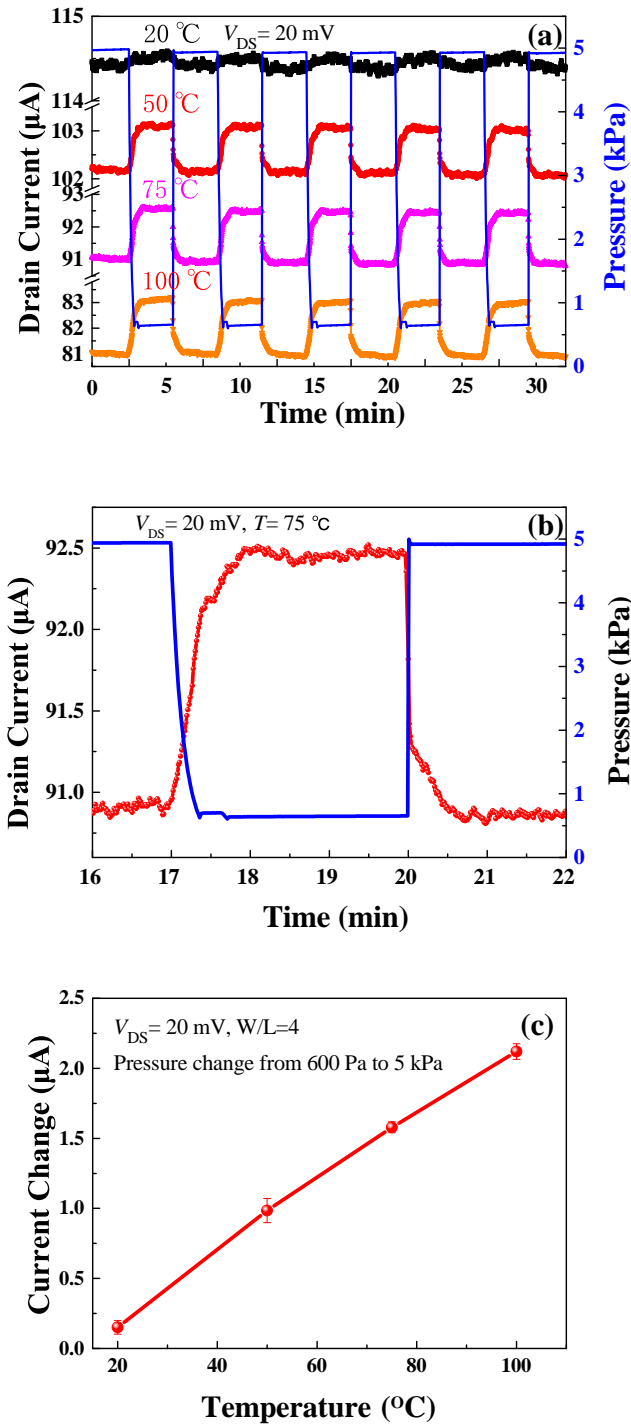


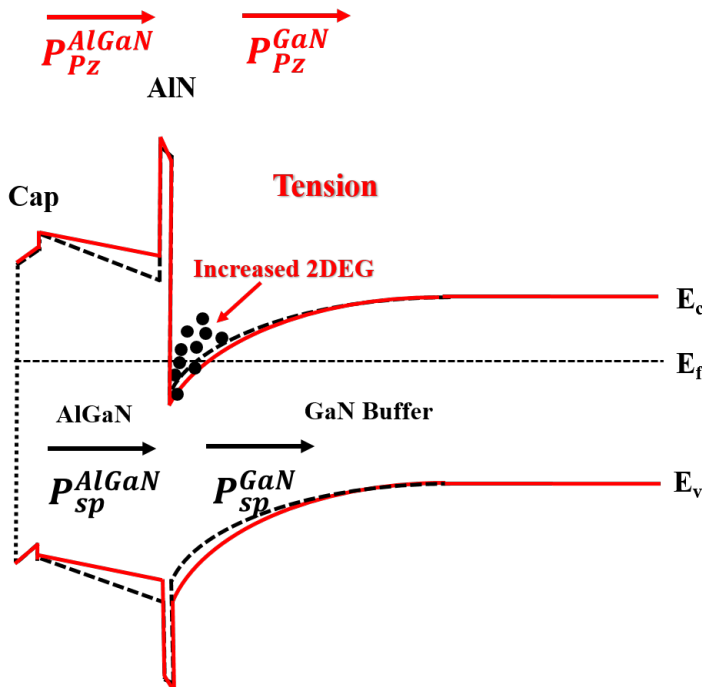
Figure 6.7: (a) Sensing repeatability of device at various temperature and pressure swept from 600 Pa to 5 kPa; (b) Drain current response follow the change of pressure during one cycle; (c) Current change versus the temperature when the pressure changes from 600 Pa to 5 kPa.

Table 6.1: Comparison of the fabricated sensor and prior works on GaN-based pressure sensors

	This work	[17]	[18]	[19]	[20]
Materials	AlGa <sub>N</sub> /Ga <sub>N</sub>	AlGa <sub>N</sub> /Ga <sub>N</sub>	AlGa <sub>N</sub> /Ga <sub>N</sub>	AlInN/Ga <sub>N</sub>	Ga <sub>N</sub>
Max. S	22.8%/kPa	0.76%/kPa	72 $\mu$ V/kPa	0.09%/kPa	0.17%/kPa
$V_{DS}$	0.02 V	1.5 V	1-5 V	0-8 V	/
T ( $^{\circ}$ C)	25-100	25-200	25	25,300	25-400
P (kPa)	0.01-96	101,131	101-1000	101-297	345-1379

suggesting a low sensing power consumption. In addition, our study applied dynamic pressure profiles, which enables the investigation of dynamic behavior and repeatability. Although Durga et al. [17] applied dynamic differential pressure, more pressure stages were adopted in this work. Most importantly, our work presented a non-linear sensitivity to the vacuum level. Especially in the low pressure range below 600 Pa, the maximum sensitivity is significantly larger than other works as 22.8 % at 100  $^{\circ}$ C, which is two magnitudes larger than recent works.

### 6.2.5. WORKING PRINCIPLE OF PRESSURE SENSING

Figure 6.8: Energy band diagram of the AlGa<sub>N</sub>/Ga<sub>N</sub> heterostructure pressure sensor.

The basic working principle was described in section 2.3.3. In order to further understand the working mechanism of the vacuum pressure sensor, the energy band dia-

gram of the AlGaIn/GaN heterostructure under tension condition is illustrated in Figure 6.8. The alignment of spontaneous and piezoelectric polarization is parallel for tensile strain and anti-parallel for compressive strain. Therefore, under tension conditions, the negative piezoelectric polarization charges are introduced along with the AlGaIn/GaN interface and the energy band of AlGaIn close to AlGaIn/AlN interface tilts upward and the energy band of GaN near AlN/GaN interface is bent down. Meanwhile, the increased sheet charge density ( $\sigma_{pol}$ ) results in more free electrons and the 2DEG increasing. In addition, the 2DEG mobility  $\mu$  is dependent on the collision time ( $\tau_c$ ) and the effective mass ( $m_{eff}$ ) of the 2DEG electron. The temperature predominantly changes the collision time ( $\tau_c$ ) and the strain changes the effective mass ( $m_{eff}$ ). The average effective mass is about 0.25 %/100 MPa under biaxial strain from [15], which could be negligible in this case. Ideally, the temperature dependence of the mobility is given by [16].

$$\mu_T = \mu_0 \left( \frac{T}{300} \right)^{-\theta_T} \quad (6.1)$$

Where  $\mu_0$  is the mobility at 300 K and  $\theta_T$  is the temperature coefficient of the mobility,  $\theta_T = 1.5$  used in [35]. Thus, the 2DEG conductivity decreases with the temperature mainly due to the decrease in the 2DEG mobility. Therefore, the base drain current ( $I_{Base}$ ) will decrease with increasing the temperature under atmospheric pressure, which is in accordance with the experimental results in Figure 6.3(a). Considering the temperature effect on the air in the sealed cavity, the pressure in the sealed cavity ( $P_{In}$ ) will increase with increasing the temperature in limit volume according to the ideal gas law,  $PV = nRT$  (where  $P$ ,  $V$  and  $T$  are the pressure, volume and temperature;  $n$  is the amount of substance; and  $R$  is the ideal gas constant). If the vacuum pressure ( $P_{Out}$ ) in the testing chamber keep constant, the difference pressure ( $\Delta P = P_{In} - P_{Out}$ ) between the inside pressure and the outside pressure also increase with increasing the temperature. Then the tensile strain will increase and the piezoelectric polarization enhanced, which results in an increase of 2EDG density. This suggests that the drain current change will increase with the temperature at the same vacuum pressure ( $P_{Out}$ ). And the temperature effect on the drain current change would more obvious at low pressure range ( $P_{Out} < 1$  kPa) because the inside pressure will increase from 101 kPa to 126 kPa when the temperature changes from 25 °C to 100 °C.

The sensor response ( $S$ ) of AlGaIn/GaN heterostructure pressure sensor increase with the temperature given by the following equation:

$$S^\dagger = \left( \frac{\Delta I^\dagger}{I_{Base}^\dagger} \right)_{T^\dagger} = \left( \frac{I_P^\dagger - I_{Base}^\dagger}{I_{Base}^\dagger} \right)_{T^\dagger} \quad (6.2)$$

where  $I_{Base}$  and  $I_P$  are the drain current of the device at air ambient and target pressure condition, respectively.  $\Delta I$  is the current change introduced by the change of pressure. Based on the measurement results, it can be concluded if the temperature  $T$  increases,  $I_{Base}$  will decrease and  $I_P$  will increase. Therefore, the sensor response would increase with the temperature when the vacuum pressures are the same. Based on our innovative structure device, the AlGaIn/GaN heterostructure pressure sensor here presented, indicates that higher sensitivity at higher temperature and vacuum pressure can be obtained.

### 6.3. CHAPTER SUMMARY

In summary, a suspended membrane AlGaIn/GaN heterostructure sensor showed a rapid response in drain current change when exposed to different vacuum pressures, especially in low pressure range. The dynamic percent current change of AlGaIn/GaN heterostructure pressure sensor was 18.75 % under pressure of 10 Pa at 100 °C with a low operating power consumption of 1.8  $\mu$ W. The maximum sensitivity was obtained as 22.8 %/kPa with pressure ranging from 600 Pa to 10 Pa. Also, the static and dynamic measurement results demonstrate the potential of suspended MEMS AlGaIn/GaN heterostructure pressure sensor for low vacuum and high temperature applications. Moreover, the basic mechanism of AlGaIn/GaN heterostructure pressure sensing and temperature effect was discussed. Under the tension strain condition, the negative spontaneous polarization led to the increase of the 2DEG density, resulting in an increase of the drain current. In terms of the effect of temperature, thermal-induced deflection of the membrane also enhanced the increase of the 2DEG density. Therefore, the larger sensor response was detected at a higher temperature.

Due to the small size and low power consumption of the AlGaIn/GaN MEMS chips, the possible applications include in-situ monitoring of vacuum insulation panels and the verification of high vacuum molecular pumps. Additional applications can be found in medical and consumer market or as calibration, especially the high temperature applications.

### REFERENCES

- [1] Z. Gong, Y. Zhang, X. Guo, and Z. Liu, "Wafer-level packaging method for RF MEMS applications using pre-patterned BCB polymer," *Micromachines*, vol. 9, no. 3, p. 93, 2018.
- [2] R. Elfrink et al., "Vacuum-packaged piezoelectric vibration energy harvesters: damping contributions and autonomy for a wireless sensor system," *Journal of Micromechanics and Microengineering*, vol. 20, no. 10, p. 104001, 2010.
- [3] R. Elfrink et al., "Vibration energy harvesting with aluminum nitride-based piezoelectric devices," *Journal of Micromechanics and Microengineering*, vol. 19, no. 9, p. 094005, 2009.
- [4] G. Wu, D. Xu, B. Xiong, Y. Wang, Y. Wang, and Y. Ma, "Wafer-level vacuum packaging for MEMS resonators using glass frit bonding," *Journal of microelectromechanical systems*, vol. 21, no. 6, pp. 1484-1491, 2012.
- [5] F. Völklein and A. Meier, "Microstructured vacuum gauges and their future perspectives," *Vacuum*, vol. 82, no. 4, pp. 420-430, 2007.
- [6] A. Górecka-Drzazga, "Miniature and MEMS-type vacuum sensors and pumps," *Vacuum*, vol. 83, no. 12, pp. 1419-1426, 2009.
- [7] A. Wang, L. Zeng, W. Wang, and Z. Luo, "Static and dynamic simulation studies on the AlGaIn/GaN pressure sensor," *Semiconductor Science and Technology*, vol. 34, no. 11, p. 115022, 2019.

- [8] J. Sun, R. Sokolovskij, E. Iervolino, Z. Liu, P. M. Sarro, and G. Zhang, "Suspended AlGa<sub>N</sub>/Ga<sub>N</sub> HEMT NO<sub>2</sub> Gas Sensor Integrated With Micro-heater," *Journal of Microelectromechanical Systems*, vol. 28, no. 6, pp. 997-1004, 2019.
- [9] J. Sun et al., "Suspended tungsten trioxide (WO<sub>3</sub>) gate AlGa<sub>N</sub>/Ga<sub>N</sub> heterostructure deep ultraviolet detectors with integrated micro-heater," *Optics Express*, vol. 27, no. 25, pp. 36405-36413, 2019/12/09 2019.
- [10] J. Sun et al., "Suppression of persistent photoconductivity AlGa<sub>N</sub>/Ga<sub>N</sub> heterostructure photodetectors using pulsed heating," *Applied Physics Express*, vol. 12, no. 12, p. 122007, 2019.
- [11] E. Le Boulbar et al., "Effect of bias conditions on pressure sensors based on AlGa<sub>N</sub>/Ga<sub>N</sub> High Electron Mobility Transistor," *Sensors and Actuators A: Physical*, vol. 194, pp. 247-251, 2013.
- [12] J. Sun et al., "Characterization of an Acetone Detector Based on a Suspended WO<sub>3</sub>-Gate AlGa<sub>N</sub>/Ga<sub>N</sub> HEMT Integrated With Microheater," *IEEE Transactions on Electron Devices*, vol. 66, no. 10, pp. 4373-4379, 2019.
- [13] A. S. Yalamarthy and D. G. Senesky, "Strain-and temperature-induced effects in AlGa<sub>N</sub>/Ga<sub>N</sub> high electron mobility transistors," *Semiconductor Science and Technology*, vol. 31, no. 3, p. 035024, 2016.
- [14] J. Ren, M. Ward, P. Kinnell, R. Craddock, and X. Wei, "Plastic deformation of micro-machined silicon diaphragms with a sealed cavity at high temperatures," *Sensors*, vol. 16, no. 2, p. 204, 2016.
- [15] M. Chu, A. D. Koehler, A. Gupta, T. Nishida, and S. E. Thompson, "Simulation of AlGa<sub>N</sub>/Ga<sub>N</sub> high-electron-mobility transistor gauge factor based on two-dimensional electron gas density and electron mobility," *Journal of Applied Physics*, vol. 108, no. 10, p. 104502, 2010.
- [16] S. Vitanov, V. Palankovski, S. Maroldt, and R. Quay, "High-temperature modeling of algan/gan hemts," *Solid-State Electronics*, vol. 54, no. 10, pp. 1105-1112, 2010.
- [17] D. Gajula, I. Jahangir, and G. Koley, "High Temperature AlGa<sub>N</sub>/Ga<sub>N</sub> Membrane Based Pressure Sensors," *Micromachines*, vol. 9, no. 5, p. 207, 2018.
- [18] X. Tan et al., "High performance AlGa<sub>N</sub>/Ga<sub>N</sub> pressure sensor with a Wheatstone bridge circuit," *Microelectronic Engineering*, vol. 219, p. 111143, 2020.
- [19] C. A. Chapin, R. A. Miller, K. M. Dowling, R. Chen, and D. G. Senesky, "In-AlN/Ga<sub>N</sub> high electron mobility micro-pressure sensors for high-temperature environments," *Sensors and Actuators A: Physical*, vol. 263, pp. 216-223, 2017.
- [20] N.-I. Kim et al., "Piezoelectric Pressure Sensor Based on Flexible Gallium Nitride Thin Film for Harsh-Environment and High-Temperature Applications," *Sensors and Actuators A: Physical*, p. 111940, 2020.



# 7

## CONCLUSIONS AND RESEARCH OUTLOOK

### 7.1. CONCLUSIONS

The research objective of this thesis is to develop a MEMS sensor platform utilizing GaN-based materials for harsh environment applications. The design, fabrication, packaging and measurement of a vacuum pressure sensor, a deep UV photodetector, and a gas sensor, three possible components of this platform, are presented and discussed.

The properties of GaN material and AlGaIn/GaN heterostructures studied, in particular the polarization effect in GaN semiconductors, the 2DEG forming in AlGaIn/GaN heterostructures, the piezoelectric, optical and chemical sensing mechanisms in these structures, clearly indicate the potential of the envisioned sensing platform for a variety of applications.

The process flow developed for the platform is stable, reproducible and of low complexity and is therefore suitable for wafer scale fabrication of the sensors and can be enriched with additional modules, such as the membrane fabrication or the metal oxide gate, for the implementation of specific sensor functionalities.

Another interesting outcome of this research is the low ohmic contact achieved by developing a suitable layer stack and annealing process. The average value of the specific contact resistance achieved is about  $3.71 \times 10^{-5} \Omega * cm^2$ . The analysis of the package influence on device performance in terms of power efficiency and stability of signal output resulted in a preferred choice of the CQFN package over the COB package. The drop in drain current after the removal of the substrate to form the membrane has been related to three possible reasons: higher temperature introduced by self-heating, the more compressive strain by the DRIE process and the source of 2DEG from the interlayer between GaN layer and substrate. The combined effect of micro-heater heating and self-heating on the membrane has been studied and modeled the first time. From the temperature and humidity study, it is clear that the device is not affected under high relative humidity ambient while the temperature influence needs to be taken into account and compen-

sated.

AlGaN/GaN HEMT sensors with an integrated micro-heater on the suspended membrane have been designed and characterized for gas detection. The adoption of nano  $\text{WO}_3$  as a functional layer result in the capability to detect low concentration of 100 ppb  $\text{NO}_2/\text{N}_2$  at about 300 °C. When exposed to a 1 ppm  $\text{NO}_2$  gas, a high sensing sensitivity of 1.1% with a response (recovery) time of 88 seconds (132 seconds) is obtained.

In addition, ppm level acetone gas response of a packaged sensor has also been investigated and an opposite behavior as for  $\text{NO}_2$  gas observed. The temperature of the sensor can be adjusted by the integrated micro-heater and the membrane structure was designed for operation at high temperature and low power. At 300 °C, a drain current change  $\Delta I_{DS}$  of 0.31 mA, as well as a high sensitivity of 25.7 % for 1000 ppm acetone were observed. Transient measurements indicated stable operation and good repeatability at different temperatures. For 1000 ppm acetone concentration  $t_{Res}$  ( $t_{Rec}$ ) reduced from 147 (656) s at  $V_H=3.5$  V (210 °C) to 48 (319) s at  $V_H=4$  V (300 °C). Moreover, the response to 1000 ppm acetone gas was significantly larger than for ethanol, ammonia and CO gases at the same 1000 ppm concentration. In fact, the introduced suspended gate recess Pt/AlGaN/GaN heterostructure  $\text{NO}_2$  gas sensor integrated with a micro-heater resulted in a dramatic enhancement of the performance of the AlGaN/GaN devices. The sensitivity and current change of AlGaN/GaN heterostructure to 1-200 ppm  $\text{NO}_2/\text{air}$  are increased up 20 times and 12 times compared to conventional gate devices respectively with the faster response time. The suspended membrane structure and integrated micro-hotplate also improve response time and sensitivity by adjusting the optimum working temperature with low power consumption. The sensitivity (response time) increases from 0.75 % (1250 s) to 3.5 % (75 s) toward 40 ppm  $\text{NO}_2/\text{air}$  when temperature increases from 60 °C to 300 °C. The repeatability and selectivity of the sensor have also been demonstrated. The characteristics of the here presented suspended nano-film  $\text{WO}_3$  functional gate and gate-recess AlGaN/GaN devices integrated with a micro-heater, form an encouraging first step towards the development of high accuracy and fast response gas sensor in industrial and medical applications.

The suspended  $\text{WO}_3$  gate AlGaN/GaN heterostructure was also used to realize a photodetector for deep UV response. Our devices show a high response to the deep UV wavelength, high responsivity ( $1.67 \times 10^4$  A/W at 240 nm) and a sharp cut-off wavelength of 275 nm. Besides the high gain of AlGaN/GaN heterostructure based on 2DEG, the dynamic response of photodetector was optimized by three heating methods.

The photodetector shows a rapid response and recovery (175 s) time under 240 nm illumination at the DC heating temperature of 150 °C. The relative long decay time introduced by the PPC effect is an important disadvantage limiting the wide application of GaN-based photodetectors. To overcome this issue we investigated possible alternatives. We demonstrated that the pulsed heating method effectively reduces the decay time of the AlGaN/GaN heterostructure photodetectors, going from 175 s by DC heating to 116 s by 50 Hz pulsed heating at the same power (280 mW). With the same pulse duty cycle and 50 Hz pulsed heating, a reduction of 30-45 % in decay time is measured compared to DC heating. More interesting, the persistent photoconductivity (PPC) effect can be eliminated by a novel method: mono-pulse heating reset (MHR) by applying a pulse voltage to the micro-heater after the removal of UV illumination. Under the illumination of both

UVA and UVC, the recovery time was reduced from hours to seconds without reducing the high responsivity and stability of the photodetector. This novel method solved the long-term problem of long decay time introduced by PPC of GaN-based photoconductive photodetectors. This mono-pulse heating reset method could also be applied to suppress the PPC effect in other photo-response materials. The here presented suspended AlGaIn/GaN devices integrated with a micro-heater, form an encouraging first step towards the development of high accuracy and fast response 2DEG-based deep ultraviolet detectors.

The suspended membrane AlGaIn/GaN heterostructure is also quite suitable for vacuum detection. The sensor showed a rapid response in drain current change when exposed to different vacuum pressures, especially in low pressure range. The dynamic percent current change of the AlGaIn/GaN heterostructure pressure sensor was 18.75 % under pressure of 10 Pa at 100 °C with a low operating power consumption of 1.8  $\mu$ W. The maximum sensitivity was obtained as 22.8 %/kPa with pressure ranging from 600 Pa to 10 Pa. Also, the static and dynamic measurement results demonstrate the potential of suspended MEMS AlGaIn/GaN heterostructure pressure sensors for high vacuum and high temperature applications.

## 7.2. RESEARCH OUTLOOK

GaN devices are already commercially available for high frequency and power devices. However, their applications in sensing is still underdeveloped and under-commercialized. Based on previously reported results and the achievements reported in this thesis, it is foreseeable that AlGaIn/GaN-based sensors will be implemented in a wide range of sensing applications in the near future.

Additional research questions and possible further development that could be considered as follow up are here briefly mentioned.

1.  $\text{WO}_3$  gate AlGaIn/GaN heterostructure gas sensor shows high sensitivity and selectivity to acetone gas, which has a huge potential in medical application, such as the acetone detection in exhale gases to distinguish type II diabetes. More measurement under lower acetone concentration (0.1-10 ppm) is necessary to verify whether this gas sensor meets the requirements.
2. Since the  $\text{WO}_3$  has proved to selectively respond to acetone, other metal-oxides, polymers or nano-structures should be considered as functionalized gate region of the sensor. These multifunctional sensors could be integrated into one chip for detecting several gases at the same time. Combined with artificial intelligence (AI) or machine learning, the gas sensor array could be a smart system in applications, such as electronic noses or battlefield awareness.
3. The mono-pulse heating method has already proven to remove the PPC effect of UV detectors. It is worth investigate if it can be employed to reduce the recovery time of gas sensors as the recovery time of 1-2 mins is still too long for some safety and emergency applications.
4. According to our results from **chapter 5**, the AlGaIn/GaN heterostructure-based

photodetector exhibits high responsivity and fast recovery by mono-pulse heating reset method. This in-suit mono-pulse heating method successfully solves the PPC effect that has long plagued photoconductive type detectors. It might be interesting to explore if this method could be applied to other photoconductive detectors based on other materials to remove the PPC effect, to make them of interest for fire detection, missile monitoring in IOT applications.

5. Based on the measurements reported in **chapter 6**, the GaN-based sensors can reliably operate at a very high temperature ( $> 400$  °C) and medium vacuum pressure ( $< 0.1$  Pa). However, more tests under high temperature and high vacuum pressure conditions are necessary to establish device reliability.

# APPENDIX A

## AlGaIn/GaN HEMT Sensor Fabrication Flowchart

### **Cleaning**

Cleaning: acetone 10-15 minutes, IPA 5 minutes, DI water 5 minutes,  $H_2SO_4 : H_2O_2$  (3:1) 10 minutes/ BOE(BHF) 5 minutes, DI water 10 minutes and dry

### **Mesa isolation**

Lithography: define the mesa windows, positive photoresist 6130

Inductively coupled plasma (ICP) etching: AST Cirie-200, 300 W/15 W,  $Cl_2$  40 sccm,  $Ar_2$  5 sccm,  $BCl_3$  5 sccm, 90-100 nm

Inorganic cleaning:  $H_2SO_4 : H_2O_2$  (3:1 4:1) 10 minutes/ BOE(BHF) 5 minutes, DI water 10 minutes and dry

Organic cleaning: acetone 10-15 minutes, IPA 5 minutes, DI water 10 minutes and dry

### **Ohmic contact metallization**

Lithography: define the ohmic contact windows, negative photoresist L-300

E-beam evaporation: Ti/Al/Ti/Au: 20/110/40/50 nm

Lift-off: photoresist removal 10 minutes, T=90 °C

Organic Cleaning: acetone 10 minutes, IPA 5 minutes, DI water 10 minutes and dry

Annealing: in  $N_2$ , 850 °C, 47 seconds

Organic Cleaning: acetone 10 minutes, IPA 5 minutes, DI water 10 minutes and dry

### **Micro-heater layer**

Silicon Oxide deposition: PECVD, thickness=200 nm

Lithography: define the micro-heater windows, negative photoresist L-300

E-beam evaporation: Ti/Pt: 30/200 nm

Lift-off: photoresist removal 15 minutes, T=90 °C

Organic Cleaning: acetone 10 minutes, IPA 5 minutes, DI water 10 minutes and dry

Silicon Oxide deposition: PECVD, thickness=300 nm

### **Via & interconnect metallization**

Lithography: define the via windows, positive photoresist 304

Silicon oxide etching: BOE solution, thickness=500 nm

Cleaning: DI water 10 minutes and dry

Lithography: define the interconnect metal windows, negative photoresist L-300

E-beam evaporation: Ti/Au: 20/300 nm

Lift-off: photoresist removal 15 minutes, T=90 °C

Organic cleaning: acetone 10 minutes, IPA 5 minutes, DI water 10 minutes and dry

Silicon Oxide deposition: PECVD, thickness=300 nm

### **Substrate polish & thinning**

Polish & thinning: silicon substrate, thickness=400  $\mu$ m

Wax cleaning: wax removal, DI water 10 minutes and dry

Table I Parameters of epitaxial wafer

Parameters	Nominal value
Thickness of GaN Cap Layer	3 nm
AlGaIn composition (%Al)	26%
AlGaIn thickness (nm)	25 nm
AlN thickness	1 nm
Thickness of GaN ( $\mu\text{m}$ )	2 $\mu\text{m}$
Thickness of buffer layer ( $\mu\text{m}$ )	$\sim 1 \mu\text{m}$
Thickness of Si (111) substrate ( $\mu\text{m}$ )	1000 $\mu\text{m}$
Sheet resistivity (ohms/sq)	290 $\Omega/\square$
Mobility ( $\text{cm}^2/\text{V}\cdot\text{sec}$ )	$>1500$ for Si substrate
Sheet concentration ( $/\text{cm}^2$ )	$\sim 1 \times 10^{13}$
Bow	$<60 \mu\text{m}$

Organic cleaning: acetone 10 minutes, IPA 5 minutes, DI water 10 minutes and dry  
**DRIE/Pad windows**

Silicon oxide deposition: PECVD, backside, thickness= $5 \mu\text{m}$

Lithography: define the backside cavity windows, positive photoresist AZ4620

ICP/RIE etching: backside, thickness= $5 \mu\text{m}$

Organic cleaning: acetone 10 minutes, IPA 5 minutes, DI water 10 minutes and dry

Lithography: define the pads windows, positive photoresist 304

Silicon oxide etching: BOE solution, thickness= $700 \text{ nm}$

Cleaning: DI water 10 minutes and dry

**Gate recess technique (two-step etching)**

Oxygen plasma: AST Cirie-200, ICP/RF= $450 \text{ W}/150 \text{ W}$ , Oxygen plasma, 180 seconds

Wet etching:  $\text{HCl} : \text{H}_2\text{O}$  (1:4), 60 seconds

Cleaning: DI water 10 minutes and dry

**Gate function materials deposition (for metal)**

Lithography: define the gate windows, negative photoresist L-300

E-beam evaporation: Cr/Pt= $2/10 \text{ nm}$

Lift-off: photoresist removal 10 minutes,  $T=90 \text{ }^\circ\text{C}$

Organic cleaning: acetone 10 minutes, IPA 5 minutes, DI water 10 minutes and dry

**Gate function materials deposition (for metal oxide)**

RF sputtering:  $\text{WO}_3=10 \text{ nm}$

Lithography: define the gate windows, positive photoresist

Wet etching:  $\text{HCl} : \text{H}_2\text{O}$  solution

Organic cleaning: acetone 10 minutes, IPA 5 minutes, DI water 10 minutes and dry

**Membrane Forming**

DRIE etching:  $400 \mu\text{m}$

Cleaning: DI water and dry

Laser Dicing:  $2 \text{ mm} \times 2 \text{ mm}$ ,  $1 \text{ mm} \times 1 \text{ mm}$

# APPENDIX B

## UV optical source information

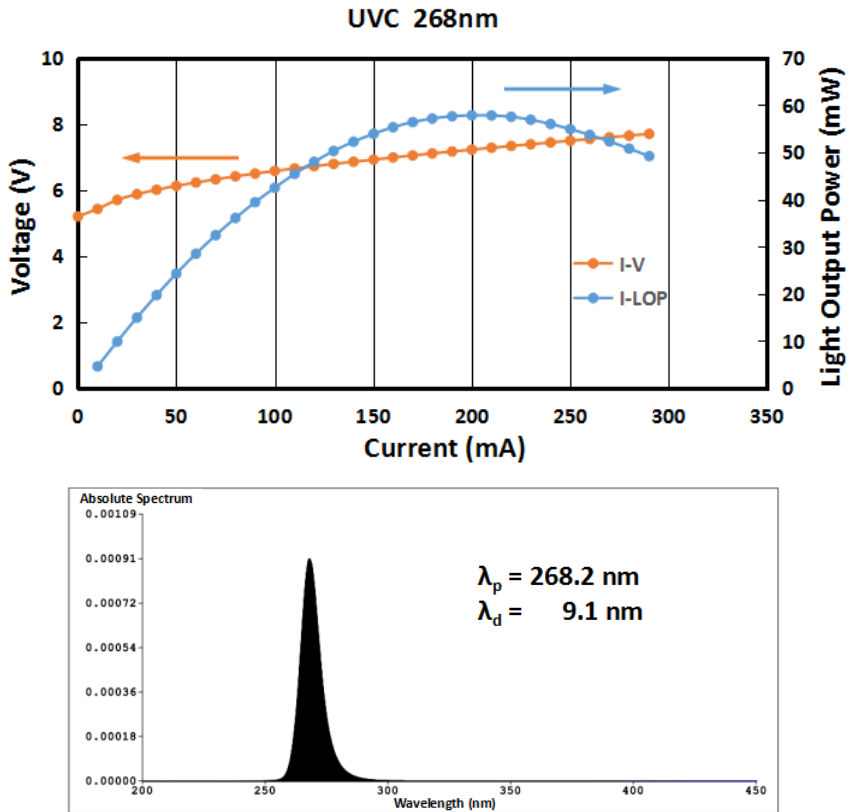


Figure 1: UVC light source: I-V, I-LOP curve and light spectrum

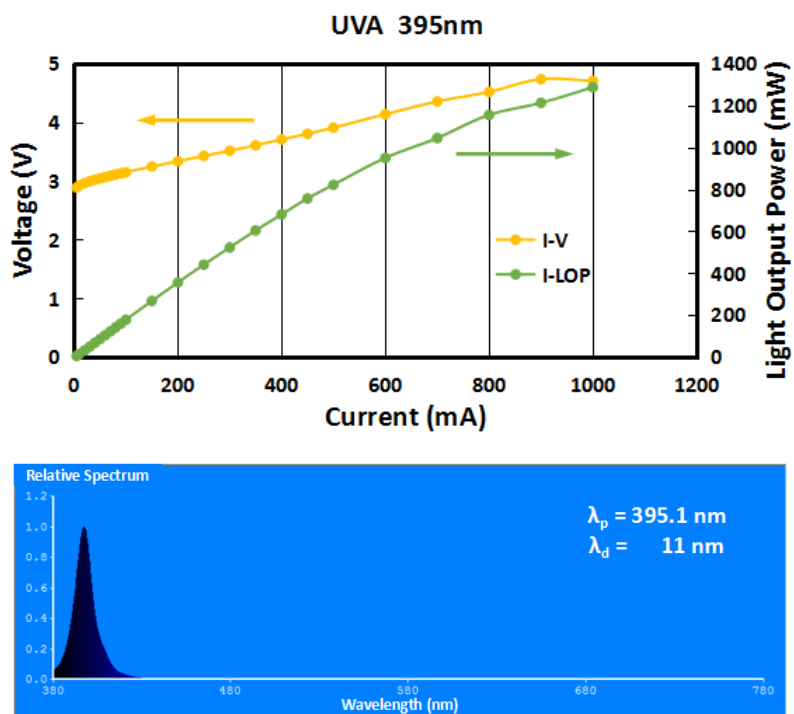


Figure 2: UVA light source: I-V, I-LOP curve and light spectrum

# ACKNOWLEDGEMENTS

There are many people who helped me during my Ph.D. research and kept my life full of happiness in the past five years. Writing this last part of my thesis, I am so full of memories and gratitude to these special people in my life who support me, uplift me, comfort me and bring joy to my soul.

First and foremost, I would like to sincerely thank my promotors, prof. dr. Pasqualina M. Sarro and prof. dr. Guoqi Zhang, for the opportunity to study and research at TU Delft, one of the top universities in the world, for all their guidance, great support, encouragement, advice and patience throughout the past five years. It is a great happiness to get guidance from one of them. I can't have imagined having two great advisors and mentors for my Ph.D. study.

When looked back the beginning time of Ph.D., I am particularly grateful to my daily supervisors dr. Fabio Santagata and dr. Elina Iervolino for their valuable and constructive suggestions during the planning and development of this research work. Their willingness to give their time and help so generously has been very much appreciated.

My special thanks must go to prof. dr. Zewen Liu in Tsinghua University. He is not only my former M.Sc. supervisor who introducing me to the MEMS world, but also life mentor encouraging and supporting when I confused or need help. Without his help and support I can't start and finish the Ph.D. program smoothly and successfully.

I am grateful to China Advanced Semiconductor Alliance (CASA), Shunyi government of Beijing municipality, Shenzhen Institute of Wide Bandgap Semiconductors (WinS) and the Key-Area Research and Development Program of GuangDong Province for supporting my research project both financially and technologically (2019B010131001). I am deeply indebt to Mrs. L. Wu, the president of CASA, who has been giving me the trust during the past 4 years, to Mr. Y.H. Zhao, the president of Wins, who generously supports the TUD-WinS cooperation. Thanks also go to Dr. Wenbo Wang and Ms. Yan Li for their guidance and operational support.

During my research I have received immense support from Institute of Semiconductor (IOS), Beijing Delft Institute of Intelligent Science and Technology (BD-IIST). I am grateful to prof. dr. Junxi Wang, prof. dr. Xuecheng Wei, Ms. Sixing Guo, Ms. Li Wang and all the technicians of Institute of Semiconductor, CAS, for their great support to my research. My special thanks go to prof. dr. Banghong Zhang, dr. Teng Zhan, prof. dr. Jingchuan Zhang, prof. dr. Jianguo Liu, prof. dr. Zhijie Wang, prof. Hui Zhu, Wei Li and all members of CAS basketball group, for the best memories during my Ph.D., even in my life.

I am truly thankful to my BRC colleagues: dr. Hongyu Tang, dr. Fengze Hou, dr. Mingzhi Dong, dr. Robert Sokolovskij for their help. Especially thanks to dr. Fengze Hou and dr. Hongyu Tang for the help to settle down in Delft. Especially, that night (from sunset to sunrise) we revised the paper together at the Delft office would be remembered forever. They could help me with any issues i encountered at any time and i

truely value the friendship we have developed.

I send my great thanks to all the members of the research group of prof. Zhang and prof. P. M. Sarro: Dong Hu, Luke Middelburg, prof. Sten Vollebregt, Joost van Ginkel, Joost Romijn, dr. Jia Wei, Zhen Cui, dr. Boyao Zhang, Tianyi Jin, prof. Huaiyu Ye, prof. Xianping Chen, prof. Jiajie Fan, dr. Leandro Nicolas Sacco, Romina Sattari, Leo Guo, Manjunath Ramachandrappa Venkatesh, Brahim Mansouri, Yue Sun, Milica Dostanic, Mojtaba Jahangiri, for their effort to make our research group home to everyone and a happy place to work. Special thanks to dr. Henk van Zeijl for helping me for the packaging and help, and thank Dong for our great cooperation of pressuer sensing. I would also like to thank Leo Guo for helping me with the translation of the summary to Dutch, thank Luke for his great pressure testing setup and helping translate the propositions to Dutch.

I wish to thank the members of my dissertation committee: prof. R. H. J. Fastenau, prof. P. J. French, prof. J. A. Ferreira, prof. X. J. Fan, prof. Y. F. Qiu for generously offering their time, support, guidance and good will throughout the preparation and review of this document.

I want to sincerely thank all my colleagues, from all the organizations that I have worked in or with, for offering their kind help during my PhD program. Without their contribution, I could not fulfill my PhD work so successfully. Though I may not have chances to express my gratitude personally, their kind help is highly and forever appreciated.

Last but not the least, I wish to thank my parents, my family, friends for their support and encouragement through my study.

# CURRICULUM VITÆ

## Jianwen SUN

16-06-1990      Born in Anhui, China.

### EDUCATION

- 2015–2020      PhD in Microelectronics  
Delft University of Technology, Delft, The Netherlands  
*Thesis:*      Design, Fabrication and Characterizations of Al-  
GaN/GaN Heterostructure Sensors  
*Promotor:*    Prof. dr. P. M. Sarro  
*Promotor:*    Prof. dr. G. Q. Zhang
- 2012–2015      Master of Engineering in Microelectronics  
Tsinghua University, Beijing, China  
*Thesis:*      MEMS PM<sub>2.5</sub> Sensor Development  
*Promotor:*    Prof. dr. Z. W. Liu
- 2007-2011      Bachelor in Electrical Automation  
Anhui University of Science and Technology



# LIST OF PUBLICATIONS

## JOURNALS PAPERS

10. **Jianwen Sun**, Shuo Zhang, Teng Zhan, Xiaoyan Yi, Junxi Wang, Jinmin Li, Zewen Liu, Pasqualina M. Sarro, and Guoqi Zhang. A high responsivity and controllable recovery ultraviolet detector based on a  $WO_3$  gate AlGaIn/GaN heterostructure with an integrated micro-heater[J]. *Journal of Materials Chemistry C*, 2020, 8(16): 5409-5416. (Back cover)
9. **Jianwen Sun**, Dong Hu, Sten Vollebregt, Zewen Liu, Pasqualina M. Sarro, and Guoqi Zhang. power AlGaIn/GaN MEMS pressure sensor for high vacuum application" *Sensors and Actuators A: Physical*. (Under review)
8. **Jianwen Sun**, Teng Zhan, Robert Sokolovskij, Zewen Liu, Pasqualina M. Sarro, and Guoqi Zhang, Enhanced Sensitivity Gate-recessed Pt/AlGaIn/GaN Heterostructure  $NO_2$  Sensor Fabricated by Oxygen-based Etching Method, To be submitted to *Sensors and Actuators B: Chemical*.
7. **Jianwen Sun**, Sokolovskij R, Iervolino E, Zewen Liu, Pasqualina M. Sarro, and Guoqi Zhang, Characterization of an Acetone Detector Based on a Suspended  $WO_3$ -Gate AlGaIn/GaN HEMT Integrated With Microheater[J]. *IEEE Transactions on Electron Devices*, 2019, 66: 4373-4379.
6. **Jianwen Sun**, Sokolovskij R, Iervolino E, Zewen Liu, Pasqualina M. Sarro, and Guoqi Zhang. Suspended AlGaIn/GaN HEMT  $NO_2$  Gas Sensor Integrated With Micro-heater[J]. *Journal of Microelectromechanical Systems*, 2019, 28(6): 997-1004.
5. **Jianwen Sun**, Zhan T, Liu Z, Xiaoyan Yi, Junxi Wang, Pasqualina M. Sarro, and Guoqi Zhang. Suspended tungsten trioxide ( $WO_3$ ) gate AlGaIn/GaN heterostructure deep ultraviolet detectors with integrated micro-heater[J]. *Optics Express*, 2019, 27(25): 36405-36413.
4. **Jianwen Sun**, Zhan T, Liu Z, Xiaoyan Yi, Junxi Wang, Pasqualina M. Sarro, and Guoqi Zhang. Suppression of persistent photoconductivity AlGaIn/GaN heterostructure photodetectors using pulsed heating[J]. *Applied Physics Express*, 2019, 12(12): 122007.
3. Hongyu Tang, **Jianwen Sun**, Fengze Hou, Sten Vollebregt, Pasqualina M. Sarro, Xuejun Fan, Willem van Driel and Guoqi Zhang. Biosensing options for the detection of respiratory viruses. To be submitted to *BME Frontiers*. (Co-first author)
2. Santagata F, **Jianwen Sun**, Iervolino E, et al. System in package (SiP) technology: fundamentals, design and applications[J]. *Microelectronics International*, 2018, 35(4): 231-243.
1. Hong H, **Jianwen Sun**, Wu C, et al. High Performance Mixed Potential Type  $NO_2$  Gas Sensor Based on Porous YSZ Layer Formed with Graphite Doping[J]. *Sensors*, 2019, 19(15): 3337.

## CONFERENCE PAPERS

1. Sokolovskij R, **Jianwen Sun**, Santagata F et al. Precision recess of AlGaIn/GaN with controllable etching rate using ICP-RIE oxidation and wet etching[J]. *Procedia engineering*, 2016, 168: 1094-1097.